1980

Evaluation of the fracture of the I79 back channel girder and the electroslag welds in the I79 complex, October 1980, 101p.

J. W. Fisher

A. Pense

J. D. Wood

J. H. Daniels

Lehigh University

AN EVALUATION OF THE FRACTURE OF THE I79 BACK CHANNEL GIRDER AND THE ELECTROSLAG WELDS IN THE I79 COMPLEX

by
J. W. Fisher
A. W. Pense
J. D. Wood
J. H. Daniels
B. T. Yen
D. A. Thomas
H. Hausammann
W. Herbein
B. R. Somers
H. T. Sutherland

Report No. 425-1(80)

Fritz Engineering Laboratory

COMMONWEALTH OF PENNSYLVANIA

Department of Transportation

Research Division

Wade L. Gramling, P.E. - Chief Research Engineer
Istvan Janauschek, P.E. - Research Coordinator

Project 77-5: Evaluation of Glenfield Bridge Fracture

AN EVALUATION OF THE FRACTURE OF THE I79 BACK CHANNEL GIRDER AND THE ELECTROSLAG WELDS IN THE I79 COMPLEX

by
J. W. Fisher
A. W. Pense
J. D. Wood
J. H. Daniels
B. T. Yen
D. A. Thomas
H. Hausammann
W. Herbein
B. R. Somers
H. T. Sutherland

LEHIGH UNIVERSITY

Office of Research

Bethlehem, Pennsylvania

October 1980

Fritz Engineering Laboratory Report 425-1(80)

TABLE OF CONTENTS

TABLE OF CONTENTS (continued)

ABSTRACT

A large crack was discovered to form in a girder of the I-79 Glenfield Bridge over the back channel of the Ohio River near Pittsburgh on January 28, 1977. A section of the girder containing the crack was removed from the structure for investigation. This report presents the results of that study. It includes detailed tests of the base metal and weld metal, metallographic and fractographic studies of the electroslag weldment and repair welds where the fracture originated, an analysis of the crack extension under cyclic loads and at instability, and recommendations for retrofitting.

After the fracture was discovered, other electroslag welds were found to exist in the 750 ft. arch span and in other locations in the back channel bridges and approach ramps. Nondestructive tests on the weldments indicated rejectable defects and cracks. Studies were also carried out on sample cores of the electroslag weldments of these structures so that their long term resistance to fatigue and fracture could be assessed and recommendations for retrofitting any defective weldments developed.

To supplement these studies, strain measurements were acquired during the repair of the fractured section. In addition, stress history studies, under random variable truck traffic, were carried out to assess the significance of repeated loads and evaluate the thermal stress response of the structure.

1. INTRODUCTION

On January 28, 1977, a tugboat captain spotted a large crack developing in the I79 Glenfield Bridge over the back channel of the Ohio River at Neville Island near Pittsburgh[1]. When first observed, the flange and the lower portion of the web were cracked. Over a period of about one hour, the crack was observed to move up the web to the bottom of the top flange.

The cracked girder is part of a continuous structure with three spans of 226 ft. (68.9 m), 350 ft. (106.7 m) and 226 ft. (68.9 m). The fracture occurred in the middle of the 350 ft. (106.7 m) long center span. The location of the fracture, the plan view and the cross-section of the bridge are shown in Fig. 1.

The fracture occurred in fascia girder G4. The superstructure consists of two main girders G3 and G4 with transverse floor beam trusses spaced at 25 ft. (7.6 m) supporting W24x68 stringers. The girders and stringers support an 8-1/2 in. (216 mm) noncomposite reinforced concrete slab. The adjacent superstructure which carries the southbound traffic also has two main girders (G1 and G2). The two superstructures are connected by diaphragms which are designed to transmit live load between the structures.

Due to the fractured girder, the deflection at midspan increased about 5 in. (127 mm) without significant damage to the road surface. The crack in the tension flange was opened about 2 in. (51 mm) when discovered. Figure 2 shows the cracked girder and the flange separation.

Inspection also showed that the top flange of girder G4 had moved laterally about an inch in the vicinity of the fracture. This movement

sheared off the narrow concrete fillet adjacent to the east edge of the top flange for a distance of 20 to 30 ft. (6.1 to 9.1 m) each side of the fracture, because of the forces developed from the girder deflection. The bottom flange also moved laterally a small amount.

The bridge was opened to traffic on September 3, 1976. The bridge carries the traffic in four lanes over the Ohio River. At the fractured cross-section the girder is composed of an 11 ft. x 1/2 in. (3.35 m x 12.77 mm) web and 3-1/2 in. x 30 in. (89 mm x 76a mm) flanges. At the crack location the web and the bottom flange were fabricated from A588 steel.

Near the crack, a vertical stiffener was welded to the web; it was not welded to the bottom flange (tight fit). At the casualty section, an electroslag groove weld (shop weld) was used to splice the 3.5 in. thick plates that form the tension flange. Shop records indicated that repairs had been made to the original weld. Radiographs were made before and after the repair and noted on the NDT reports, but these records were never subsequently located. About 2 in. from the fractures cross-section, a submerged arc welded splice had been made in the web. The geometry of the girder and the crack are shown schematically in Fig. 3.

On January 28, 1977, the day when the fractured web was observed, the temperature dropped 25° to 35° F (from 14° C to 19° C) within 90 minutes as a cold front passed through the area. On January 17, 1977, the temperature had reached a low of -17° F (-27° C), when an earlier cold front had passed through the area.

The fractured section was inspected by J. W. Fisher; Pennsylvania Department of Transportation; Federal Highway Administration; and

Richardson, Gordon and Associates personnel on February 6, 1977. The photographs shown in Fig. 2 indicate the condition of the member at that time.

A large section of the girder containing the crack in the tension flange was removed from the structure for investigation. Prior to removal of the fractured section, pieces of angle were welded to the girder web as illustrated in Fig. 4. This prevented the crack surfaces from being rubbed together when the section was cut from the member. Figure 5 shows the sections of the casualty girder that were removed. Material from these sections was used to evaluate the characteristics of the base metal and weld metal. These results are discussed in Section 3. Detailed fractographic studies were conducted on the fracture surface and these results are discussed in Section 4. The section adjacent to one fracture face was disected and detailed. Metallographic studies and exploration of the material was made to assist in assessing the causes of the fracture.

The girder was repaired by installation of a bolted field splice on the web and tension flange after removal of part of the fracture section and opened to traffic on March 31, 1977[2]. During the repair, strain measurements were taken at the failure cross-section in order to independently monitor the jacking forces and determine the distribution of stress on the cross-section. The results of these measurements are given in Section 2.

During the summer of 1977, stress history studies were carried out on the structure in order to determine the random variable stresses of truck traffic, obtain the response of the structure to controlled loading and

observe the thermal stresses. The results of these studies are given in Section 5.

Shortly after the fracture was discovered, it was found that nine electroslag flange welds existed in the tie girders of the 750 ft. arch span of the Glenfield Bridge complex at Neville Island. Nondestructive tests (ultrasonic and radiographic) were carried out on these weldments[3]. This indicated that rejectable discontinuities and cracks existed in at least one electroslag weldment. As a result, a sample was removed from the structure in order to assess the weldment, determine the nature of the defect and establish the fracture resistance of the tie girder. The results of these studies are given in Sections 3, 4 and 8.

Since significant numbers of electroslag weldments existed in the back channel bridges and the approach ramps, it was decided to splice those weldments whose failure would lead to significant structural damage[4]. Five core samples were removed from five of the spliced connections in order to evaluate the characteristics of the electroslag weldments and assess the long term performance of other electroslag weldments that remained in the structure. The results of these tests are given in Section 3 and the results evaluated in Section 8.

2. REPAIR OF FRACTURED GIRDER

The girder was repaired by the installation of a bolted field splice on the web and tension flange after removal of a 30 in. x 60 in. (762 mm x 1524 mm) segment of the girder[2]. The web splice consists of two 126 in. x 55-1/2 in. (3.2 m x 1.4 m) plates. The tension flange splice consists of two top plates 14 ft. - 5-1/4 in. x 14 in. x 2-3/4 in. (4.4 m x 356 mm x 70 mm) and one bottom plate 14 ft. - 5-1/4 in. x 30 in. x 2-3/4 in. (4.4 m x 762 mm x 70 mm). The total area of the splice plates is 159.5 in.^{2} (1029 cm^2).

The field splice of girder G4 was installed in three main steps as follows:

1. The web and tension flange splice plates were bolted to the south side (Fig. 1) of the fracture cross-section.
2. Four 300-ton (2669 kN) capacity horizontal hydraulic jacks anchored to the tension flange north of the fracture cross-section (two on top, two below) near the unbolted ends of the tension flange splice plates, pulled on the flange splice plates with sufficient force to bring the bridge deck back to near original vertical alignment and essentially restore the dead load bending moment distributions in girder G4.
3. The remaining bolts in the web and tension flange splice plates were installed to complete the repair.

During step 2, the compression flange of girder G4 was also pulled slightly west to bring it back to its original position relative to the concrete slab in the vicinity of the fracture cross-section.

Figure 6 shows the horizontal hydraulic jacking equipment mounted to the tension flange of girder G4. The two heavy C-clamp yoke plates installed to hold the splice plates together are to the left. Four jacking rods passed through the yokes and attached to the four 300-ton (2669 kN) capacity center hole jacks that were positioned on the north (right end) side of the fracture. The jack reacted against the jacking abutments and brackets attached to the girder at that point. Greater detail is given in Ref. 2.

Section 2 presents the results of strain measurements made on the tension flange splice plates, on several girder cross-sections and on other members of the superstructure during the jacking operation. These measurements were used to:

1. Provide an independent check during the jacking operation of the total force in the tension flange splice plates. The jacking operation was controlled by others using calibrated pressure gages.

2. Determine the incremental change in strain that was introduced into girders G2, G3, and G4 at four selected cross-sections, during the jacking operation.

3. Determine the incremental change in strain that was introduced into certain floor beam truss members and certain bottom lateral bracing members.

4. Correlate the measured strain distributions with the predicted strain distributions obtained from mathematical models of the structure.

Strain measurements were acquired on March 16 and 17, 1977, at two cross-sections of girder G4. Strains were also measured at one cross-section each of girders G2 and G3, on several members of the floor beam truss immediately south of the fracture and on two members of the bottom lateral bracing system adjacent to the fracture. Measurements were made prior to starting the jacking operation and at several intermediate load levels up to restoration of the dead load bending moment in girder G4. Measurements were also made after high strength bolts were loosened in all floor beam-to-girder connections which showed overstress. Bolts were loosened in the lateral bracing and floor beam connections at two intermediate stages of jacking.

Strain measurements were also acquired from the tension flange splice plates. The resulting total force in the splice plates was used to provide an independent check, during the jacking operation, of the jack loads as determined by others using calibrated pressure gages.

2.1 Instrumentation

Figure 7 shows the strain gages that were mounted on two cross-sections of girder G4, on one cross-section each of girders G2 and G3, on several members of the floor beam truss immediately south of the fracture, and on two members of the bottom lateral bracing system adjacent to the fracture. Strain gages were also mounted on the edges of the tension flange splice plates as shown in Fig. 8.

The gages used were 1/4 in. (6 mm), 120 ohm electrical resistance strain gages. They were mounted parallel to the direction of flexural stress in

the girders and splice plates and parallel to the direction of axial stress in the floor beam truss members. A quarter-bridge, three-wire hookup was used, which automatically provides lead-wire and temperature compensation to all gages.

Signals from all strain gages were brought to switch boxes and an automatic self-balancing strain recorder located inside a van which was parked on the bridge deck.

2.2 Force in Splice Plates and Jack Force

The relationship between the computed force in the splice plates in kips (from measured strains) versus the closing displacement of the tension flange in inches, at the fracture cross-section is shown in Fig. 9. The relationship between the total jack force as determined from calibrated pressure gages, versus the closing displacement of the flange is also shown in Fig. 9 for comparison. The flange was closed in increments of 1/4 in. (6 mm) until 1-1/4 in. (32 mm) relative closing displacement was reached. Then two additional increments were added until the total relative displacement reached 1-23/32 in. (43.7 mm).

The jacking operation commenced at 1:00 P.M., March 16, 1977. The air temperature was 52° F (11° C). Initial strain readings were taken at this time at all strain gage locations. When a 1/2 in. (12.7 mm) relative closing displacement was reached, some bolts at the west end of the floor beam truss just south of the fracture cross-section were loosened to relieve the locked-in forces from plastic deformation. The force in the splice plates increased slightly (points S2 and S3, Fig. 7). The force at the hydraulic

jacks however did not change (points J2 and J3). Additional bolts in the floor beam truss north of the fracture cross-section were loosened next without any further change in the force in the splice plates or the hydraulic jacks. The compression flange of girder G4 near the fracture cross-section was then pulled slightly west, to align the girder, with supplementary jacks[2].

When 1-3/8 in. (3.5 mm) displacement was reached (points S7 and J7), additional bolts were loosened on both floor beam trusses. Bolts were also loosened on the bottom lateral bracing members between girders G3 and G4 in the vicinity of the fracture cross-section. The force in the splice plates increased (S7 to S8) while the jack force decreased (J7 to J8). The jack force was brought back to its original value (points J7 and J9). The force in the splice plates again increased slightly (point S9).

At this point, at 6:30 P.M. on March 16, 1977, the air temperature was 50° F (10° C). The jack force was then dropped to zero (J10) while lock nuts on the four pull rods maintained the tension in the splice plates (S10).

At 7:30 A.M., March 17, 1977, prior to increasing the jack force (J11), the strain measurements indicated that the force in the splice plates had increased 200 kips (890 kn) or 1.25 ksi (8.6 MPa) (S10 to S11) due to an air temperature change from 50° F (10° C) to 35° F (2° C). Such a change would be expected in a 3-span continous structure as a result of the temperature differential between the concrete slab and the steel structure. At 9:50 A.M., March 17, 1977, the jack force was increased from zero until a slight movement of the tension flange was observed (J12). Unfortunately no corresponding measurement of the force in the splice plates was made. At 10:00 A.M.,

March 17, 1977, the jack force was increased so that the original gap that existed between the fracture surfaces was eliminated. The resulting jack force is shown in Fig. 7 by point J13. The corresponding force in the splice plates is shown by point S13. At this time the hydraulic jacks were retracted (J14). The tension in the splice plates was maintained by the four pull rods. At 12:00 noon, March 17, 1977, the final measurement of the splice plate force was made (S14). The measured force in the splice plates at this time (S14) was 1674 kips (7446 kN).

2.3 Stress Distributions in Girders

The measured stress distributions in girder G4 are shown in Fig. 10. Figure 10a shows the stress distributions on Section 1 (Fig. 7) near the fracture cross-section. The measured stress on each side of the girder at Section 1 is plotted, and averaged to show the stress distribution in the girder (Solid Curves). Stress profiles are shown corresponding to splice plate forces of 685 (3047kN) (S3), 1305 (5805kN) (S5), and 1674 (S14) kips (7446kN). The difference in the measured stress in the tension flange and at mid-depth is relatively small. However, the difference is particularly apparent in the top flange where a transverse jack force was applied to align the girder. Figure 10b shows the stress distributions on Section 2 (Fig. 7) at the same levels of splice plate forces. Note that two plotted points were available on the bottom flange, but only one each at middepth and on the compression flange.

The measured stress distributions in girders G2 and G3 are shown in Fig. 11. Figure 11 shows the stress distributions on Section 1 (Fig. 7)

of girder G2 corresponding to splice plate forces of 685, 1305, and 1674 kips. Only one bottom flange stress level was recorded at 1674 kips (7446kN) because one of the two G2 bottom flange strain gages (Fig. 7) was out of commission at the completion of the jacking operation. Figure 11b shows the stress distributions on Section 1 (Fig. 7) of girder G3 at the same levels of splice plate forces.

2.4 Stresses in Other Members

Table I shows the measured and computed strains and stresses in selected members of the floor beam truss and bottom lateral bracing system near the fracture cross-section (See Fig. 7 for location of strain gages).

Columns 1 to 6 inclusive show the measured strains and computed stresses (E = 29,500 ksi) at each of six locations corresponding to measured splice plate forces of 685, 1305, 1674 kips. These levels of splice plate forces were selected so that the results shown in Table 1 would correlate with those given in Figs. 10 and 11.

Columns 7 to 10 inclusive give the strains and stresses predicted in Ref. 2. Reference 2 used a predicted total jack force of 1950 kips (8674kN). The values given in Ref. 2 were modified assuming linear elastic behavior to show predicted strains and stresses at the measured 1674 kip (7446kN) level. Reference 2 assumed that the total jack force and the splice plate force would be equal. It is believed that differences between the analysis and measured values is primarily due to thermal effects.

2.5 Comparison of Measured Splice Plate Force with Total Jack Force

It is evident from an examination of Fig. 9 that the splice plate force, as determined by strain gages (Fig. 8), does not completely agree with the total force as determined by calibrated pressure gages. The force in the splice plates is consistently lower whenever the jacks are under pressure and closing the tension flange. There appear to be three main reasons for the discrepancy:

1. The pull rods are eccentric to the splice plates as shown in Fig. 6. The large "C" shaped plates, connecting pairs of pull rods top and bottom, are designed to minimize separation between the splice plates and the tension flange under the "C" plate. It was observed during jacking, however, that both "C" plates distorted and opened up. It was apparent that the splice plates were bending and that a compressive force was being developed between the ends of the splice plates (just left of the anchor block bolted to the tension flanges as shown in Fig. 6) and the tension flange. A lubricant placed on the surfaces of the splice plates to relieve the resulting friction forces was ground off prior to jacking.

   It is believed that substantial friction forces were developed at the ends of the splice plates, resulting in higher jack forces. This conclusion is supported by the behavior at 1/2 in. (12.7 mm) displacement shown in Fig. 9. When bolts were loosened in the floor beam truss, the force in the splice plates increased slightly as shown by points S2 and S3. An increase in splice plate force

would be expected due to a reduction in torsional restraint to girder G4 upon loosening the bolts. The jack force did not change (J2 and J3). This would be expected if frictional forces developed between the splice plate gages and the hydraulic jacks. In addition, at 1-3/8 in. (35 mm) displacement (Fig. 9), when the jack force was increased from J8 to J9 to bring the jack force to the same level at J7, the force in the splice plates increased only about one-third as much, which would be consistent with an assumption of friction forces developing. It is unlikely that relative tension flange displacement began with nearly zero jack loads as shown. It is likely that the jack loads reached 100 (445 kN) to 200 kips (890 kN) before large displacement was observed due to friction. Thus, the vertical difference between the two curves in Fig. 9 varies from about 200 kips (890 kN) at low displacement to about 400 kips (1780 kN) at the higher displacements. This difference can be accounted for by the presence of friction forces at the ends of the splice plates which increase as the jack loads and bending of the splice plates increase.

2. The strain gages on the splice plates (Fig. 8) were placed in the field. The splice plates were not calibrated, thus some inaccuracy is possible in the measurement of the splice plate forces. However, errors were minimized by placing four gages on the edges of each splice plate and averaging the readings at each displacement increment.

3. Differential temperature conditions between the concrete slab and the steel superstructure also introduces stresses into the 3-span continuous structure. This is particularly noticeable from the differences between the splice plate force at S10 and S11. As noted this measured increase was observed over a thirteen-hour period (6:30 P.M. to 7:30 A.M.) when the air temperature decreased by 15° (8.3° C). Measurements during June 1977 further confirmed these observations.

2.6 Stress Distribution in Girders

Figure 12 shows the finite element (FE) model used to determine the stress distribution on section 1 of girder G4. A portion of girder G4, south of the fracture cross-section, was selected for modeling. The web of girder G4 was modeled by 320 plane stress elements while 64 truss or bar elements model the top and bottom flanges. The horizontal roller support at the fracture cross-section accounts for the continuity of the steel top flange and concrete slab above the fracture location. The two vertical roller supports are arbitrarily located sufficiently distant from section 1 so as to have a negligible effect on the stress distribution at section 1 which lies in a region of constant bending moment.

Figure 12b is an enlargement of the shaded area in Fig. 12a and shows the distribution of bolt forces applied to the girder. The bolt forces were applied by the flange splice plates during jacking. They are consistent with the final measured 1674 kip (7446 kN) force in the splice plates.

The FE model of girder G4 was used to analyze three different cross-sections: (1) the steel girder alone; (2) composite section consisting of steel girder and 8-1/2 ft. (2.59 m) wide slab; and, (3) composite section consisting of steel girder and 22 ft. (6.7 m) wide slab. To simplify the analysis, the transformed concrete areas of the composite sections were included in the areas of the top flange elements with no modification of the depth of the cross-section.

Figure 13 shows the two composite cross-sections which were used in the FE analysis. The smaller cross-section was selected to agree with Ref. 2 which used an 8 ft.-6 in. (2.59 m) slab together with a modular ratio, n, of 10 in predicting strains at sections 1 and 2 of girder G4 (Fig. 7) under composite action. The 22 ft. (6.7 m) slab width was selected to represent one-half the concrete roadway between girders G3 and G4 and to include the mass of concrete forming the railing wall. A modular ratio of 8, corresponding to 4000 psi (27.6 MPa) concrete, was used in transforming the 22 ft. (6.7 m) wide slab.

The three stress profiles obtained from the FE analysis for section 1 of girder G4 are plotted in Fig. 10. Good agreement is obtained between FE analysis using the 22 ft. (6.7 m) wide slab and the measured stress distribution under the 1674 kip (7446 kN) force in the splice plates. The FE analyses using the 8 ft.-6 in. (2.59 m) slab width and for the steel girder alone differ greatly from the measured stress profile above the neutral axis. Although the bridge superstructure was designed noncomposite, the response of girder G4 during the jacking operation indicates that nearly full composite action existed between the steel girder and the concrete slab throughout the jacking operation. The behavior was also observed under traffic (see Section 5).

The measured stress profiles in Fig. 10a are fitted to the average stresses recorded by the three pairs of strain gages on section 1 of G4. Under ideal plane bending conditions, the flexural stresses obtained from the individual strain gages in a pair of gages would be equal. The stresses plotted in Fig. 10 a show a spread of up to 5 ksi (34.5 MPa) for the pair of gages on the top flange. A smaller difference exists in the bottom flange. The difference can be attributed mainly to lateral bending of the top flange during the jacking operation. As mentioned earlier, lateral bending was introduced while pulling the compression flange of girder G4 west to bring it to its original position relative to the concrete slab in the vicinity of the fracture cross-section. In addition, the tension flange would move laterally as it realigned under the applied jack loads.

The pair of strain gages on the bottom flange at section 2 of girder G4 also exhibit a smaller stress differential which also can be attributed to lateral bending. The single strain gages on the web and top flange at section 2 do not permit an averaging of the measured stresses. Thus, the measured stress profiles shown in Fig. 10b are unable to completely account for lateral bending of girder G4.

The measured stress profiles at section 1 of girders G2 and G3 are presented in Figs. 11a and 11b. The stress differential across the bottom flange of each girder is believed due to lateral bending caused by alignment of girder G4 during the jacking operation. Since single gages were placed on the webs and top flange the average flexural stress at these locations cannot be obtained. Only one bottom flange strain gage on girder G2 was operational at the 1674 kip (7446kN) load level.

Figures 11a and 11b also include predicted stress profiles from Ref. 2 based upon an expected total jacking force of 1950 kips (8674 kN). The values given in Ref. 2 were also modified to show predicted stress profiles also at the 1674 kip (7446 kN) level. The composite section used in Ref. 2 included a slab width of 8-1/2 ft. (2.59 m) (Fig. 13).

The measured top flange stresses shown in Fig. 11a and 11b are less than stresses predicted on the basis of composite action using the 8-1/2 ft (2.59 m) slab width. Thus, the amount of concrete contributing to the composite action of girders G2 and G3 was obviously greater than the 8-1/2 ft. (2.59 m) width assumed in Ref. 2, appears closer to the 22 ft. (6.7 m) slab (half-width) assumed in the FE analysis of girder G4.

3. MATERIAL PROPERTIES

In order to determine the physical characteristics of the electroslag welds in the tied arch span, a sample plug was removed from the north end of the downstream truss. Material from the sections removed from the fractured girder were used to evaluate the electroslag weldment, repair weld and base metal of the casualty girder. In addition, five sample cores were removed from five spliced details of the back channel span and ramps. This section summarizes the results of these studies.

3.1 Tied Arch Girder

The sample plug was removed from the top flange electroslag joint of piece 201T2 at the north end of the downstream truss. At this location, a cracklike discontinuity was observed in a radiograph of the electroslag joint.

The sample plug was removed from the structure on February 16, 1977. Figure 14 shows the inside of the box with the sample core removed. Immediately after removal from the structure, the plug was taken to the PDM plant at Neville Island and radiographed. However, these radiographs were not able to identify the location of the discontinuity in the thickness direction.

Figure 15 shows the top and bottom surfaces of the plug. The top surface view in Fig. 15a also shows the longitudinal fillet weld used to connect the 7/8 in. (22 mm) A514 steel web plate to the 42 in. wide 2-3/4 in. (1067 mm x 70 mm) thick A588 flange plate. The balance of the

top surface is the electroslag weldment. The vertical line on the plug is the lap surface of the web and flange plates. The bottom surface shown in Fig. 15b shows the small segment of the web and weldment removed with the plug. Also visible is the fillet weld which attached the 7/8 in. (22 mm) A514 steel web to the flange plate.

The radiographs taken by Pittsburgh Testing Laboratory had indicated that the cracklike discontinuity was near the fusion line of the electroslag weldment and the A588 flange plate as can be seen in Fig. 16. Prior to removing the plug, ultrasonic examination had located a discontinuity on the inside surface and this was identified as the discontinuity seen in the radiograph. However, radiographs of the plug indicated a discontinuity at the top surface. Hence, both the top and bottom surfaces of the plug were carefully examined before slicing the plug into sections for test samples.

The plug was then sliced into five segments as shown schematically in Fig. 17. Segment TF was about 0.55 in. (14.1 mm) thick and contains the top crack. Segments C1, C2 and C3 are 10 mm thick and segment BF is the bottom flange segment which is 0.55 in. (14 mm) thick and contained a second crack. Each surface of segments C1, C2 and C3 were then polished and etched. These can be seen in Figs. 18, 19 and 20 for segments 1, 2 and 3. The light colored areas on the left side of each surface is the electroslag weldment. The fusion line is apparent in each surface.

Charpy V-notch specimens were then prepared from each of the three 10 mm thick slices as can be seen in Figs. 21, 22 and 23. These specimens were notched at either the fusion line or in the coarse grain heat affected zone. Because the fusion line bowed into the plate, segments C2 and C3 had

an inclined fusion line. As a result, the Charpy V-notch was placed in the coarse grain heat-affected zone in specimens C11, C12, C13 and C21. The notch was placed at the fusion line in the remaining specimens (C22, C23, C31, C32 and C33).

Except for specimen C11, all notches were located so that the fracture path would be away from the web. This provided the weakest resistance direction as the plug was removed from the starting end of the electroslag weldment and the grain orientation would permit the crack to follow the weakest orientation. There was inadequate length of the specimen available to place the notch at the fusion line away from the web side for specimen C11.

ASTM standards require the specimen to be 55 mm long, centrally notched. The pivot points for the specimen in the Charpy Impact Test machine are only 40 mm apart. Thus, the notch was located in these specimens such that at least 24 mm of specimen length remained on each side of the notch. Testing of the specimen was done with the notch directly opposite the striking hammer. The specimens are shorter in length than ASTM specifications indicate; however, from the mechanics of the test, this will not significantly influence the test results.

The Charpy V-notch test results are summarized in Table 2 and plotted in Fig. 24. The fracture surfaces at 0° F (-18° C) showed no evidence of fibrous fracture. It is also apparent that no significant difference exists between the fusion line and the heat affected zone fracture toughness.

Segment TF (see Fig. 17) contained the natural crack. A three-point bend specimen, which contained the natural crack, was prepared by welding

extensions onto a regular segment. The resulting bend specimen was tested at -30° F (-34° C) to determine its fracture resistance and expose the crack surface. The resulting fracture toughness K_c at a 1 sec. loading rate was found to be 35.5 ksi $\sqrt{in.}$ (39 MPa $\sqrt{m}$). Figure 42 shows the broken segments of the test specimen.

A second bend specimen was prepared from the adjacent material. It was notched and fatigue precracked along the fusion line. During precracking, the stress intensity range was larger than desired and this resulted in some yielding. The fracture test at -30° F (-34° C) provided a fracture toughness K_c of 65 ksi $\sqrt{in.}$ (71.5 MPa $\sqrt{m}$).

The chemistry of base metal and weld metal was obtained by General Testing Laboratories, Inc. on material residuals from the sample core. Both mass spectrographic analysis and wet chemistry was used. The results are given in Table 3. The only chemical element that is on the high side is the carbon content of the tied arch base metal.

3.2 Casualty Girder

The south section of the fracture was used to evaluate the physical characteristics of the weld metal and base metal as well as detailed metallographic and fractographic studies of the fracture. Figure 25 shows the layout of the flange and the identification of the various segments. Prior to cutting the section into pieces, the flange tips were etched in order to establish the location of the electroslag weldment.

The web was sawed off the flange about 2 in. (51 mm) above its surface. Then several segments were cut from the section as can be seen in Fig. 26.

A 2 in. x 3-1/2 in. (51 mm x 89 mm) section was removed from the east edge (segment I). This was then sliced into seven layers, each about 1/2 in. (11 - 12 mm) thick (see Fig. 27). The fracture surface had previously been cut from the sample. The five interior slabs were then ground to a final thickness of 10 mm. One side of each slice was then polished and etched so that the weldment, fusion line and heat affected zone were apparent. Figure 28 shows the surface of slabs 1 and 4. It is visually apparent that, within the 2 in. (51 mm) length along the weldment, the fusion line for both slabs is in about the same location.

Figure 28 also indicates that the weldment was started from this end of the flange. The coarse grain structure of the weldment shows the grain orientation associated with welding from this end. Because the fusion line moved further into the plate as the weld was made, the edge toward the beam web provided a longer section of weld metal. As a result, all specimens notched in the weld metal were taken from that side of each plate.

Four Charpy V-Notch specimens were made from slices 1, 2, 4 and 5, as these provided nearly replicate thickness conditions (i.e. 1 and 5, 2 and 4). Slice 3 from the midpoint of the plate thickness was used to assess the weldment fracture toughness at the centerline of the weldment. An extension was attached by electron beam welding.

Figure 29 shows the Charpy V-notch specimens that were made from slices 1 and 4. All specimens were notched so that the fracture path would be in the direction of the electroslag weldment which provides the weakest orientation. Eight specimens were notched in the weld metal at about the quarter-point position and eight at the fusion line or adjacent

heat affected zone. All specimens from slices 1 and 2 were tested at 0° F (-18° C). All specimens from splices 4 and 5 were tested at 40° F (+4° C). Additional tests were made on specimens prepared from segments B and D (see Fig. 25).

The test results of all Charpy V-notch specimens are tabulated in Table 4 and summarized in Fig. 30. The results suggest that the heat-affected zone and fusion line provide a lower bound to the data. The fusion line absorbed energy does not experience a sharp transition as does the weld metal. The weld metal toughness is slightly better than provided by the tied arch weldment.

Segment II near the midwidth of the girder flange was carefully etched and polished on each surface. Figure 31 shows the top, bottom and back surfaces of this portion of the flange. A significant amount of weld repair was detected in that region, as is readily apparent. Charpy V-notch specimens were prepared from the weld repair metal and tested at 0° F (-18° C) and 40° F (+4° C). The results are tabulated in Table 5 and summarized in Fig. 32. These results indicate that the multiple pass repair weldment had lower fracture toughness than the lower bound values obtained from the electroslag weldment.

Tests were also carried out on the A588 base metal. The Charpy V-notch tests are tabulated in Table 6 and summarized in Fig. 33. The base metal did satisfy the AASHTO requirements for Zone II. The transition temperature is about 40° F (+4° C).

The yield point of the base metal at 75° F (24° C) was 55.6 ksi (383.4 MPa) and the tensile strength was 83.6 ksi (576.4 MPa). At 0° F

(-18° C) the yield point was 59 ksi (406.8 MPa) and the tensile strength was 93.4 ksi (644.0 MPa) (see Table 7). The mill report indicated the yield point to be 60.9 ksi (419.9 MPa) and the tensile strength 84 ksi (579.2 MPa).

Several compact tension tests were carried out on base metal specimens. Both 1 in. (25 mm) and 1.75 in. (44 mm) thick specimens were fabricated. The results are tabulated in Table 8. All tests were 1 sec. tests to provide an "intermediate" loading rate.

Chemical tests of the base metal and weld metal are given in Table 3. The carbon, phosphorous, sulfur and silicon content was obtained by wet chemistry and the remaining elements by mass spectrographic analysis.

The chemical composition of the repair weld metal in the girder is also listed in Table 3

The Charpy V-notch tests and the few fracture toughness tests on the casualty girder weld metal (electroslag and multiple pass repair welds) were used to estimate the fracture toughness of the casualty section. Data from the literature was also used to help provide reasonable fracture toughness - temperature relationships.

Benter[5] provides some data for K_{Ic} fracture toughness for electroslag weldments connecting A588 steel. Data is also available from tests carried out at Lehigh[6] on similar steel (A537G) with electroslag weldments. These tests are summarized in Fig. 34 and compared with the dynamic fracture toughness values estimated from the Charpy V-notch test data using Barsoms[7] correlation

$$K_{Id} = (5 \cdot E \cdot CVN)^{1/2} \qquad (1)$$

It can be seen, that the static fracture toughness for the weld metal and the heat affected zone reported in Ref. 5 varies between 55 ksi $\sqrt{in.}$ (60 MPa $\sqrt{m}$) and 75 ksi $\sqrt{in.}$ (80 MPa $\sqrt{m}$) for a temperature of -40° F (-40° C). Similar variations of resistance can be expected from the electroslag weldment and the multiple pass repair weld of the casualty girder based on the Charpy V-notch results. The charpy V-notch test results for the electroslag weld metal of the casualty girder show a transition temperature of about 68° F (20° C) as it can be seen from Fig. 30 the CVN-values increase rapidly over a small increase of temperature. The predicted K_{Id}-value therefore changes rapidly in the same temperature region (see Fig. 34). The static (1 sec.) fracture toughness values were obtained by shifting the dynamic fracture toughness values. The maximum temperature shift expected for these materials is between 117° F and 126° F (65° C and 70° C). For the 1 sec. loading time 75% of shift was used and a temperature shift of 90° F (50° C) results. The band of 16-values for the intermediate loading rate for the electroslag weldment is shown in Fig. 34. They compare well with the static fracture toughness estimates reported by Benter[5]. Because of the temperature shift, the transition temperature is about 0° F (-18° C). The CVN-values for the fusion line and the heat-affected zone of the electroslag weld (Fig. 30) and the repair weld material (Fig. 32) provide a lower bound fracture toughness and suggest that the transition temperature is higher. The K_{Id}-values for these materials are also plotted in Fig. 34.

The estimated range of fracture toughness at an intermediate loading range is cross-hatched in Fig. 34. A fracture toughness between 68 ksi $\sqrt{in.}$ and (75 MPa $\sqrt{m}$) and 110 ksi $\sqrt{in.}$ (120 MPa $\sqrt{m}$) would be expected at 0° F (-18° C).

3.3 Back Channel Samples

Five samples were removed from the back channel structure and ramp H electroslag weldments that were spliced. Following is a summary of their location in the structure, the thickness of the connected plate and the diameter of the core.

Specimen Core	Sample Location	Plate Thickness	Core Diameter
9G11	Span 9, G1 S21	3.75 in. (95 mm)	4 in. (102 mm)
9G1A	Span 9, G1 S17 Ah	3.32 in. (84 mm)	4 in. (102 mm)
9G1B	Span 9, G1 S17 Bk	3.32 in. (89 mm)	4 in. (102 mm)
9G4	Span 9, G4 S11 Bk	3.50 in. (89 mm)	3 in. (76 mm)
H2	Span H2 S13	2.80 in. (71 mm)	3 in. (76 mm)

The sample cores were sliced into cylindrical wafers as shown schematically in Fig. 35. Detailed metallographic examinations were made of each slice and this is discussed in Section 4.

Charpy V-notch specimens were fabricated from slices H21, H22 and H2B of core H2, from slices 9G1A2 and 9G1A4 from core 9G1A, from slices 9G1B2 and 9G1B4 from core 9G1B, from slice 9G11 from core 9G1 and from slices 9G41, 9G42, 9G44 and 9G45 from core 9G4. The CVN specimens were placed as near to the quarter thickness as practicable.

The results of the Charpy V-notch tests are summarized in Tables 9 and 10. Table 9 shows the average absorbed energy that was obtained at the notch locations indicated. The centerline location is specified by AWS[8]. Most of the specimens were tested at 0° F (-18° C). However, two specimens were tested at 70° F (21° C) from plugs 9G1A, 9G1B and 9G4. Two specimens were also tested at 100° F (38° C) from sample 9G1A.

The results indicate that only one sample plug clearly failed to meet the average absorbed energy level specified by AWS. That was plug 9G4 which had an average absorbed energy of 6 ft-lbs. (8 J) at 0° F (-18° C). Plug H2 provided an average value of 16.5 ft-lbs. (22.4 J) if all six specimens were considered.

Eliminating the high and low values results in an average value of 13.1 ft-lbs. (17.8 J). This is a marginal condition. The other three sample plugs all satisfied the AWS requirement of 15 ft-lbs. (20 J) at 0° F (-18° C).

The results of the back channel Charpy V-notch tests are all summarized in Fig. 36. The specimens fabricated from plug 9G4 fall at the lower bound of the scatterband of test results

Fracture toughness tests were carried out on the thicker slices from each weld core sample. Compact tension specimens were fabricated from the slice and tested at -30° F (-34° C). The results of these tests are summarized in Table 11. All tests were carried out at a 1 sec. loading in order to simulate the behavior in the bridge structure. The results are also plotted in Fig. 37 and compared with the scatterband developed in Fig. 34. This comparison shows that the measured fracture toughness values are in good agreement with the temperature shifted mean and lower bound dynamic fracture toughness derived from Eq. 1. These data are also comparable to the values obtained in Ref. 5.

4. METALLOGRAPHIC AND FRACTOGRAPHIC STUDIES

Detailed studies were carried out on the sample cores and the fractured sections. The results of these studies are described in this section for the tied arch girder, the casualty girder and the back channel structures.

4.1 Tied Arch Girder

The sample plug removed from the north end of the downstream truss was examined in detail.

Figures 38 and 39 show the polished and etched surfaces of the plug. The top surface in Fig. 38 shows the fillet weld along the edge of the flange plate. The large grains of the electroslag weldment can be seen in the top section of the plug. A crack about 3/4 in. (19 mm) long was observed to run through the porosity visible in Fig. 38. This crack was compatible with the crack observed in the PTL radiograph in its configuration. The fusion line and heat-affected zone (HAZ) are also apparent. The dark area surrounding the crack was found to be the heat-affected zone of a surface repair weld.

Figure 39 shows the bottom surface of the plug after the web extension was cut away. The large grain structure of the electroslag weld is clearly visible as is the HAZ of the A588 steel flange. The A514 steel web plate end is fused into the electroslag weld and the unfused edges of the flange and web plate are apparent. A crack in the bottom surface of the A588 steel flange is also evident. This crack occurs in the dark area which is the heat affected zone of the web-to-flange weld.

This crack, which extends into the portion of weld that was removed (see Fig. 15b), is the discontinuity detected by the PTL ultrasonic inspection.

Once the cracks in the top and bottom surfaces of the core were identified, the portion of the electroslag weld fused into the end of the A514 steel web plate and the web plate were cut from the core. The flat side surface of the weld and flange was then polished and etched. This can be seen in Fig. 40a. This examination showed that the crack in the top flange surface was about 3/16 in. (5 mm) deep at the edge. The radiograph indicates a maximum depth of about 1/4 in. (6 mm) which is about 1/4 in. (6 mm) in from the plate edge. A higher magnification view of this crack, taken from the three point bend specimen subsequently made from the core is seen in Fig. 40b.

Figures 18, 19 and 20 show the polished and etched surfaces of the three slices used to fabricate Charpy V-notch specimens. No evidence of grain boundary fissures was detected in any of the surface layers. Cracking in the plug removed from the tie girder was confined to the conditions shown in Figs. 38 to 40.

The natural crack in Fig. 38 was exposed by fabricating a three-point bent fracture toughness test specimen from the surface slice as shown in Fig. 41. The specimen was tested at -30° F (-34° C). The fracture surfaces are shown in Fig. 42. The surfaces of the precracked adjacent beam specimen are shown in Fig. 43.

Examination of the fracture surfaces and the areas adjacent to the fracture were undertaken using light microscopy, electron-optical examination and microanalysis techniques (the scanning electron microscope and the

microprobe analyzer). These instruments permit high magnification examination of the surface contours of the fracture surface and chemical composition measurements in areas as small as .04 mils (10^{-3} mm) and supplement information obtained from light microscope studies.

Prior to fracture of the bend specimen, the surfaces were polished and etched as seen in Fig. 40b. The crack clearly extends down the fusion line. The weld metal lies to the right of the crack and the base metal to the left. Between these two regions lies an unusual area with a microstructure unique to the region adjacent to the crack. This region appears to be acicular ferrite but is different from the weld metal to its right (and is separated from it by a distinct boundary) as well as the base plate to the left. In addition, as clearly seen in Fig. 40a, there is a dark etching region covering the weld metal and base plate fusion line in the cracked region. This is the remainder of a repair weld pass placed on top of the crack and which covered it over. The porosity in this dark region is produced when material in the cracked area was heated by the repair pass and gases produced passed through the solidifying repair weld metal. Some of the weld metal from the repair pass can be seen bridging the crack surface at the top of Fig. 40b, and the heat affected zone from this pass can be seen at the top of Fig. 44a. Part of the repair pass was removed in polishing the top surface of the plug for examination. It can be seen that the repair weld pass did not extend more than ≃ 1/8 in. (3 mm) into the plate - weld interface and was thus ineffective in repairing the preexisting crack.

The fractured specimen was also metallographically polished and etched to determine the microstructure up to the fracture surface itself. This

microstructure is seen in Figs. 44a and b. The top surface of the plug (the top surface of the flange) is at the top of Fig. 44a with the bulk of the specimen being a cross-section of the weld metal. The natural crack surface lies to the left of the figure. The weld metal is made up of acicular ferrite and carbide particles, which is typical of weld metals in general and electroslag welds as well. The portion of the weld metal to the left of the photomicrograph has the large elongated grain structure typical of that close to the fusion line in electroslag welds, with ferrite veins extending into the acicular structure from the fusion line. The unique acicular ferrite region is at the crack surface in the lower left of Fig. 44a.

Extended X-ray microprobe analysis was performed on the area of the weld adjacent to the crack surface as seen in Fig. 44b. Chemical analyses were performed on four regions of the microstructure in Fig. 44b: (1) the bulk weld metal, (2) the acicular weld grain centers, (3) the ferrite veins around the grains, and (4) the unique ferrite rich layer right adjacent to the crack surface (marked S). These regions are marked on Fig. 44b. Multiple points were sampled in each of these regions, and their results are listed, for convenience, in Table 44b (see Fig. 44b).

The bulk chemical composition of the weld metal in Table 44b should be compared to that of the weld metal, which is listed in Table 3. It can be seen that the bulk weld chemistry [see (1) Table 44b] in this location is more or less an average of the proeutectoid ferrite veins [see (3) Table 44b) and the grain centers [see (2) Table 44b] that make it up. It should be noted that in this region, the copper content of the weld metal is never above 0.16% and averages in the bulk analysis about 0.080 - 0.10%.

The bulk manganese content in this area averages about 1.4% and the chromium content about 0.37%. By sharp contrast, the ferrite rich layer [see (4) Table 44b] has a copper content between 0.43 to 0.49%, no detectible manganese and very little chromium. From this examination, the region adjacent to the crack was determined to be of unique chemical composition, matching neither the base plate or surrounding weld metal and enriched in copper, but depleted in other normal alloy elements.

Scanning electron microscope studies of the fracture surface of the opened crack was also employed. Due to the size of the sample, a replication technique was used. In this procedure, replicas of the surface are made using cellulose acetate tape and standard surface replication techniques. The tape is softened with solvent and pressed into the surface until it assumes the surface contours. The solvent evaporates and when the tape has hardened sufficiently, it is stripped from the surface. The replica is then lightly coated with carbon to make it conducting and examined under the scanning electron microscope (SEM). In this instrument, not only are the contours of the replica observed at higher magnifications then possible in the light microscope, but also semiquantitative chemical composition data are obtained using an energy dispersive spectrometer (EDS) attachment. Because of the way the replicas are made and stripped from the fracture surface, discrete particles adhering to the fracture surface are removed on the replica and can be examined for chemical composition. The results of examinations of a number of replicas from the fractured bend specimen made from the natural crack are seen in Fig. 45. Three types of particles are seen on the replica, as seen in Figs. 45a and

b. Most prominent are particles of iron oxide (see Fig. 45a), probably rust or corrosion product. Also found on the replicas are two other types of particles, seen in Fig. 45b. The larger (#2), dumbbell shaped particle is conclusively identified as almost pure copper with a small amount of iron. The second particle (#1), is iron with copper as an impurity and a small amount of chromium and manganese. The EDS traces for these two particles are shown on Fig. 45b. The height of the peak each element produces in the trace is proportional to the amount present in the particle. In general, the copper particles are infrequent in the replicas.

4.2 Casualty Girder

The pieces removed from the casualty girder (see Fig. 5) were separated and the fracture surfaces exposed.

Figures 46a and b show the flange and part of the web fracture surfaces. All indications based on the macro-examination indicated that the fracture started near the center of the flange width beneath the web to flange weld. A close-up of this center section is shown in Fig. 47 for the half shown in Fig. 46b. Figure 48 shows a close-up view of this region for the half shown in Fig. 46a. A small lack of fusion zone at the web-to-flange weld is apparent in both Figs. 47 and 48. This did not have a significant effect on the fracture.

The photographs show a large flower-like region directly below the web. This region is egg-shaped and is about 1-1/2 in. x 2.5 in. (38 mm x 63.5 mm) in area. Also, apparent is a penny-shaped-like region in the center of the flange that has its center at the web-to-flange

connection and has about a 3 in. (76 mm) radius. Thereafter, a more crystalline type fracture surface is apparent. The small zone at the bottom of the flange in Figs. 46 is the inert material used to make a "footprint"[9]. This material is readily removed.

Prior to cutting the south section into pieces, the flange tips were etched at all four corners of the two sections. These can be seen in Figs. 49 and 50 for the east and west edges of the fracture surface. Figures 49a and b show the west edge which had been previously etched in the field by Bristol Steel and Iron Works. Figures 50 shows the east edge. It is visually apparent that the fracture existed near the middle of the electroslag weld at the west edge and near the north fusion line at the east edge. A slightly darkened region is visible at the bottom corner. This is the heat-affected zone of a repair weld. This corresponds to the region noted on sheet 3 of the Richardson, Gordon and Associates field notes dated February 1, 1977. There it is noted that vertical striations occur over a 7-1/2 in. (190 mm) length. These are the smaller grain structures resulting from the manual weld repair.

During inspection (radiography) of the original electroslag weld, several flaws were detected which required repair[10]. Although none of these radiographs are available, the records indicate that a rejectable flaw was present in the original weldment. After repair, it was indicated to be acceptable by a subsequent radiograph.

A detailed metallographic examination of the south piece removed from the casualty section showed that several repairs had been carried out on the electroslag weldment. These are shown schematically in Fig. 51. This

indicated that several fusion line repair passes were made (see Fig. 51a) prior to excavating a major boat-shaped cavity through the weld and into the connected plates in the longitudinal direction (see Fig. 51b). Figure 31a shows the polished and etched top surface of the flange and weld adjacent to the webs. The transverse fusion line weld passes that were made prior to the longitudinal repairs can be seen. The top and bottom surfaces shown in Fig. 31a and b also show the major weld repair that is shown in Fig. 51b. The back surface of Section II shown in Fig. 31c is about 3-1/2 in. (89 mm) from the fracture surface. It indicates that the major repair extends just over halfway through the flange thickness at this location. The longitudinal passes shown in Fig. 31a at the end of the piece are seen to be just cosmetic passes at the end of the section shown in Fig. 31c.

A section was cut about 1 in. (25 mm) back of the fracture surface as was shown schematically in Fig. 25. The etched section just behind the fracture surface is shown in Fig. 52. This demonstrates that the repair was full thickness at that location. The repair extended south of the fracture about 5 in. (127 mm), as can be seen from the etched edge of piece K which is shown in Fig. 53.

From a visual inspection of the crack surfaces it was apparent that the crack had propagated in different stages through the tension flange. Both sides of the fracture surface are shown in Fig. 46 and close-ups of the embedded initial flaw are given in Figs. 47 and 48. Just below the web, the crack surface shows a zone with a shiny black oxide appearance and irregular contours. The fracture surface was flat and coated with a

light coat of oxide near the middepth. The irregular shaped discontinuity is about 2.75 in. (70 mm) wide and 2 in. (50 mm) and has been outlined in Fig. 54. One of the longitudinal web-flange fillet welds can be seen to penetrate into the discontinuity where it came to the top flange surface. The absence of shear lips in this region suggests that the discontinuity was partially exposed at the flange surface. Both the top and the bottom flange surfaces show small shear lips except where the black zone exists. Examination of the crack surface with the transmission electron microscope indicated that interdentritic separation in the weld metal had occurred (see Fig. 56a). Hot cracking apparently occurred during welding and high temperature oxides formed on the fracture surface. This zone provided the initial flaw and is outlined in Fig. 54.

Fracture surface replicas were obtained at four locations around the black area which was the initial flaw for the transmission electron microscope investigation. These locations are identified as circles 1 to 4 in Fig. 54. Two other locations were examined, one in the center of the flaw and the other at the edge of the 3 in. radius. These are identified as circles 5 and 6 in Fig. 54. The fractographic investigation showed striation markings around the periphery of the initial discontinuity. An example of markings from locations 1 and 3 are shown in Fig. 55.

Striation markings are a sign of fatigue crack growth. The striations were observed to exist over a 1/32 - 1/16 in. (1 - 2 mm) wide band. (No exact measurements could be made because of the irregular shape and the corrosion of the fracture surface.) Measurements of the striations spacings showed that they were between 4×10^{-7} in. and 4×10^{-6} in. (1.0×10^{-5} mm

and 1.0×10^{-4} mm) apart around the boundary of the initial flaw. Fatigue crack growth was the extension mode during this stage of crack enlargement.

Figure 56 shows the condition that was found to exist in region 5 near the center of the initial flaw. Examination of this region with transmission electron microscope replicas, using the technique described previously on p. 32, shows the features seen in Fig. 56a. In this case the surface is irregular and rounded with deep grooves surrounding the smooth areas. It is probable that these regions are dendrite boundaries in the weld metal, but is is also possible that they are evidence of a ductile fracture mode in steel called dimpled rupture. No evidence of striations were detected in this region. The mottled appearance provided by Fig. 56b shows evidence of corrosion, which has obscured other fracture features.

To further determine the nature of the original flaw in this weld, the dark egg-shaped region in Fig. 47, the fracture surface was cut into a number of individual segments which were coded as seen in Fig. 57. The sides of each of these segments were polished and etched for metallographic study. The results of this study showed that two additional cracks exist in the repair weld area about 0.80 in. (21 mm) behind the fracture surface in area C2. The appearance of this crack, which was 0.40 in. (10 mm) long is seen in Fig. 58. The second crack found was 0.16 in. (4 mm) long and was 0.33 in. (8.5 mm) from the fracture surface. The irregular shape of this crack, which spans several layers of repair weld metal is irregular and in part follows the weld metal grain structure, though not exclusively so. It appears that this crack path parallel to as that seen in Fig. 56a. In the view seen in Fig. 58, the crack is seen in cross-section (elevation

view) and at low magnification whereas in Fig. 56 it is seen in plan view at high magnification. Because of the general appearance of this crack and the fact that it extends across a number of weld passes in the repair weld area, it is concluded that this is a hydrogen assisted stress induced crack.

This type of cracking has been recently reported in the technical literature[22], and probably occurs starting in the intermediate temperature range, at about 1000 - 800° F (538 - 427° C). It is a result of high residual stresses and can be eliminated by an appropriate level of preheat during and after the welding process. The chemical composition of the repair weld metal in this girder (see Table 3) is consistent with this analysis. It is very high in carbon content for a weld metal and the manganese content is also very high. The high manganese content has a tendency to produce hydrogen induced (cold) cracking in steels and the high carbon content is also determental in this respect. It is also possible, because the high carbon content promotes hot (solidification) cracking, that a combination of hot crack initiation and cold crack (hydrogen induced) propagation occurred. The "carbon equivalent" for this weld metal 0.6, and it is thus susceptible to cold cracking.

Outside the regions of fatigue crack propagation, the crack surface showed evidence of cleavage. This indicated that after traffic sharpened the crack, it enlarged suddenly in a brittle fracture mode.

The brittle fracture (crack instability) likely occurred in part of the flange and web. The brittle fracture was arrested in the flange when the crack reached a semicircular size of 3 in. (76 mm) radius as shown in

Fig. 54. The zone within the semicircle was slightly corroded. One location along the semicircular crack front was investigated (see circle 6) and striation markings were found there as well. Figure 59 shows the condition that was detected at this location. The zone where fatigue crack growth occurred was very small [less that 1/32 in. (1 mm)]. Crack growth around the initial flaw had to occur before January 1977. It appears highly probable that the enlargement to the 3 in. (76 mm) radius developed near January 17, 1977 when the temperature reached -17° F (-27° C). The final fracture of the bottom flange and the web was observed on January 28, 1977. The appearance of fracture surface outside the 3 in. (76 mm) radius is crystalline and distinctly different from the origin.

The crack front in the web did not move along the weld in the web.

4.3 Back Channel Girders

The five sample cores removed from the back channel girders were extensively examined for evidence of cracking, grain boundary fissures and other possible problems. Figures 60 and 61 show polished and etched surface of several of the core slices (see Fig. 36). The metallographic examination indicated that only one sample exhibited any evidence of cracking. This was observed in sample core 9G1A. These cracks are much smaller than observed in the Brady Street welds and were also different in character (see Fig. 61). They were less that 1/32 in. (1 mm) long and occurred in a small circular feature that may be portions of either the electrode or consumable guide tubes that did not completely melt and mix into the molten metal pool. No other cracks were discovered.

During the nondestructive examination of weld 4 on girder 27G4C, ramp D, a surface imperfection was detected[10]. Figure 62 shows the bottom surface of the girder flange and the porous paint-filled discontinuities that were observed at that location. Both top and bottom surfaces of the flange were ground smooth at the electroslag weldment and etched with a 15% nital solution. Figure 62b shows that the discontinuity was along the fusion line. A repair weld pass was apparent at the location which extended over the weld metal. In many respects the discontinuity was much like the condition that was detected in the top flange electroslag joint of piece 201T2 at the north end of the downstream truss of the I79 tied arch. This is shown in Fig. 38. The extensive porosity along the weld repair line had been up to 1/8 in. (3 mm) deep. These porosity holes were connected by very fine hairline cracks which became apparent as the etchant acted like a penetrent.

As a result of the comparability of the surface defects shown in Fig. 62 to the discontinuity found in the tie girder, it was recommended that the electroslag weldment in span D be spliced[11]. A sample core was removed from ramp D at the defect location and is shown in Fig. 63. Figure 64 shows a close-up view of the suspect region with the paint-filled pores.

A more detailed examination was conducted in the laboratory where core sample D was cut into segments as shown in Fig. 65. The individual slices, numbered 1-5 were etched to reveal the presence of any defects and to reveal the location of the butt weld in this core.

The etching of the slices revealed that the weld defect in the core was about 1 in. (25 mm) from the butt weld, which was on the thinner side of the transition in thickness at this location. The top slice of the core was therefore sectioned again transverse to the line of the repair bead and polished and etched to determine the depth of the pass in this location since it was not clear that it was well separated from the butt seam and did not correspond to any other weld in the structure. These polished and etched sections appear in Fig. 66. From the etched section it can be seen that the repair pass is quite shallow and has no other weld passes under or near it. The purpose for this pass, containing both cracks and porosity, is therefore unknown. Under the circumstances however, its removal was prudent as will be described later.

5. STRAIN HISTORY AND TEMPERATURE MEASUREMENTS IN BACK CHANNEL, SPAN 9

During June 1977, strain and temperature gages were attached to girders G3 and G4 of the I79 back channel structure in Span 9. Gages were attached at four locations along the span. At pier 9, strain and temperature gages were attached to the top and bottom flanges and the web of girder G4 as shown schematically in Fig. 67. About 80 ft. (24 m) from pier 9 at the haunch region (see Fig. 1) strain and temperature gages were attached to the web and the bottom flange of girder G4. Near the centerline (adjacent to the repair splice) strain and temperature gages were attached to the top and bottom flanges and the girder web of girder G4 and to the bottom flange and web of girder G3 (see Fig. 67). All strain gages are 1/4 in. (6.4 mm) electrical foil gages. The temperature gages were of the electrical resistance type and were read using a digital recorder.

Because of the length and location of the structure, it was necessary to position the data acquisition van on the parking lane of the southbound structure. All wiring was carried under the structure and over the parapet on the downstream side. Figure 68 shows the test van parked on the southbound structure.

Strain variations due to traffic and controlled test runs were recorded on magnetic tape and on analog trace recorders mounted in the FHWA test van.

Temperature changes were measured at predetermined intervals of time using a switch box and a portable recorder. The ambient air temperature was also monitored throughout the test. Truck traffic was continuously monitored for a six day period. In order to assess thermal-induced stresses

as a result of temperature differential between the top and bottom of the steel girders, simultaneous strain and temperature readings were taken for gages attached at midspan and over the supports at piers 9 and 10.

5.1 Stresses Due to Traffic

From the recorded analog and digital records, the stress range excursions for traffic using the structure were determined. Figure 69 shows typical strain-time variations at midspan in the bottom tension flange and over the supports at piers 9 and 10 in the top tension flange. It is apparent from Fig. 69 that one primary stress excursion occurred as a truck crossed the structure.

As expected, the stress distribution on the steel girder cross-section was not symmetric at either the midspan or in the negative moment regions at piers 9 and 10. Figure 70 shows the strain gradients at the maximum strain response for these three cross-sections. It is readily apparent that the neutral axis under live load is near the top flange for all cross-sections. Hence, the structure was responding to the live load in a "composite" manner even though the slab was not attached with shear connectors to the steel girders.

The maximum recorded stress range due to traffic was 3.0 ksi (20.7 MPa) at the midspan of the structure in girder G4. The maximum stress range recorded in the top tension flanges at piers 9 and 10 was 1.0 ksi (6.9 MPa).

The stress range occurrence data for the casualty cross-section is shown in Fig. 71 where the frequency of occurrence is shown for various

stress range levels. The measured stress range spectrum exhibits the characteristic skewed distribution observed on other bridge structures in Pennsylvania[18].

The stress range spectrums for interior girder G3 at midspan and exterior girder G4 near the haunch are shown in Figs. 72 and 73. The largest stress range measured on the structure occurred near the haunch where a reversal of stress develops. The maximum stress range was equal to 3.4 ksi (23.4 MPa). The interior and exterior girders provided about the same stress range spectrums near midspan.

5.2 Thermal Stresses

The temperature gages at midspan, at pier 9 and at the haunch were read concurrently with the strain gages at those cross-sections during the period June 13 to June 16, 1977. Figure 74a shows the time temperature variation in the bottom flange and at the top of the web at midspan and compares it to the ambient air temperature at the bridge site. It is readily apparent that the bottom flange temperature follows the ambient air temperature more closely than the top of the girder web.

The differential temperature distribution in the cross-section resulted in a thermal stress cycle each day as illustrated in Fig. 74. When the bottom flange temperature exceeded the top of the web temperature, compression thermal stresses were introduced in the bottom flange at the midspan cross-section. When the temperature in the bottom flange was less than the temperature in the top web, tensile thermal stresses were introduced into the bottom flange. This is particularly apparent on

June 15 when a drop in the air and bottom flange temperatures before dawn, followed by an increase during the morning, resulted in a 2.3 ksi (15.9 MPa) stress range between 0600 and 1200 hours in the bottom flange. The air temperature had dropped about 24° F (-13.3° C) and the differential temperature in the steel girder at midspan was about 10% as the bottom flange temperature changed about 14° F (-28° C).

Figure 75a compares the bottom flange temperature at midspan and at pier 9. The variation between the temperature in the bottom flange at these two locations was not great. They generally followed rapid changes in air temperature about the same way. Figure 75b compares the thermal stress variation at midspan and at pier 9 for the bottom flange of the girder. In general a larger thermal stress response was observed at the midspan location.

It should also be noted that when the sun was shining directly on east girder G4 near midday, the girder temperature often exceeded the ambient air temperature.

The 2.3 ksi (16 MPa) thermal stress introduced into the bottom flange of the girder at midspan on June 15 developed over a six hour period as a result of a 14° F (-28° C) temperature differential. This suggests that the rapid decrease in temperature experienced in Pittsburgh on January 28, 1977 likely resulted in a differential temperature between the bottom flange and slab of 30 to 40° F (16.7 to 22° C) as the ambient air temperature dropped about 40 to 60° F (16.7 to 22° C) when a cold front passed through the area. Since this decrease developed in a much shorter time

frame, a much larger temperature differential would be expected. Hence, a thermal tensile stress cycle between 6.5 and 10 ksi (45 and 69 MPa) in magnitude would result as the bottom flange decreased more rapidly than the top flange.

6. ANALYSIS OF FRACTURE OF BACK CHANNEL GIRDER

6.1 Initial Defect

The fracture of the failed girder, 25G4C, was initiated by a discontinuity in a multiple repair area of an electroslog weld. The discontinuity was demonstrated by light and electron microscopy to be a welding crack, probably hydrogen assisted, that occurred during or shortly after welding. Other cracks of the same type were found adjacent to the initial defect in the same weld repair area. Residual stresses resulting from extensive weld repair and the unusual composition of the weld metal undoubtedly contributed to the conditions producing cracking. At least three weld repairs were successively made to the electroslag weld in the defect area, the initiating defect for the most part lying in the second repair area. Growth of this discontinuity by fatigue and fast fracture, as described hereafter, led to the ultimate failure of the girder.

6.2 Stress Distribution in the Flange in the Vicinity of the Crack

The discontinuity that existed at the midspan of casualty girder 25G4C was subjected to stresses from loads and residual welding stresses. Only stresses in the longitudinal direction were considered. These stresses are caused by the dead load (weight of the structure), the live load (traffic), from welding (residual stresses) and from temperature gradients over the cross-section of the continuous bridge.

From the design calculations it was found that the dead load stress at the critical location is 18.85 ksi (130 MPa) [2]. This calculation is

based on the assumption of noncomposite behavior which is reasonably compatible with the construction method of the structure. The dead load stress in the bottom flange is not affected by the composite behavior of the bridge. It is assumed that the stress is uniformly distributed over the flange plate.

The live load is lane load governed. The design live load plus impact results in a live load stress range of 7.5 ksi (52 MPa). Stress history measurements were made during summer 1978 (see Section 5) and resulted in the stress spectrum shown in Fig. 71 and tabulated in Table 12. The stress events given in Table 12 yield an equivalent stress range (Miner's Rule) of 0.77 ksi (5.3 MPa). The peak measured stress was 3 ksi (20.7 MPa). The equivalent stress range considered all the recorded 5099 stress events. The stress due to the actual traffic is obviously much smaller than the design stress. The difference between the design and the measured stress results from several factors. This included the number of vehicles on the bridge, the magnitude of impact, composite behavior and the three-dimensional behavior of the structure. The measured live load stresses were mainly due to the passage of single trucks.

In addition to the stress range response from truck traffic, the measurements obtained during the repair of the fractured girder and several measurements during the stress history examination indicated that significant thermal stress cycles developed (see Sections 2 and 5). Hence, it appears that larger stress cycles developed at slow strain rates. These resulted in daily stress ranges of 2 to 4 ksi (13.8 to 27.6 MPa). When sudden frontal movements passed through the Pittsburgh area, even larger

stress cycles developed.

Residual stresses in the bottom flange are from different origins. Longitudinal stresses are initially introduced in the flange by the electroslag welding procedure. During electroslag welding, the two plates are connected by liquid metal. The hot metal cools faster on the outside than on the inside of the weld. This results in residual stresses in the longitudinal direction of the weld. Near the weld surface, the material is in compression and tension develops in the center of the plate[5]. The assumed initial residual stress distribution is shown in Fig. 76 for the electroslag weld. The stresses are indicated for three horizontal planes in the flange: near the interior surface, at the middle of the plate and near the exterior surface. It is assumed that the stresses vary linearly in between. This initial residual stress distribution was later altered by repair welds.

During inspection (radiography) of the original electroslag weld, several flaws were detected which required repair. The repair was made in different stages by air arc gouging and replacing the material with manual welding passes. Different stages of the repair are shown schematically in Fig. 51. The metallographic examination indicated that one repair was made by gouging a boat-shaped cavity through the weld and in the connected plate in longitudinal direction. This excavation was located about 2 in. (51 mm) from the center line of the flange and was made from the bottom flange surface. At the crack plane the repair weld was the full flange thickness (see Fig. 52). A schematic of the repair weld at the crack plane and along the member is shown in Fig. 77. The removing

of the material also affected the residual stress in that area. The assumed residual stress distribution from the repair weld is shown in Fig. 77. The residual stresses shown in Fig. 77 are in equilibrium with the residual stresses away from the repair weld in the flange and web.

The repair weld was made manually; the repair cavity was filled by depositing many passes of weld metal. The resulting residual stress distribution in the electroslag weld after repair is shown in Fig. 78.

After repair of the flange plate, the web was attached to the flange with automatic submerged arc fillet welds. The web-flange welds only alter the residual stresses in the electroslag weld in a finite region[12]. The submerged arc fillet welds heat and melt the flange plate and a small portion of the electroslag weldment as they pass along the plate and over the weld. This provides some relaxation to the residual stresses in existance prior to making the weld. It is believed that this release is small compared with the undistributed zones and that the changes can be neglected. The residual stress field due to the flange-web fillet welds is shown in Fig. 79. This residual stress field was estimated based on residual stress measurements on welded steel girders with flange and web plate thickness of similar dimensions and fabricated from the same grade of steel[13].

Residual stress also exists due to other sources but were not considered here. Flame cutting the flange plates introduces tensile residual stresses. However, these stresses are maximum at the edges of the flange and would not appreciably affect the residual stress field near the middle of the flange. Residual stresses may also be present due to rolling and

straightening the plate.

Stresses in the girder flange are also caused by temperature gradients through the depth of the bridge cross-section. On the day the final fracture was discovered, the temperature dropped rapidly in the Pittsburgh area when a cold front moved through. The concrete slab cools down much slower than the completely unprotected steel girders. It was estimated in Section 2 on the basis of strain measurements that a temperature difference between the slab and the bottom flange of 14° F (8° C) would result in thermal tensile stresses of about 2.3 ksi (28 MPa) in the bottom flange. Hence, a 40 to 60° F (22 to 33° C) differential would develop from 6.5 to 10 ksi (45 to 69 MPa) thermal stress.

6.3 Analysis of Crack Growth

The various stages of crack growth in the casuality girder are shown schematically in Fig. 80. These have been identified as Stages I to V.

Stage I (Initial Discontinuity)

Stage I is believed to have occurred in the electroslag during the weld repair. The initial discontinuity in the weldment was taken as the initial crack size.

Stage II (Fatigue Crack Enlargement)

During Stage II, fatigue crack growth developed from the initial flaw under traffic and environmental loading. The crack in the flange was modeled as an elliptical-shaped flaw subjected to uniformly-applied stress. The diameter of the ellipse was taken so that the ellipse circumscribed

the irregular initial flaw shape (see Fig. 80). The shape and size of the ellipse is shown in Figs. 80 and 81. The stress intensity factor for an elliptical crack in a finite plate under uniform tension is given by Eq. 2, (see Fig. 82 for a crack in an infinite plate):

$$K = \sigma\ (\pi a)^{1/2}\ F_e\ F_w \tag{2}$$

where F_e is the correction factor for the shape and F_w takes the finite thickness into account. The crack shape factor F_e is [14]

$$F_e = \frac{1}{E(k)} \left(\sin^2 \phi + \left(\frac{a}{c}\right)^2 \cos^2 \phi\right)^{1/4} \tag{3}$$

because of void coalescence, growth due to cleavage fracture and growth due to corrosion[15].

Quantitative expressions have been developed for the striation mechanism of growth. Estimates are not available on the number of load cycles and their magnitude that are needed to advance the crack front through grain boundaries. Bates and Clark[16] developed an empirical relationship between the stress intensity range and the distance between the striation marks. They found that the distance Δs can be approximated by

$$\Delta s = 5.4 \left(\frac{\Delta K}{E}\right)^{2.1} \tag{4}$$

Eq. 4 was developed from measurements made on aluminum alloy under constant cyclic stress amplitude and a minimum stress intensity factor equal to zero (R = 0). In order to generalize the equation for use with other material, ΔK was normalized by dividing by Young's Modulus of Elasticity.

Other studies[15] have indicated that the ΔK value estimated from striation measurements is only accurate to within 40%. This relationship was extended by Hertzberg and VonEuw[15] for R-ratios larger than zero. They related the striation markings to an effective stress intensity range ΔK_{eff}. The test data was also acquired on 2024-T3 aluminum alloy and a more general relationship was developed as:

$$\Delta s = 24 \left(\frac{\Delta K_{eff}}{E}\right)^2 \tag{5}$$

where ΔK_{eff} was determined empirically for 2024-T3 aluminum as

$$\Delta K_{eff} = (0.5 + 0.4\ R)\ \Delta K \tag{6}$$

This relationship takes into account the fact that the crack will be closed near the tip during a part of the unloading cycles even if $R > 0$. This behavior was first proposed by Elber and verified by compliance measurements[15].

Equations 4 and 5 were both developed for constant amplitude stress cycles. The traffic crossing a bridge results in random variable load. Measurements of stress range suggest that most of the stress cycles will be below the fatigue crack growth threshold. Those cycles that exceed the crack growth threshold will only infrequently exceed the level of crack growth [10^{-7} in./cycle (2.5×10^{-6} mm/cycle)] that can be detected from the striation markings. Hence, the crack front can be advanced between striation marks by a relatively large number of stress cycles. This will cause the measured striations to be further apart than would be estimated by either Eqs. 4 or 5. Or conversely, any estimate of ΔK based on stri-

ation markings is overestimated. Striation markings are therefore useful to verify the crack growth mode, but quantative statements are difficult to make based on these markings. It is also possible that small markings may have been eliminated when cleaning the oxidized fracture surface.

For an empirical crack shape correction factor $c = 1.0$ in Eq. 3 and with the R-ratio equal to 0.8, a stress intensity range between 4.9 ksi $\sqrt{in.}$ (5.4 MPa $\sqrt{m}$) and 14.7 ksi $\sqrt{in.}$ (16.2 MPa $\sqrt{m}$) results from the striation measurements. Equation 3 indicates that a ΔK-value of 1.15 ksi $\sqrt{in.}$ (1.2 MPa $\sqrt{m}$) results from the effective Miner-stress range of 0.77 ksi (5.1 MPa). The maximum measured stress range of 3 ksi results in an initial stress intensity range for stage II of 4.5 ksi $\sqrt{in.}$ (5 MPa $\sqrt{m}$). Both the Paris-power-law and Eq. 5 indicate that for a ΔK-value of 4.9 ksi $\sqrt{in.}$ (5.4 MPa $\sqrt{m}$), on the average only every 19th cycle would produce a marking. By assuming that only stress cycles larger than 1.5 ksi (10.3 MPa) produce striation markings and the smaller stress ranges increase the crack length, every 23rd cycle larger than 1.5 ksi (10.3 MPa) would produce one marking. The relationship for the effective K-value due to the applied ΔK-value (Eq. 6) was developed on homogenous materials. In homogenous materials the crack front is straight and the applied ΔK-value can be directly related to the effective ΔK value. In the weld material, the crack front is irregular and the crack closing effect is affected by adjacent crack fronts.

Albrecht's[21] laboratory studies on fatigue striations at weld toe cracks in A588 steel showed that the striation marks only exist on about 10% of the fracture surface (about 70% of the fracture surface of aluminum

shows striation markings). Some of the remaining fracture surface was covered with so called quasi striations, whose spacings are an order of magnitude larger than the expected growth rate for A588 steel. Albrecht also found that if an overload was applied between every 10 and 100 cycles, then the average striation spacings were spaced further apart than predicted by the Bates and Clark Equation. (Eq. 4).

A correction factor of 1.59 was introduced to take into account the local irregularities in the estimated crack growth rate da/dN. The measured random variable stresses in the flange under traffic and the measured striation spacing provide comparable conditions when this adjustment is introduced. About every 19th stress cycle would be expected to produce detectable crack growth during stage II.

Stage III (Brittle Crack Extension)

During cold temperature and under live load stress the embedded elliptical flaw became unstable and enlarged by cleavage fracture (see Section 4). The brittle fracture was arrested when the stress intensity factor was less than the dynamic fracture toughness and/or the crack tip reached a zone with a higher fracture toughness.

The contributions to the stress intensity factor due to residual stress, dead load, and live load can be obtained by superposition of these different effects. Since the live load stress and the dead load stress are nearly uniformly distributed over the crack surface, Eq. 2 can be used to estimate their contribution to the stress intensity factor. The stress intensity factor due to the varying residual stress can be obtained by numerical integration of the K-values due to a splitting force applied at

a point on the crack surface. The K-value for the concentrated force[14] shown in Fig. 83 at one location on the crack front is:

$$K = \frac{P\, a^{1/2}}{\pi^{3/2}\, \ell^2} \left(\frac{r}{R}\right)^{1/2} \left\{ \frac{\left(\frac{1}{\alpha^2} - 1\right)^{1/2}}{(1 - k^2 \cos^2 \phi)^{1/4}} \right\} \tag{7}$$

The parameters in Eq. 7 are defined in Fig. 83. The crack surface was approximated with a 0.028 x 0.02 in. (0.7 x 0.5 mm) mesh. A computer program was used for the integration. A uniform stress distribution was also numerically integrated and compared with the closed form solution given by Eq. 2. Comparison showed that the numerical solution was within ±10% of the exact value, depending on the location on the crack front. A correction factor for each point on the crack tip was calculated and this individual correction factor was used to adjust the stress intensity factor due to the residual stress calculated with the numerical integration. The stress intensity factor was also adjusted for the finite width correction factor.

The stress intensity factor along the elliptical crack front due to residual stress and due to stresses from the dead and live load are shown in Fig. 84. The maximum K-value along the crack tip was 94.5 ksi $\sqrt{\text{in.}}$ (104 MPa $\sqrt{\text{m}}$), and occurs directly under the web-flange connection.

The material toughness tests (K_Q) of the A588 steel electroslag weldments (both back channel and from Ref. 5) and the curves for the toughnesses of A537G steel electroslag weldments (from Ref. 6) were summarized in Fig. 34. Also shown in Fig. 34 are the dynamic fracture toughness K_{Id}

which was estimated from Charpy V-notch data. This included electroslag weld and repair weld data. An envelope of the estimated fracture resistance was constructed and shifted to approximate the conditions for an intermediate strain rate. These results were used to bound the material toughness of the material at the crack as a function of temperature. The K_{Ic}-value is indicated as a band in Fig. 85. The estimated maximum K-value of 94.5 ksi $\sqrt{in.}$ (104 MPa $\sqrt{m}$) is compared with the experimental results. From the comparison it can be seen that crack instability is possible at temperatures between 20° F and -20° F (-7° C and -29° C). It seems highly probable that crack instability developed from the original defect at temperatures below 0° F (-20° C). It was necessary for the initial flaw to be sharpened by cyclic live load and fatigue crack propagation. This fatigue crack extension of the initial flaw and the decrease in material fracture resistance with the cold temperature in Pittsburgh in early January 1977 resulted in a crack instability and a sudden enlargement of the crack to a penny-shaped crack shown in Figs. 54 and 80.

Stage III (Crack Arrest)

The initial brittle fracture was arrested after the crack had assumed a semicircular shape with a radius of about 3 in. (76 mm). The crack was arrested because the crack tip stress intensity decreased as a result of the crack tip entering a zone of higher material toughness, and because the stress at the crack tip had decreased. Figure 34 indicates that the material toughness varies by ±13.5 ksi $\sqrt{in.}$ (±15 MPa $\sqrt{m}$) at a given level of temperature.

The stress intensity factor of the semicircular crack due to the changed residual stress distribution can be calculated using the procedure that was used to estimate the residual stress effects at the initial flaw and its limits of fatigue crack extension. The K-value must also be corrected by factors that take the finite width of the plate and the free surface into account. Reference 17 gives the correction factor for the free surface as

$$F_s = 1.211 - 0.186\ (\sin\phi)^{1/2} \tag{8}$$

The angle ϕ is defined in Fig. 82. The finite width of a plate is taken into account by the F_w factor. For an edge crack $F_w \cdot F_s$ is defined as[14]

$$F_w \cdot F_s = \left(\frac{2b}{\pi a}\tan\frac{\pi a}{2b}\right)^{1/2}\left\{\frac{0.752 + 2.02\,\frac{a}{b} + 0.37\,\left(1 - \sin\frac{\pi a}{2b}\right)^3}{\cos\frac{\pi a}{2b}}\right\} \tag{9}$$

where a is the crack length and b the plate width. Equation 8 overestimates the value of the $F_w \cdot F_s$ correction factor for a circular crack because the physical behavior of an edge is different from the behavior of a semicircular crack. The maximum crack length, a, for a circular crack is provided at 90°. At that location, the adjacent material restrains the plate from bending and the crack from opening. Hence, the finite width correction factor is calculated for an equivalent crack length. For the equivalent crack length a* it is assumed that the stress intensity factor for a semicircular (or semielliptical) crack in an infinite plate is the same as the factor for an edge crack in a semiinfinite plate. The stress intensity factor for an edge crack is[14]

$$K = 1.1215\ \sigma\ (\pi a)^{1/2} \tag{10}$$

and for a semielliptical surface crack[14]

$$K = F_s \cdot \frac{\sigma\ (\pi a)^{1/2}}{E\ (k)} \left(\sin^2 \phi + (\frac{a}{c})^2 \cos^2 \phi \right)^{1/4} \qquad (11)$$

The free surface correction factor for the semielliptical surface crack is between 1.0 and 1.30[17]. For convenience it was taken as 1.1215 in this analysis. Equations 10 and 11 can be used to estimate the equivalent crack length a* as:

$$a^* = a \frac{1}{E^2(k)} \left(\sin^2 \phi + (\frac{a}{c})^2 \cos^2 \phi \right)^{1/2} \qquad (12a)$$

This becomes

$$a^* = 0.405\ a \qquad (12b)$$

for a semicircular crack. Using the equivalent crack length a*, the finite width correction factor can be expressed as

$$F_w = \frac{1}{F_s} \cdot (\frac{2b}{\pi a^*} \tan \frac{\pi a^*}{2b})^{1/2} \left\{ \frac{0.752 + 2.02 \frac{a^*}{b} + 0.37\ (1 - \sin \frac{a^*}{2b})^3}{\cos \frac{\pi a^*}{2b}} \right\} \qquad (13)$$

The crack sizes shown in Fig. 81 were evaluated for various stress conditions. Figures 86, 87, and 88 show the resulting distribution of K-values around the crack tip including the effects of the residual stresses due to the electroslag welding, the repair weld, the web-to-flange weld and the stress due to the dead and live load. This shows that the maximum stress intensity factor decreased from its peak value of 94.5 ksi $\sqrt{in.}$ (104 MPa $\sqrt{m}$) at the start of fracture to about 64 ksi $\sqrt{in.}$ (70 MPa $\sqrt{m}$).

The dynamic fracture resistance of the electroslag weld can be estimated from the dynamic Charpy V-notch tests and from the static K_{IC} tests

when a temperature shift is considered. The full temperature shift is about 125° F (70° C) for the electroslag weld material. The estimated stress intensity level at crack arrest is plotted in Fig. 85. The comparison of the data with the stress intensity estimate suggests that the initial crack instability developed at about 15° F. It is probable that the irregular crackfront and blunting effects as the crack enlarged provided a higher level of fracture resistance than indicated. The stress intensity for crack sizes less than 3 in. (76 mm) is smaller than 64 ksi $\sqrt{in.}$ (70 MPa $\sqrt{m}$). This assisted in decreasing the velocity at which the crack was moving and helped arrest the crack at the 3 in. (76 mm) radius.

Stage IV (Fatigue Crack Extension)

After brittle fracture was arrested, the crack size was increased by fatigue crack growth. Fatigue crack growth was verified by striation markings at crack tip location 6 (Fig. 54). The fatigue crack extension sharpened the crack tip. About 0.04 in. (1 mm) of crack growth was observed.

Stage V (Flange Fracture)

When the temperature dropped and again decreased the fracture toughness of the weldment on January 28, 1977, the stress conditions and the resulting stress intensity factor reached the materials fracture resistance and the remaining section of the tension flange fractured. The cold front that passed through the Pittsburgh area on January 23, 1977 also produced a temperature gradient in the structure and resulted in additional thermal tension stresses in the bottom flange. The estimated

K-value at the time of fracture, considering the residual stress, dead and live load stresses and the thermal stress [assumed to be about 8 ksi (56 MPa)] was 83 ksi $\sqrt{in.}$ (91.3 MPa $\sqrt{m}$). The estimated K-value at flange fracture is compared with the material toughness in Fig. 89. The estimated K-value falls within the static fracture resistance band at the temperature believed to exist on January 28, 1977 when the crack was first observed.

6.4 Summary

Brittle fracture of the tension flange of a girder in the I79 Glenfield Bridge developed because a large initial weld defect enlarged in fatigue and exceeded the fracture resistance of the material. Variations in material toughness and changes in the stress field as a result of residual stresses from welding permitted the crack to arrest at a relatively large crack size. For the large crack size the fatigue crack growth rate was increased and small cyclic applied stresses continued to enlarge the crack so that fracture of the girder was inevitable.

Most of the fatigue life of the member was exhausted after the first brittle fracture occurred, and the embedded irregular elliptical-shaped flaw became unstable and resulted in a 3 in. (76 mm) semicircular surface crack. Brittle fracture was arrested because of the decrease in maximum stress (residual stress) and materials fracture toughness variations.

7. ANALYSIS OF DEFECT IN TIED ARCH GIRDER

7.1 Initial Defect

The discontinuity found in the west tie girder and removed as a core sample was shown by electron-optical analysis to be associated with copper contamination of the weld fusion line. This establishes the discontinuity to be a solidification (hot) crack produced during the electroslag welding process. The most probable source of copper contamination is local melting of the copper cooling shoes used in the electroslog welding process due to variations in welding parameters such as arcing during start up or due to low flux level. The defect was therefore present from the time the weld was made. The existance of a repair weld covering the surface of the crack, the remainder of which can be seen in Fig. 38, indicates that the defect was detected during fabrication and that repair, although ineffective, was attempted at that time.

7.2 Stress Distribution in Box Tie Girder

The discontinuity that was discovered in the electroslag weld in the west tie girder of the main tied arch crossing was subjected to stresses from dead and live load and residual stresses from welding. The discontinuity was primarily a semielliptical-shaped surface defect located along the fusion line and heat affected zone of the electroslag weld as shown in Figs. 16 and 38 for member 201T2.

The design calculations indicated that the dead load stress at the plane of the defect was 20.5 ksi (141.5 MPa)[19]. This value is primarily due to the axial force in the tie girder [7696 kips (3.4×10^7 N)] and a

nominal amount of bending.

The design live load and impact is based on lane loading. It provides a live load stress range of 6.75 ksi (46.6 MPa). Obviously, the probable maximum stress range the structure would experience is much less. Based on the experimental results acquired on the back channel structure and on other stress history measurements, a stress range of 3 ksi (20.7 MPa) was assumed as a reasonable estimate of the maximum stress range the defect would be subjected to.

Residual stresses in the tie girder which are of primary concern result from the electroslag weld, the surface weld repair over the defect and the web flange welded connections. Longitudinal fillet welds connected the 7/8 in. (22 mm) A517 steel web to the 2-3/4 in. (70 mm) thick A588 steel flange plates on the north side of the joint. On the south side of the electroslag weld, 1/2 in. (13 mm) groove welds attached the 1/2 in. (13 mm) A588 steel webs to the 2-3/4 in. (70 mm) A588 steel flange plate. Because of the extensive weld repair and the number of intersecting end crossing weldments, it was assumed that the residual stress field that the surface discontinuity was embedded in was at the yield point of the A588 steel flange plate. This results in a stress level of 60 ksi (4.19 MPa) for the residual stress effects.

Figure 90 shows the assumed residual stress distribution on the box cross-section. This distribution is based on available experimental and theoretical studies[20]. A schematic of the crack surface and its relationship to the geometry of the joint is shown in Fig. 91.

7.3 Analysis of Surface Crack

(a) Fatigue Crack Propagation

The crack was modeled as a semielliptical surface crack which extended to the edge of the flange plate where an abrupt change in geometry existed (see Figs. 15a, 38 and 91). Because of the transition in web plate thickness, a notchlike condition existed at the edge of the flange. This resulted in the discontinuity residing in a stress concentration area at that location.

The stress intensity range was estimated from the relationship:

$$\Delta K = F_e \; F_s \; F_w \; F_g \; \sigma_r \; \sqrt{\pi a} \qquad (14)$$

The crack-shape correction, F_e, the free surface correction F_s and the finite width correction F_w were all taken as unity. The stress gradient correction, F_g accounts for the stress concentration effect of the notchlike condition at the edge of the crack. With the termination of the longitudinal fillet weld connecting the web plate to the edge of the flange plate and the notchlike condition from the change in width of the flange plate, a stress concentration condition analogous to a welded attachment existed. A value of 1.5 was used to account for the stress gradient factor. Since the discontinuity resided in a high residual stress field, the threshold stress intensity factor ΔK_{TH} was taken as 2.75 ksi $\sqrt{\text{in.}}$ (3.0 MPa $\sqrt{\text{m}}$).

$$K = 1.5 \times 3 \sqrt{\pi \; (0.25)} = 4 \text{ ksi } \sqrt{\text{in.}} > \Delta K_{TH} \qquad (15)$$

This suggested that crack growth could develop under the traffic which would use the structure. If the stress gradient correction factor F_g was less than estimated, the fatigue crack growth threshold might still be

exceeded. By setting Eq. 14 equal to K_{TH}, the value of F_g needed for crack propagation can be estimated as:

$$\Delta K = 3\ F_g\ \sqrt{\pi\ (0.25)} = 2.66\ F_g = \Delta K_{TH} \tag{16}$$

$$F_g = \frac{2.75}{2.66} = 1.03$$

It seems clear that the possibility of fatigue crack growth existed at the crack in the tie girder flange under service loads.

(b) Fracture Resistance

The fracture resistance of the crack in the west tie girder was estimated by considering the crack to be subjected to yield point stress as a result of the dead and live loads and the residual stress conditions.

This results in a maximum stress intensity estimate of

$$K_{max} = \sigma_y\ \sqrt{\pi a} \tag{17}$$

$$= (60)\ \sqrt{\pi\ .25} = 53\ (\text{ksi}\ \sqrt{\text{in.}}\ )$$

The Charpy V-notch test data obtained at the fusion line and heat-affected zone are summarized in Fig. 24. The results suggest that the fracture toughness is comparable to the lower bound provided in Fig. 34 for the fusion line and heat-affected zone of the tie girder weld. Figure 92 shows the estimates of stress intensity and their relationship to the fracture resistance of the tied arch materials. Also shown are the test data for the two three Point bend specimens that were prepared from the top surface layer (see Fig. 17) and tested at -30° F (-34° C). The results indicate that the fracture resistance is equaled or exceeded at service temperatures between 0 and -30° F (-18° C and to -34° C).

7.4 Summary

The analysis of the defect discovered in the west tie girder of the I79 main river span indicated the initial discontinuity was produced in the welding process and that fatigue crack propagation was possible under service loads.

In addition, the defect was found to provide a stress intensity value under the most severe estimates of dead load, live load and residual stress that was equal to the estimate fracture resistance of the electroslag weldment.

Furthermore, it seemed highly probable that all electroslag weldments in the tie girders had comparable levels of fracture toughness. Hence, corrective action and retrofitting was desirable for all nine of the splices that existed in the tie girders. The retrofit included the addition of bolted splice plates to each tie girder flange. In addition, slots were placed in the tie girder web directly above the electroslag weldment as shown in Fig. 93. This served to isolate the flange welds from the girder webs. Any cracking in the electroslag weldment would be prevented from entering the girder webs by the "crack arrest" holes. Removing the web and weld material directly over the electroslag weldment also reduced the residual tensile stress acting on the joint.

8. ANALYSIS OF SAMPLES AND DEFECTS REMOVED FROM THE BACK CHANNEL STRUCTURES

No failures developed in any of the other channel girders that were spliced and cored for further study. The core removed from the ramp D structure was found to have extensive surface discontinuities as shown in Figs. 62 and 64. This sample was removed from weld 4 of girder 27G4C.

The porosity discontinuity in the span D weld was not rejectable according to the 1977 AWS Code and the Peabody Tests[10] on the basis of size, although cracking is rejectable at any size. It was visually apparent that it had characteristics similar to the fusion line discontinuity that was detected in the tied arch structure. The weld repair placed across the surface of the weldment at the apparent fusion line insured that any defect was subjected to yield point residual stress.

The electroslag weld at the suspect point connected a 2-1/2 in. (63.5 mm) thick flange plate to a 3-1/4 in. (82.5 mm) thick plate and was in a transition. Hence, the geometric change in thickness provided a stress concentration condition at the plate surface. Although the repair weld was ultimately found to be separated from the electroslag weld, analysis of the defect as observed in the field made removal prudent for the reasons indicated hereafter.

8.1 Fatigue Crack Propagation

The stress intensity range for the discontinuity is provided by the relationship

$$\Delta K = F_e \, F_s \, F_w \, F_g \, \sigma_r \sqrt{\pi a} \tag{18}$$

Since the discontinuity was rather long, the product of the crack shape and free surface correction, $F_e \, F_s$ was taken as 1.12. With the finite width correction F_w as unity, Eq. 18 becomes

$$\Delta K = 1.12 \, F_g \, \sigma_r \sqrt{\pi a} \tag{19}$$

The porous condition with hairline-like cracks between the pores was about 0.2 in. (5 mm) deep. The stress intensity range was equated to the crack growth threshold and yielded

$$\Delta K = 1.12 \, F_g \, \sigma_r \sqrt{\pi \, (0.2)} = 2.75 \text{ ksi } \sqrt{\text{in.}} \tag{20}$$

$$(3.0 \text{ MPa } \sqrt{\text{m}} \,)$$

Therefore $F_g \, \sigma_r$ = 3.1 ksi (21.4 MPa)

This indicated that the stress range - stress gradient product would be exceeded during the service life of the ramp structure. The stress range measurements on the back channel structure had demonstrated that live load stress ranges of 3 to 3.4 ksi (20.7 to 23.4 MPa) were possible. Comparable stress range conditions were probable on ramp D. Hence, fatigue crack propagation would develop with time regardless of location with respect to the electroslag weld.

No significant discontinuities were detected in other back channel weldments. Therefore, it is probable that no crack growth would develop unless the crack growth threshold is less than assumed or else discontinuities have not been detected. This is particularly true for those electroslag weldments that are located in the tension flanges of the negative moment regions. The maximum measured stress range at piers 9 and 10 indicated that the live load stress range would not exceed 1 ksi (6.9 MPa).

In addition, the thermal stress effects did not appear to be as significant as those that developed in the bottom flange near midspan.

8.2 Fracture Resistance

The maximum stress intensity factor for the natural crack condition that existed on Ramp D would depend on the residual stress state at the defect and its exact location. An upper bound estimate can be provided by assuming yield point stress acting on the crack from the combined dead load, live load and residual stress conditions. This results in a maximum stress intensity estimate of:

$$K_{max} = 1.12 \times 60 \sqrt{\pi\ (0.2)}\ F_g \qquad (21)$$
$$= 53.3\ F_g$$

Assuming no stress concentration effect results in a stress intensity of 53.3 ksi $\sqrt{in.}$ (58.6 MPa $\sqrt{m}$), any stress gradient effect will increase the magnitude of the maximum stress intensity.

As can be seen in Figs. 36 and 37, the fracture toughness of the back channel structures was not significantly greater than the casualty girder. Hence, the reserve fracture capacity of the ramp D girder was not adequate for a defect located at an electroslag weld. This was particularly true since crack extension was possible under the service loads.

8.3 Summary

The analysis of the defect that was detected near the electroslag weldment on ramp D indicated that fatigue crack propagation was probable. The fracture toughness of the back channel weldments were not greatly

different than observed in the casualty girder. Since the maximum stress intensity approached the lower bound fracture toughness of the material, based on the field inspection of the girder it was apparent that retrofitting was prudent.

Although no defects were detected in other back channel weldments, those located in positive moment region tension flanges were spliced because of the low fracture toughness and the uncertainties of the nondestructive inspection. At the splice locations, maximum stress ranges between 3 and 4 ksi (20.7 and 27.6 MPa) were anticipated which increased the possibility of fatigue crack propagation.

In the negative moment regions the composite action of the steel girder and concrete slab decreased the maximum stress range to 1 ksi (6.9 MPa). This significantly reduced the possibility of fatigue crack propagation. Hence, no splices were provided in those regions pending further study. In order to minimize the possibility of fracture and to isolate the electroslag weldment from the girder web, slots were placed in the girder web as shown in Fig. 94. These slots were installed at all electroslag weld locations. This included the spliced bottom flange tension joints and the top flange tension joints in the negative moment regions.

9. SUMMARY AND CONCLUSIONS

This report presents the results of a detailed study that was carried out on the fracture that developed in the I79 back channel crossing at Neville Island. It includes the results of material tests, metallographic and fractographic studies, measurements of stress in the girder section and an analysis of the conditions causing fracture.

The report also presents the results obtained from sample cores removed from the tie girder of the main channel crossing and from other electroslag weldments in the back channel structure and ramps.

1. The fracture that developed in an electroslag weld in Girder G4 of the back channel structure was found to occur as a result of a large crack that was fabricated into girder at the time the weldment was made. The initial crack was elliptical in shape and was primarily embedded in a multiple pass weld repair (about 75%). Fatigue crack propagation was found to occur on the boundary of this crack. The crack was found to suddenly enlarge by cleavage fracture to a 3 in. radius. Further, fatigue crack growth was detected along the crack front prior to a final fracture of the flange. The available facts indicate the final fracture developed on January 28, 1977.

2. The multiple pass repair weld in which most of the initial crack was embedded had very low fracture toughness. It was equal or less than the fracture toughness provided by the electroslag weldment at the casualty section.

3. The electroslag weldment in the casualty girder had less notch toughness than the weld qualification test.

4. Sample cores removed from other back channel electroslag weldments indicated that only one sample core failed to meet the absorbed energy requirement of the AWS Specification.

5. The natural crack removed from the top flange electroslag weldment of piece 201T2 at the north end of the downstream truss was found to have been produced at the time of welding to be in a weldment of very low fracture toughness. None of the CVN specimens satisfied the AWS Specification requirements and the results were much lower than the weld qualification test.

6. The core removed from ramp D Girder 27G4C had a surface imperfection in many respects similar to the condition detected in the tied arch downstream truss. Subsequent examination of the core revealed that the discontinuity was not as severe as the condition in the tie girder.

7. Strain measurements recorded during the repair of the back channel fractured section indicated that the desired stress distribution was reestablished at the cracked section. These measurements also showed that the slab was acting compositely with the main longitudinal girders.

8. Stress measurements under random truck traffic indicated that the maximum recorded stress range at the casualty section was 3 ksi. The maximum value recorded at piers 9 and 10 in the top tension flanges was 1.0 ksi.

9. Thermal strain measurements on the back channel structure suggested that a thermal tensile stress cycle between 6.5 and 10 ksi was possible if a large change in air temperature developed over a short time interval.

10. The analysis of the defect discovered in the west tie girder of the tied arch span indicated that fatigue crack propagation was possible under service loads. In addition, the electroslag weldment did not provide an adequate level of fracture toughness for the crack and stress conditions that existed. Hence, it was necessary to retrofit the electroslag weldments in the tie girders in order to insure their integrity.

11. The analysis of the defect detected in the electroslag weldment on ramp D also indicated that fatigue crack propagation was probable. Since the fracture toughness of many of the back channel weldments were not greatly different than observed in the casualty girder, it was desirable to retrofit that joint as well.

12. Other electroslag weldments in positive movement region tension flanges of the back channel structures were also retrofitted because of the uncertainties of the nondestructive inspection and the erratic levels of fracture toughness observed in the sample cores.

TABLE 1

MEASURED AND COMPUTED STRAINS AND STRESSES IN SELECTED MEMBERS OF THE FLOOR BEAM TRUSS AND BOTTOM LATERAL BRACING SYSTEM

	Measured						Ref. 3			
Jacking Force →	685 kips		1305 kips		1674 kips		1674 kips		1950 kips	
Location	ε μin/in	σ ksi	ε μin/in	σ ksi	ε μin/in	σ ksi	ε μin/in	σ ksi	ε μin/in	σ ksi
	(1)	(2)	(3)	(4)	(5)	(6)	(7)	(8)	(9)	(10)
a	- 64	-1.9	-176	- 5.2	-252	- 7.4	- 630	-18.6	- 734	-21.7
b	+175	+5.2	+337	+ 9.9	+372	+11.0	+1186	+35.0	+1381	+40.7
c	+ 15	+0.4	+ 51	+ 1.5	- 68	- 2.0	+ 87	+ 2.6	+ 101	+ 3.0
d	+296	+8.7	+582	+17.2	+830	+24.5	+1241	+36.6	+1446	+42.7
e	+225	+6.6	+446	+13.2	+670	+19.8	+622	+18.3	+ 725	+21.4
f	-116	- 3.4	-182	- 5.4	-238	- 7.0	-	-	-	-

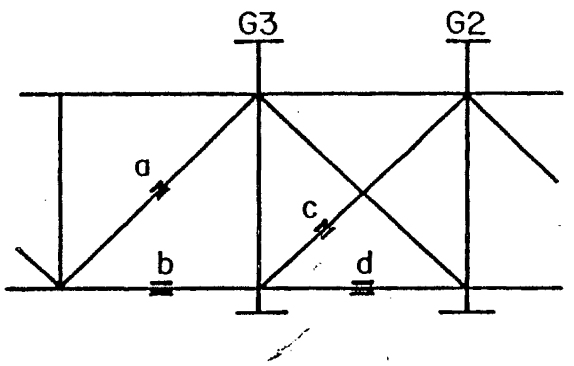

Elevation of Floor Beam Truss (Sect ① Fig. 3)

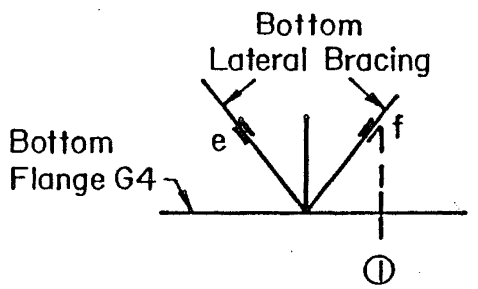

Plan of Bottom Lateral Bracing (Fig. 3)

TABLE 2

TIED ARCH SPAN

(a) Charpy V-Notch Test Results

Specimen	Location of Notch	Temperature	Absorbed Energy ft-lbs.
C11	Coarse Grain HAZ	0° F	10.0
C21	Coarse Grain HAZ	0° F	8.1
C12	Coarse Grain HAZ	40° F	16.0
C13	Coarse Grain HAZ	40° F	14.5
C22	Fusion Line	0° F	5.5
C32	Fusion Line	0° F	14.5
C33	Fusion Line	0° F	12.5
C23	Fusion Line	40° F	10.5
C31	Fusion Line	40° F	23

(b) K_c Test Results

Specimen	B	W	a/W	K_Q ksi $\sqrt{in.}$
Natural Grade	0.65	0.55	0.32	35.5
Adjacent Fusion Line	0.65	0.55	0.32	65

TABLE 3

CHEMICAL ANALYSIS

	Back Channel Glenfield Bridge				Tied Arch I-79 Main Span	
	I1T-B	I1T-W	I2T-W	I2T-B	Weld Metal	Base Metal
Mn	1.100	0.985	0.983	1.103	1.166	1.045
Ni	0.123	0.390	0.387	0.126	0.110	0.135
Cr	0.444	0.286	0.291	0.443	0.201	0.482
Cu	0.297	0.365	0.367	0.297	0.173	0.350
Mo	0.0045	0.0040	0.0023	0.0040	0.0155	0.0065
V	0.029	0.021	0.023	0.029	0.018	0.044
Al	0.0113	0.0035	0.0035	0.0070	0.0070	0.0252
C	0.183	0.126	0.131	0.120	0.164	0.235
P	0.034	0.038	0.041	0.030	0.032	0.036
S	0.038	0.040	0.035	0.029	0.033	0.037
Si	0.290	0.221	0.244	0.202	0.170	0.204

CASUALTY GIRDER

REPAIR WELDMENT

	#6	#7
Mn	2.20	2.18
Ni	0.030	0.030
Cr	0.46	0.46
Cu	0.141	0.141
Mo	0.008	0.009
V	0.014	0.014
Al	0.018	0.018
C	0.210	0.282
P	0.091	0.090
S	0.024	0.026
Si	1.18	1.12

TABLE 4

CHARPY V-NOTCH TESTS ON CASUALTY GIRDER

Specimen	Location	Temperature °F	Absorbed Energy, ft-lbs.
D22	HAZ*	0	4
D41	HAZ	0	6
D53	HAZ	0	3
DB1	HAZ	0	38
DB2	HAZ	0	20
DB3	HAZ	0	23
B21	WM	0	12
B22	WM	0	10
D21	HAZ	40	6
D43	HAZ	40	8
D51	HAZ	40	19
D52	HAZ	40	37
B23	WM	70	96
B24	WM	70	85
B25	FL	70	16
B26	FL	70	14
I1T1	FL*	70	15
I1T2	FL	0	9
I1T3	WM	0	12
I1T4	WM	0	11.5
I2T1	FL	0	10
I2T2	FL	0	11
I2T3	WM	0	11
I2T4	WM	0	12.5
I4T1	FL	40	22
I4T2	FL	40	28.5
I4T3	WM	40	33.5
I4T4	WM	40	19
I5T1	FL	40	16.5
I5T2	FL	40	25
I5T3	WM	40	31
I5T4	WM	40	20

TABLE 5

CHARPY V-NOTCH TESTS OF WELD REPAIR

Specimen Identification	Test Temperature	Energy (ft. - lb.)	Lateral Expansion (mils)
14	40° F	6	4
7	40° F	13	6
1	40° F	18	8
8	40° F	21	10
11	40° F	12	5
6	0° F	8	5
15	0° F	4	3
3	0° F	9	4
2	0° F	8	4
10	0° F	7	4

TABLE 6

CHARPY V-NOTCH TESTS ON CASUALTY GIRDER
FLANGE-BASE METAL

Specimen	Temperature °F	Absorbed Energy, ft-lbs.
G33	-30	3
G34	-30	2
G35	-30	4
G36	-15	6
G21	0	6
G22	0	10
G23	0	9
G51	20	15
G24	40	43
G25	40	15
G26	40	58
G31	40	11
G32	40	40
G52	55	60
G53	70	55
G54	70	61
G55	70	81
G56	95	107
G61	120	114
G62	120	104
G63	120	110
G64	150	117
G65	212	115

TABLE 7

TENSILE PROPERTIES I79 FLANGE

Sample	Temp. °F	% Elongation	Yield (ksi)	Ultimate (ksi)
H_1	75°	25.6	56.5	83.75
H_2	75°	25.0	63.75	84.38
M_6	75°	29.6	55.0	83.0
M_4	75°	24.7	56.2	84.25
M_2	0	21.1	63.0	99.35
M_3	0	28.5	55.0	87.5
H_3	0	19.9	61.16	90.9
H_4	0	20.4	59.0	89.5

M - Longitudinal Tensile Specimen

H - Transverse Tensile Specimen

TABLE 8

FRACTURE TOUGHNESS OF BASE METAL

Specimen	Test Temp. °F	B (in.)	W (in.)	a/w	J Ic	K_J ksi$\sqrt{in.}$	P_{max} Kips	K_{max} ksi $\sqrt{in.}$
WEB I-79								
2	0	.499	2.005	.615	2831	307	4.5	
3	0	.499	2.002	.591	3679	350	4.7	
5	-30	.500	2.010	.587	2107	265	4.8	
6	-30	.499	2.012	.596	2952	314	4.5	
7	-30	.503	2.008	.582	2770	304	4.7	
8	-100	.499	2.009	.619	2220	272	4.2	
9	-100	.501	2.019	.601	1799	245	4.8	
4	-100	.499	2.009	.601	499	122	4.5	
FLANGE								
L-5	+80	1.707	3.992	.508	697	152	41.0	128
L-4	+80	1.706	3.993	.503	455	123	35.0	99
J-4	+73	1.001	2.001	.529	102		9.1*	68
F-2	+73	1.003	2.001	.509	165	74	10.3	71
L-2	+32	1.709	3.998	.515	670	149	38.0	112
L-3	+32	1.713	3.994	.511	188	79	25.6	74
L-6	0	1.711	3.994	.517	217	85	26.0	77
L-7	0	1.709	3.992	.494	275	96	29.0	80
J-2	-30	1.004	1.998	.518	58	44	6.2	44
F-4	-30	1.003	2.003	.525	164	74	10.3	74
L-8	-30	1.700	4.001	.516	197	81	23.5	70
F-1	-100	.845	2.007	.503	81	52	6.4	52
J-1	-100	.845	2.005	.500	77	51	6.3	51

* Pop-in at 8.2 kip

TABLE 9

I79 BACK CHANNEL STRUCTURE AVERAGES

Specimen	Average Absorbed Energy	Location	Temperature
H2	16.4	Centerline	@ 0° F
9G1A	17.2	Centerline	@ 0° F
	35.7	Centerline	@ 70° F
	46.7	Centerline	@ 100° F
	28.5	1/4 width	@ 0° F
	25.5	Fusion Line+	@ 0° F
9G1B	26.0	Centerline	@ 0° F
	38.5	Centerline	@ 70° F
	34.5	1/4 width	@ 0° F
	4.5	Fusion	@ 0° F
9G11	15.6	Centerline	@ 0° F
	17.7	Fusion Line	@ 0° F
9G4	6.1	Centerline	@ 0° F
	22.3	Centerline	@ 70° F
	18.1	1/4 width	@ 0° F
	20.9	Fusion Line	@ 0° F

+ Single Specimen

TABLE 10

I79 BACK CHANNEL STRUCTURES

Specimen	Notch Location	Absorbed Energy	Temp. F	Specimen	Location	Absorbed Energy	Temp. F
H21-1	CL*	13.5	0	H21-2	1/4 width	26.0	0
H21-4	CL	39.0	0	H21-3	1/4 width	16.0	0
H22-2	CL	7.5	0	H22-1	1/4 width	17.0	0
H22-3	CL	7.0	0	H22-4	1/4 width	41.5	0
H2B-1	CL	20.0	0	H2B-2	1/4 width	32.5	0
H2B-3	CL	11.5	0				
9G1A2-2	CL	11.5	0	9G1A2-1	1/4 width	23.0	0
9G1A2-5	CL	17.0	0	9G1A2-7	1/4 width	27.0	0
9G1A2-4	CL	43.0	70°	9G1A4-1	1/4 width	39.0	0
9G1A2-6	CL	28.5	70°	9G1A4-7	1/4 width	25.0	0
9G1A4-3	CL	20.0	0	9G1A2-3	FL**	25.5	0
9G1A4-4	CL	17.0	0				
9G1A4-6	CL	20.5	0				
9G1A4-2	CL	47.5	100°				
9G1A4-5	CL	46.0	100°				
9G1B2-3	CL	24.0	0	9G1B2-1	1/4 width	38.5	0
9G1B2-4	CL	22.5	0	9G1B2-6	1/4 width	19.5	0
9G1B2-5	CL	33.0	0	9G1B2-7	1/4 width	42.0	0
9G1B2-2	CL	35.0	70°	9G1B4-1	1/4 width	32.5	0
				9G1B4-2	1/4 width	34.0	0
9G1B4-3	CL	22.0	0	9G1B4-6	1/4 width	40.5	0
9B1B4-5	CL	28.5	0				
				9G1B4-7	FL	4.5	0
9G1B4-4	CL	42.0	70°				
9G11-1	CL*	16.0	0	9G11-3	FL/HAZ**	7.0	0
9G11-2	CL	14.5	0	9G11-4	FL/HAZ	15.0	0
9G11-6	CL	17.5	0	9G11-5	FL/HAZ	31.0	0
9G11-7	CL	14.5	0				
9G41-2	CL	6.0	0	9G41-1	1/4 width	9.0	0
9G41-3	CL	6.0	0	9G44-1	1/4 width	29.0	0
9G41-4	CL	4.0	0	9G44-4	1/4 width	20.5	0
				9G45-1	1/4 width	14.0	0
9G42-1	CL	8.0	0				
9G42-3	CL	7.0	0	9G44-3	FL***	31.5	0
				9G45-2	FL	16.0	0
9G42-2	CL	13.5	70°	9G45-3	FL	21.5	0
9G42-4	CL	31.0	70°	9G45-4	FL	14.5	0
9G44-2	CL	6.0	0				

* Centerline
** Fusion Line/Heat Affected Zone
*** Fusion Line

TABLE 11

FRACTURE TESTS OF BACK CHANNEL CORES

Specimen	Test temp. °F	B in.	W in.	a/W	K_Q ksi $\sqrt{in.}$
H23	-30	0.91	1.5	0.75	73.5
9G1A31	-22	0.42	1.44	0.53	84.4
9G1A32	-30	0.42	1.44	0.55	101.6
9G1B31	-22	0.42	1.44	0.55	59.1
9G1B32	-30	0.42	1.44	0.55	62.8
9G111	-22	0.42	1.44	0.53	81.4
9G112	-30	0.42	1.44	0.48	93.8

TABLE 12

STRESS RANGE FREQUENCY

Gage B8 Near Crack, Bottom Flange

0 ksi	No. of Events	%
0.25	754	14.79
0.50	2133	41.83
0.75	936	18.36
1.00	360	7.06
1.25	438	8.59
1.44	401	7.86
1.68	66	1.89
1.92	5	0.10
2.16	4	0.08
2.40	0	0
2.64	0	0
2.88	1	0.02
3.12	1	0.02

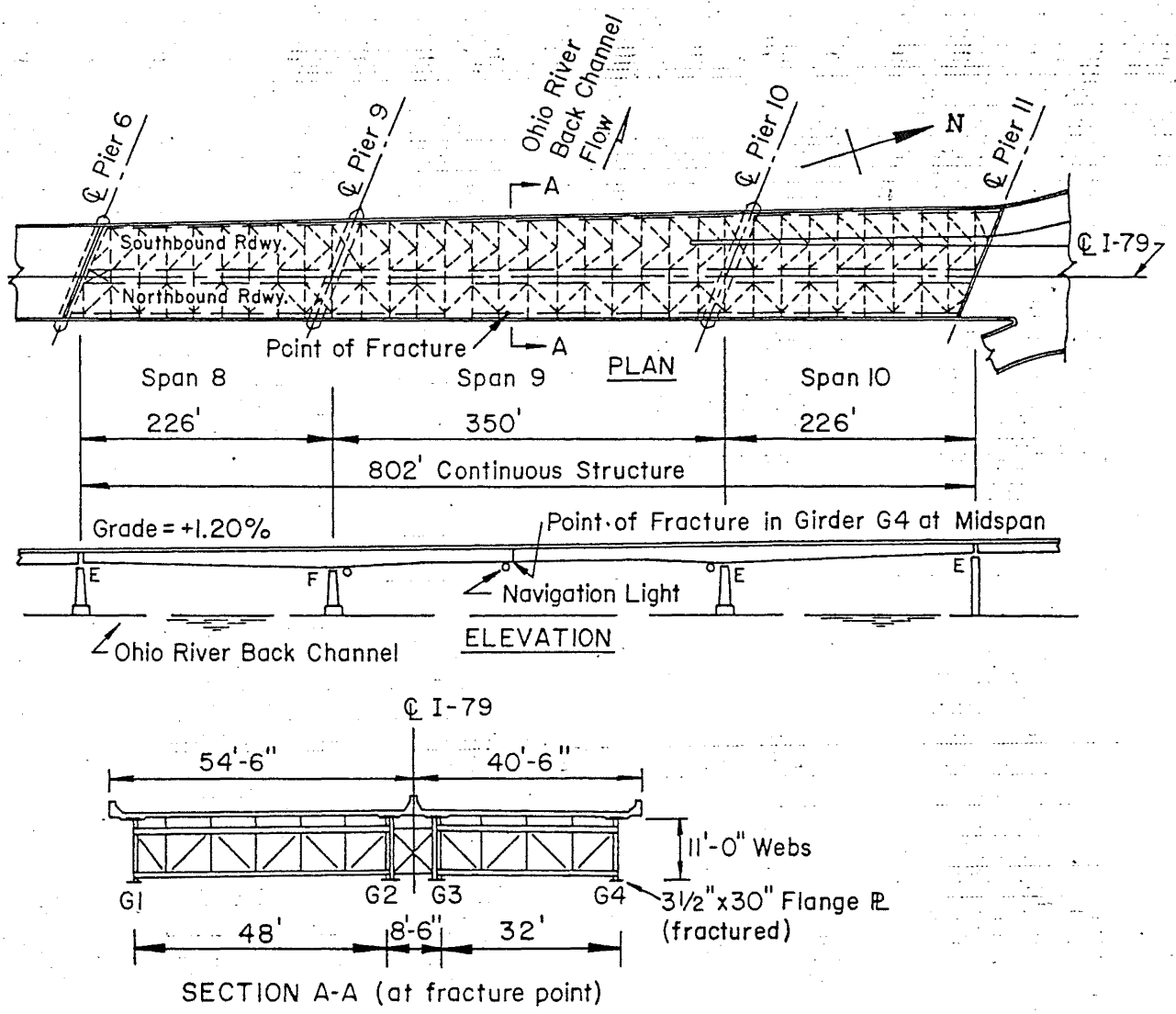

Fig. 1 Schematic of the I79 Back Channel Structure

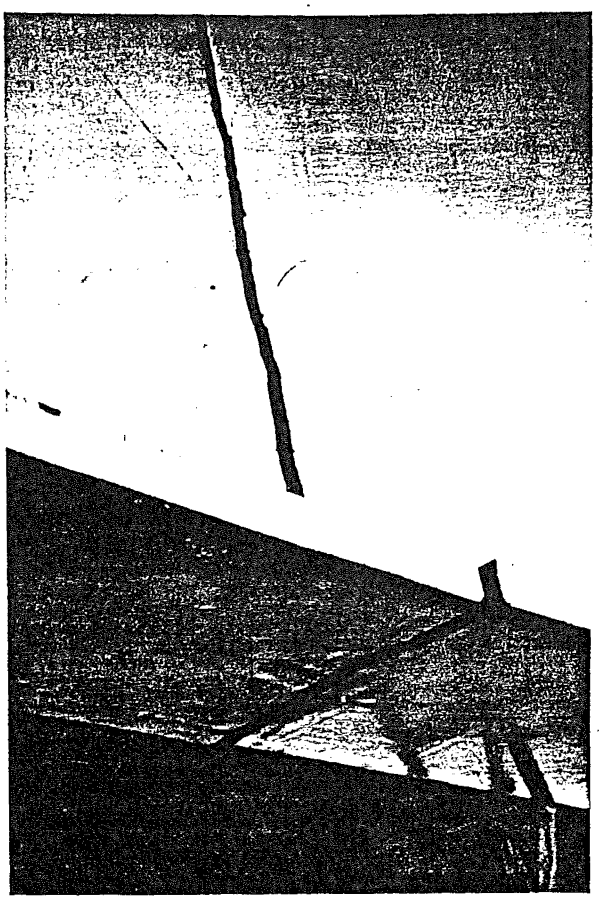

Fig. 2a Photo of Structure Near Midspan Showing Crack in Outside Girder

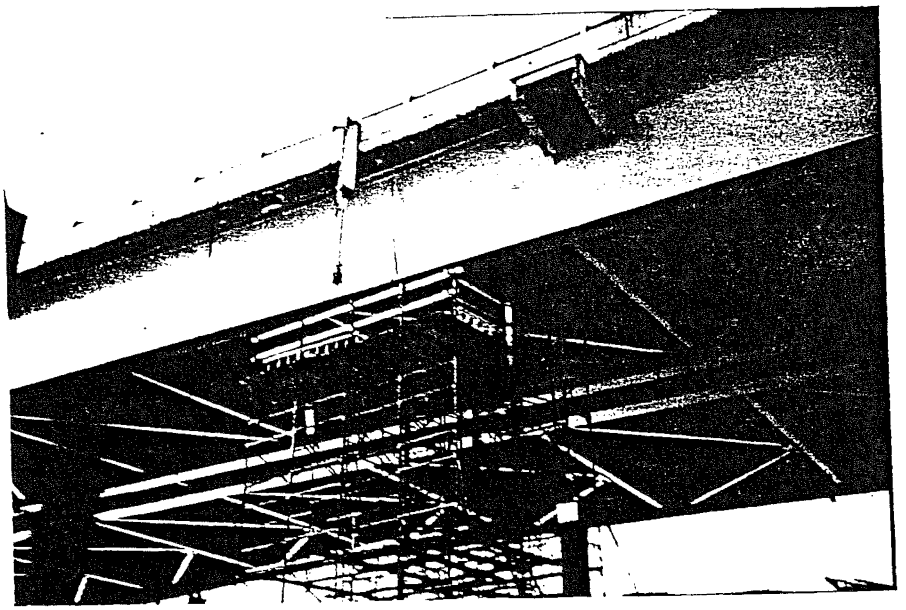

Fig. 2b Cracked Girder Showing Separation of the Flange and Lower Web

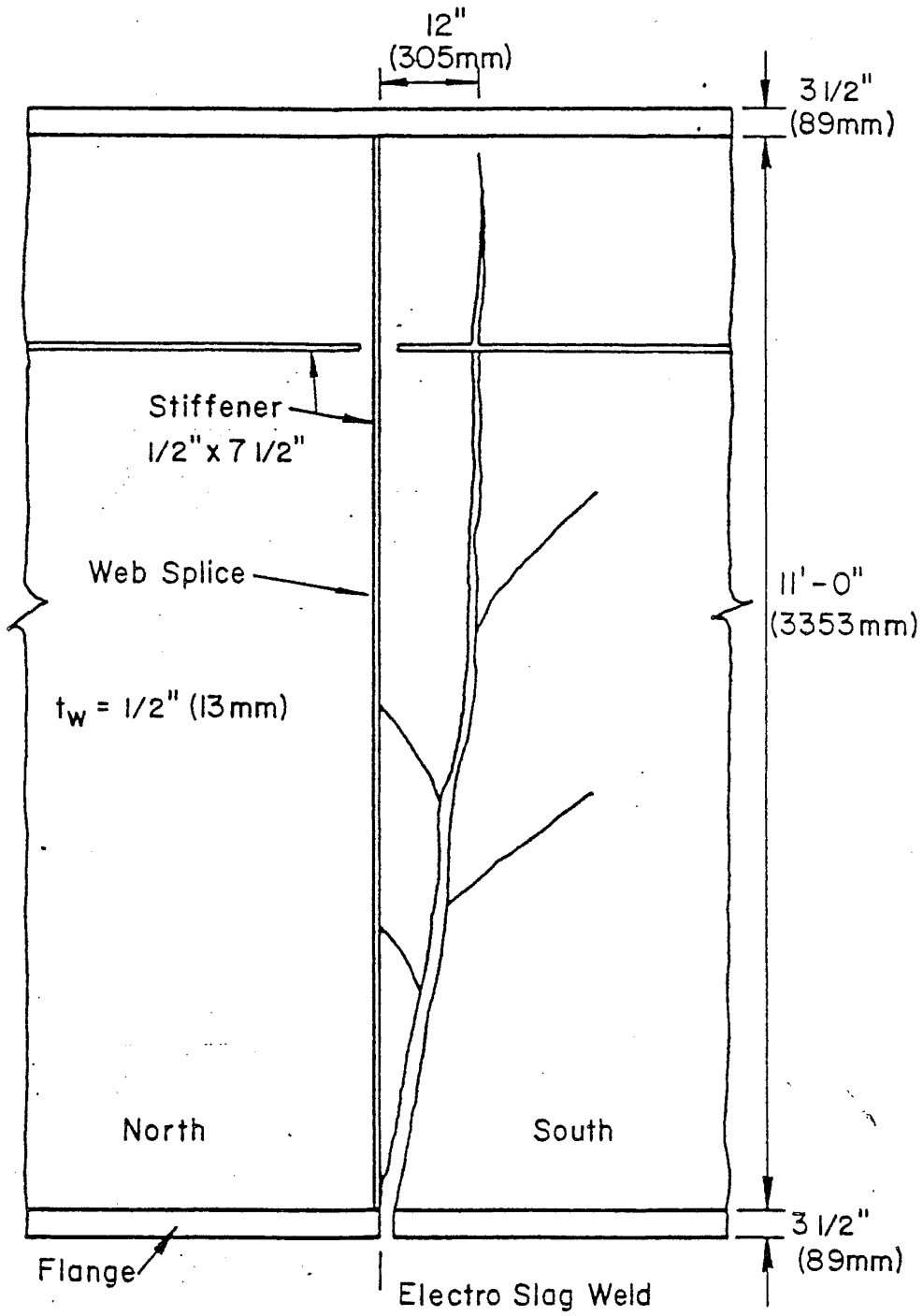

Fig. 3 Schematic of Crack at the Fractured Section

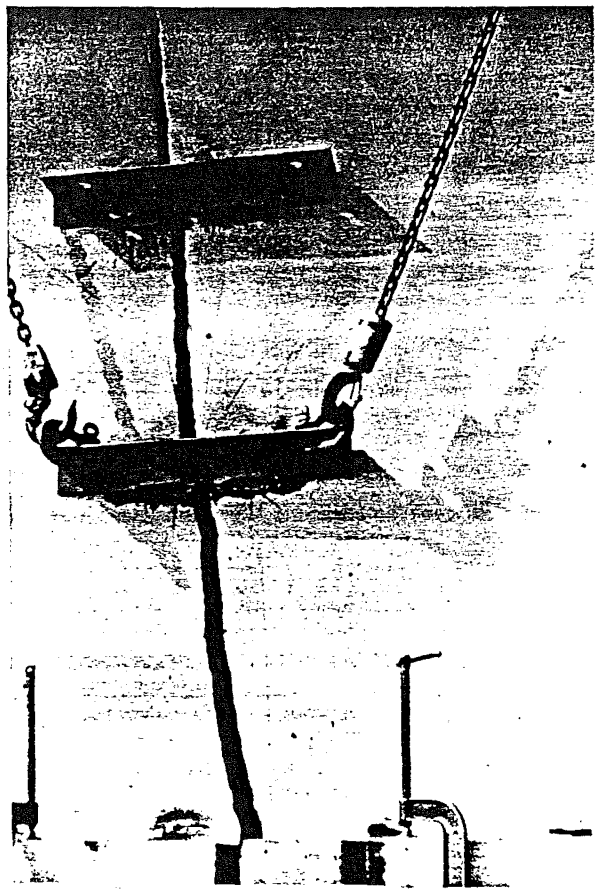

Fig. 4 Angles Welded to Girder Web Each Side of Crack to Prevent Damage to Fracture Surface

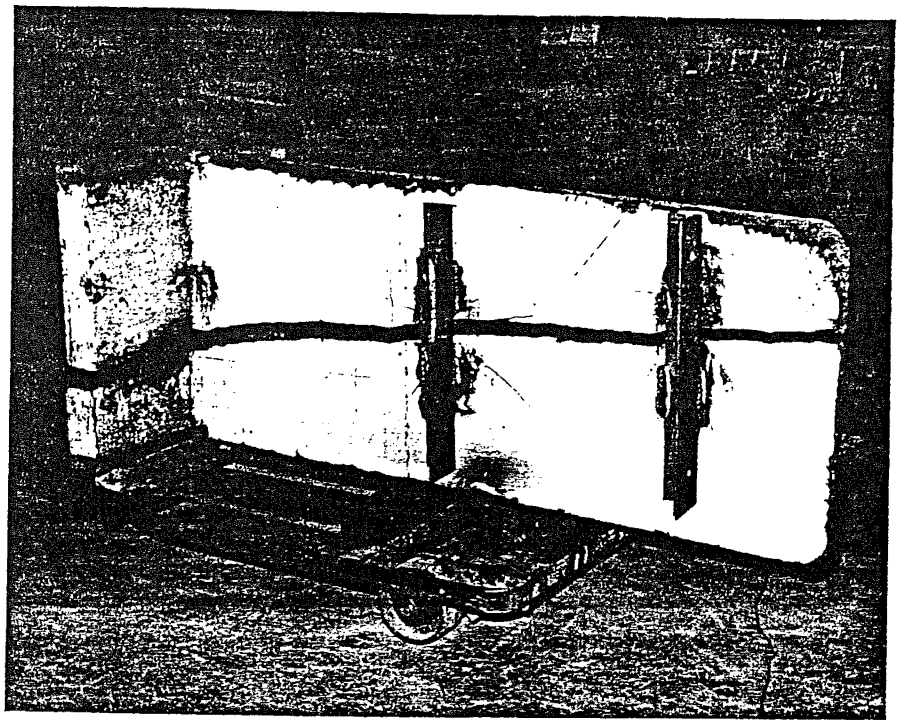

(a) Outside Web Surface Showing Angles Used to Keep Crack Surfaces Apart

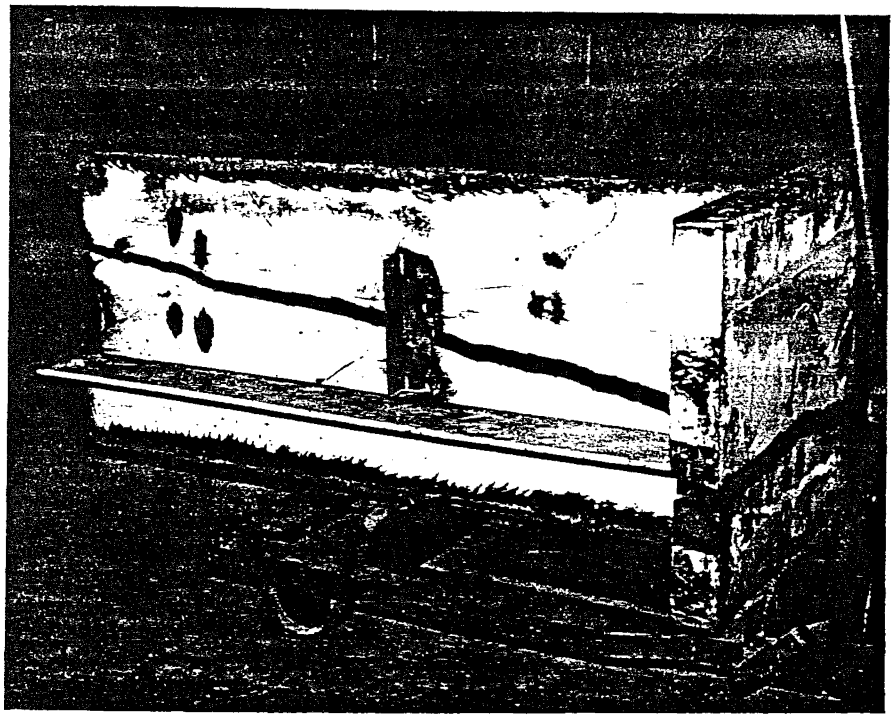

(b) Inside Web Surface Showing Transverse Stiffener

Fig. 5 Sections of Fractured Girder Removed

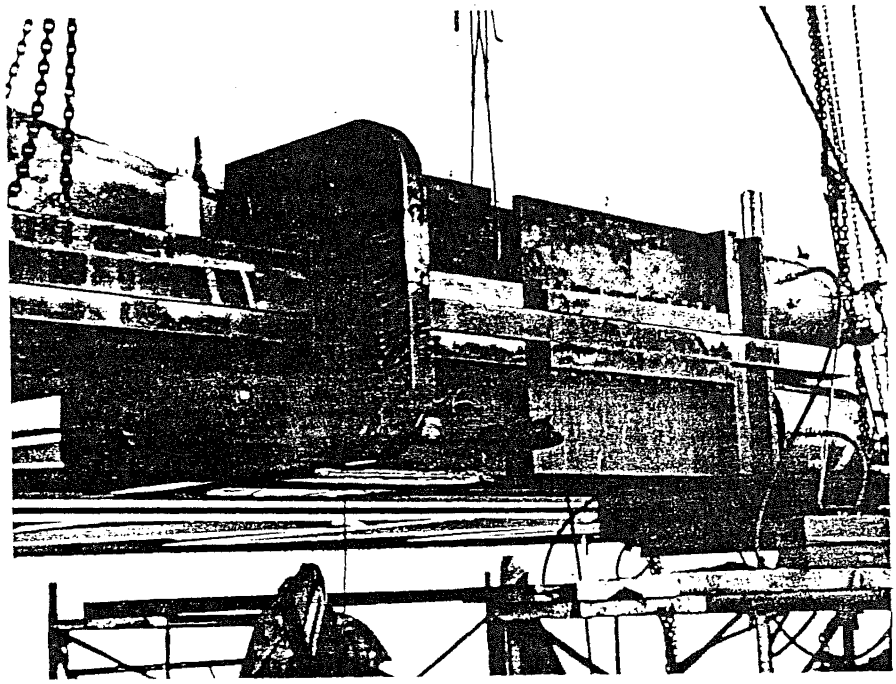

Fig. 6 Horizontal Hydraulic Jacking Arrangement
Mounted on Tension Flange of Girder G4

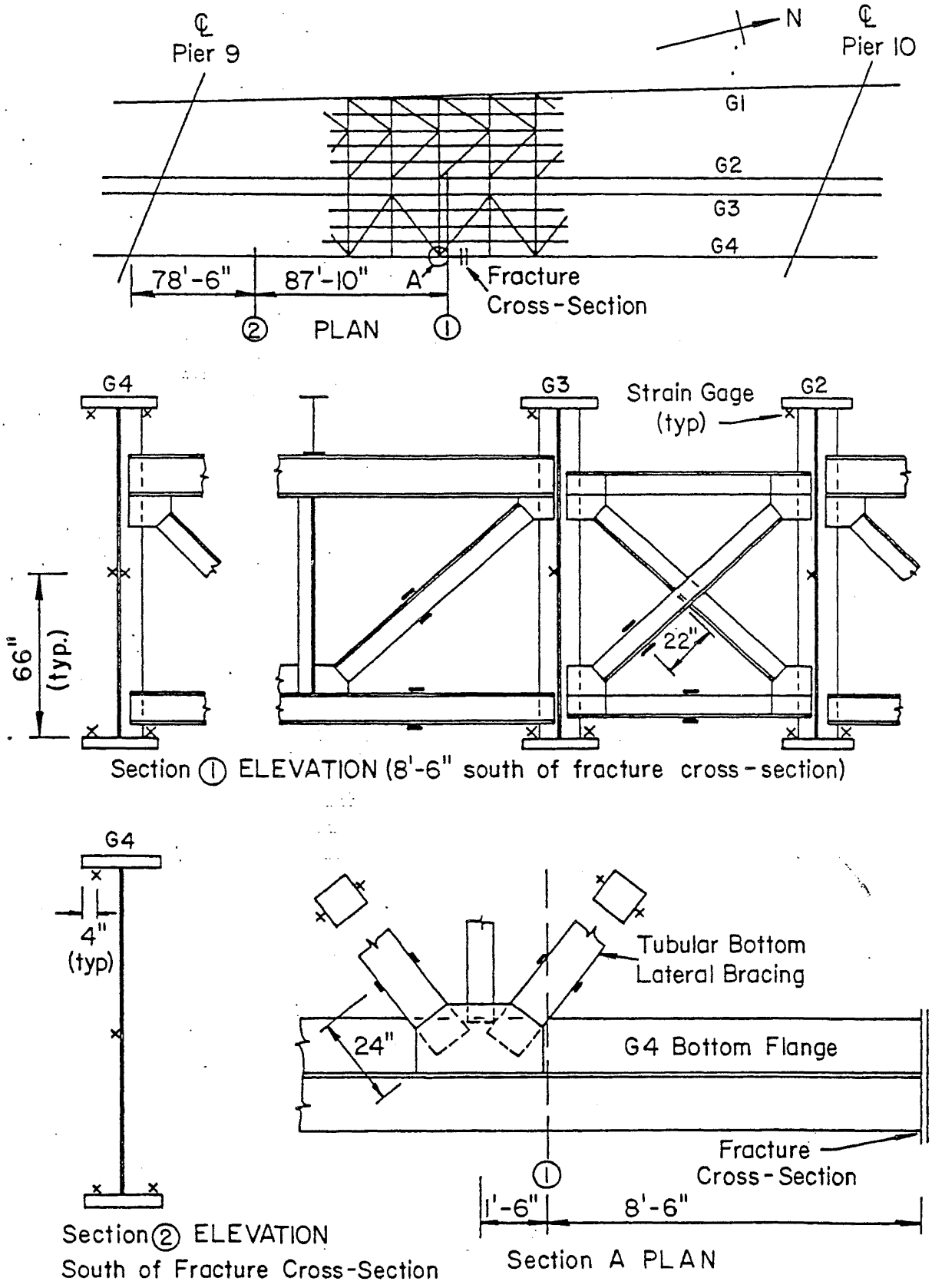

Fig. 7 Schematic Showing Location of Strain Gages During Jacking Operation

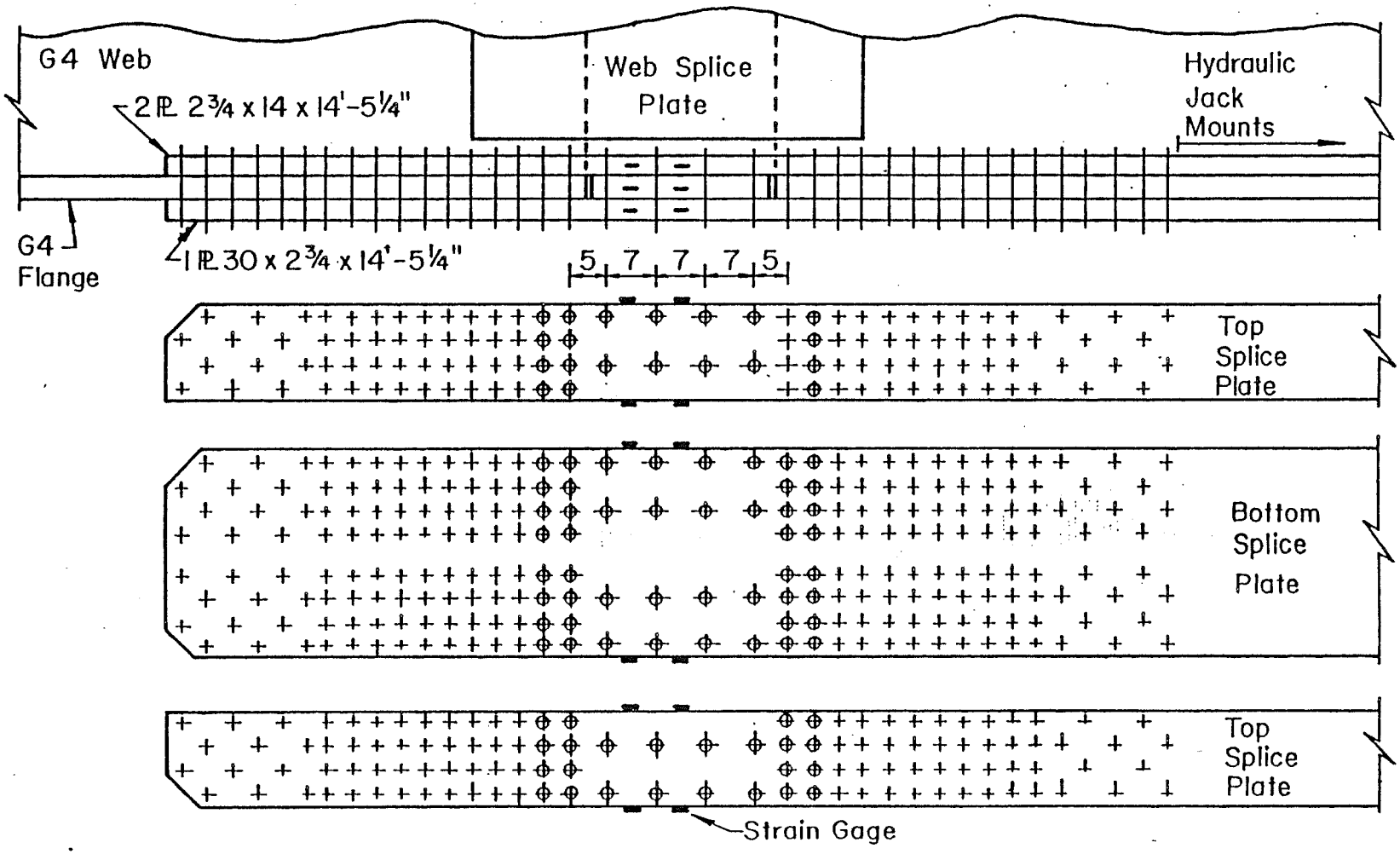

Fig. 8 Instrumentation of Splice Plates

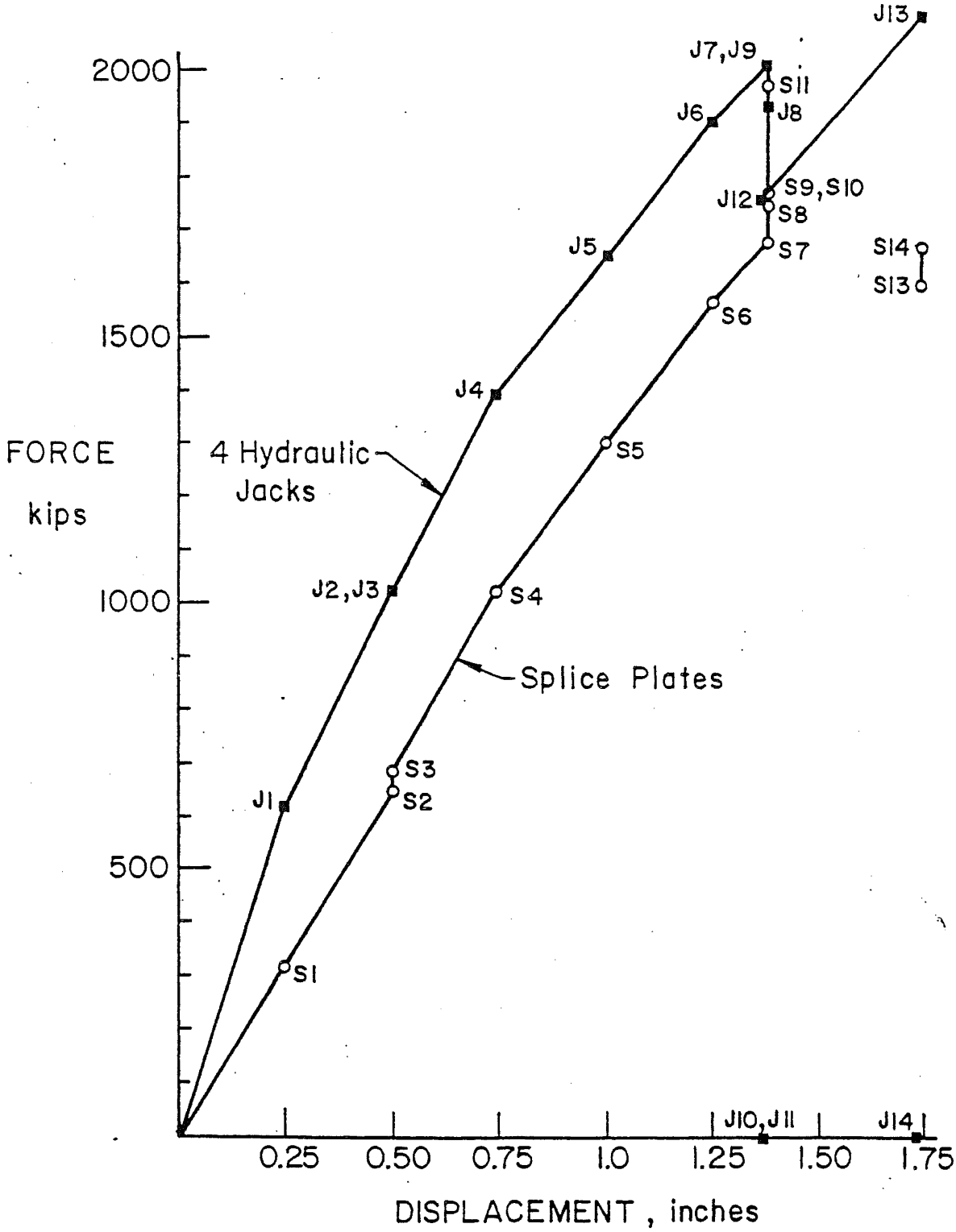

Fig. 9 Relationship Between Measured Force in Splice Plates and Force in Hydraulic Jacks Versus the Relative Closing Displacement of the Tension Flange

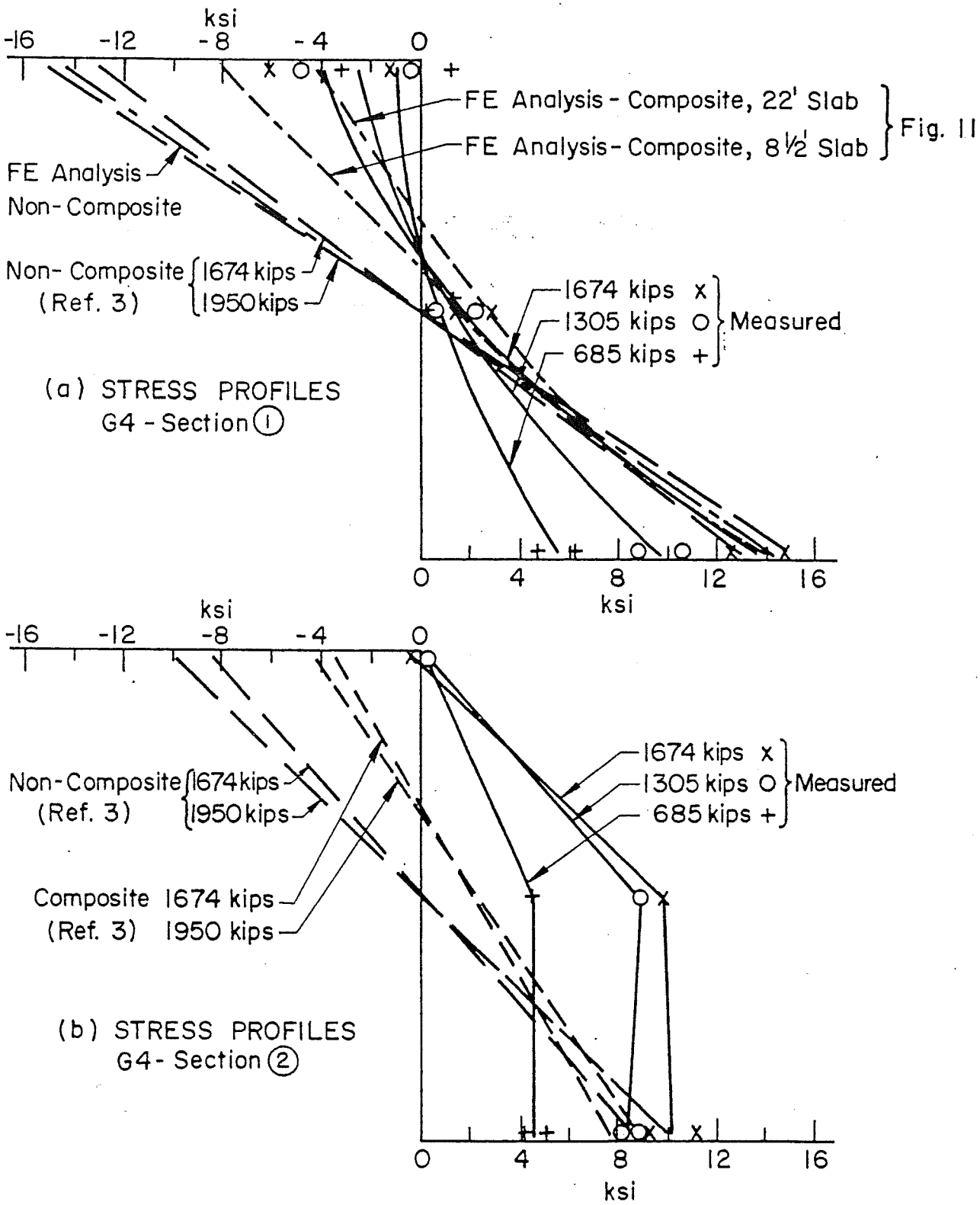

Fig. 10 Comparison of Stress Distribution in Girder G4 With Predicted Values

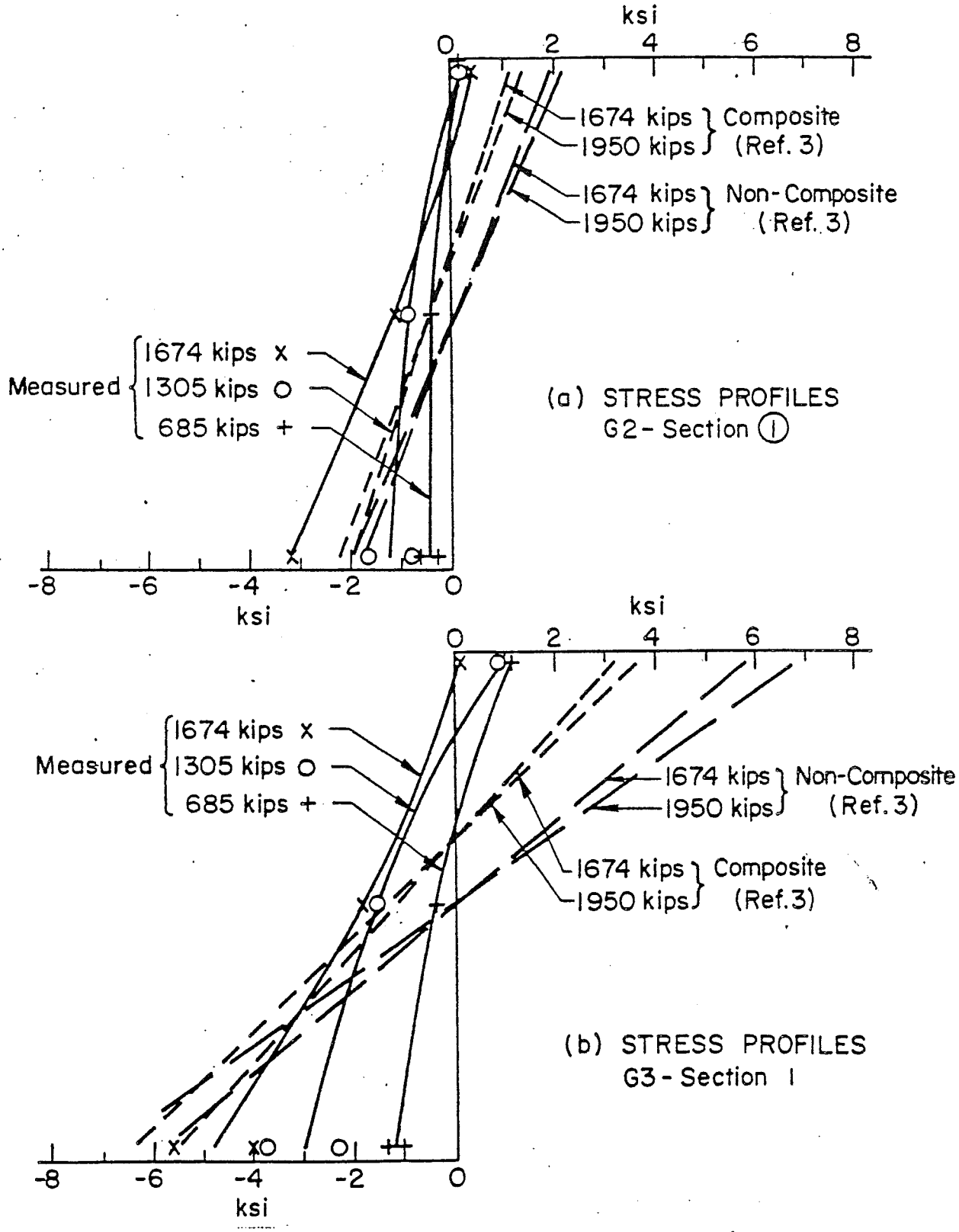

Fig. 11 Comparison of Stress Distributions in Girders G2 and G3 with Predicted Values

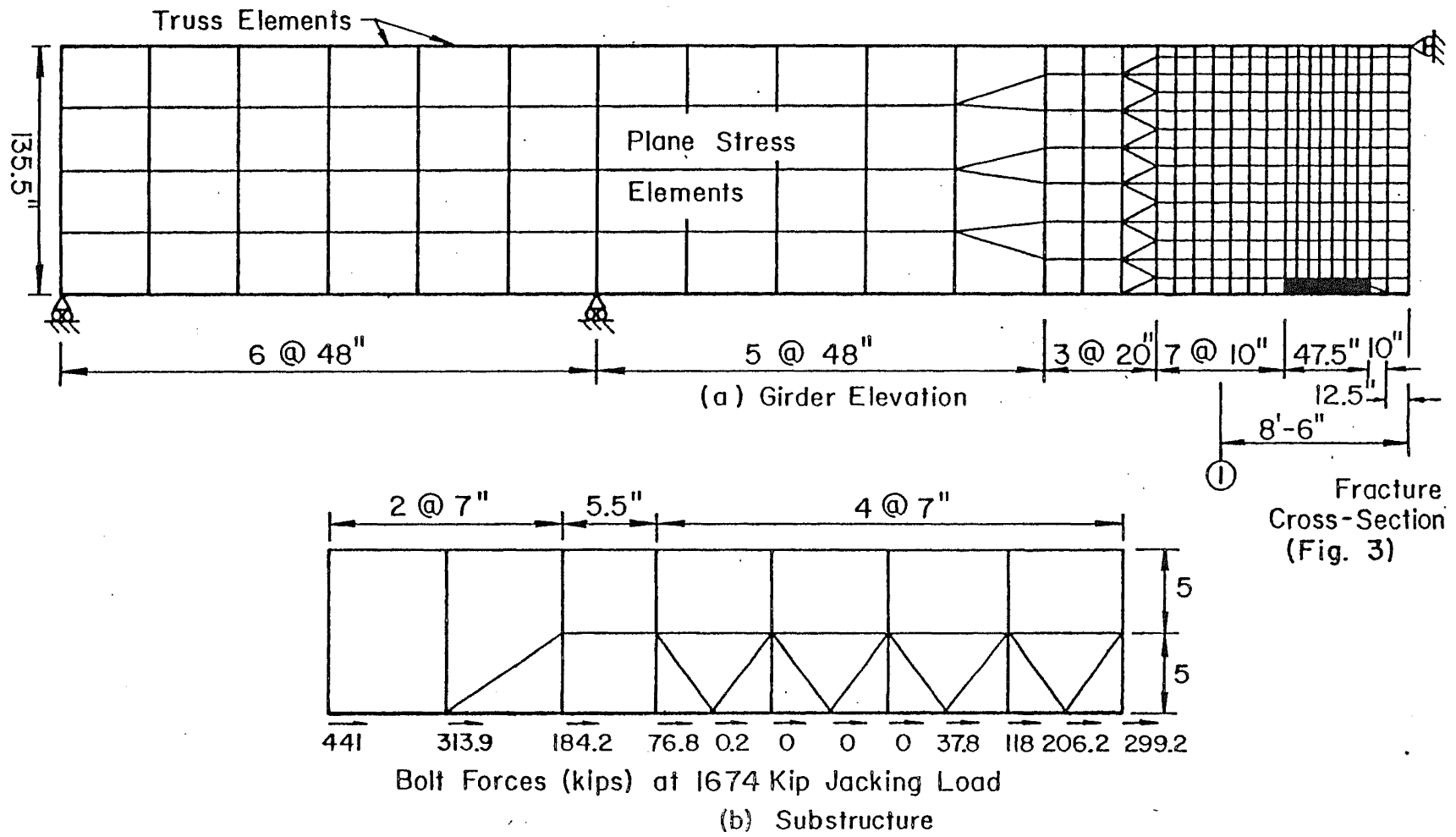

Fig. 12 Finite Element Model of Girder G4 South of Fracture Cross-Section

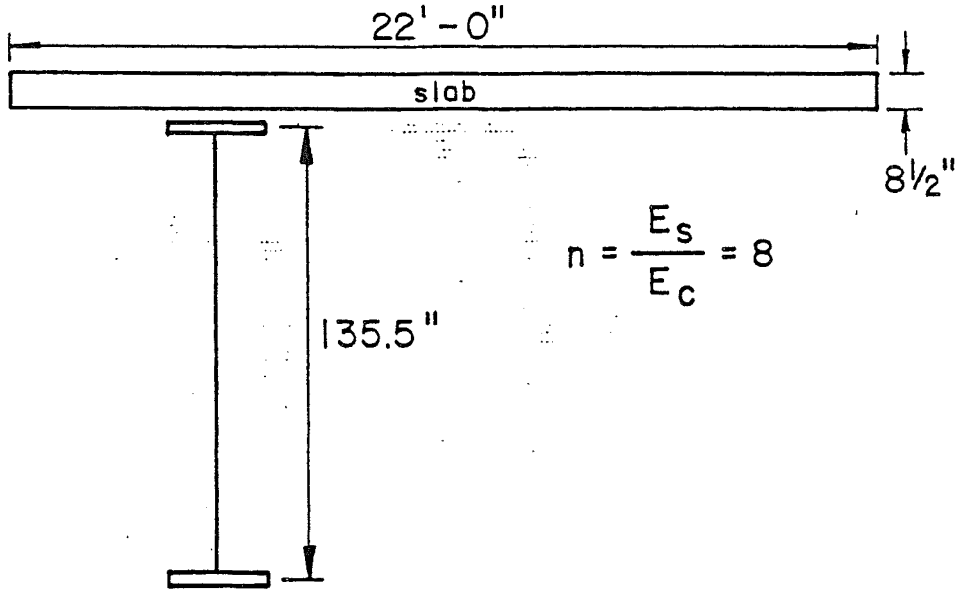

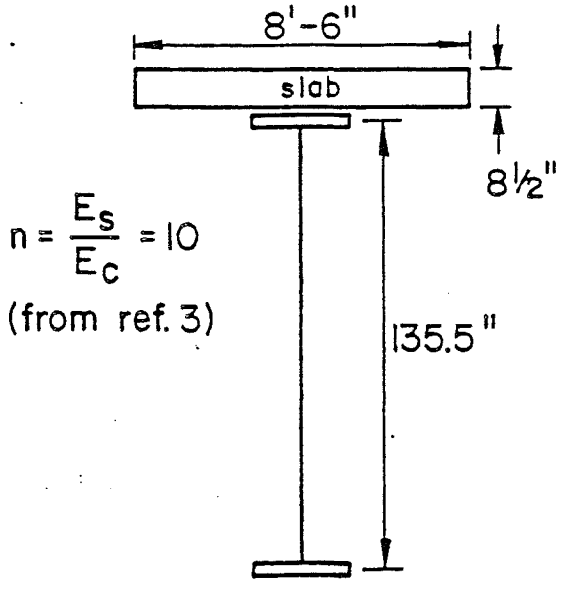

Fig. 13 Composite Girder Cross Section Used in Finite Element Analysis

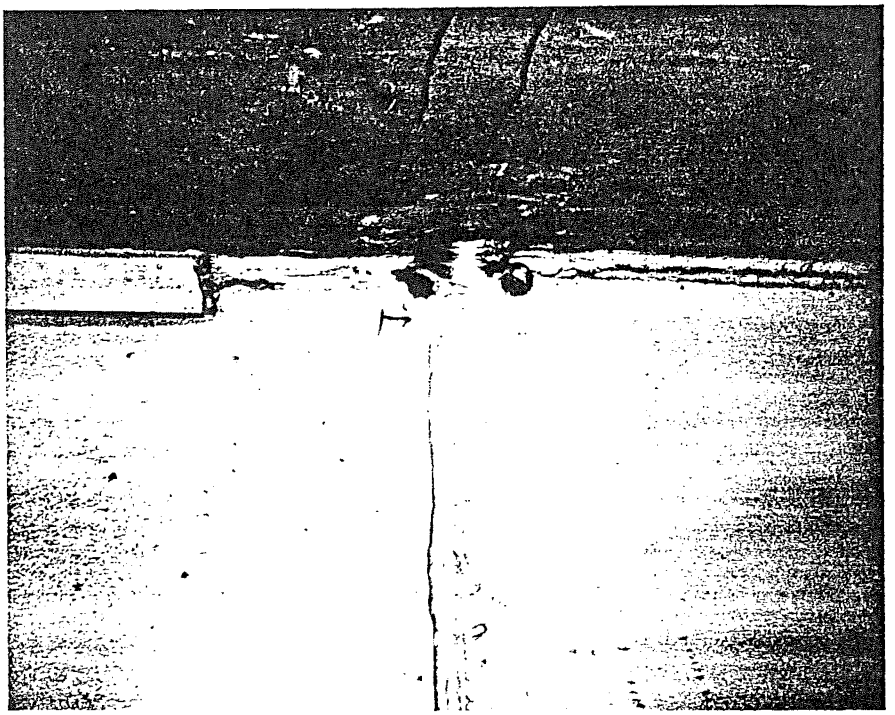

Fig. 14 Inside of Tie Girder Showing Holes in Web and Flange After Removal of Core

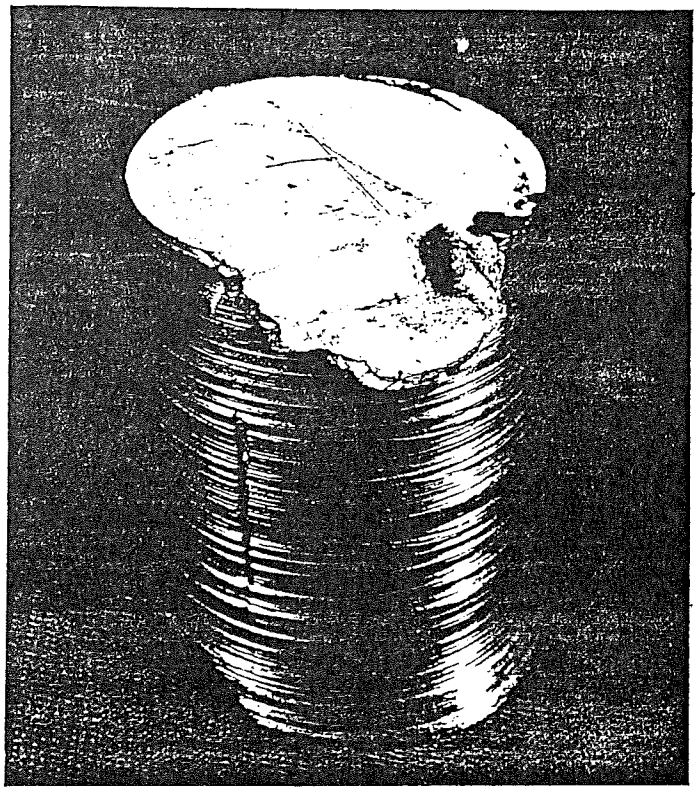

Fig. 15a View of Core Removed from Tied Arch Top Flange Surface

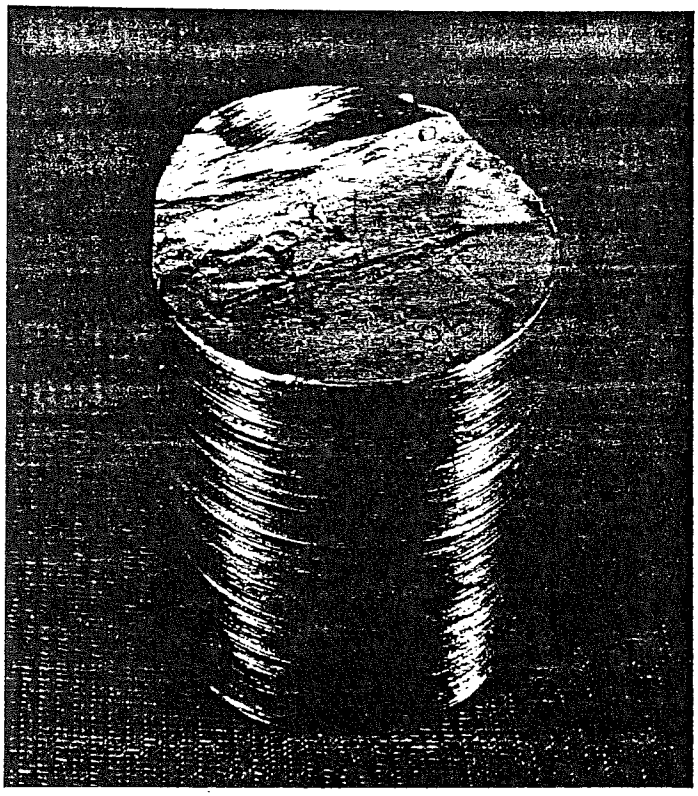

Fig. 15b View of Core from Tied Arch Showing Inside Surface and Longitudinal Weld

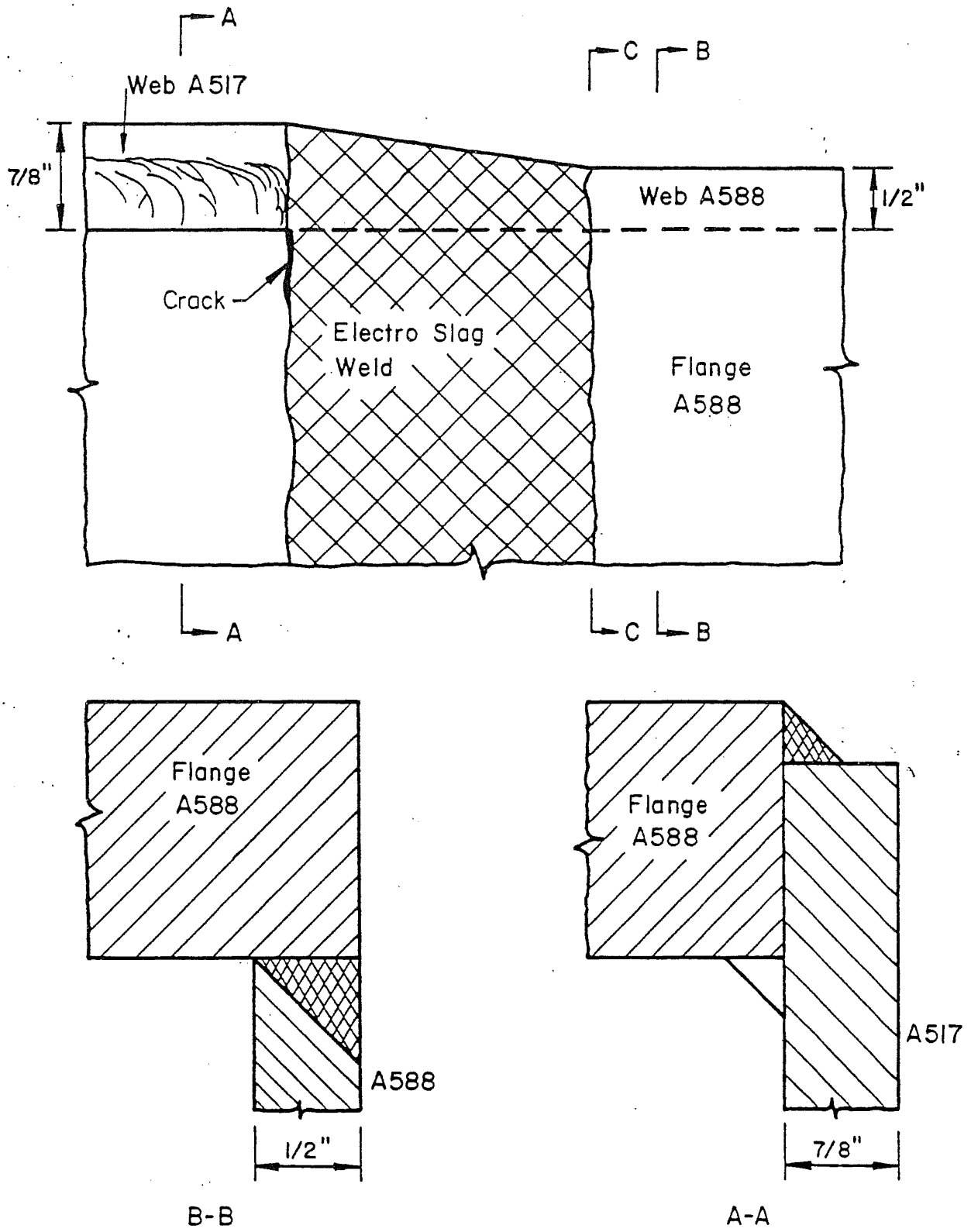

Fig. 16 Schematic of Top Flange Surface at 201T2 showing crack location.

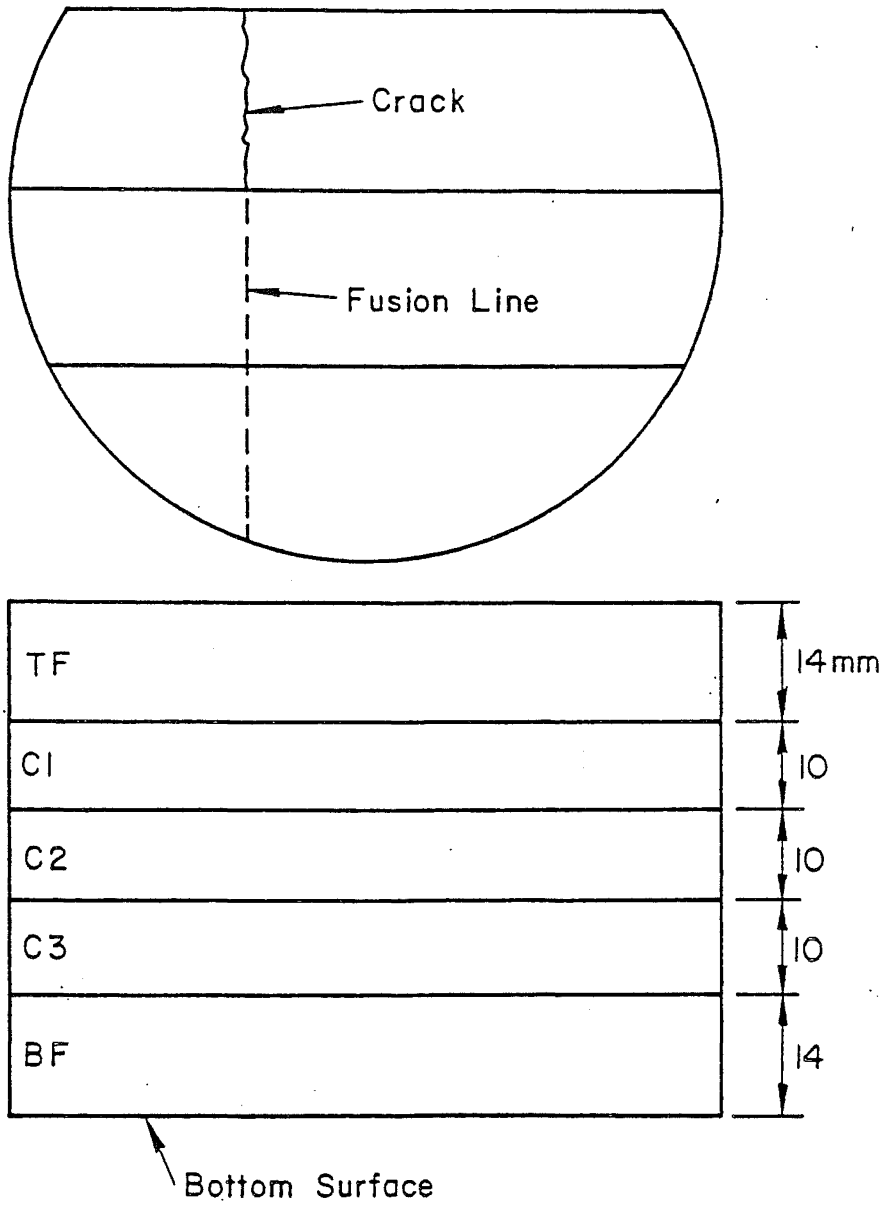

Fig. 17 Schematic of Core Showing Layout for Test Specimens

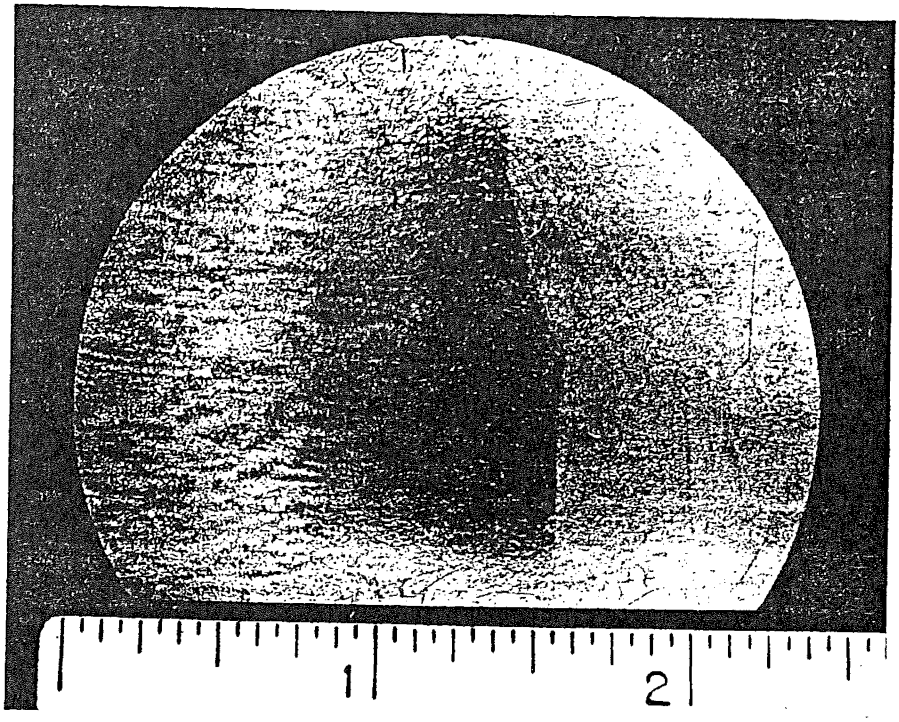

(a) Top Surface of Slice C1

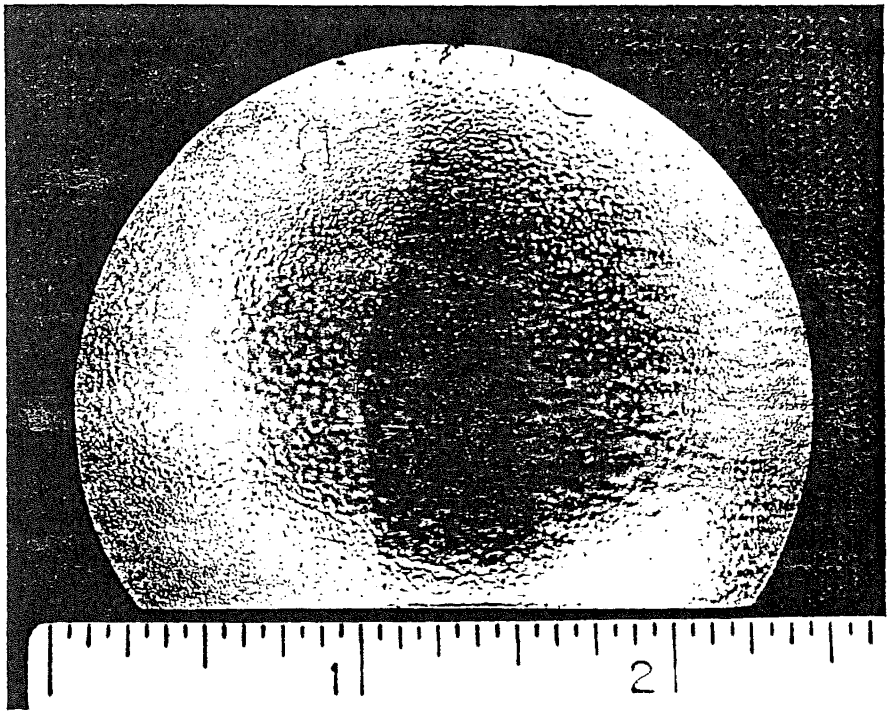

(b) Bottom Surface of Slice C1

Fig. 18 Polished and Etched Surfaces of Splice C1 Prior to Cutting Into Charpy V-Notch Specimens

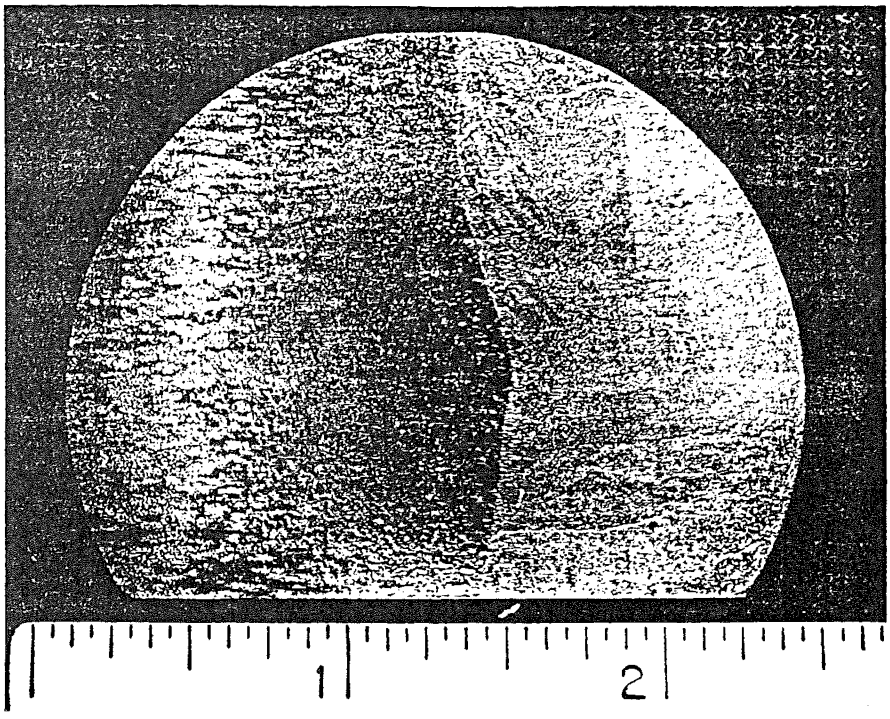

(a) Top Surface of Slice C2

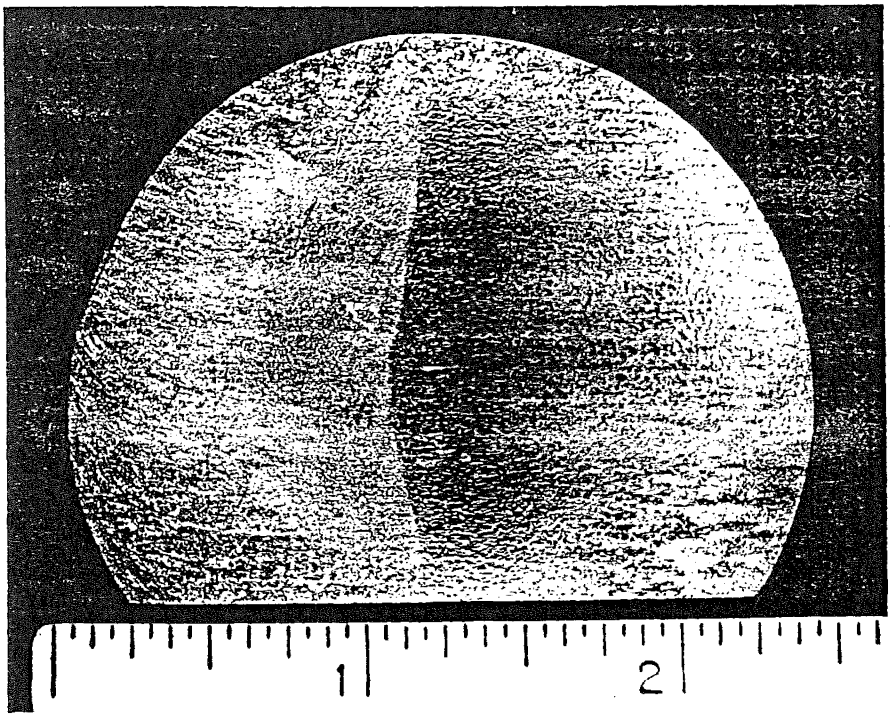

(b) Bottom Surface of Slice C2

Fig. 19 Polished and Etched Surfaces of Slice C2 Prior to Cutting Into Charpy V-Notch Specimens

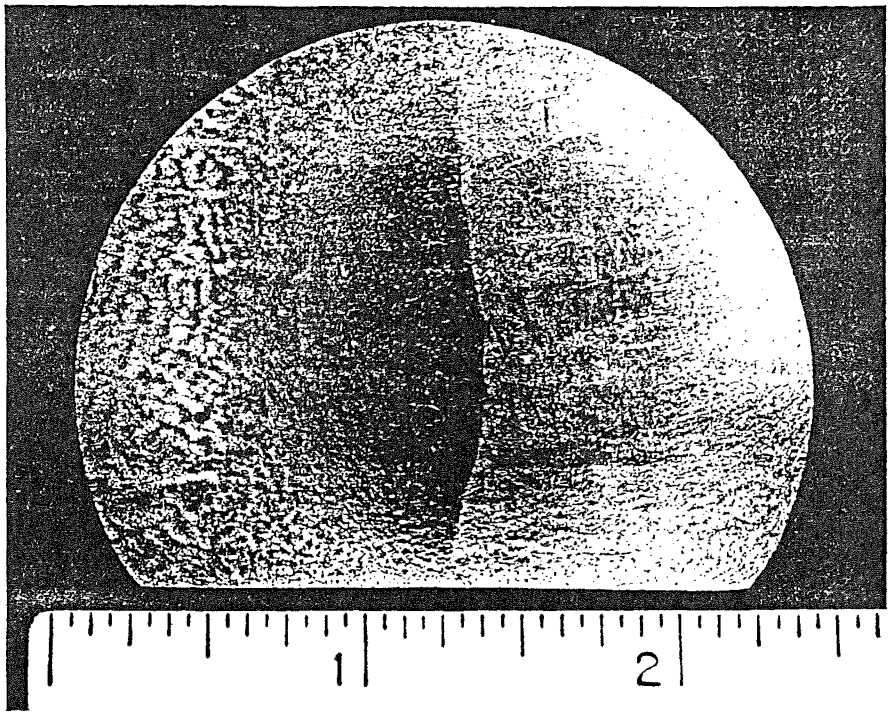

(a) Top Surface of Slice C3

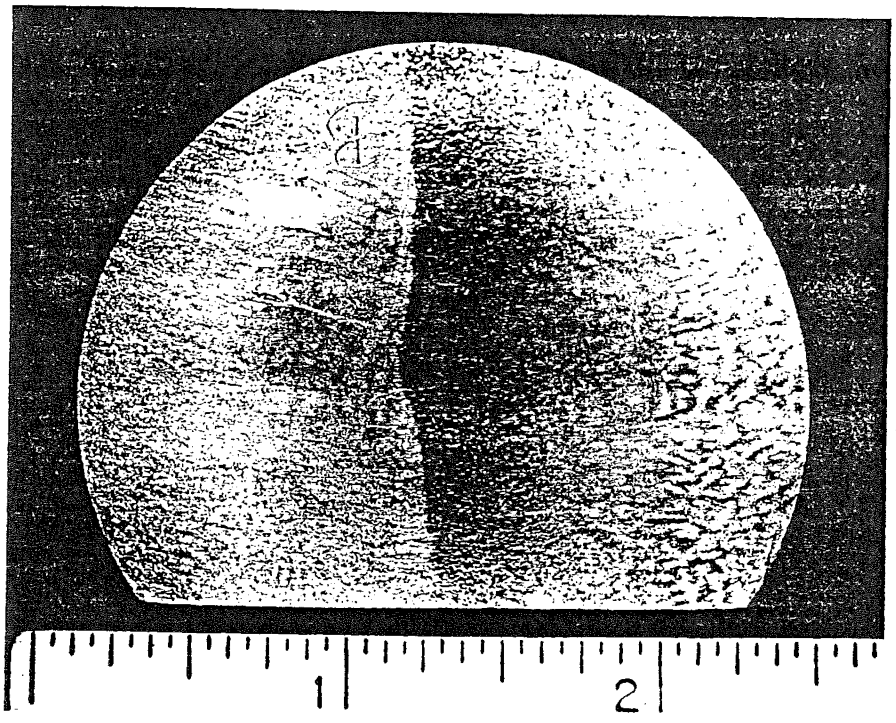

(b) Bottom Surface of Slice C3

Fig. 20 Polished and Etched Surfaces of Slice C3 Prior to Cutting into Charpy V-Notch Specimens

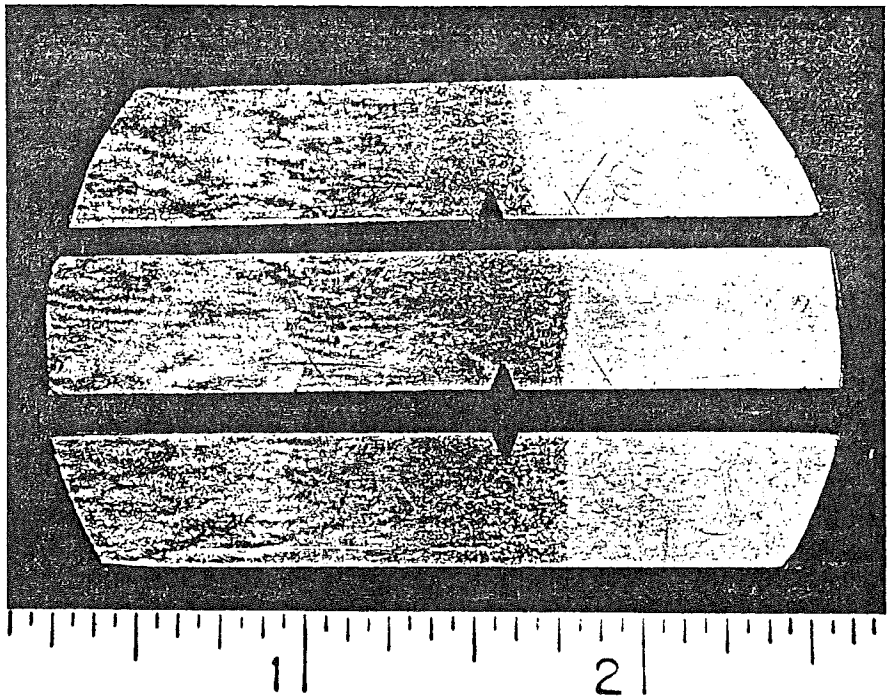

(a) Top Surface of Slice C1

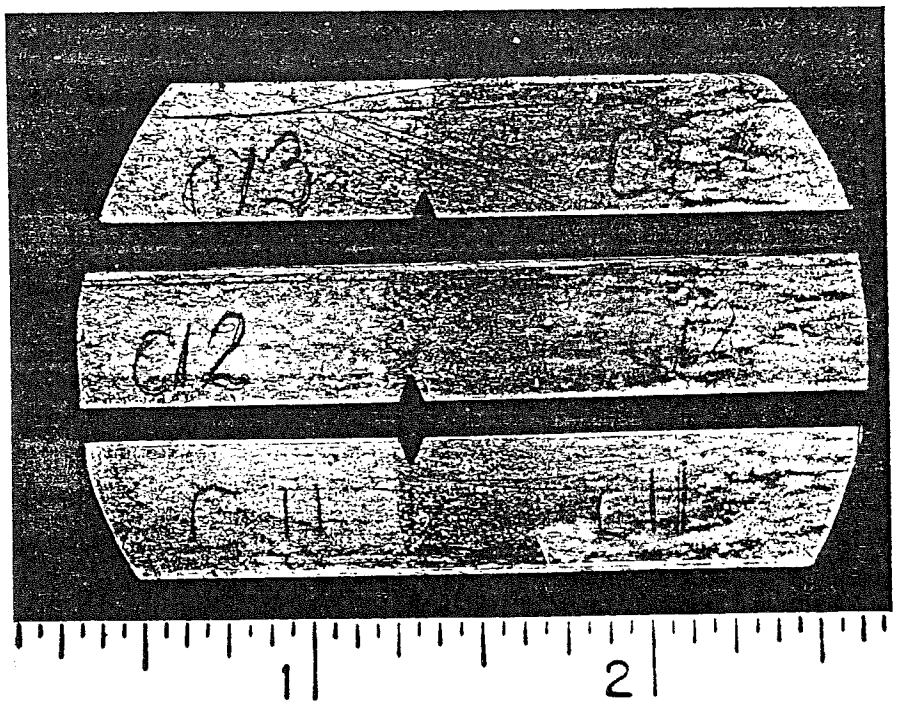

(b) Bottom Surface of Slice C1

Fig. 21 Charpy V-Notch Specimens from Slice C1 With Layout of Notches

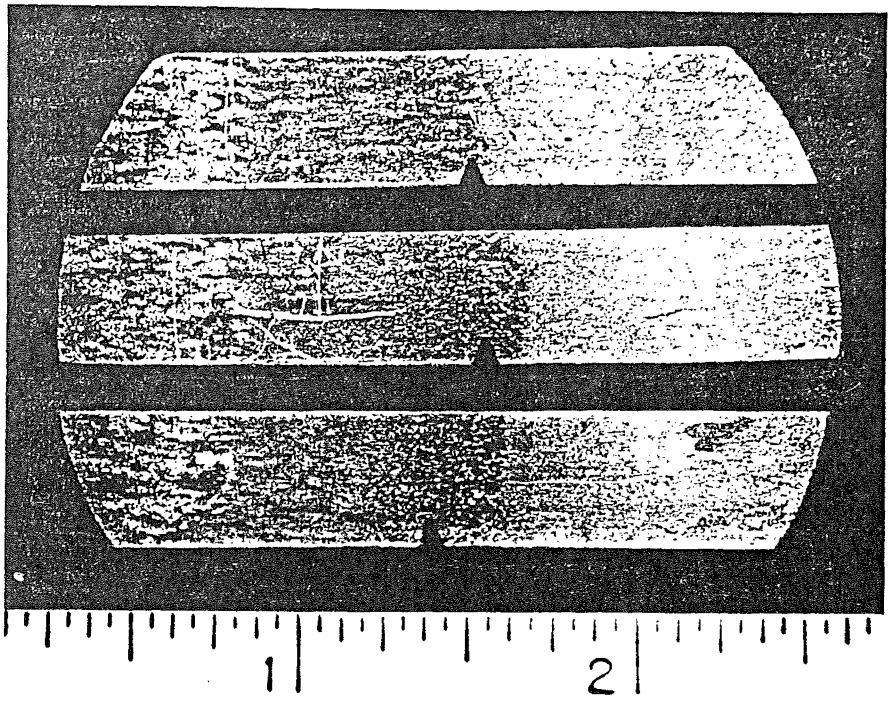

(a) Top Surface of Slice C2

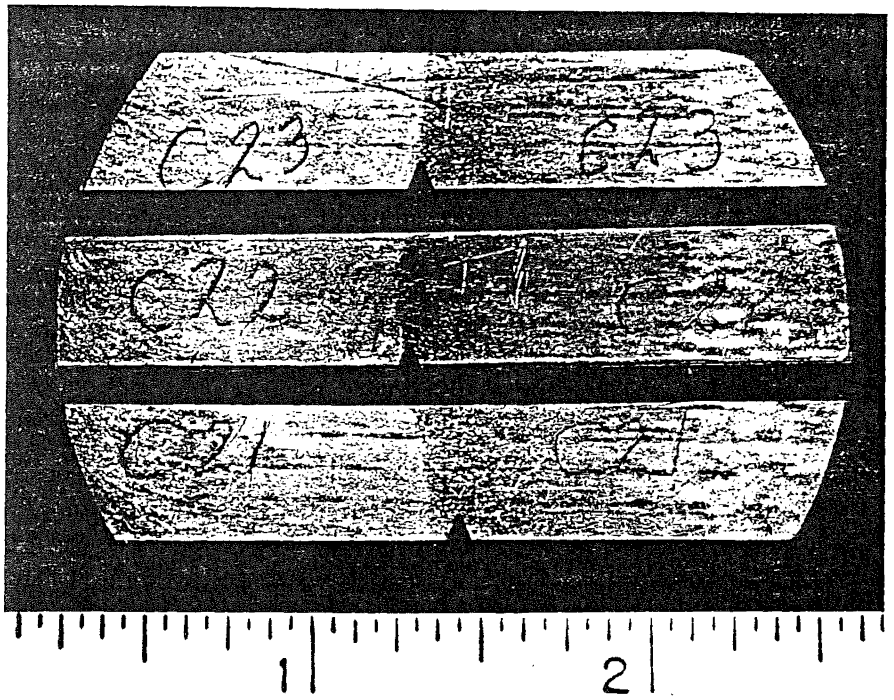

(b) Bottom Surface of Slice C2

Fig. 22 Charpy V-Notch Specimens from Slice C2 Showing Layout of Notches

(a) Top Surface of Slice C3

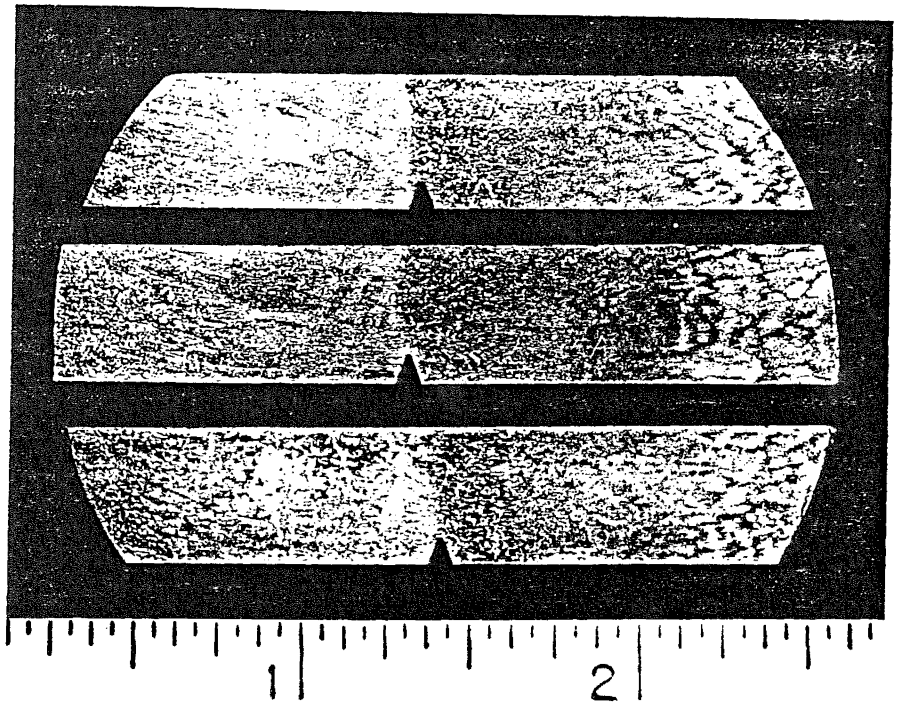

(b) Bottom Surface of Slice C3

Fig. 23 Charpy V-Notch Specimens from Slice C3 Showing Layout of Notches

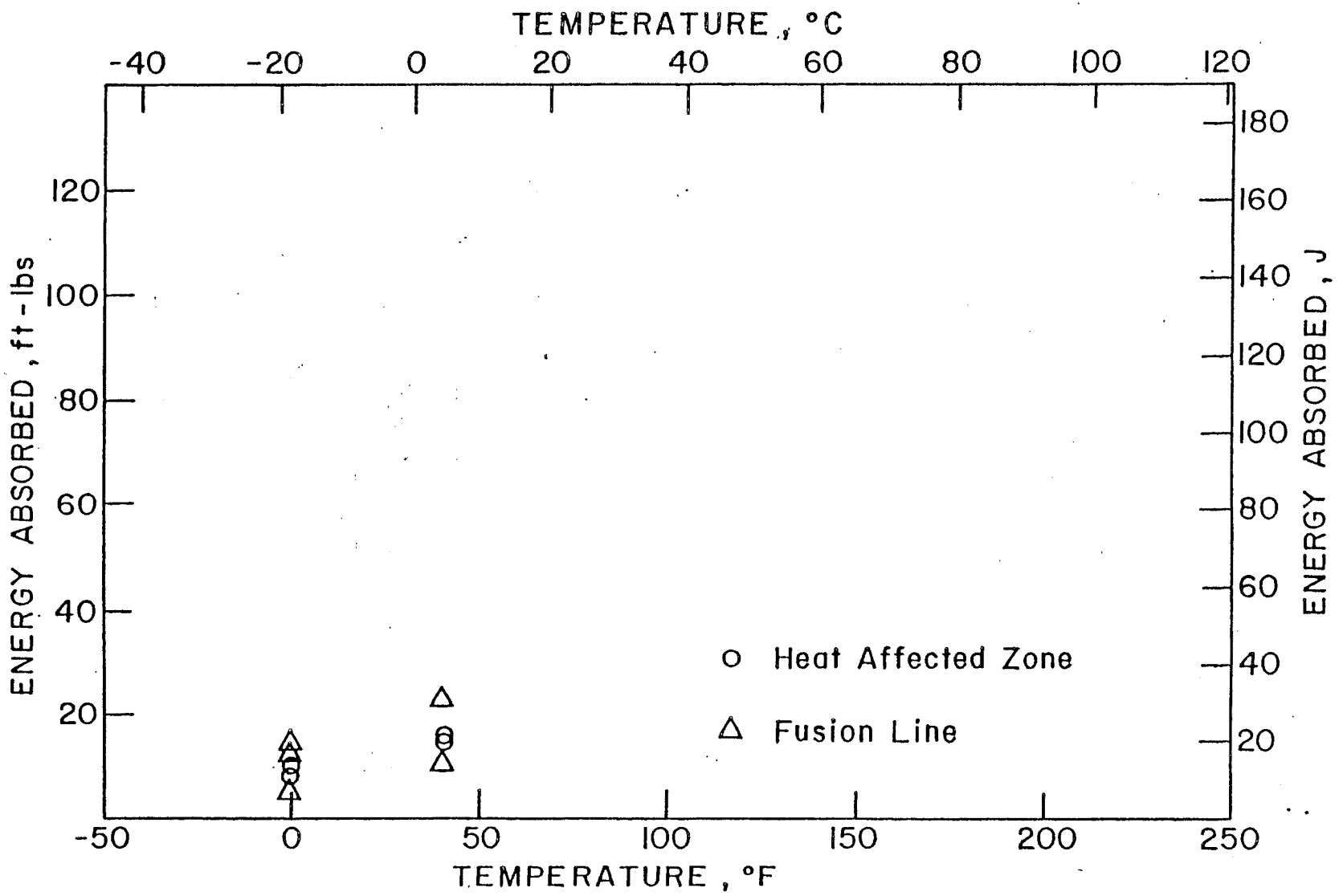

Fig. 24 Summary of Charpy V-Notch Tests from the Tie Girder Core

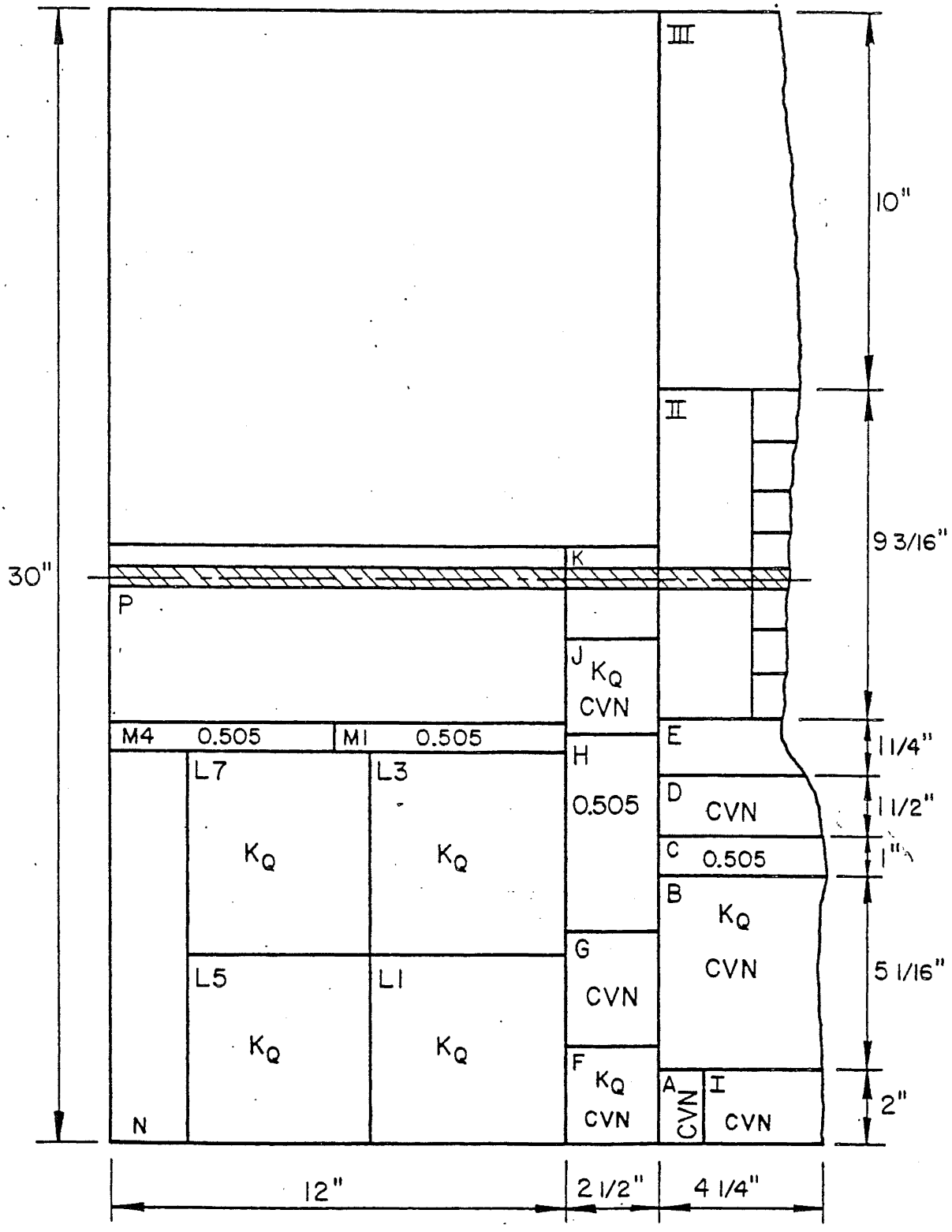

Fig. 25 Layout of Test Specimens on the South Half of the Fractured Girder Flange

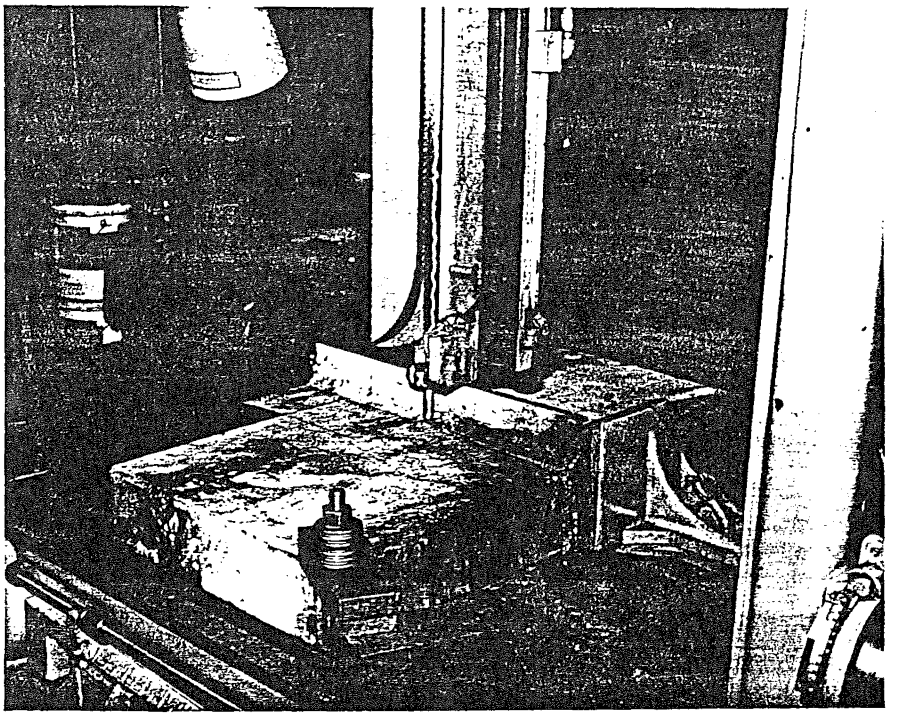

Fig. 26 South Section of Casualty Girder with Web Cut-Off and Segments Being Cut from the Flange

Fig. 27 Section from East Edge Sliced into Seven Segments

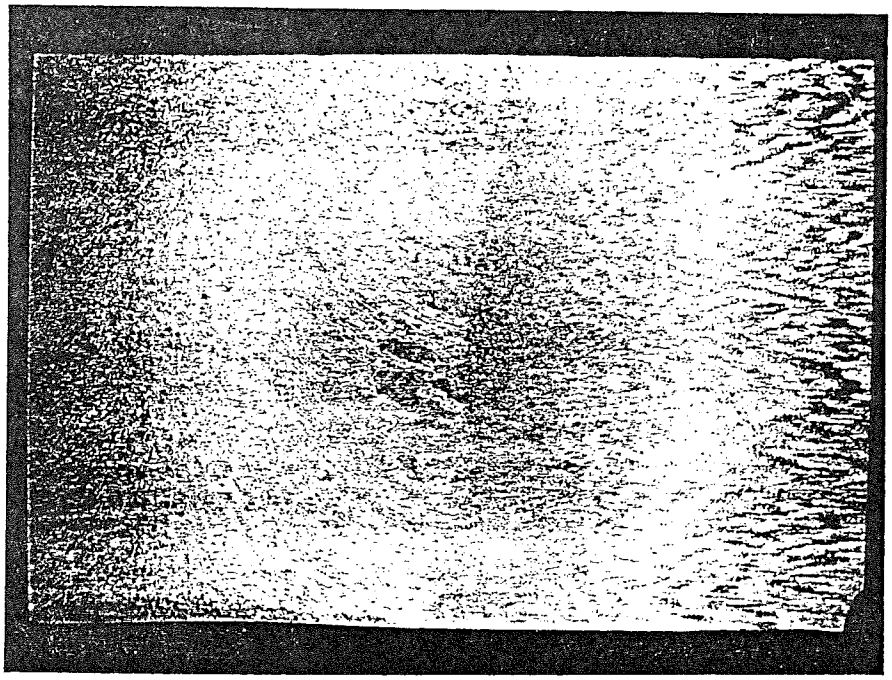

Fig. 28a Polished and Etched Surface of Slice 1

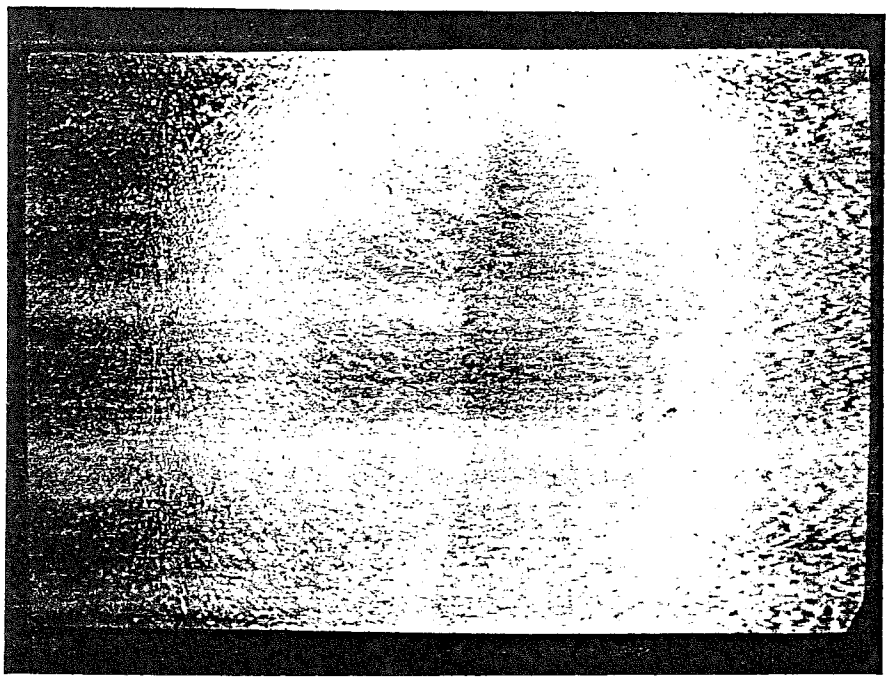

Fig. 28b Polished and Etched Surface of Slice 4

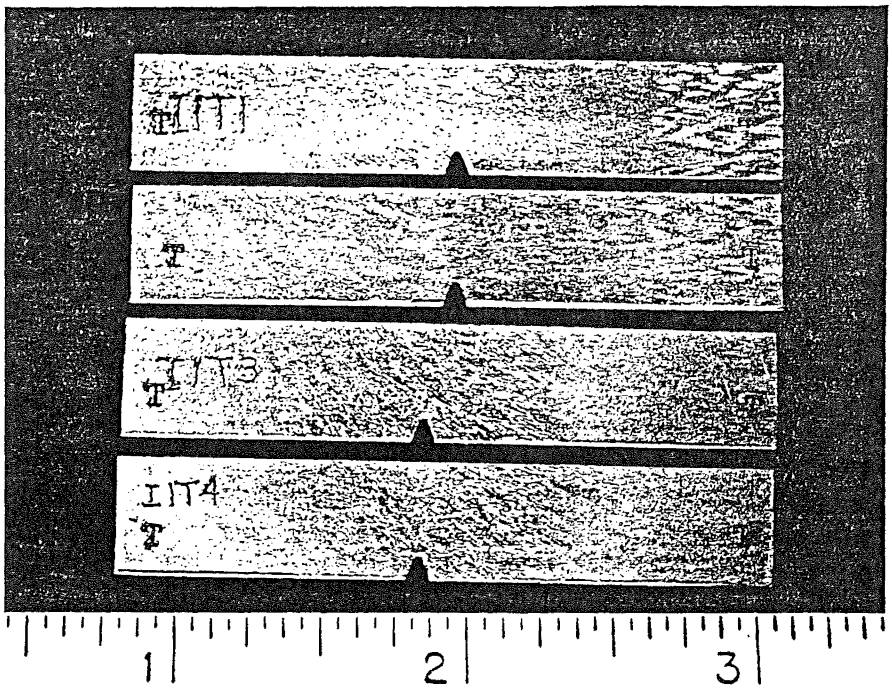

(a) Charpy V-Notch Specimens from Slice 1

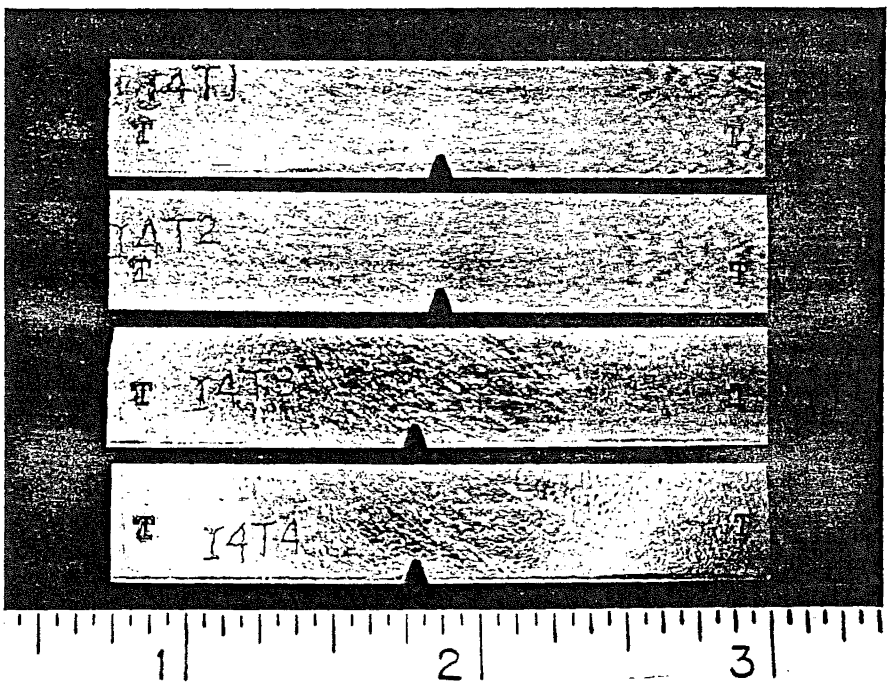

(b) Charpy V-Notch Specimens from Slice 4

Fig. 29 Layout of Charpy V-Notch Specimens from East Edge of Casualty Section

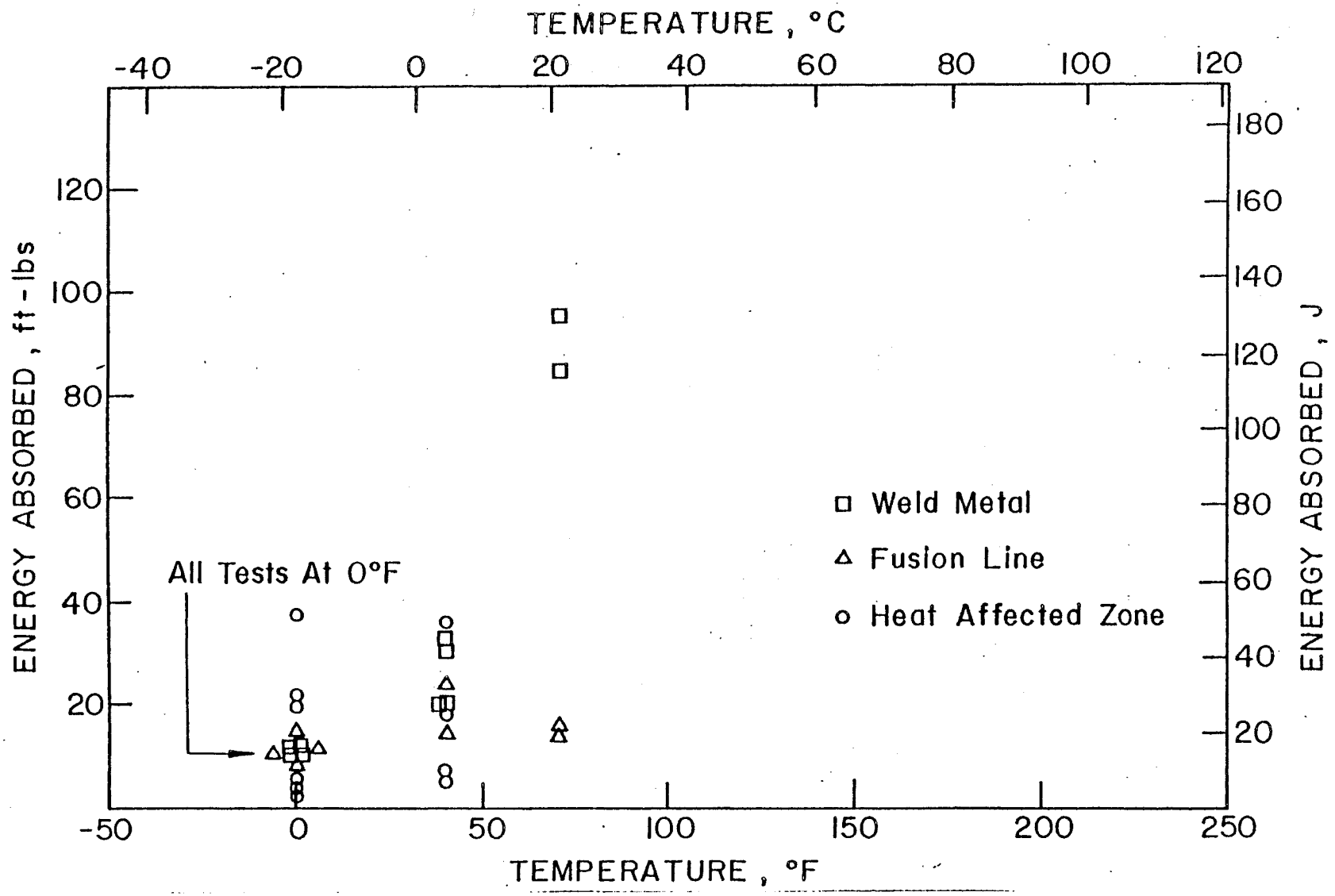

Fig. 30 Results of Charpy V-Notch Tests from Casualty Girder Weldment

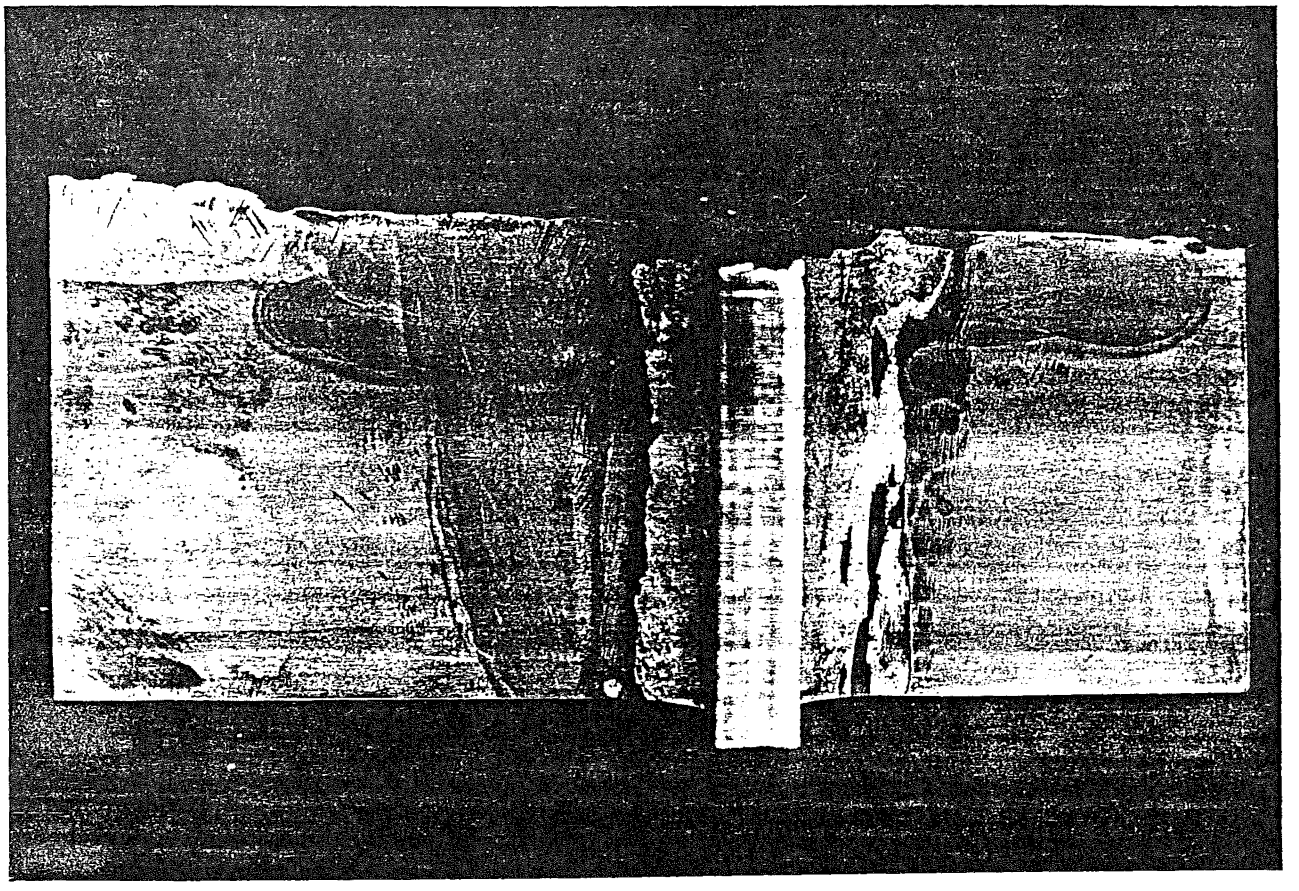

Fig. 31a Etched Top Flange Surface Showing
Weld Repair Passes and Edge of Crack

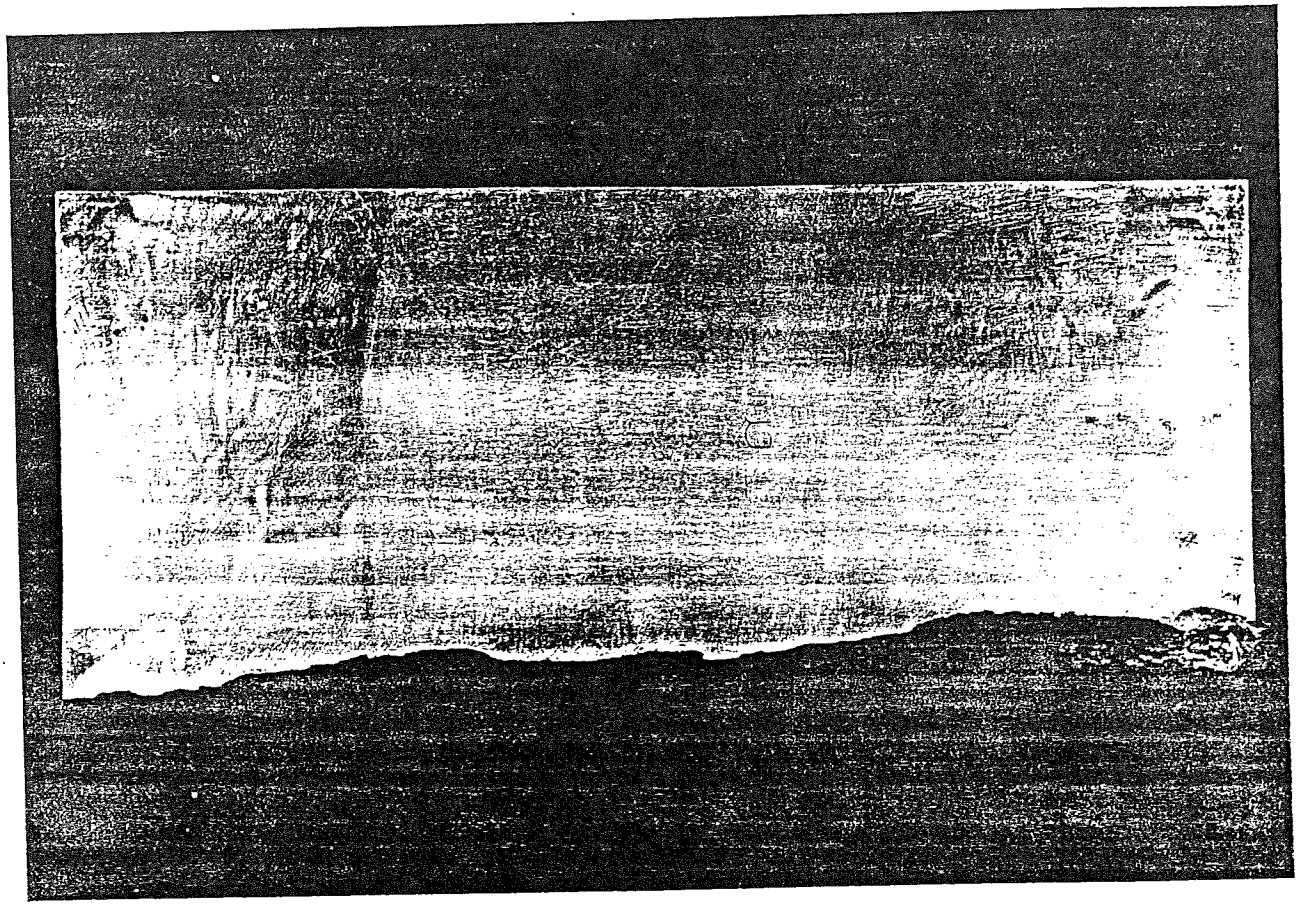

Fig. 31b Etched Bottom Surface of Flange Showing Multiple Pass Repairs

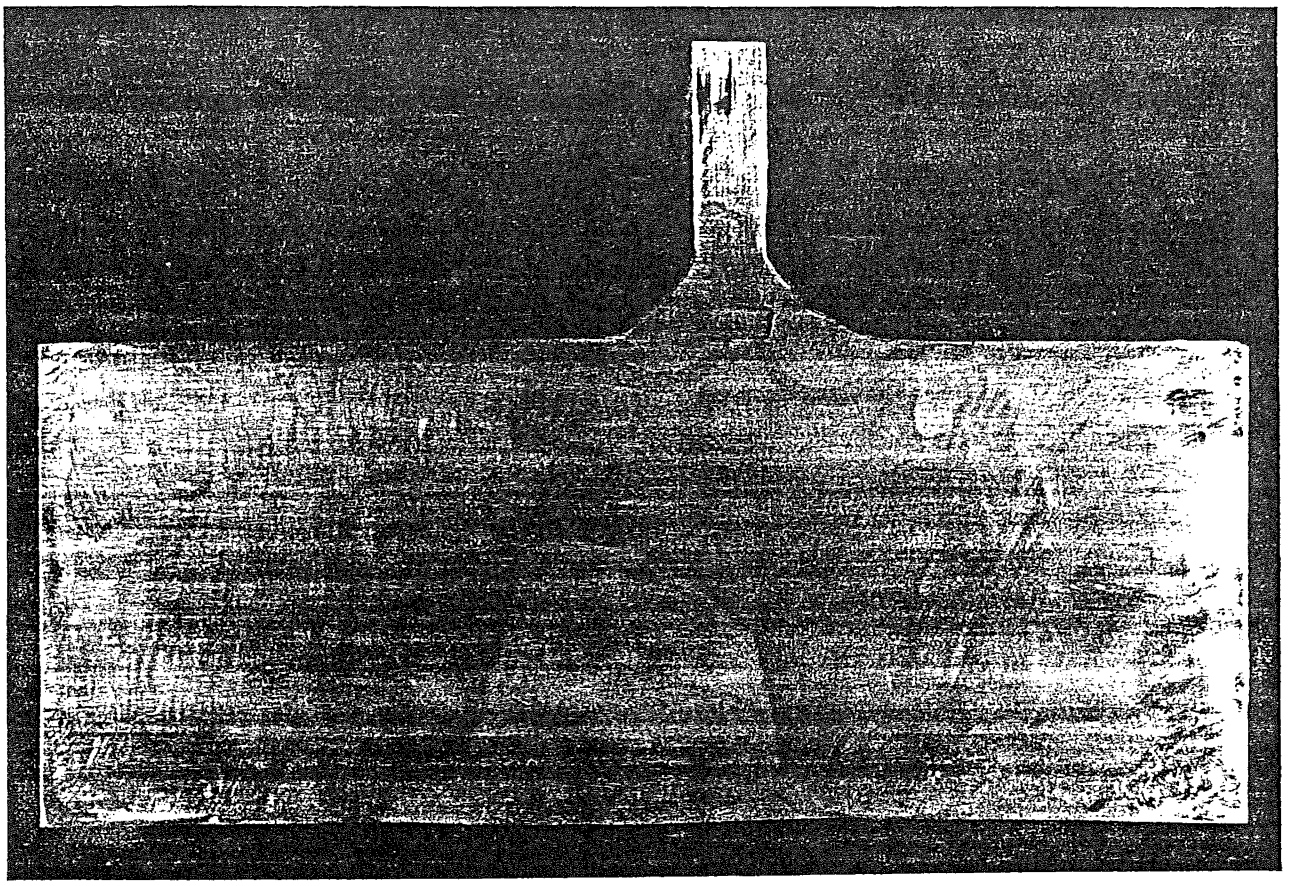

Fig. 31c Etched Surface of Flange about 3 1/2 Inches Behind Crack

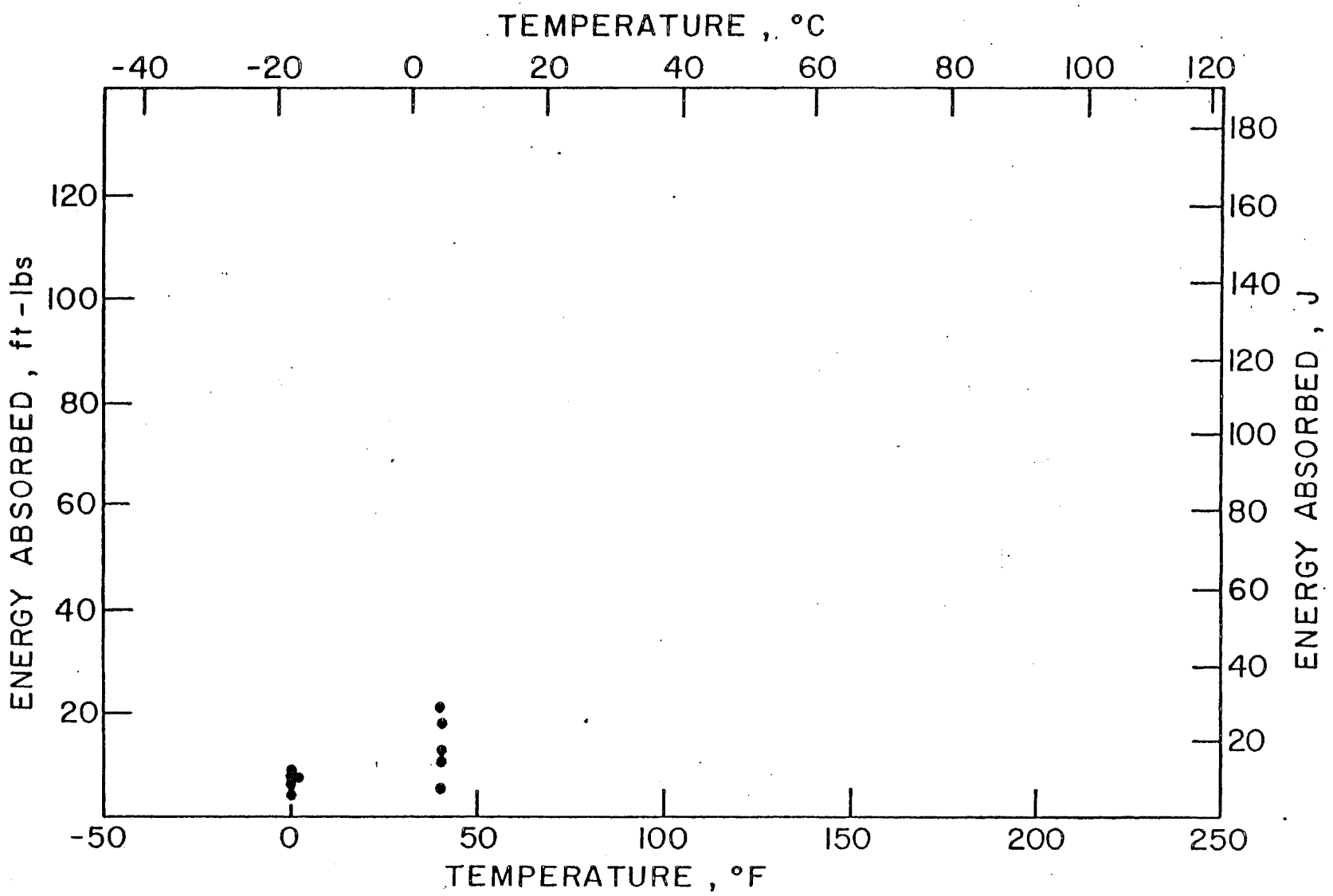

Fig. 32 Results of Charpy V-Notch Tests of Weld Repair Metal

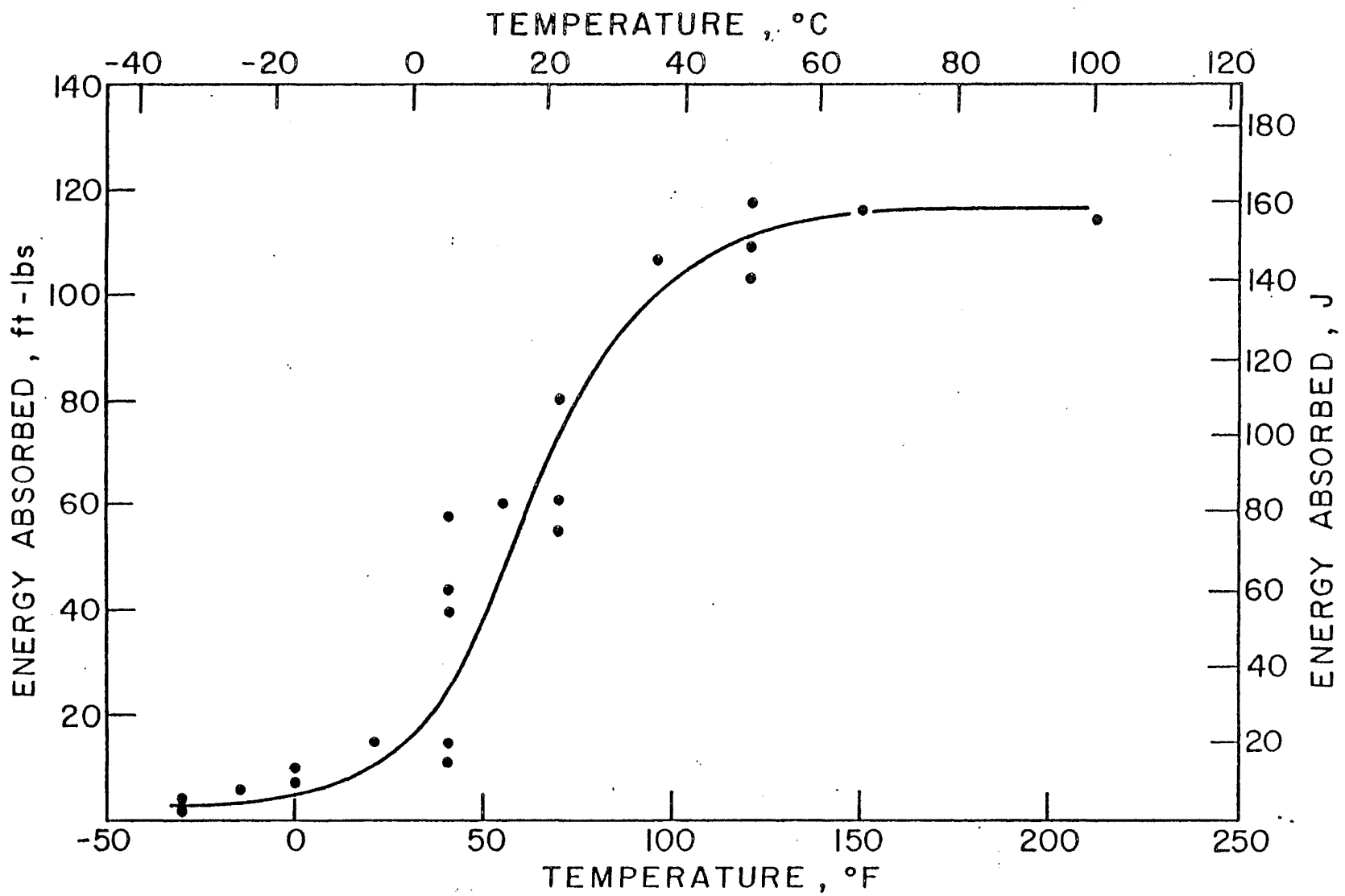

Fig. 33 Charpy V-Notch Test Results of Flange Base Metal

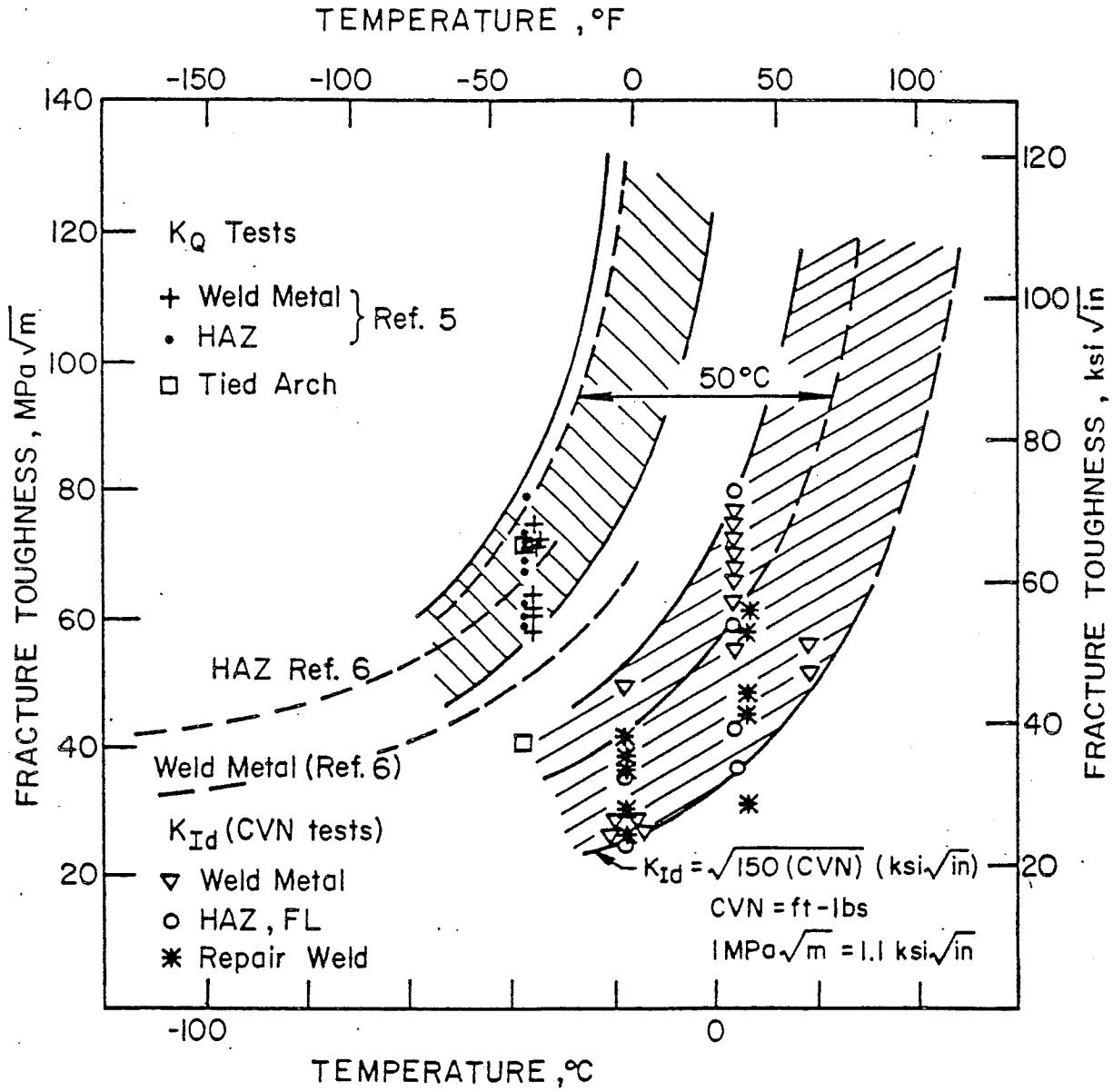

Fig. 34 Comparison of Estimated Fracture Toughness from Charpy V-Notch Tests on Casualty Girder and Tie Girder with K_Q tests reported by Benter and Tied Girder Beam Tests

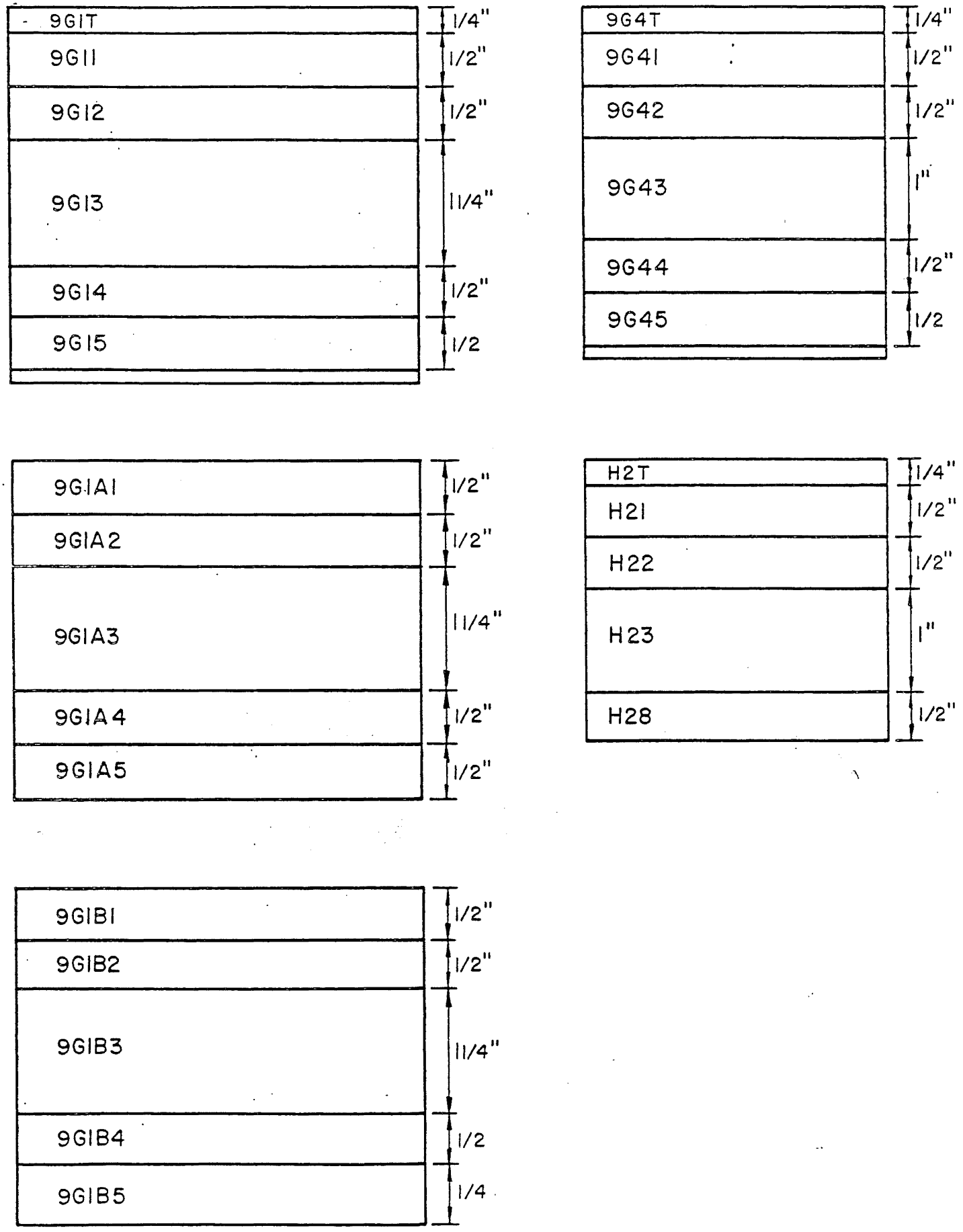

Fig. 35 Layout of Specimen Slices in Cores Removed from Back Channel Structures

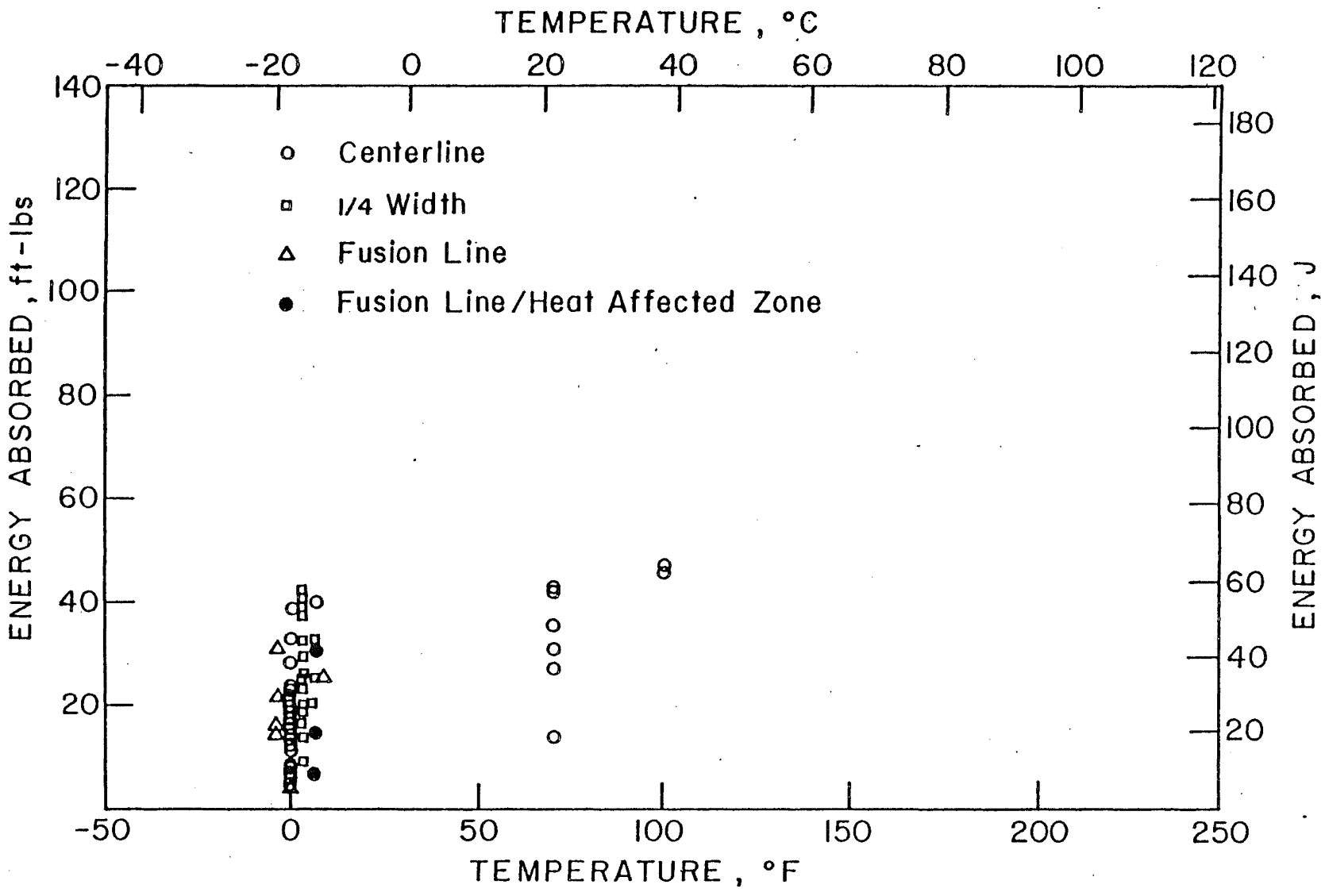

Fig. 36 Results of Charpy V-Notch Tests on Back Channel Cores

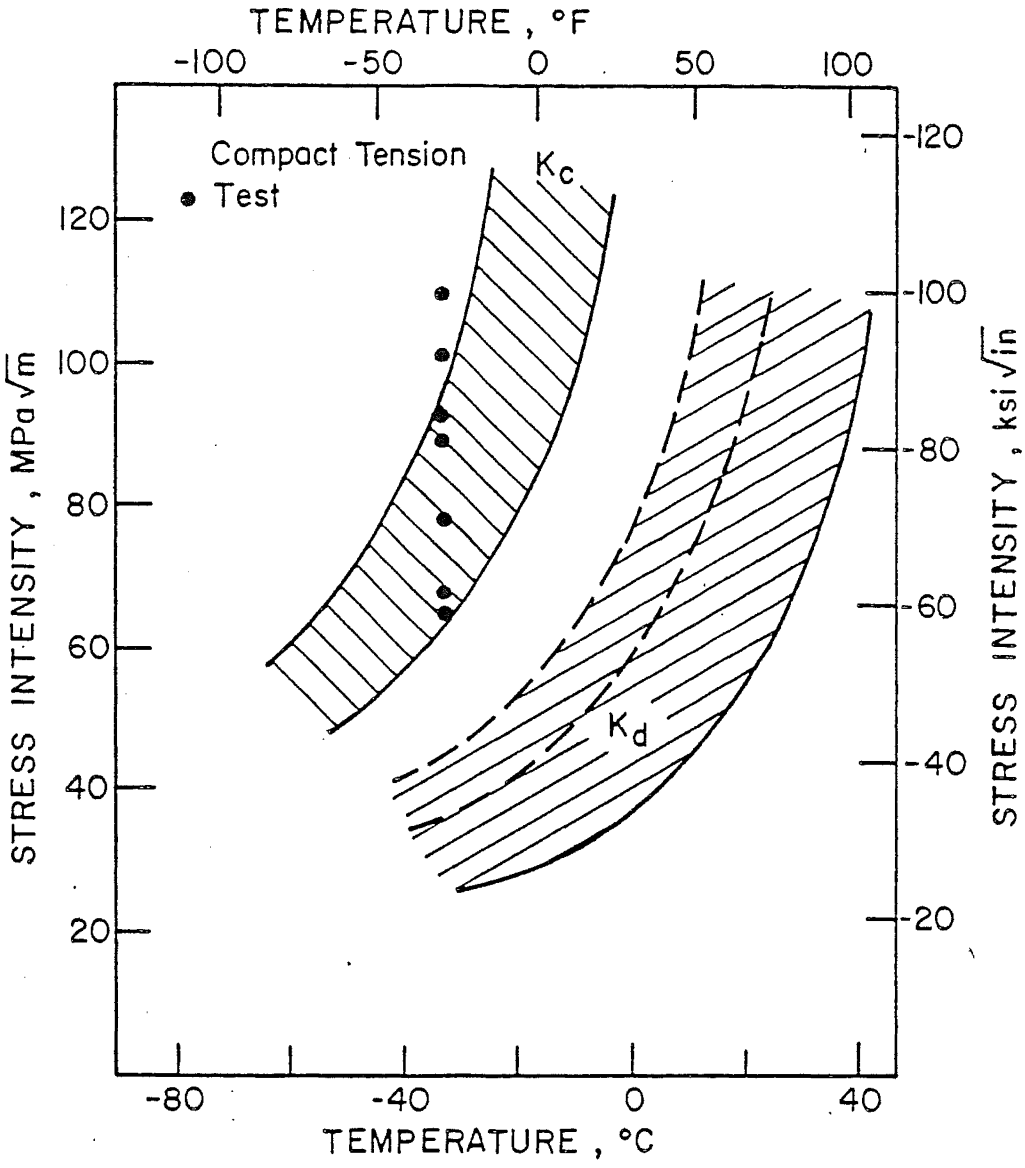

Fig. 37 Comparison of Compact Tension Tests on Back Channel Cores with Charpy V-Notch Estimates

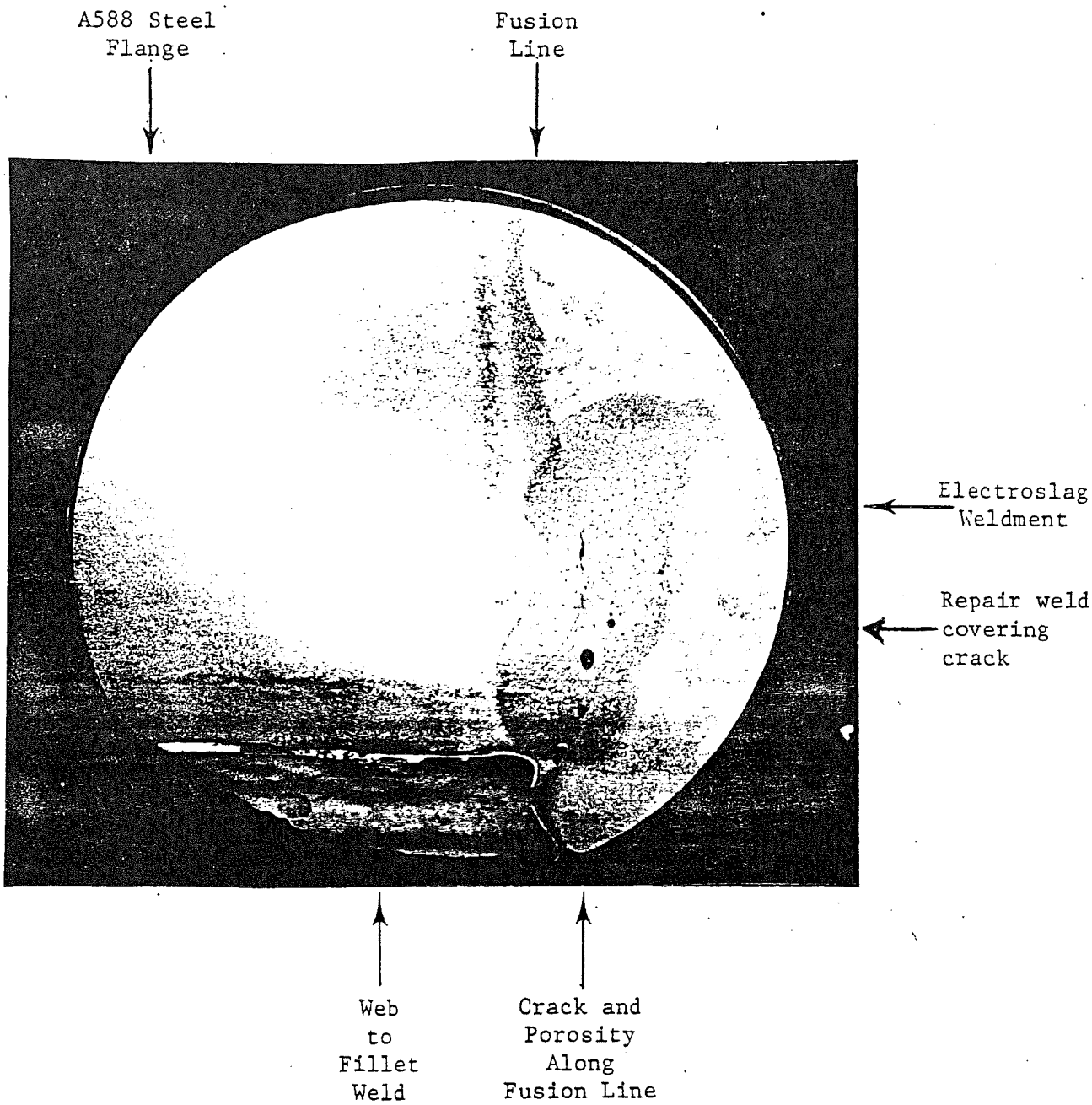

Fig. 38 Polished and Etched Surface of Top of Tie Girder Core
Showing Porosity and Crack Along Fusion Line

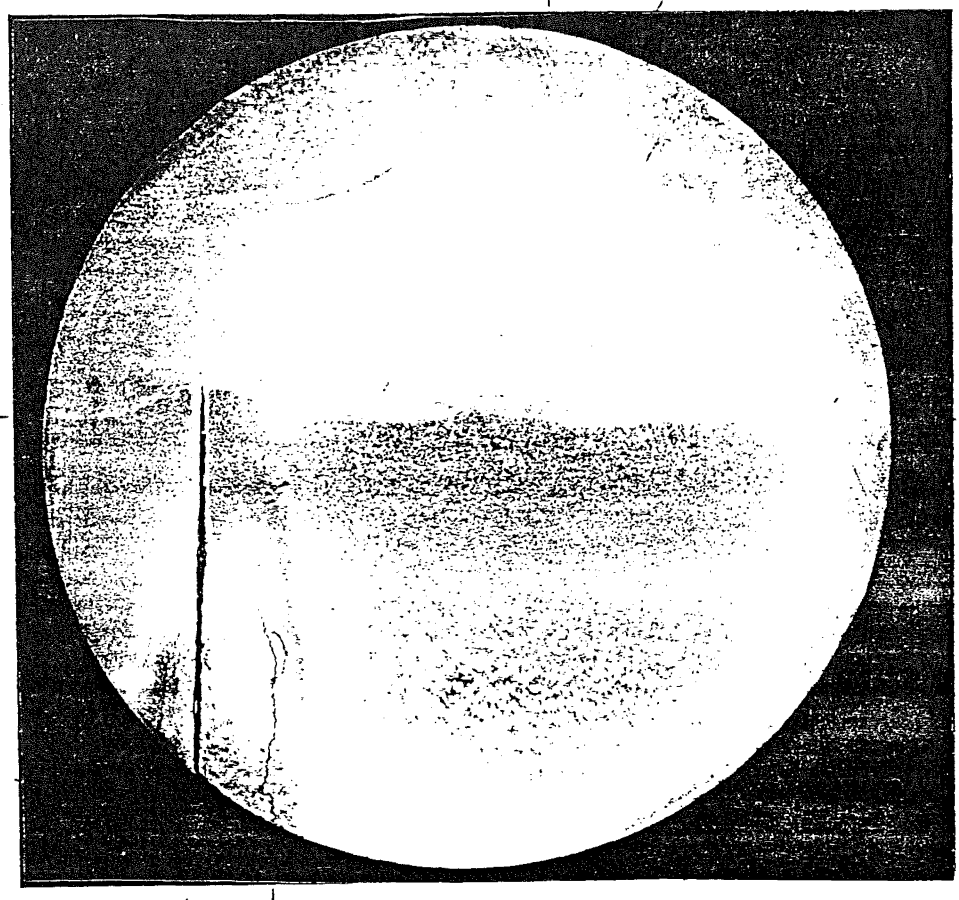

Fig. 39 Polished and Etched Surface of the Bottom Surface of Tie Girder Core Showing Crack in A588 Steel Flange Plate

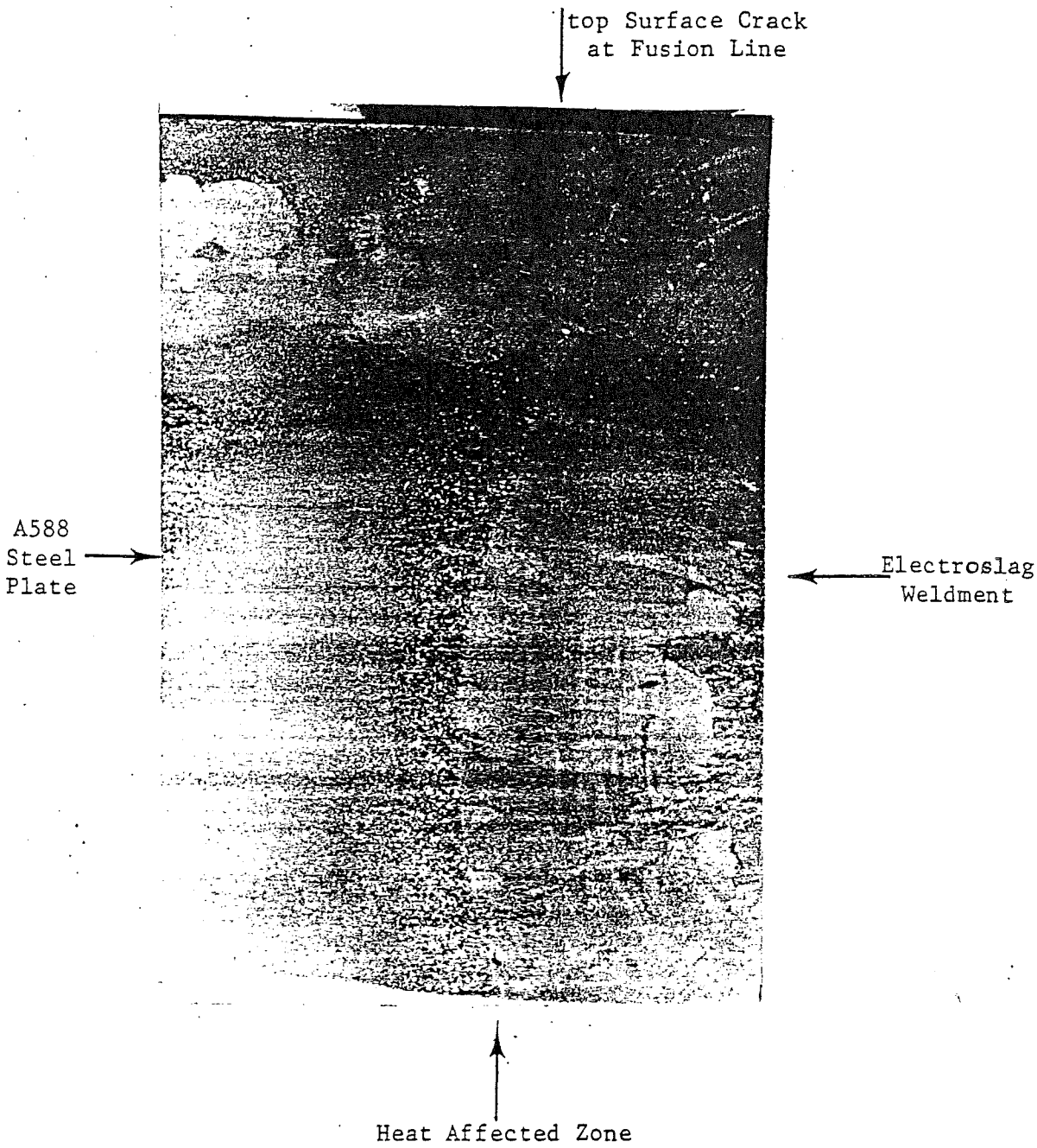

Fig. 40a Polished and Etched Edge of Flange Plate
and Electroslag Weldment from the Girder

Fig. 40b Higher magnification view of natural crack in weldment after preparation of small beam specimen.

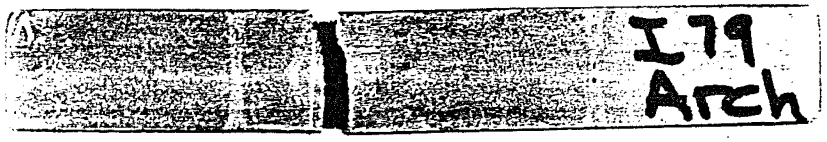

Fig. 41 Small Beam Specimen Fabricated From Tie Girder Slice With Natural Crack

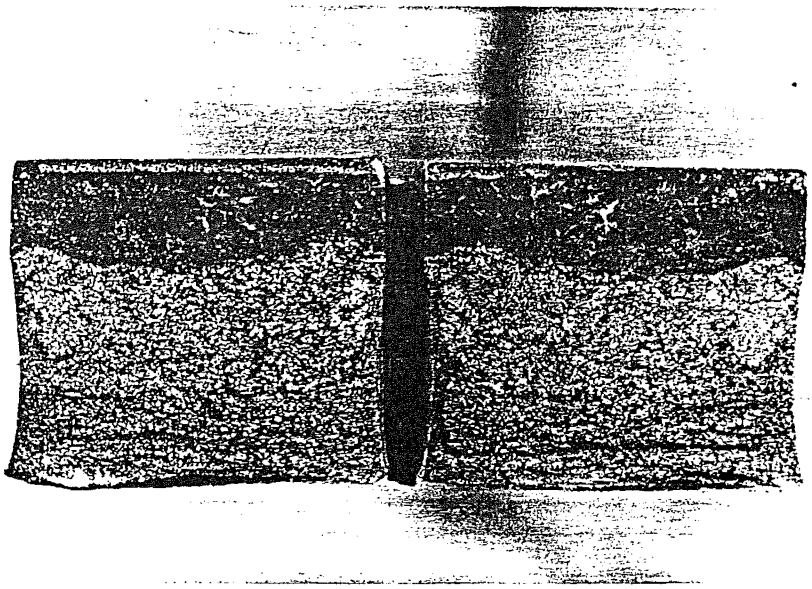

Fig. 42 Surface of Fractured Beam Specimen Showing Natural Crack in Tie Girder

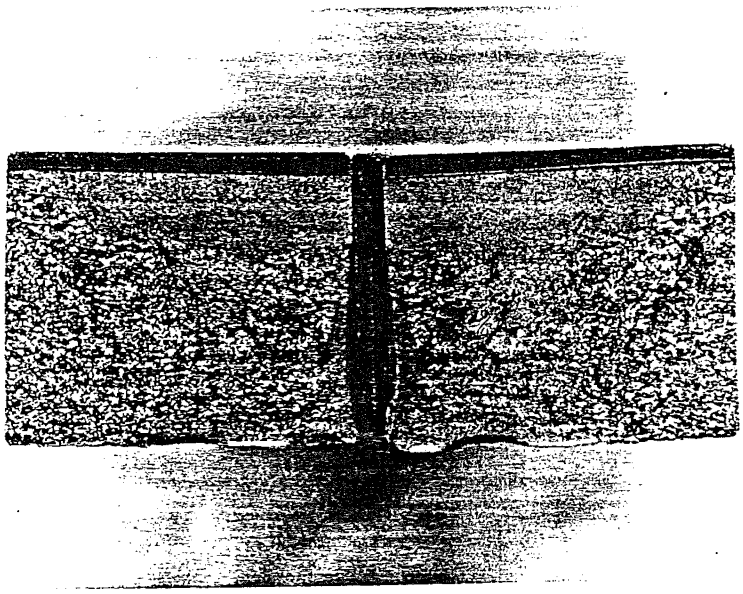

Fig. 43 Surface of Precracked Beam Specimen From Tie Girder Weld

Crack Surface

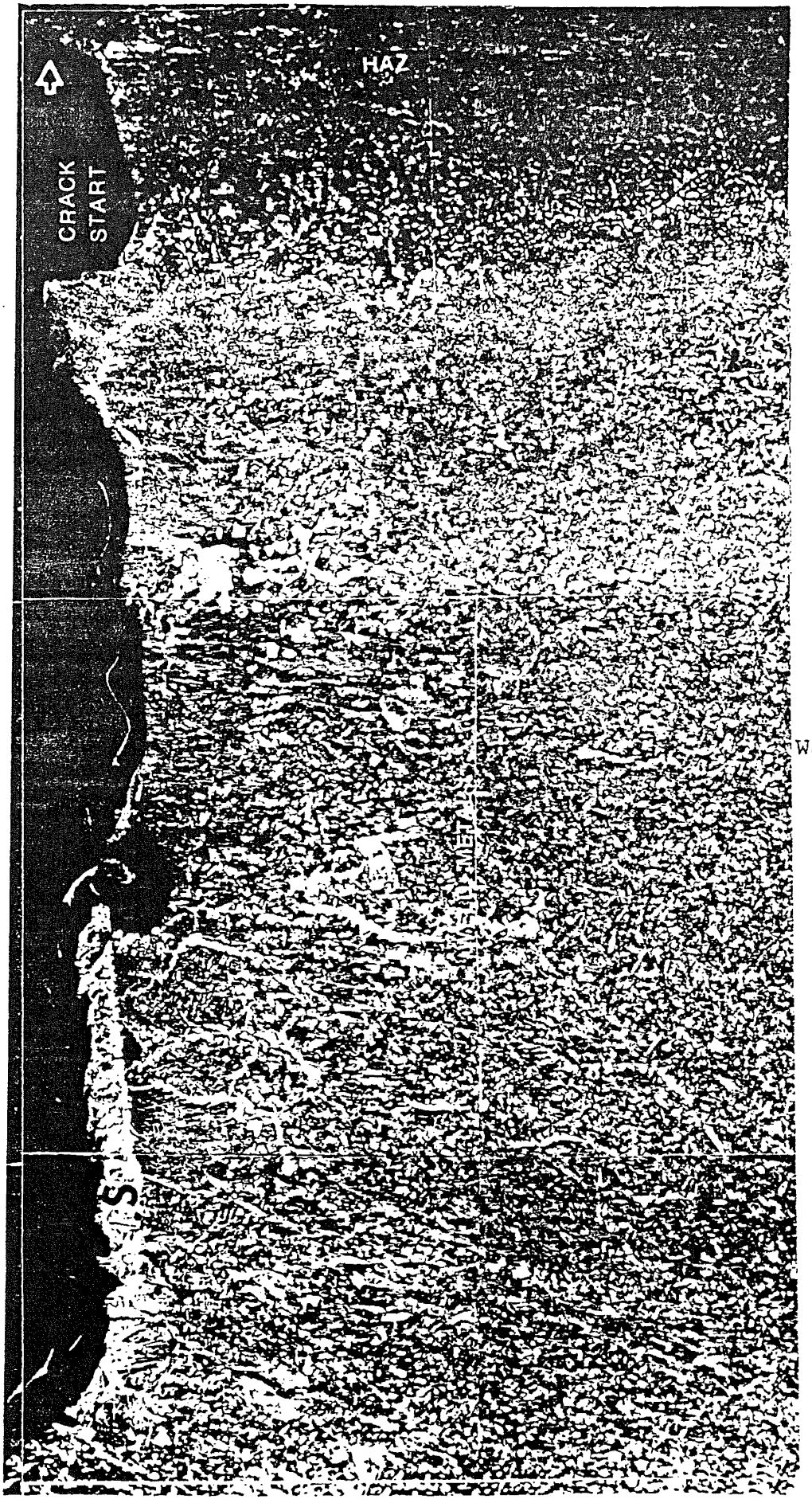

Weld Metal

Figure 44a Microstructure Near Crack Surface
100X Nital Etch

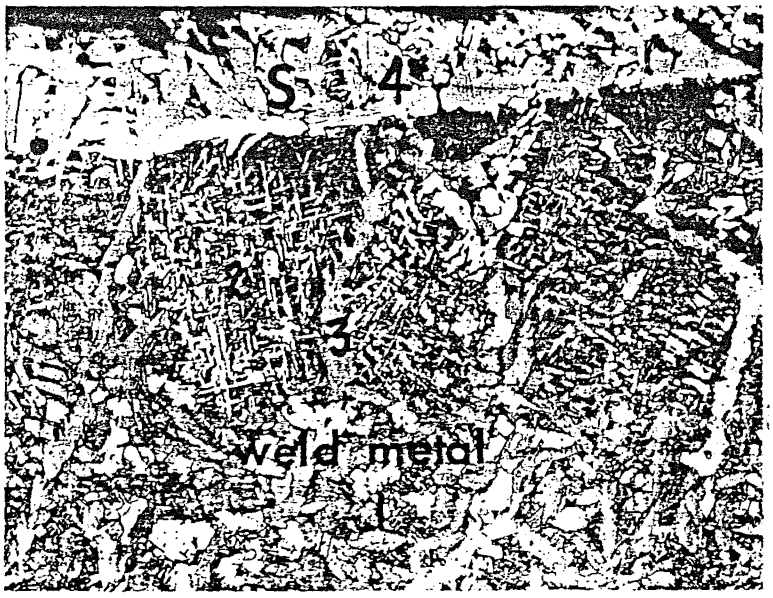

Fig. 44b

Electron Microprobe Chemical Analysis of Designated Areas

1. Bulk Weld Metal

% Cu	% Cr	% Mn
0.07	0.37	1.41
0.09	0.39	1.38
0.10	0.39	1.32
0.08	0.38	1.45

2. Acicular Grain Centers

% Cu	% Cr	% Mn
0.13	0.37	1.54
0.13	0.38	1.49
0.16	0.39	1.35

3. Proeutectoid Ferrite Veins

% Cu	% Cr	% Mn
0.03	0.36	1.21
0.06	0.37	1.45
0.05	0.37	1.38
0.08	0.39	1.63

4. Unique Ferrite Rich Layer

% Cu	% Cr	% Mn
0.49	0.02	0.00
0.44	0.07	0.00
0.46	0.04	0.00
0.43	0.09	0.00

Fig. 44b Microprobe Analysis of weld adjacent to crack

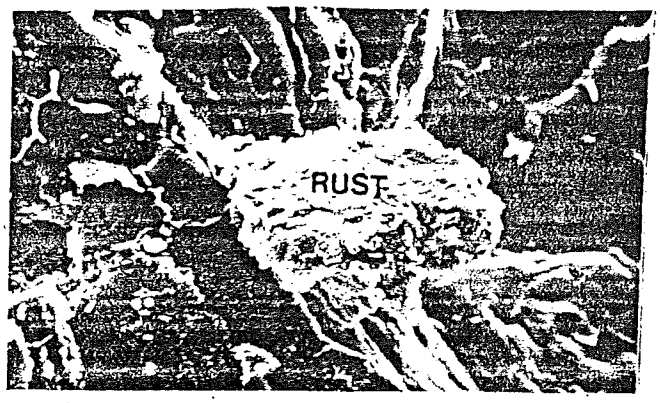

a. Iron Oxide, probably Corrosion Product, on Surface
Scanning Electron Microscope Micrograph 600X

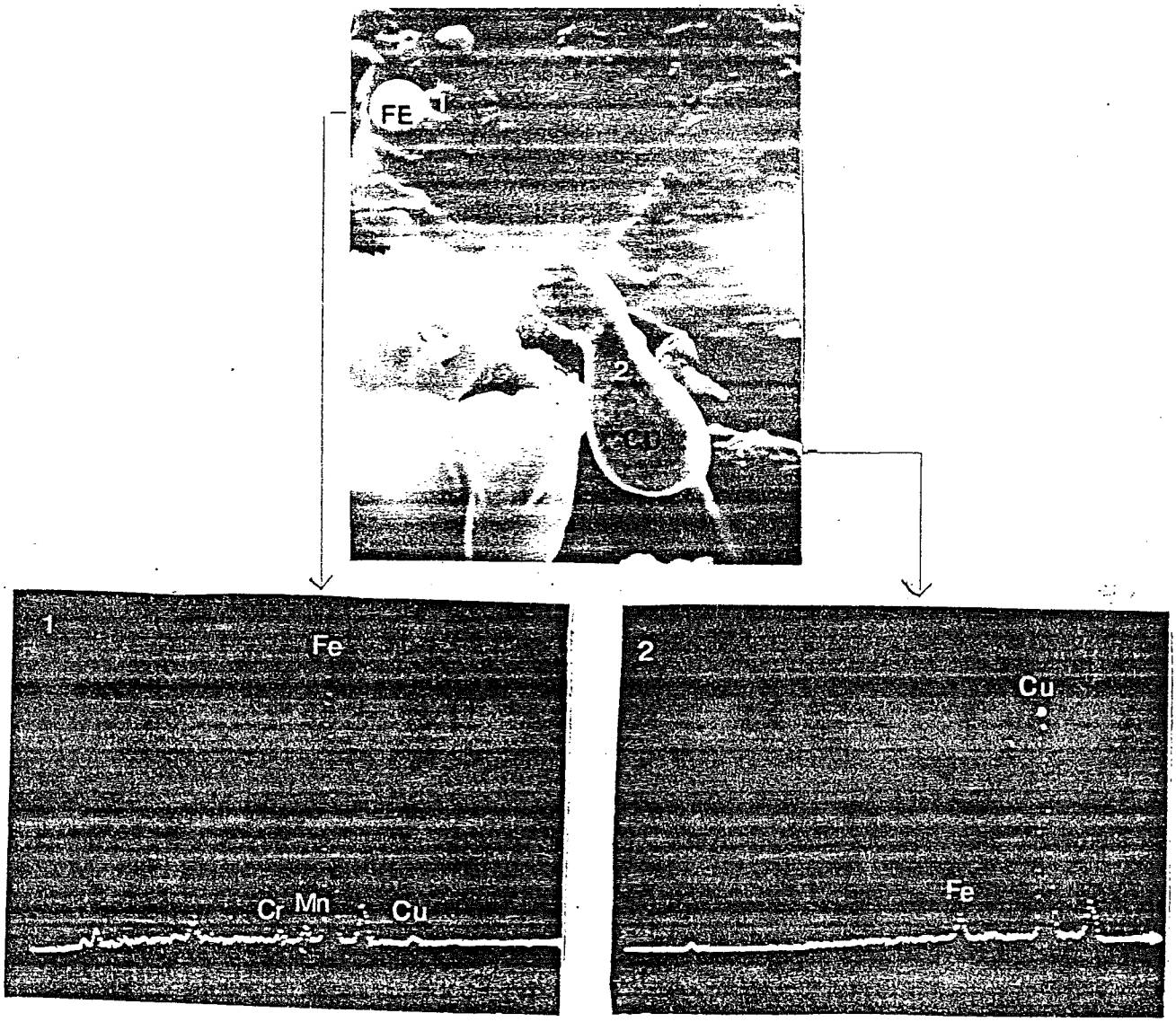

b. Scanning Electron Microscope Micrograph of Iron and Copper Particles (3000X) with Energy Dispersive Spectrometer Trace Showing Composition

Fig. 45 SEM Micrographs of Surface Extension Replica

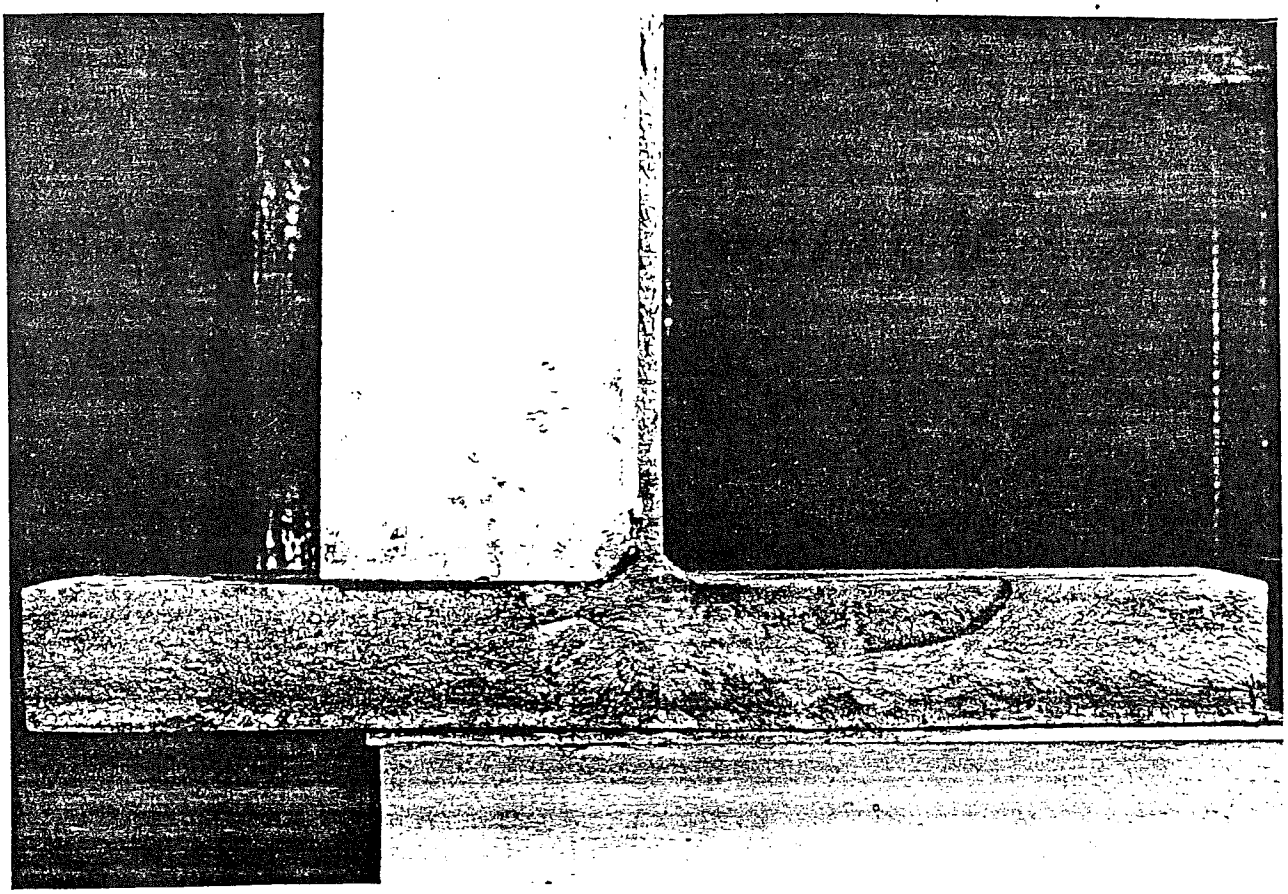

(a) Fracture Surface - North Section

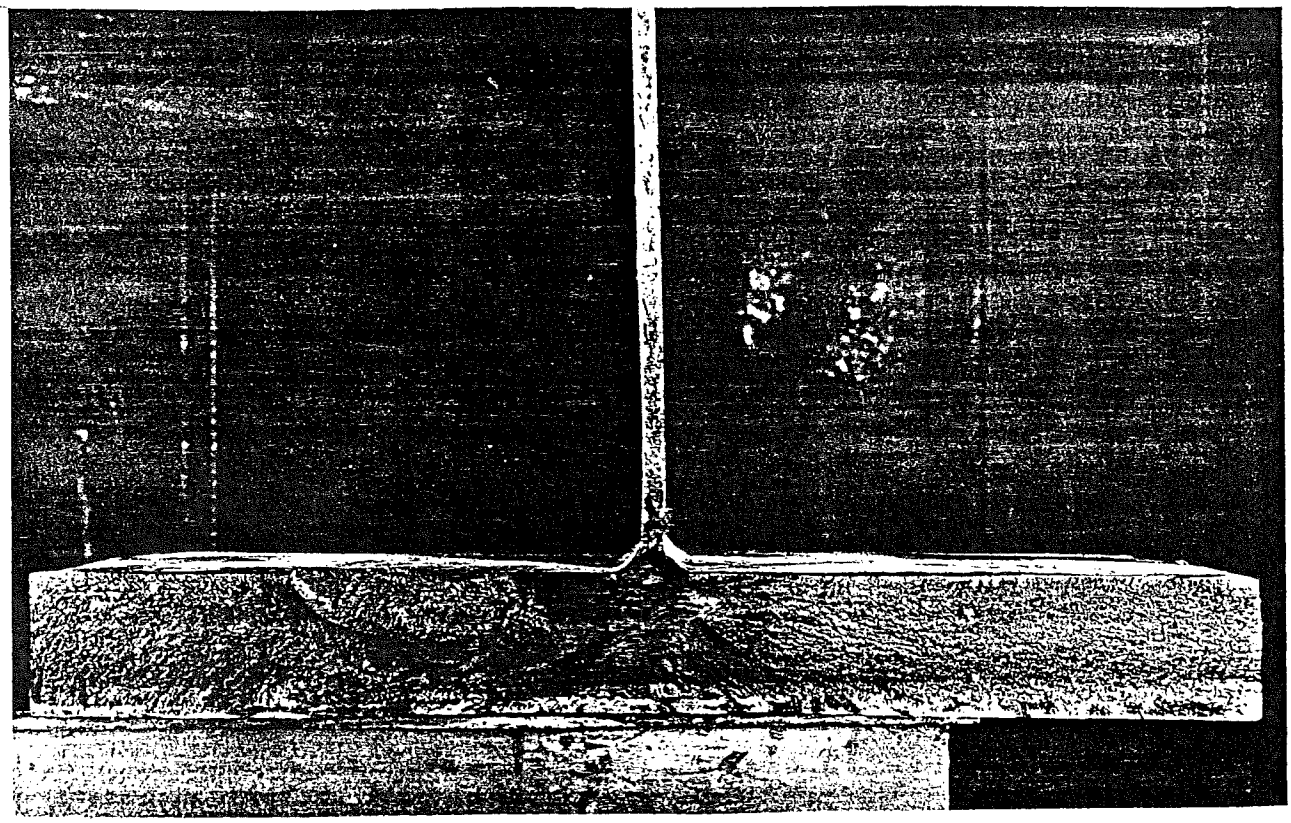

(b) Fracture Surface - South Section

Fig. 46 Photographs of the Fracture Surface of Back Channel Girder 25G4C

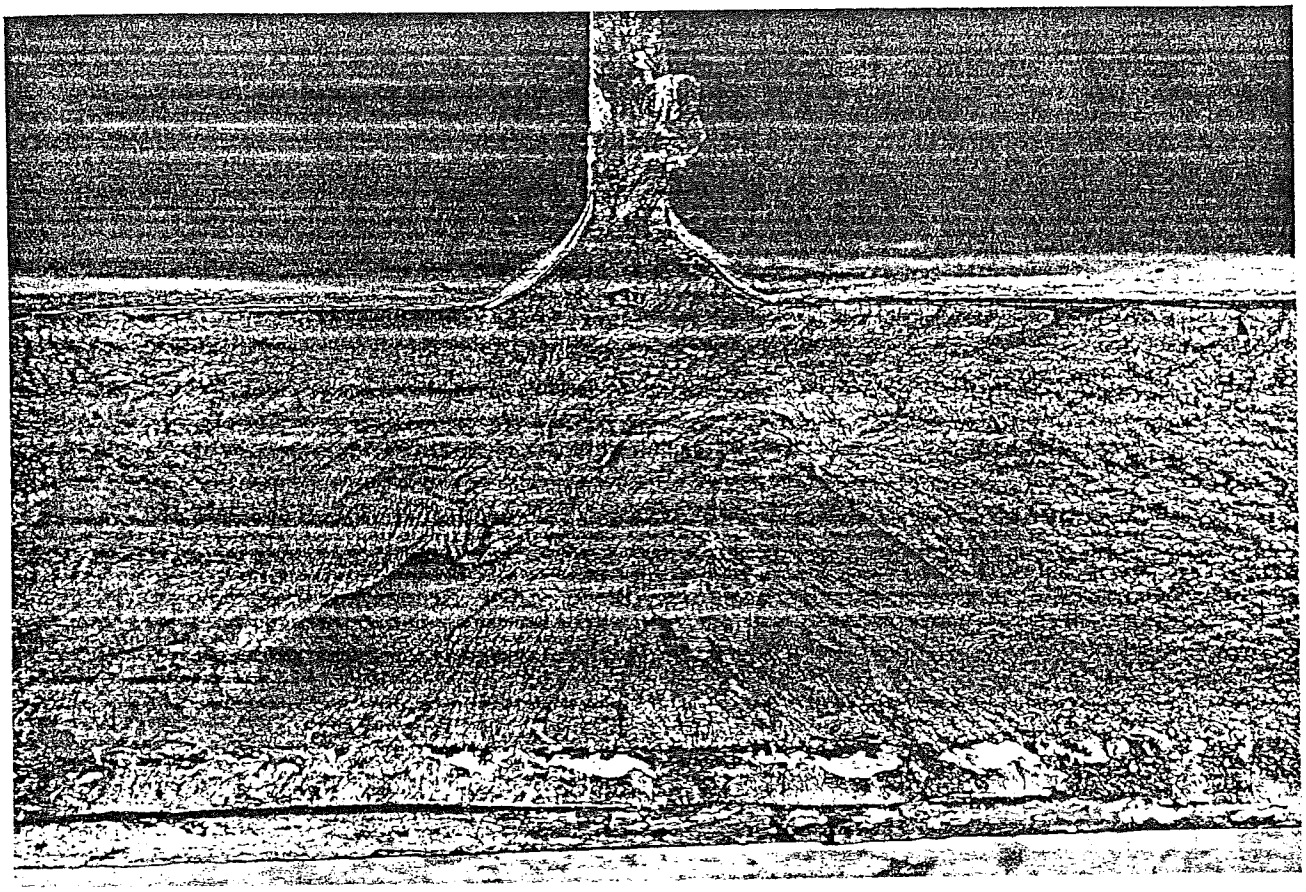

Fig. 47 Close-up of Flange and Web Fracture Surfaces from South Section Showing Probable Initial Crack and Half Circular Crack Arrest Zone

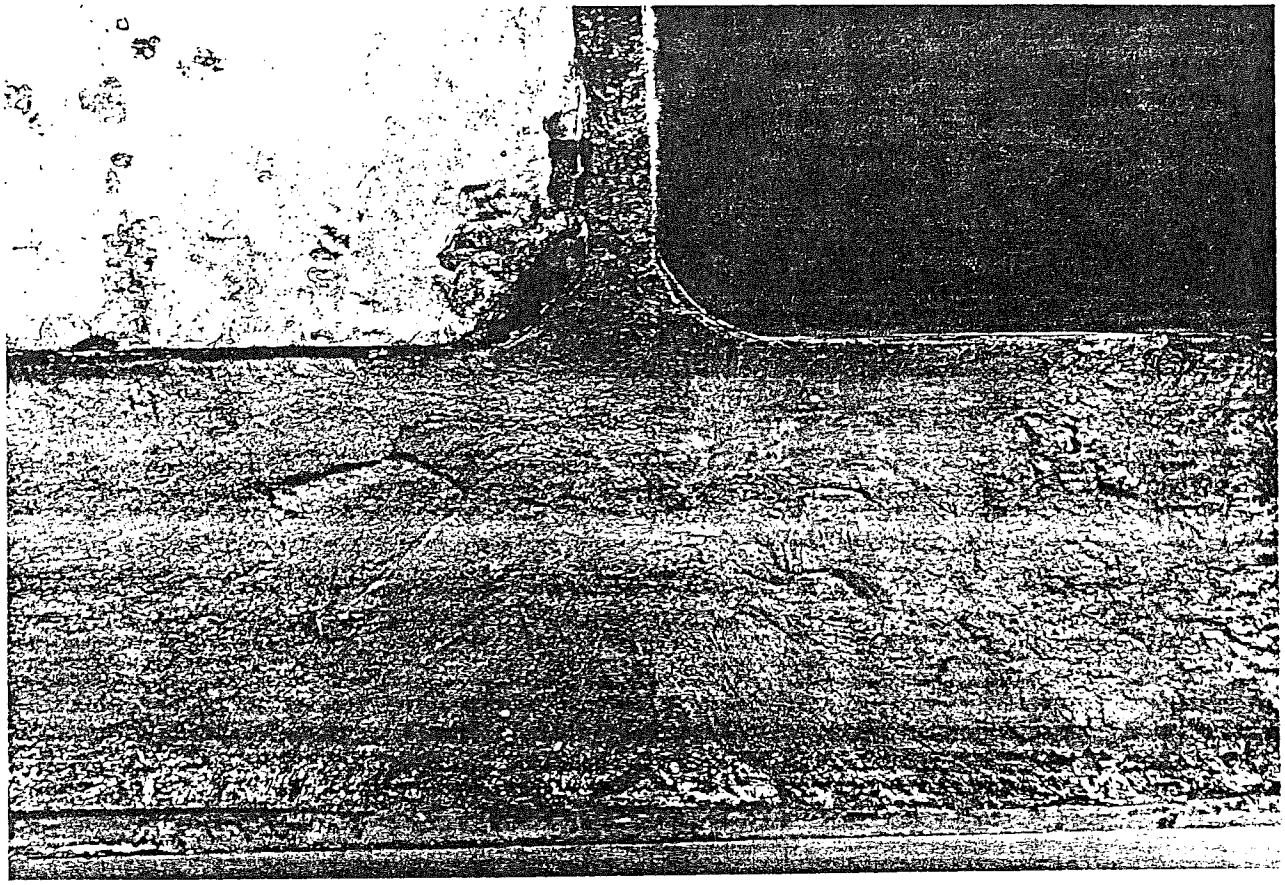

Fig. 48 Close-up of Fracture Surface from North Section

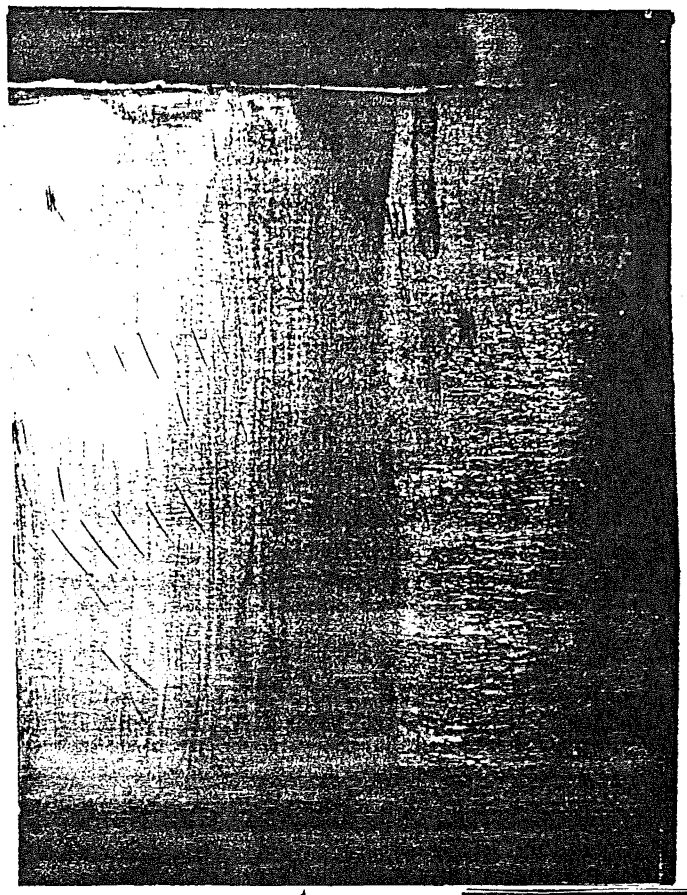

North Section

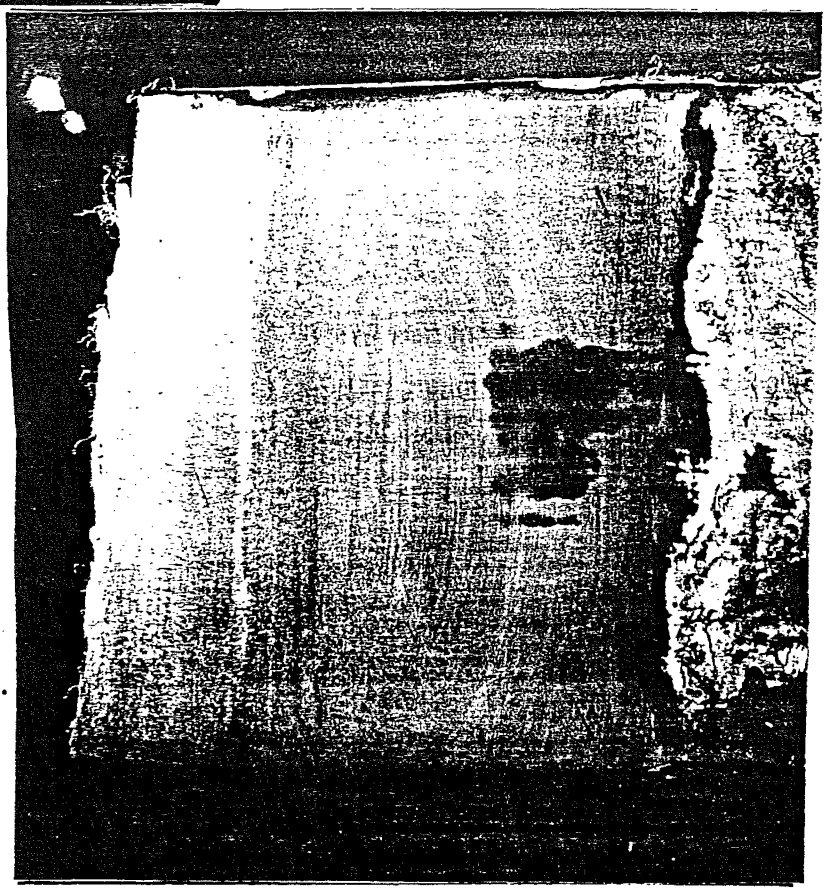

South Section

Fig. 49 West Edge of Flange at Fracture

South Section

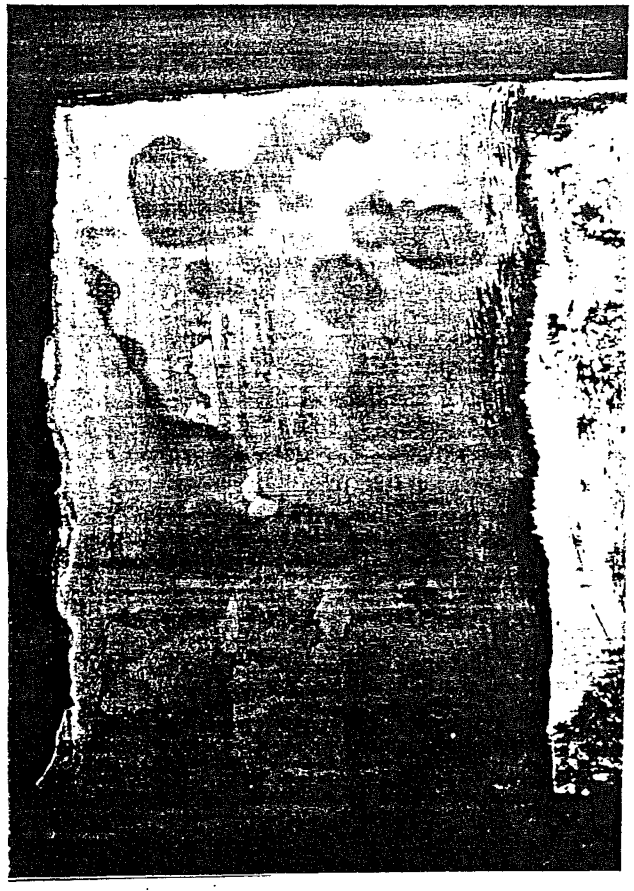

North Section

Fig. 50 East Edge of Flange at Fracture

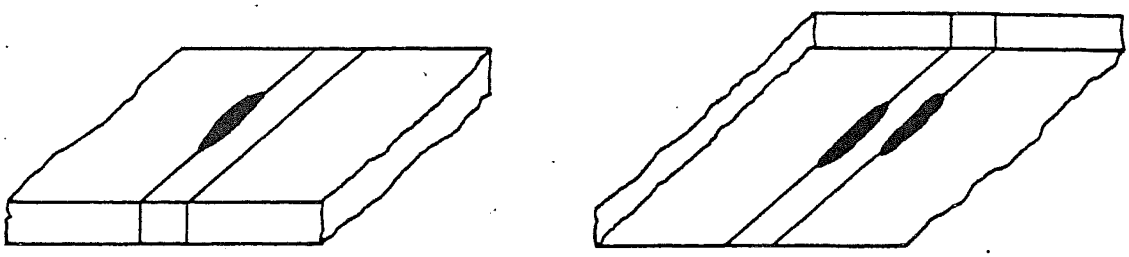

a) 1 st. Repair (weld passes on the fusion line)

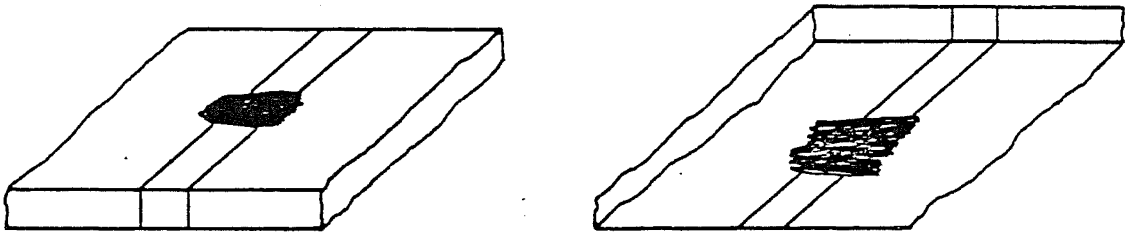

b) 2 nd. Repair (primary repair, after gouging out defect)

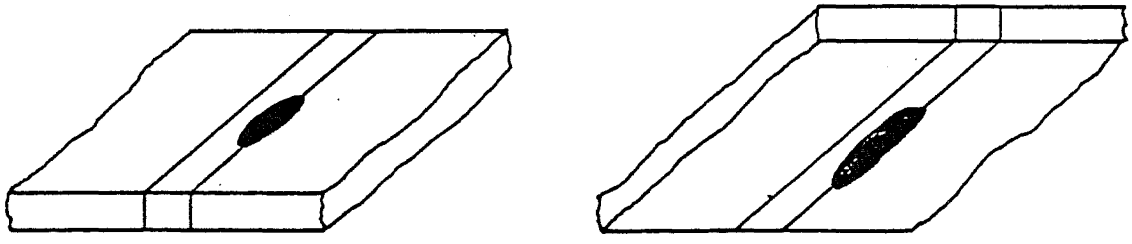

c) 3 rd. Repair (weld passes near fusion line)

Fig. 51 Schematic Showing Repair Sequence at the Casualty Section

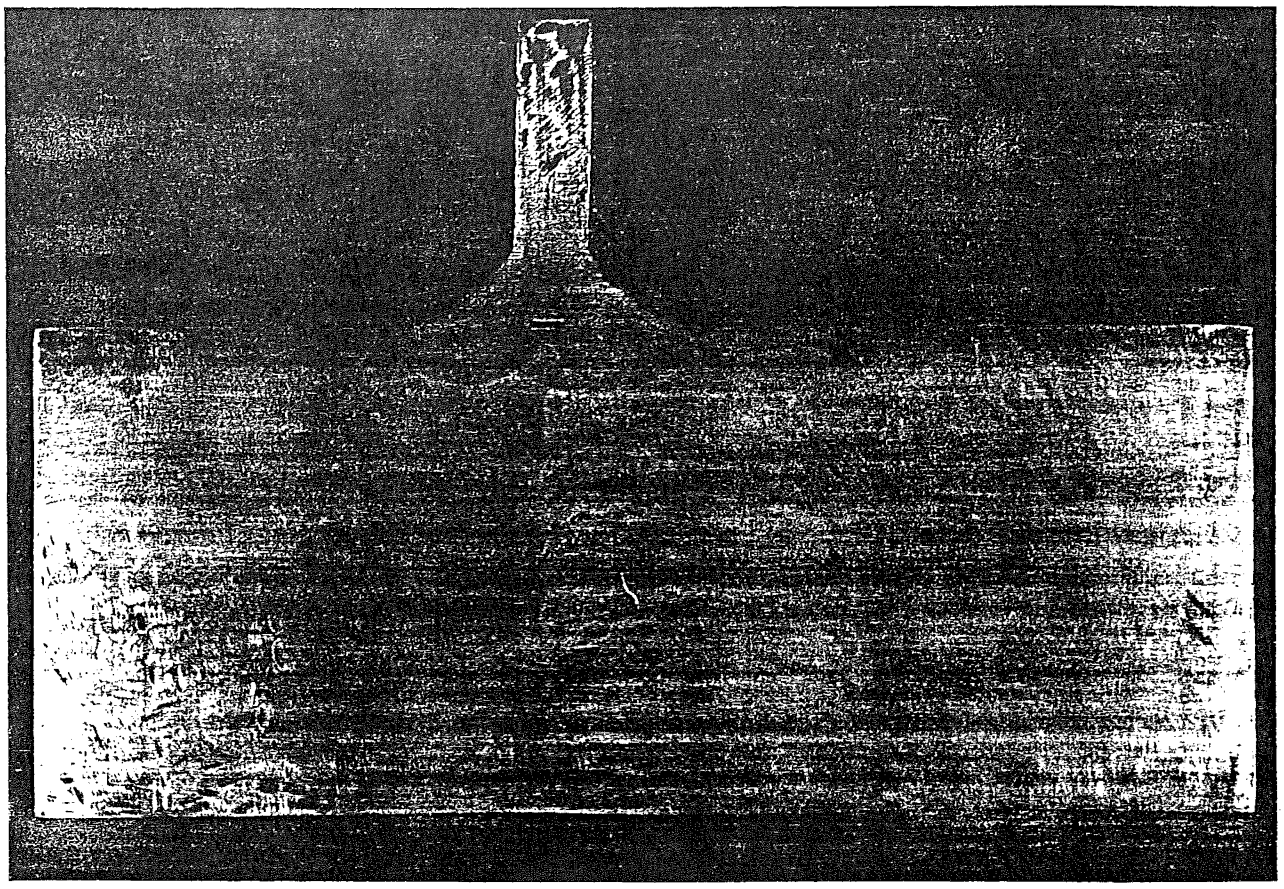

Fig. 52 Polished and Etched Surface of Flange Just Behind the Fracture

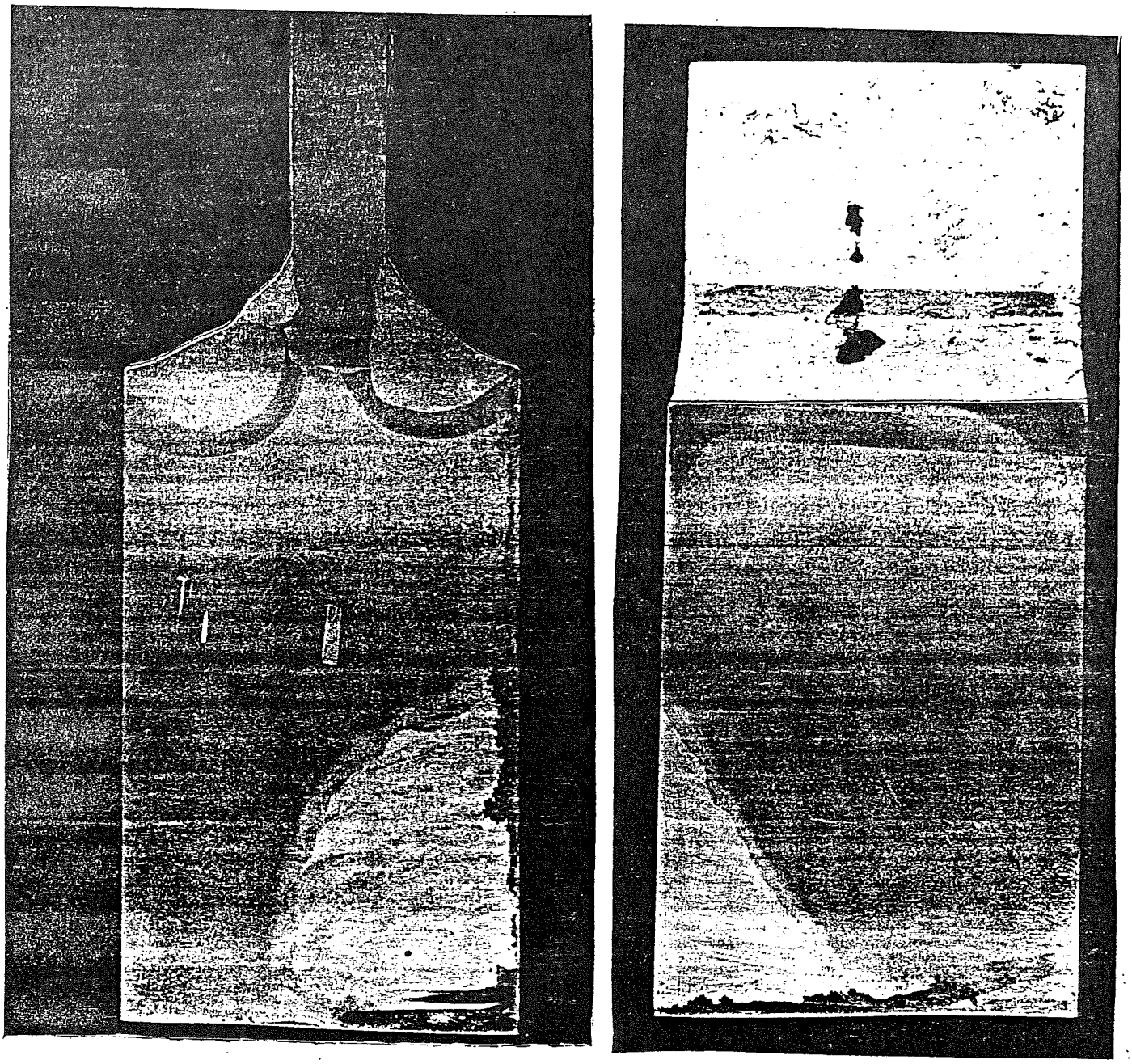

Fig. 53 Polished and Etched Surface of Piece K
(see Fig. 25) Showing Weld Repair

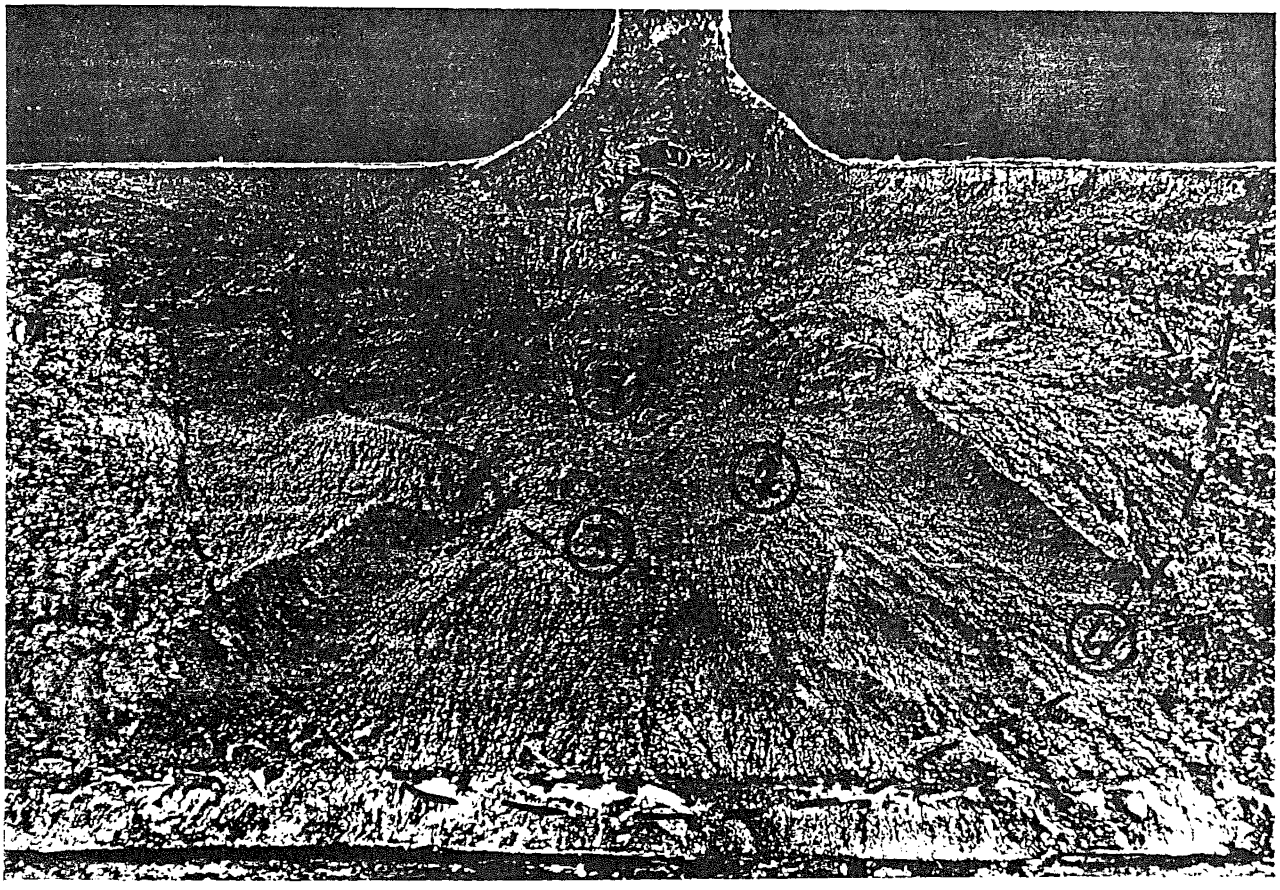

Fig. 54 Close-up of Crack Surface Showing Locations Where Replicas Were Obtained for Electron Microscope Studies

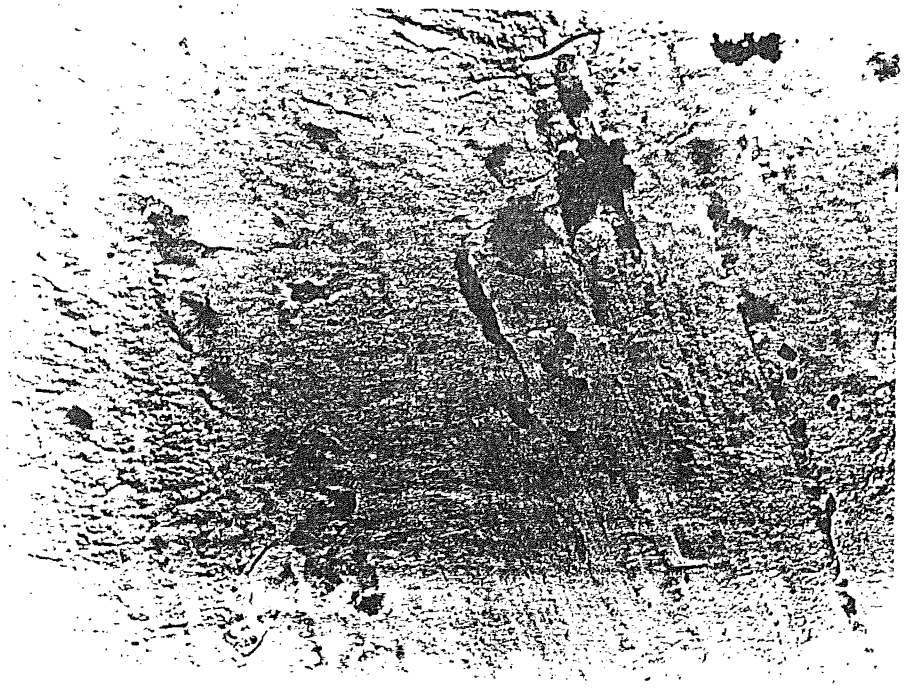

(a) Typical Striations Observed in Region 1
(See Fig. 54) X25200

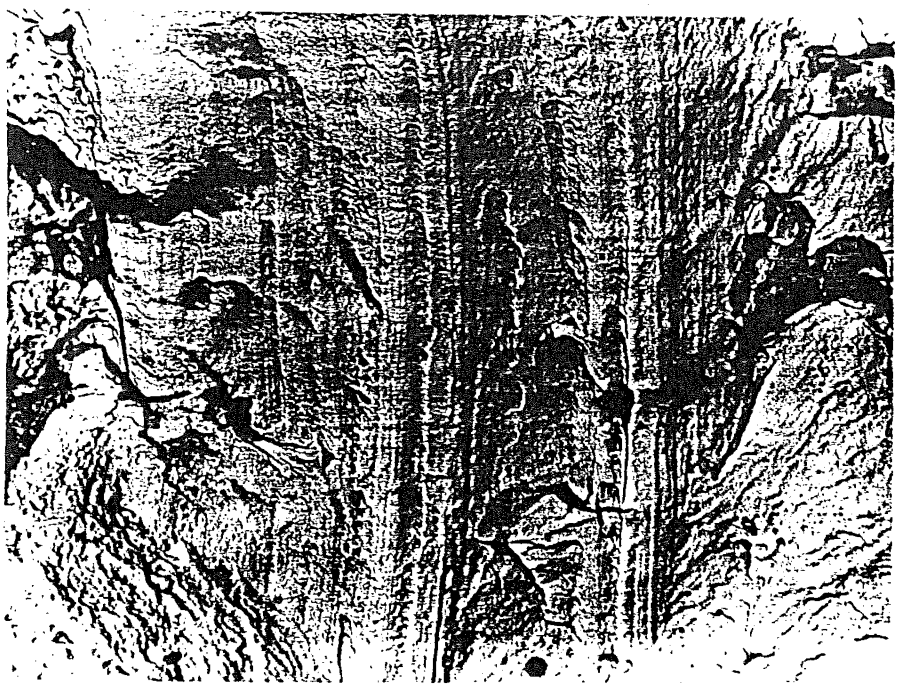

(b) Typical Striations Observed in Region 3
(See Fig. 54) X48240

Fig. 55 Fatigue Crack Growth Striations
Around Boundary of Initial Flaw

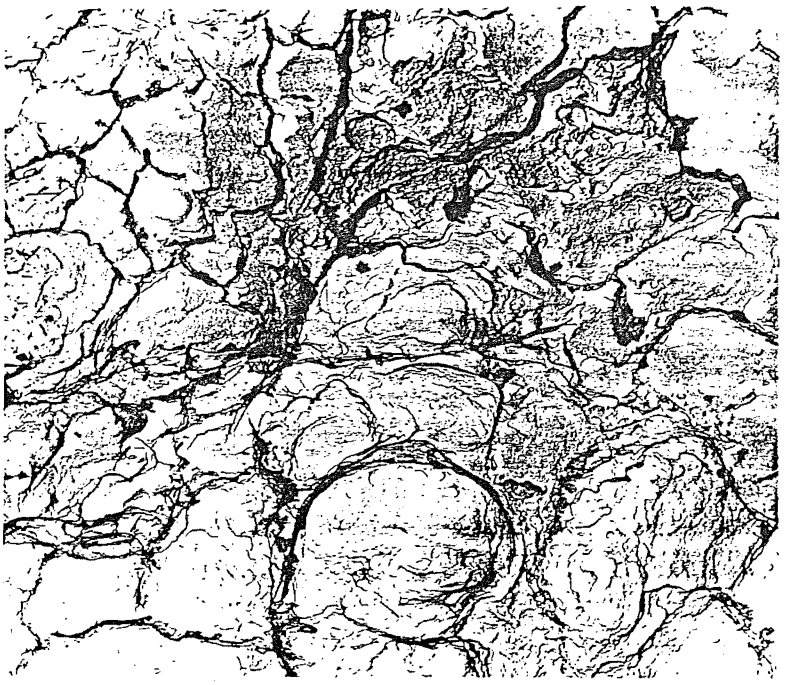

(a) Surface Features in Region 5 - X5535

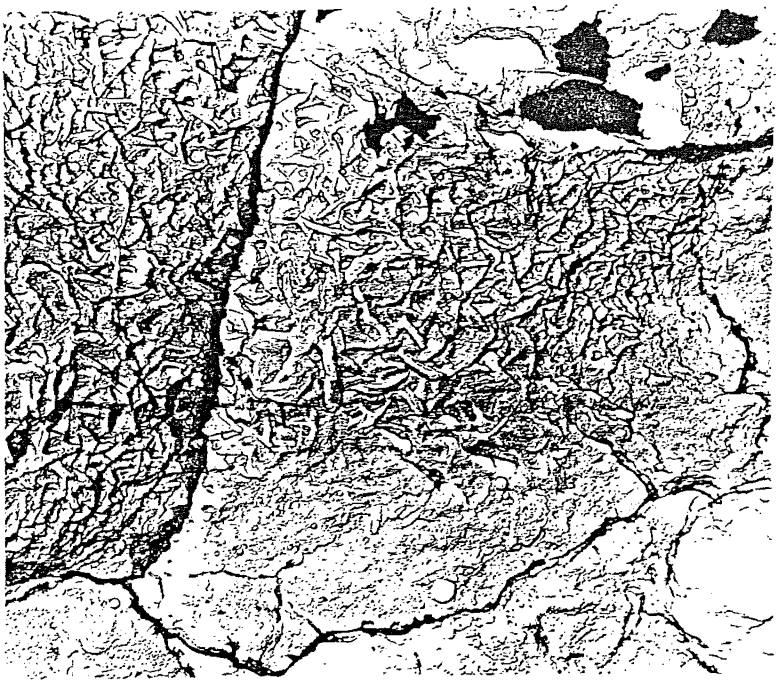

(b) Surface Features in Region 5 Showing Corrosion Product X2618

Fig. 56 Transmission Electron Microscope Photomicrographs of the Surface of Initial Flaw

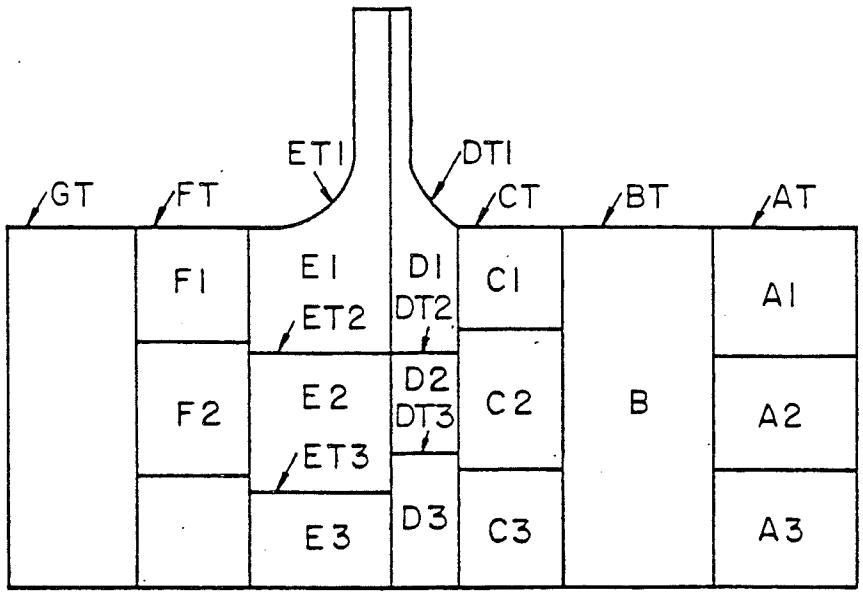

Fig. 57 Fracture Surface Cutting Scheme for Metallography of I-79 Fracture

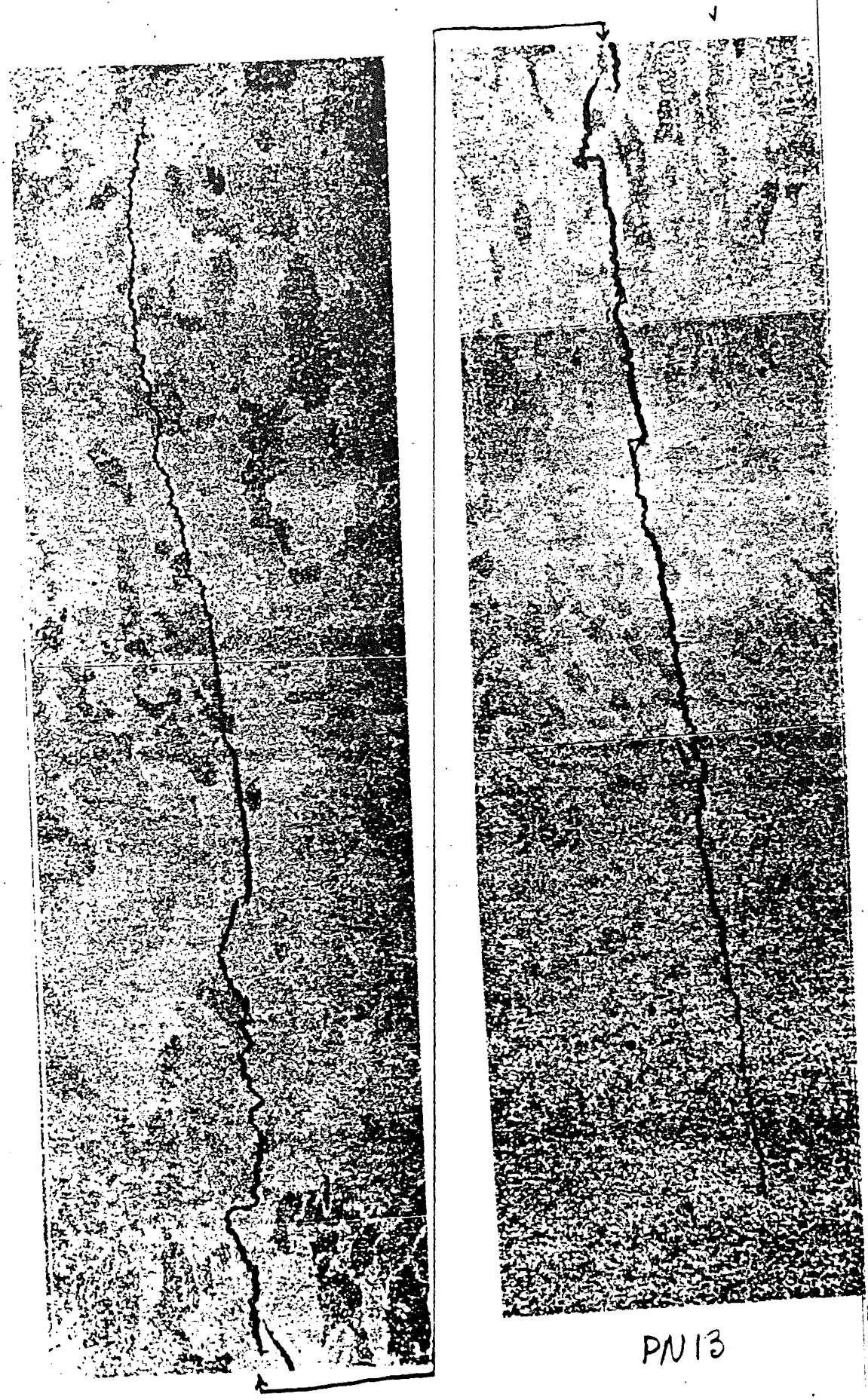

Fig. 58 Cross-section view of crack in area C2.
(at C2-D2 surface) 40X Nital Etch

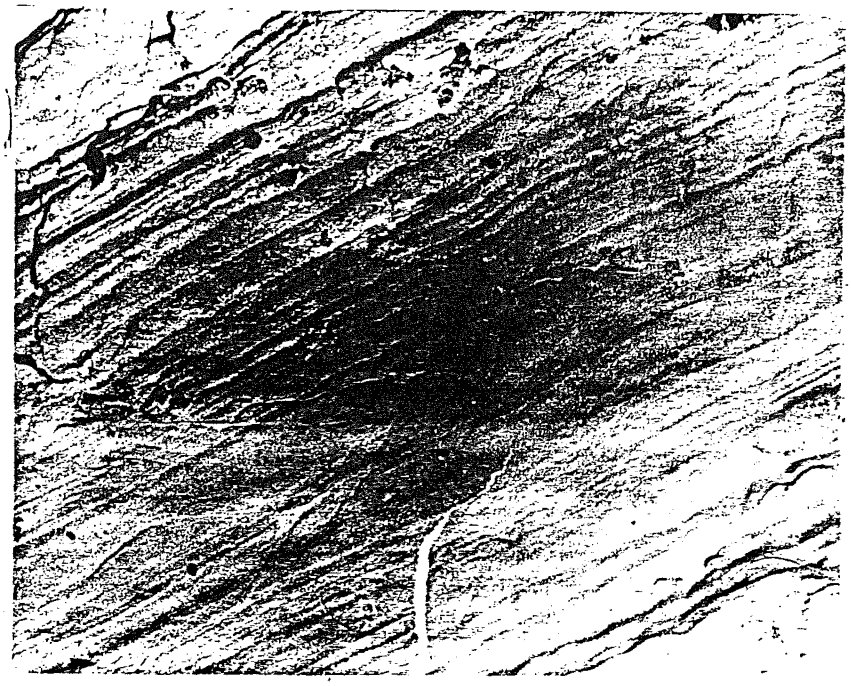

Surface Features in Region 6 X32640

Fig. 59 TEM Photomicrographs
of the surface of the Initial Flaw

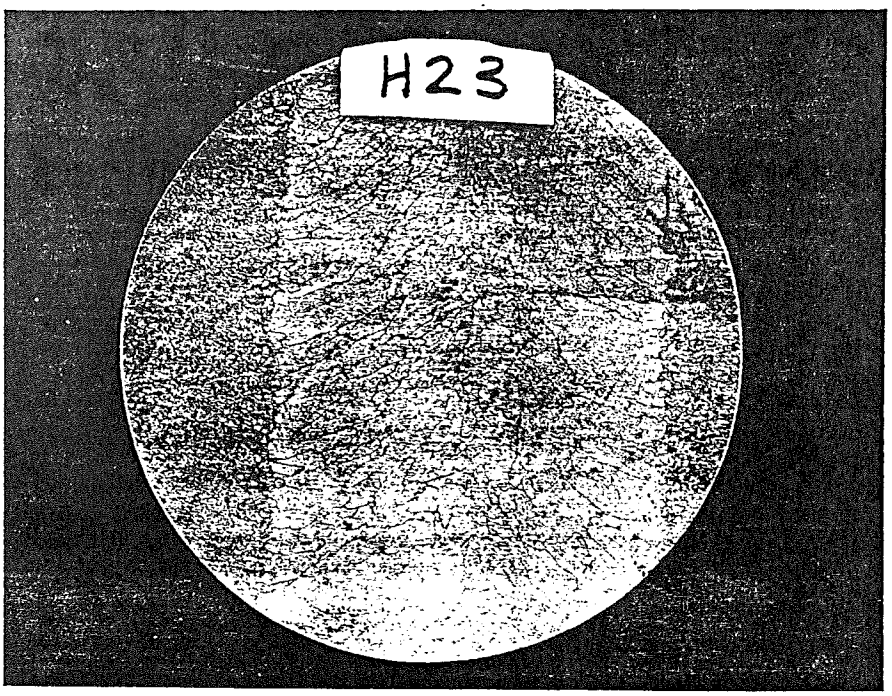

(a) Top Surface of Slice 23 Near Quarter Point

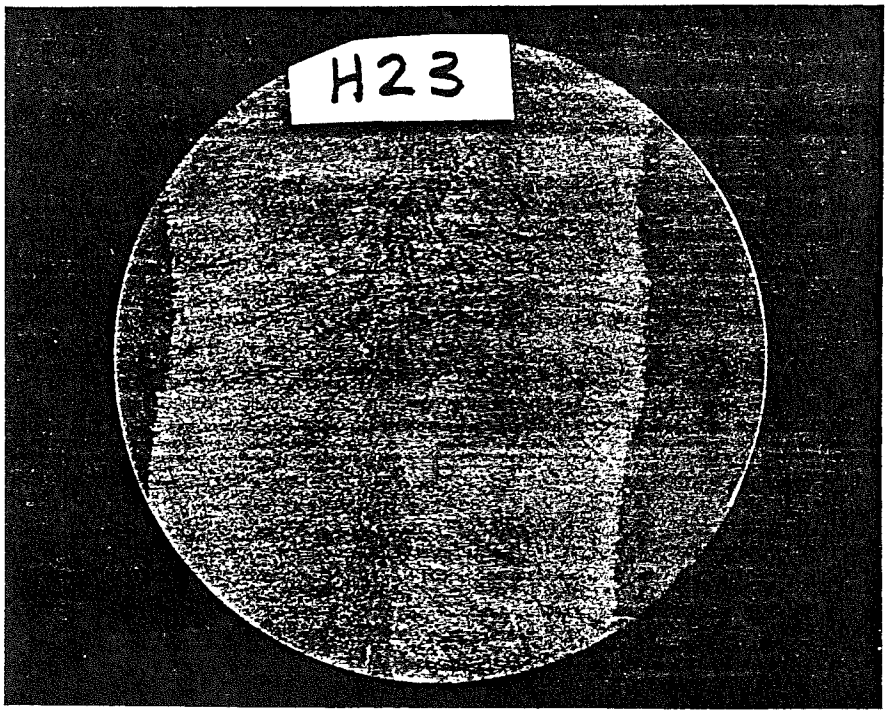

(b) Bottom Surface of Slice 23 Near Midthickness

Fig. 60 Polished and Etched Surfaces of Core Removed From Ramp H

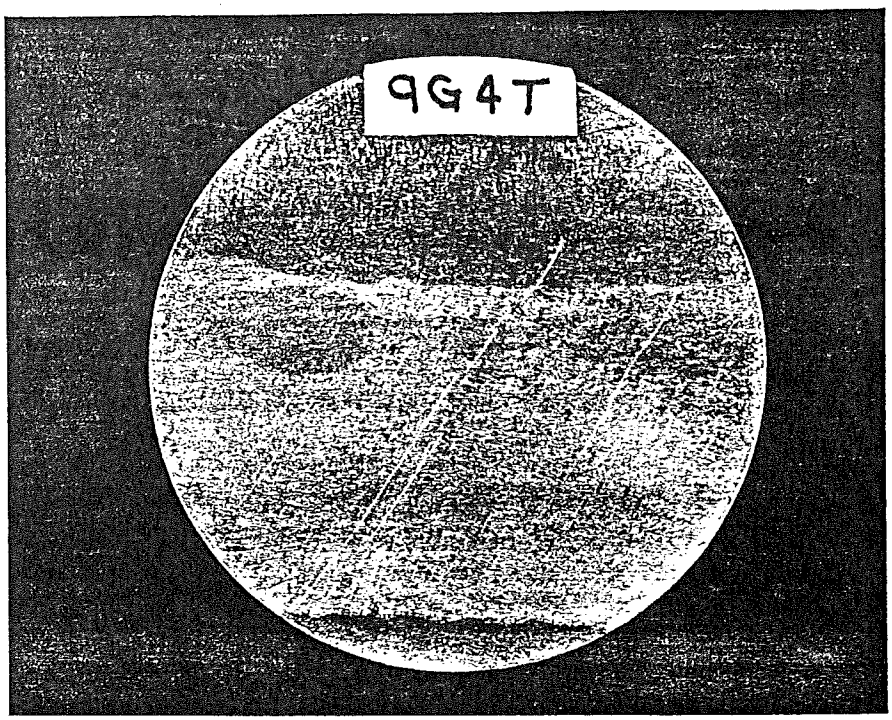

(a) Polished and Etched Surface of Core 9G4
Showing Weld Repair

(b) Polished and Etched Surface of Core 9G1A
Showing Small Grain Boundary Fissures

Fig. 61. Polished and Etched Surfaces of Electroslag Welds
From Back Channel Structures

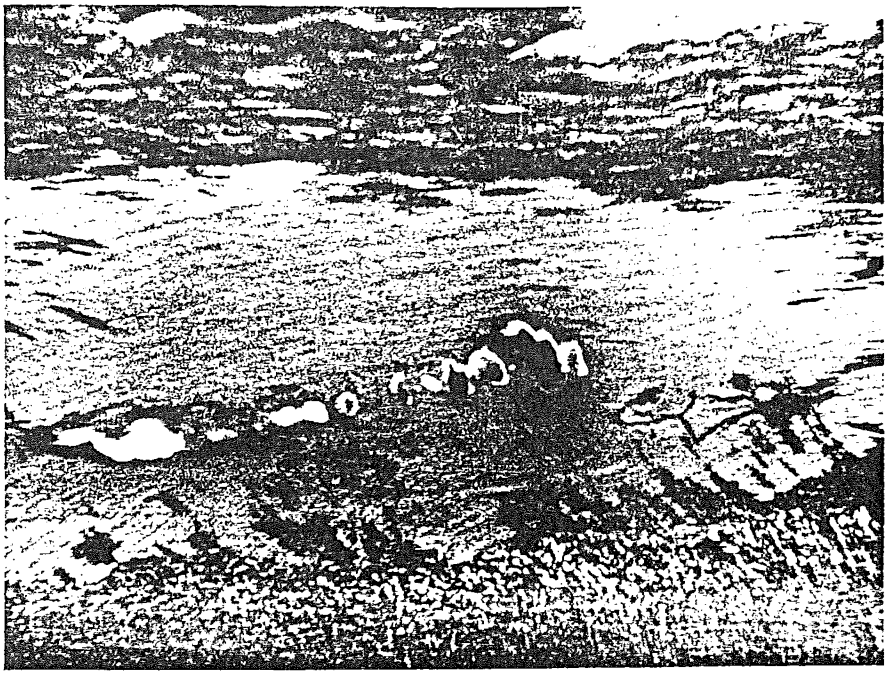

(a) Defect Found in Bottom Flange Surface at Weld 4 - Girder 27G4C of Ramp D

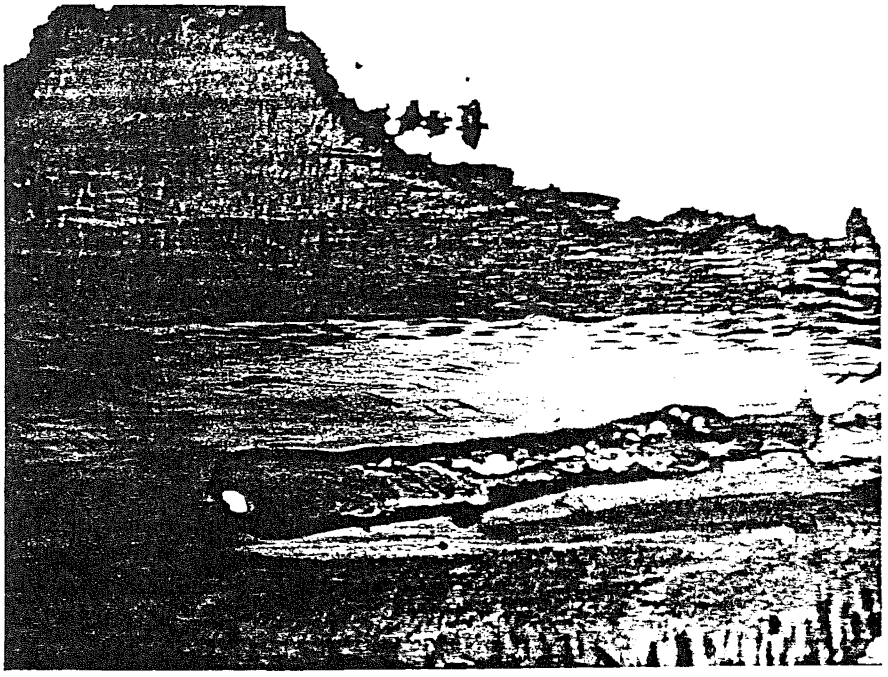

(b) Polished and Etched Surface Showing Weld Repair

Fig. 62 Defect Observed in Girder 27G4C of Ramp D Structure

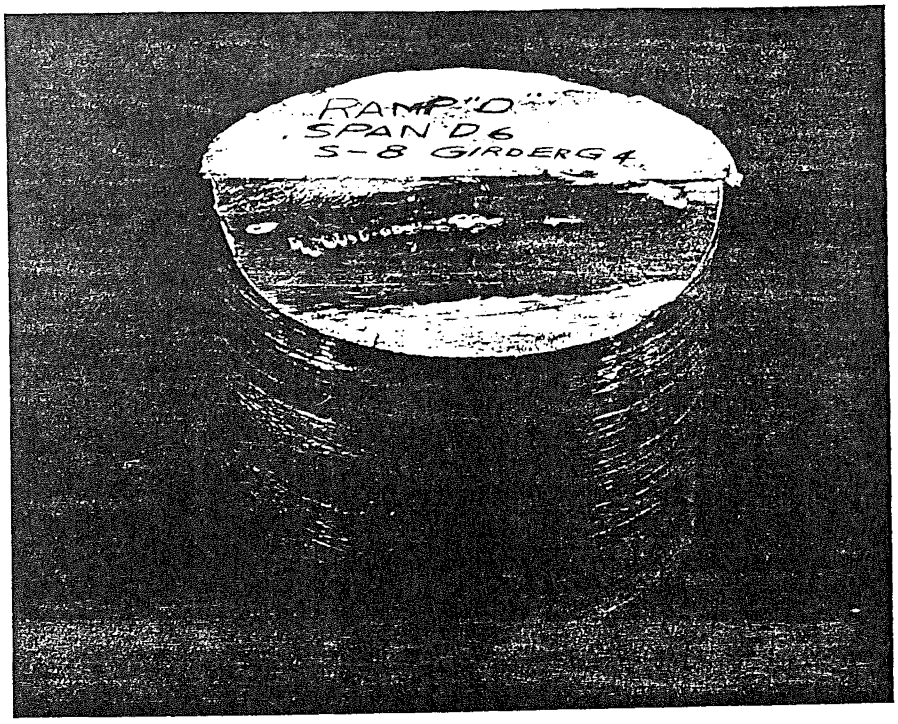

Fig. 63 Sample Core Removed from Ramp D

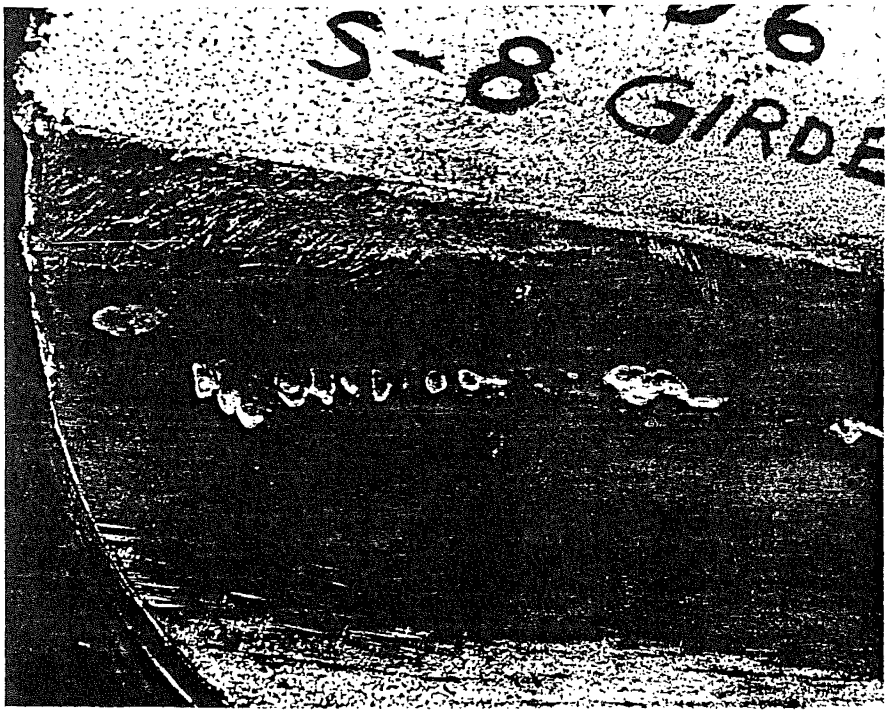

Fig. 64 Close-up View of Defect Region Showing Paint Filled Holes in Core

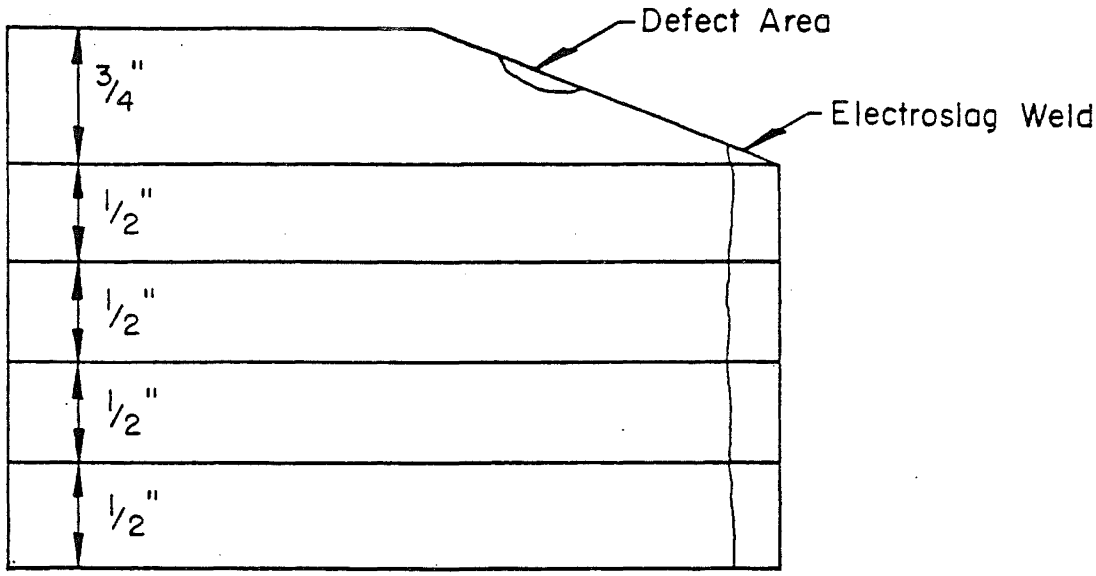

Fig. 65 Schematic Showing Cutting Scheme used for D ramp core

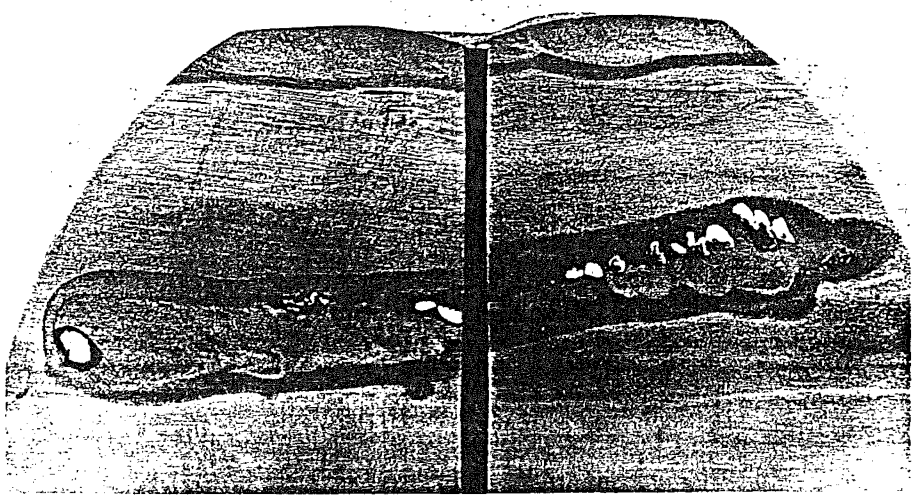

(a) Plan View of Core Sample Slices

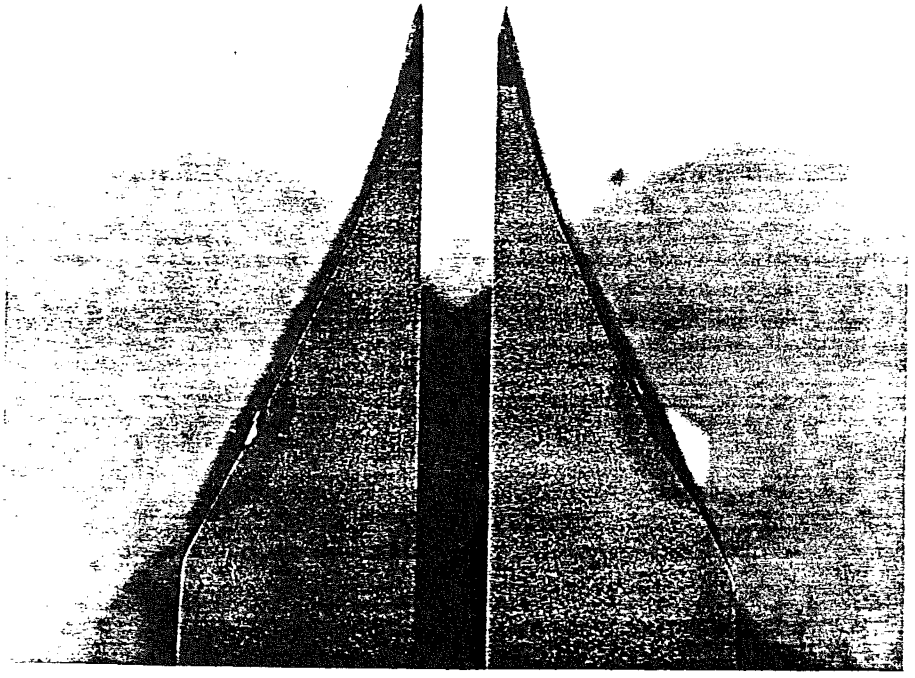

(b) Elevation View of Top Slice of Core

Fig. 66 Photographs of Weld Defects in Core Sample "D"

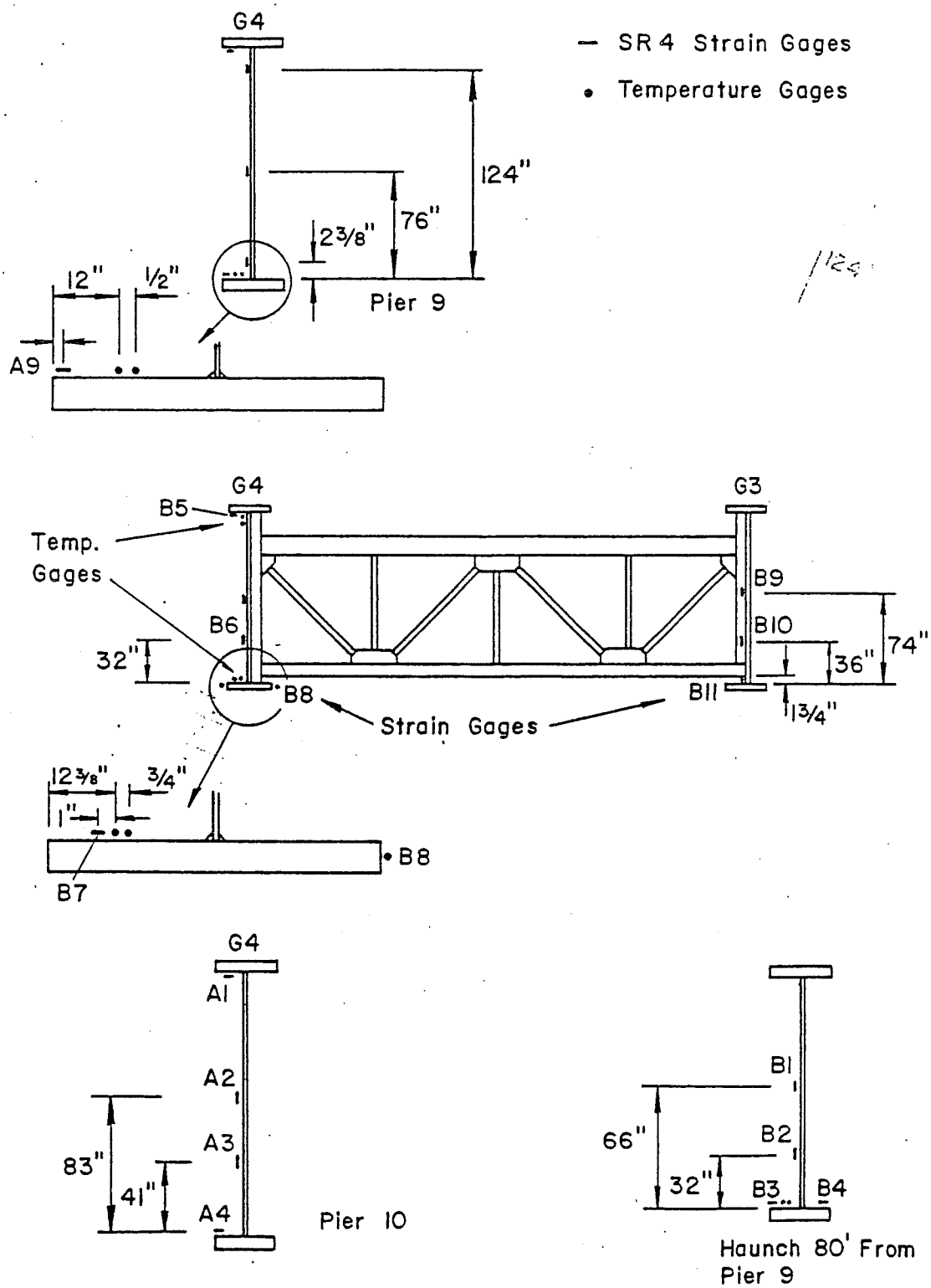

Fig. 67 Strain and Temperature Gage Locations in Span 9 of Back Channel Structure

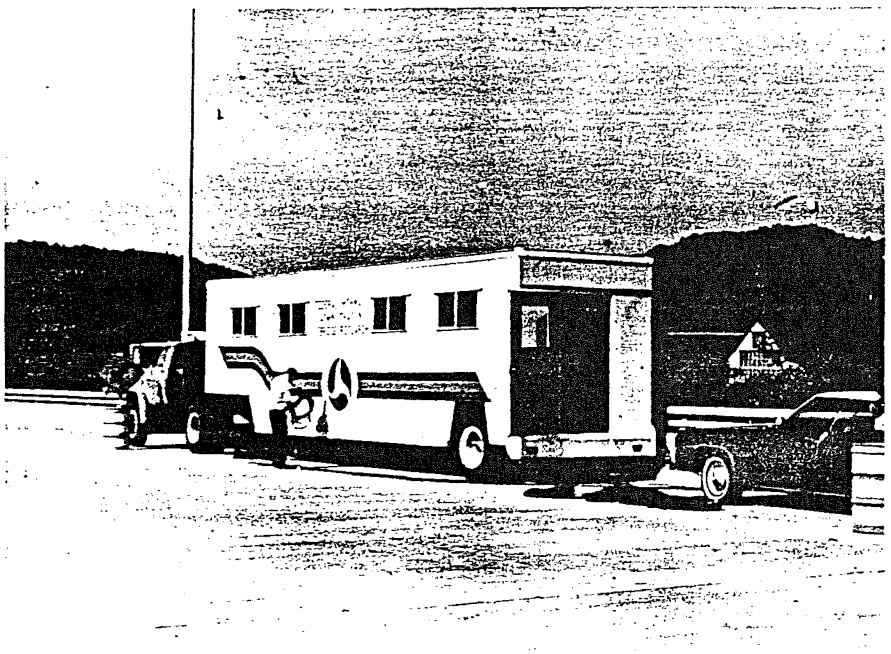

Fig. 68. Test Van Parked on Southbound Structure Near Span 9

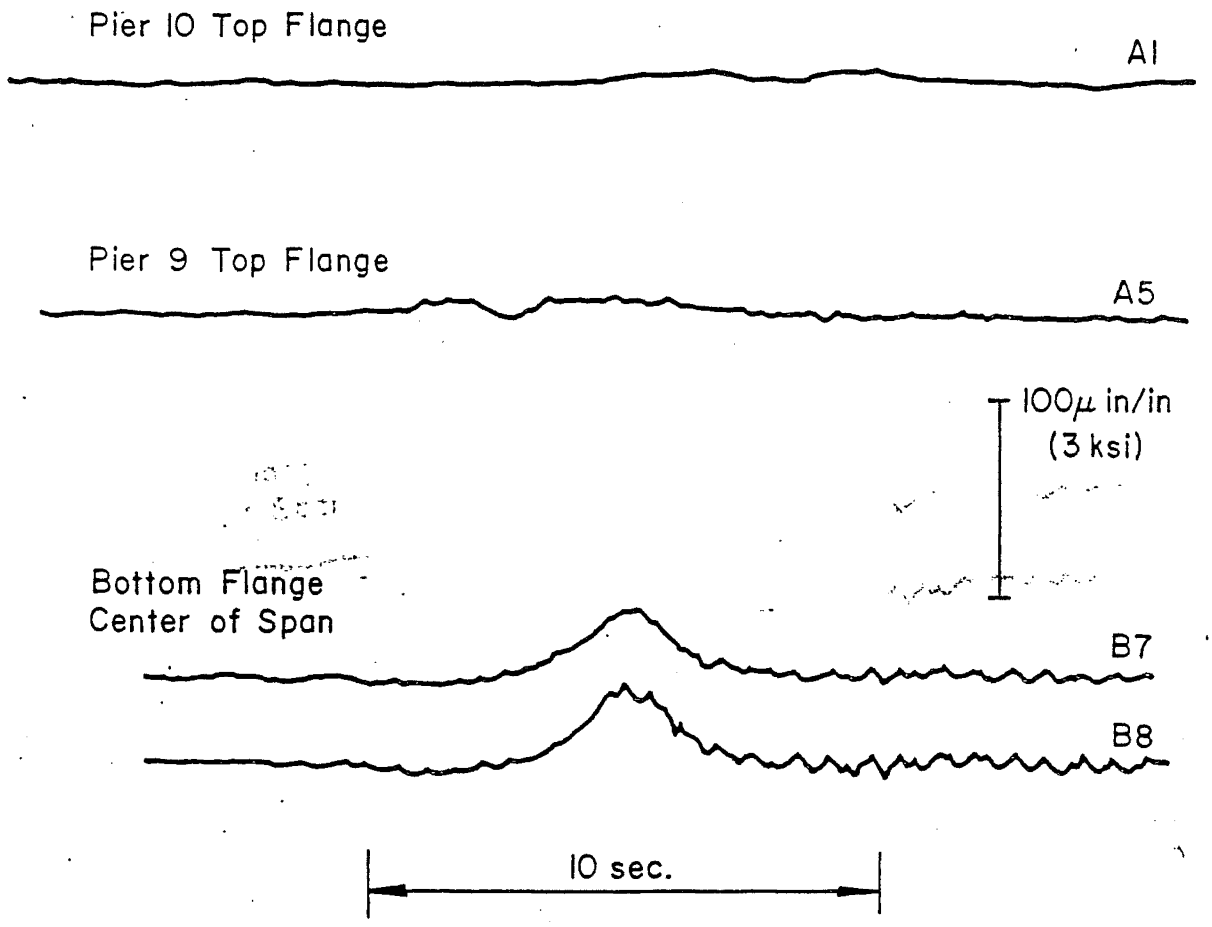

Fig. 69 Typical Time Strain Records Obtain from Span 9 as Truck Crossed over Bridge in Northbound Lanes

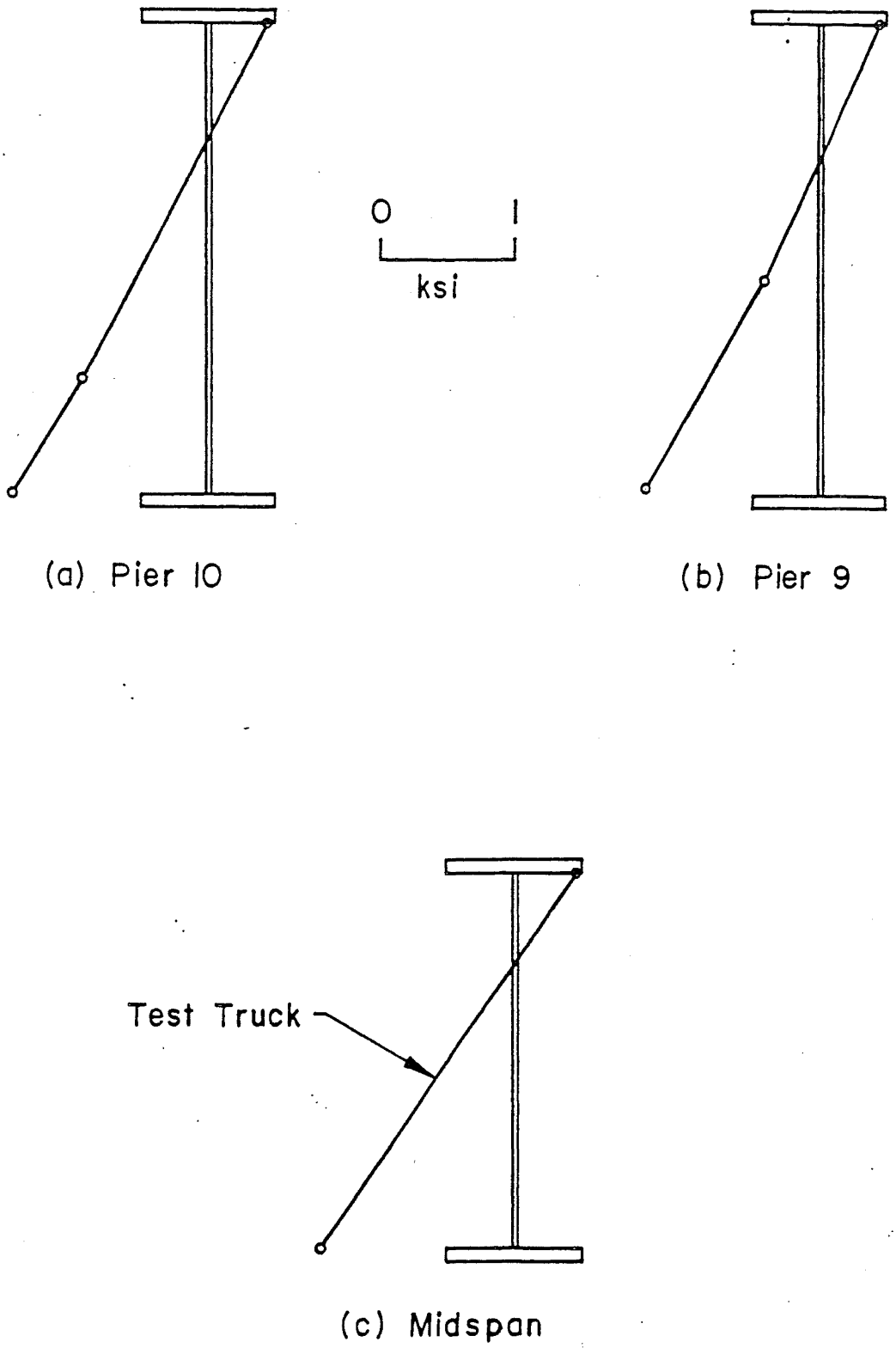

Fig. 70 Strain Gradients that Were Found to Exist in Span 9

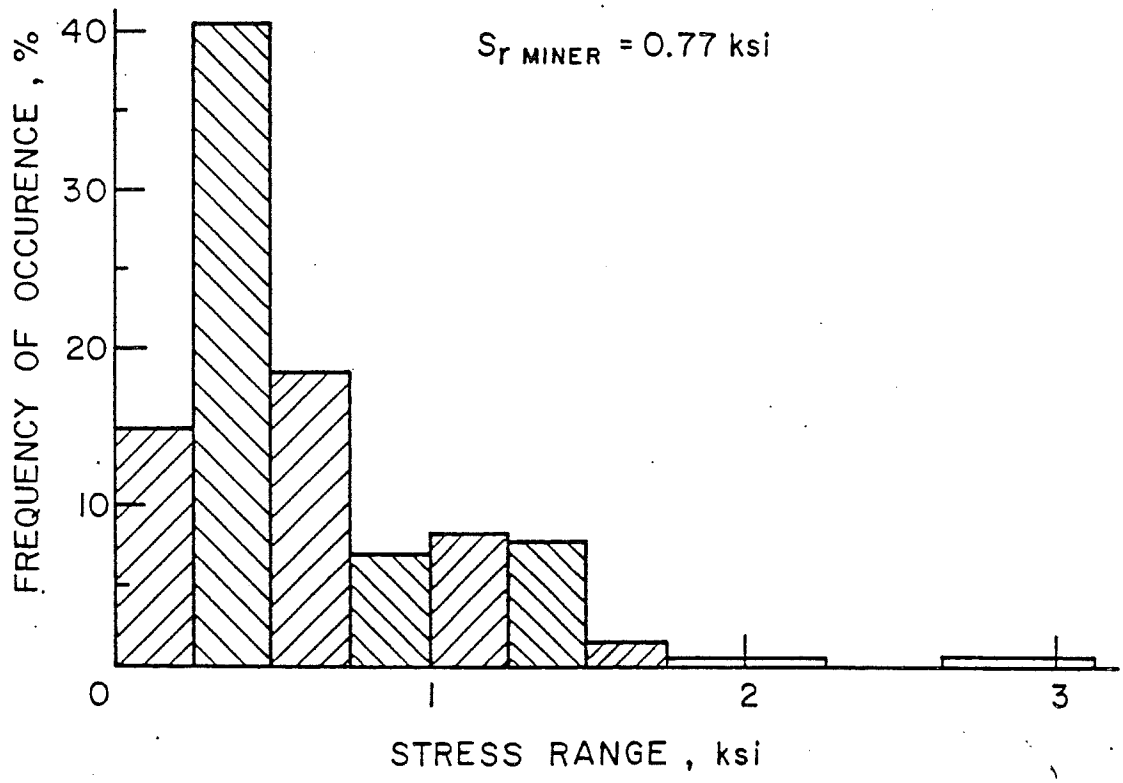

Fig. 71 Measured Stress Range Spectrum Near the Midspan Casualty Section of Span 9

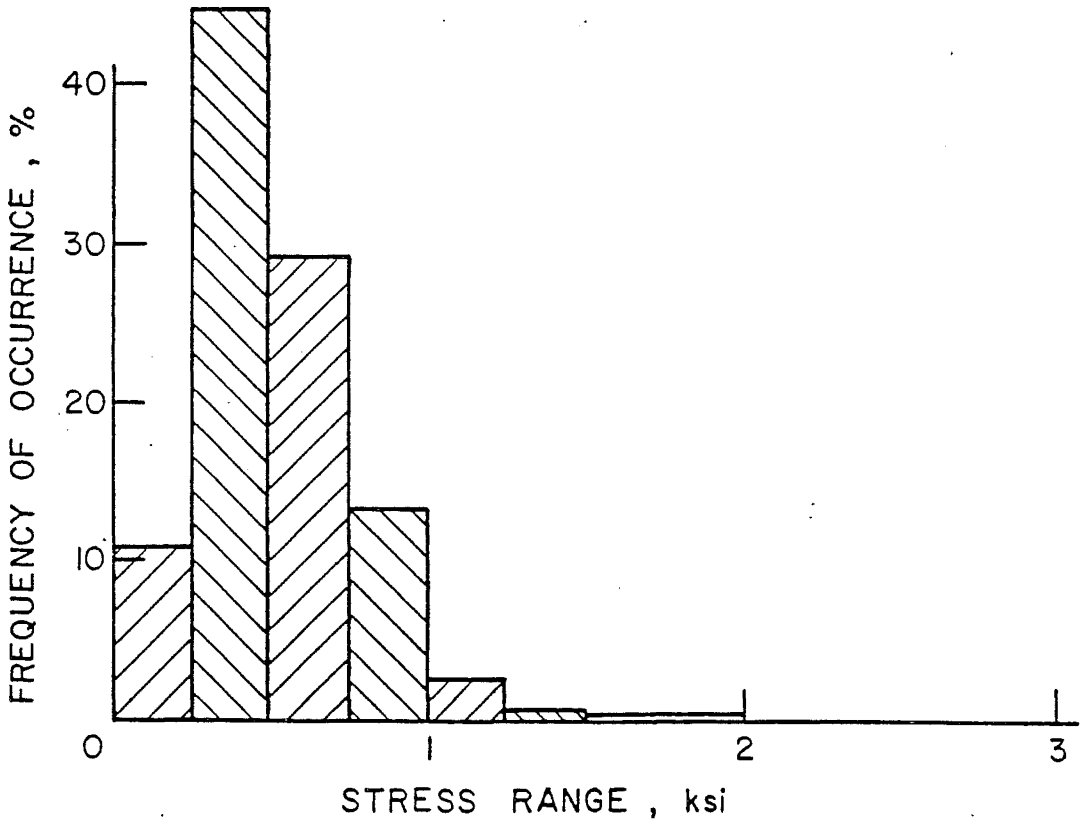

Fig. 72 Stress Range Spectrum Observed in Interior Girder G3 at Midspan of Span 9

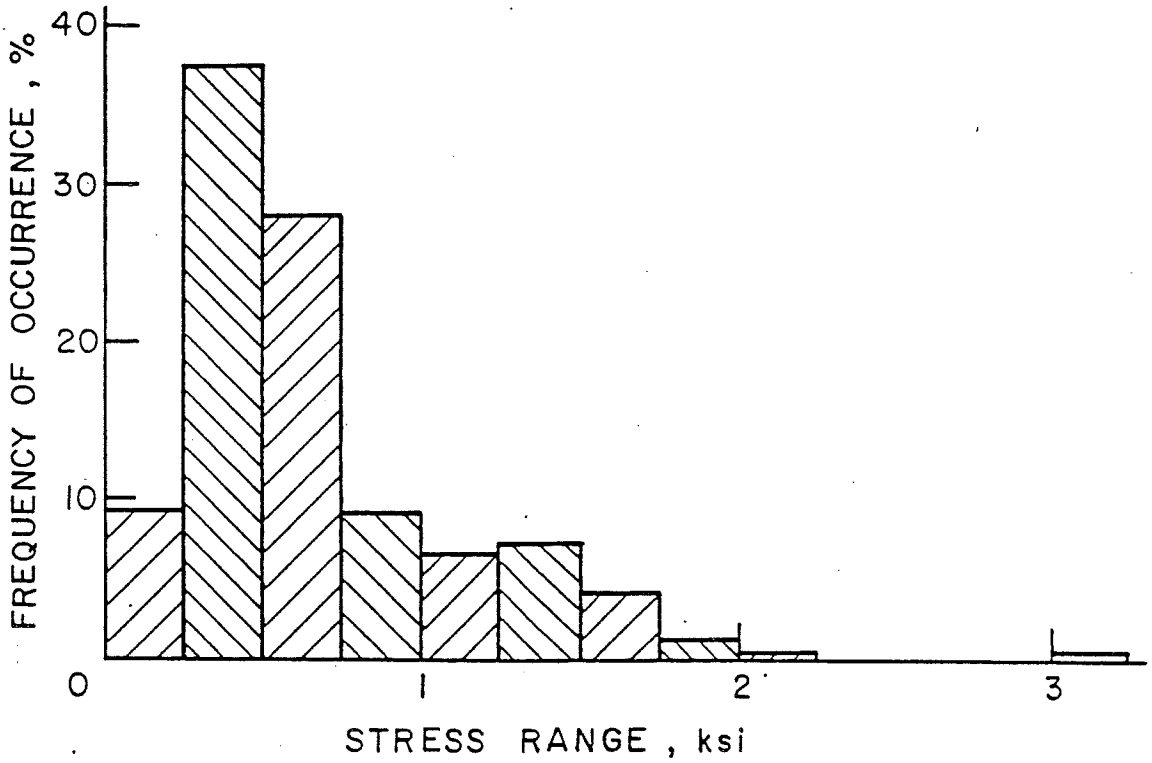

Fig. 73 Stress Range Spectrum Measured Near Haunch 80 Ft. from Pier 9

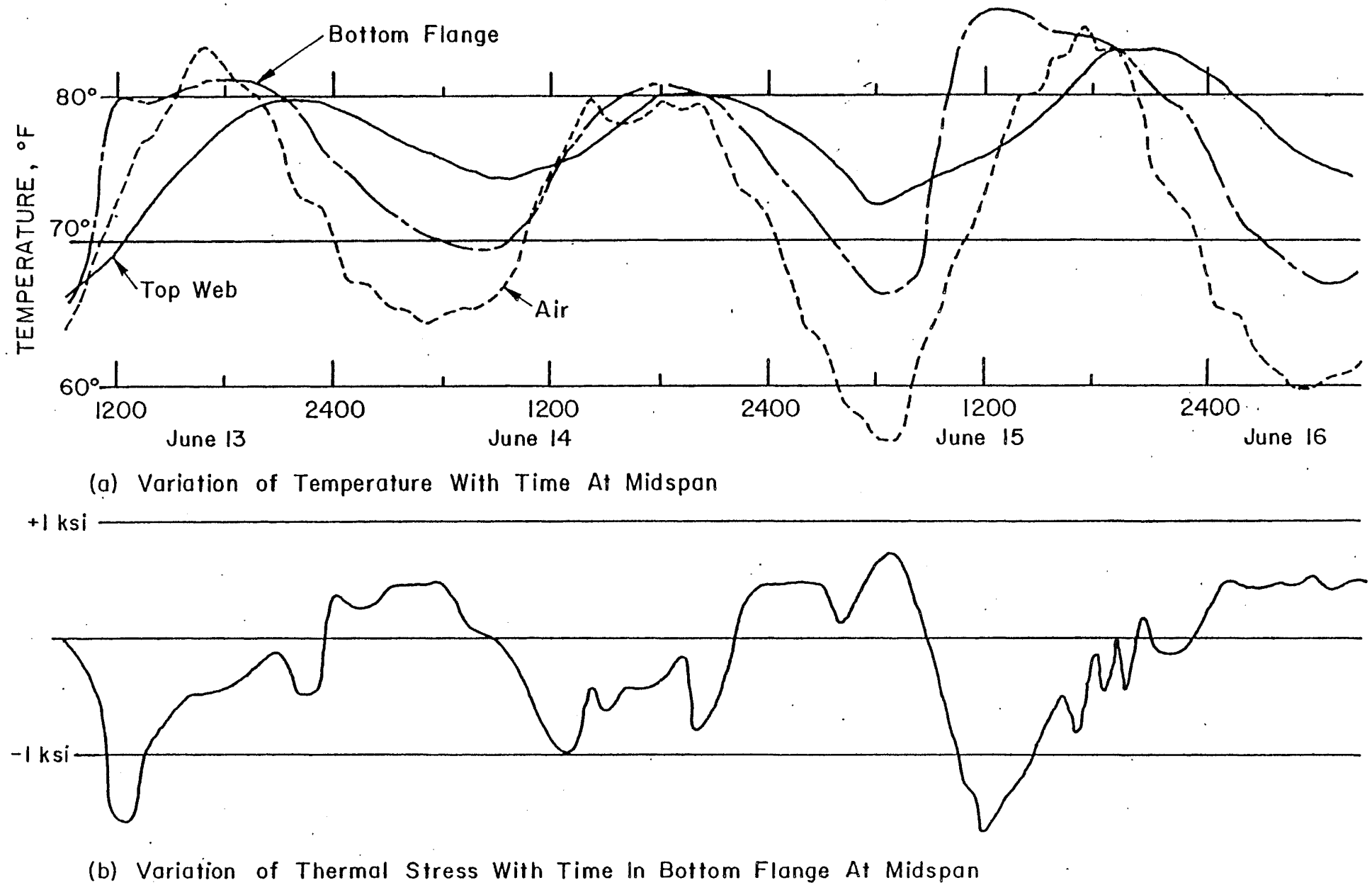

Fig. 74 Comparison of Measured Temperatures in Casualty Girder Near Midspan and the Resulting Variation in Thermal Stress in the Bottom Flange

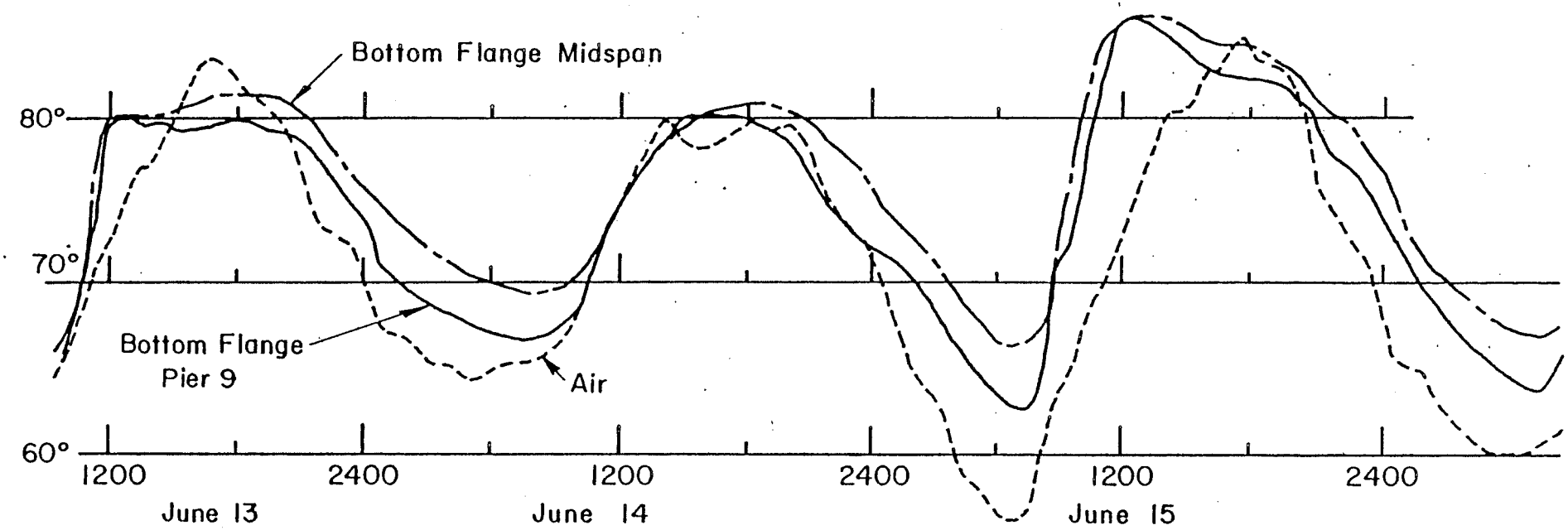

(a) Comparison Of Bottom Flange Temperature Variation - Midspan And Pier 9

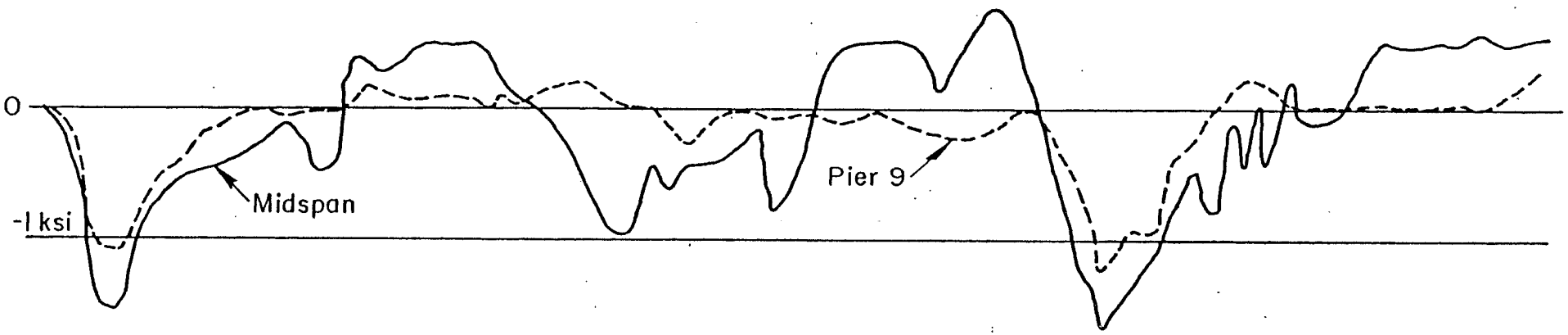

(b) Comparison Of Thermal Stress At Midspan And At Pier 9

Fig. 75 Comparison of Measured Temperatures at Pier 9 and Midspan with Corresponding Thermal Stresses in Bottom Flange at Midspan and at Pier 9

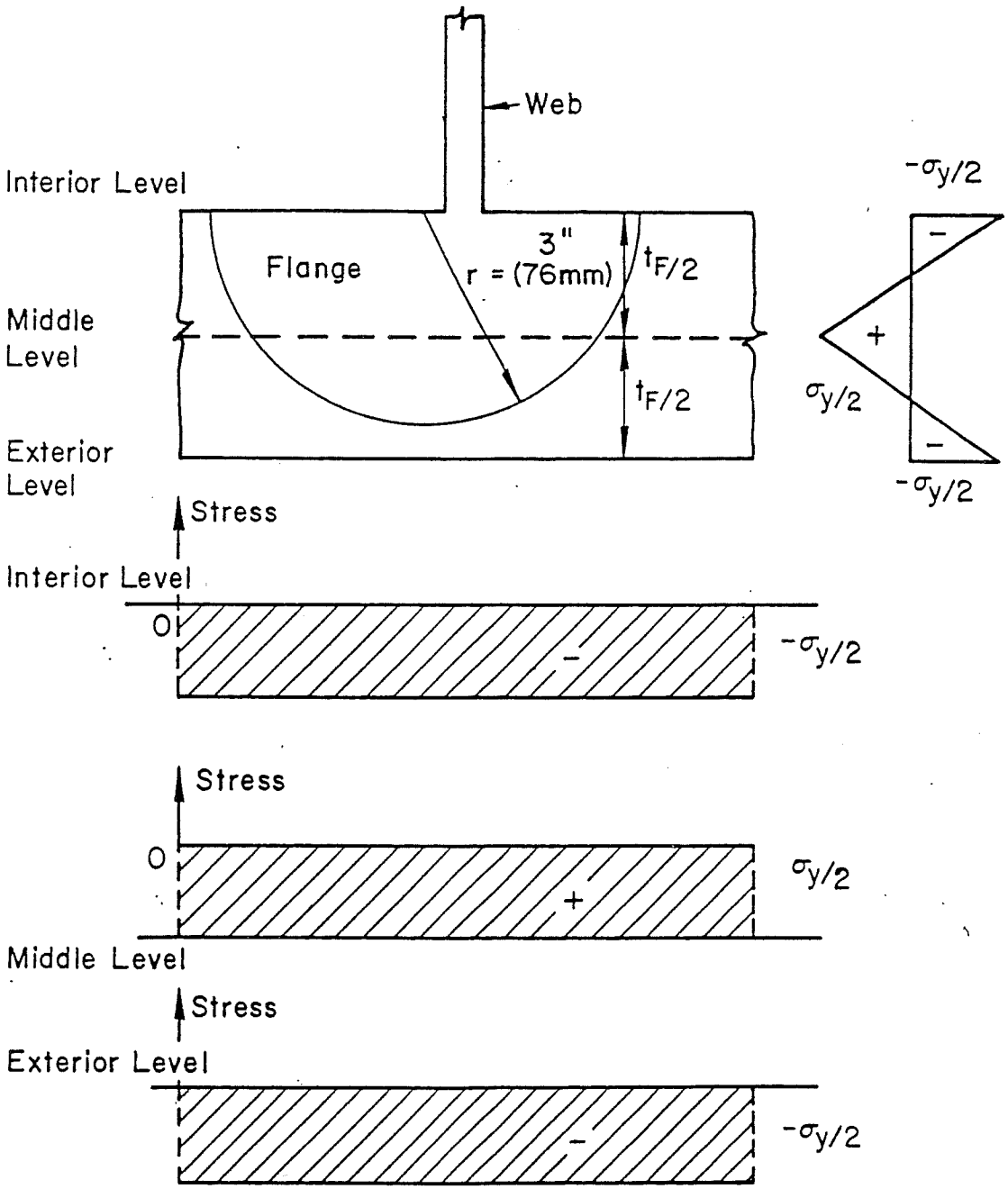

Fig. 76 Idealization of the Residual Stress Distribution in the Electroslag Weld at the Casualty Section

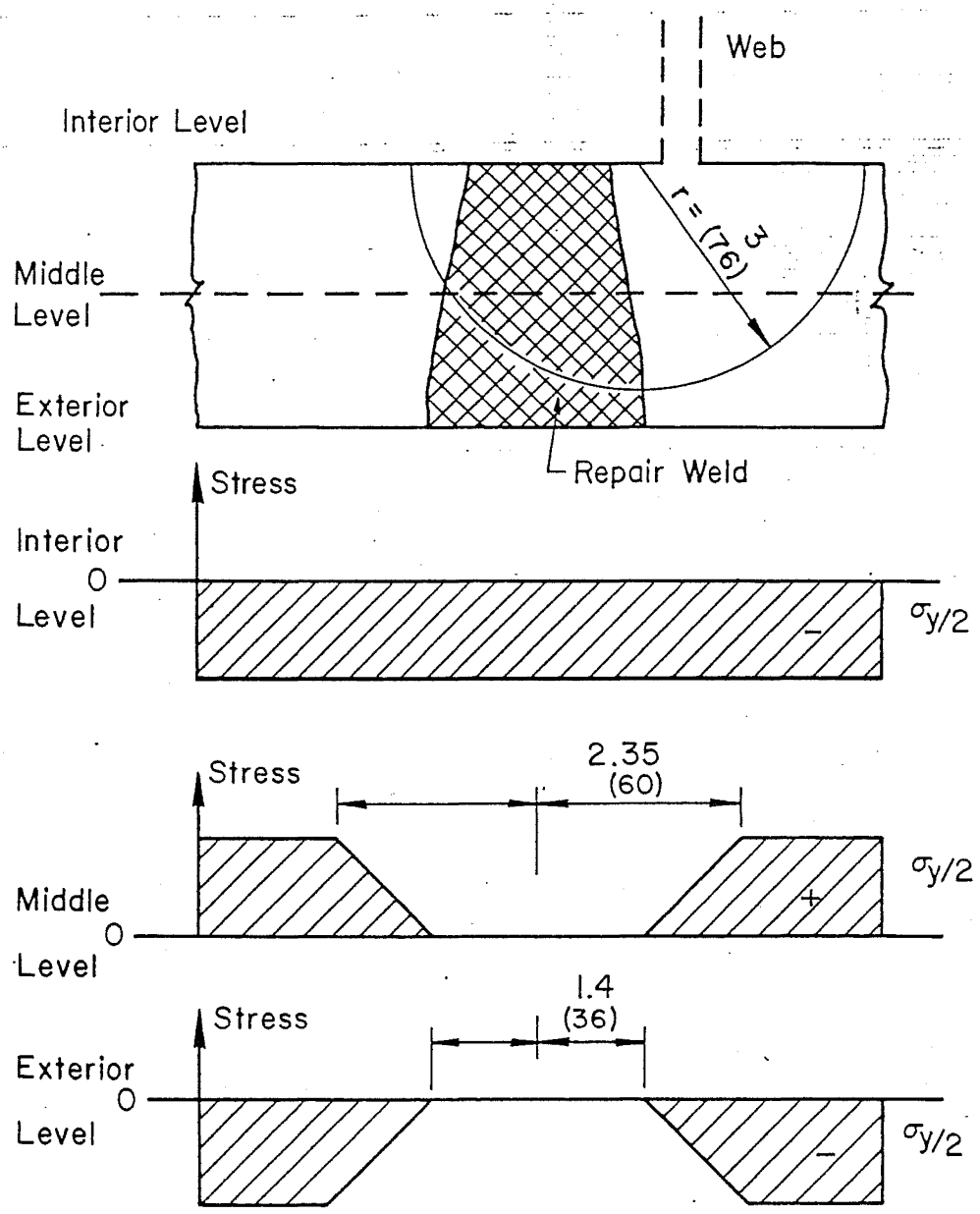

Fig. 77 Idealization of the Repair Weld at the Crack and the Assumed Alteration to Original Electroslag Weld Residual Stress Distribution

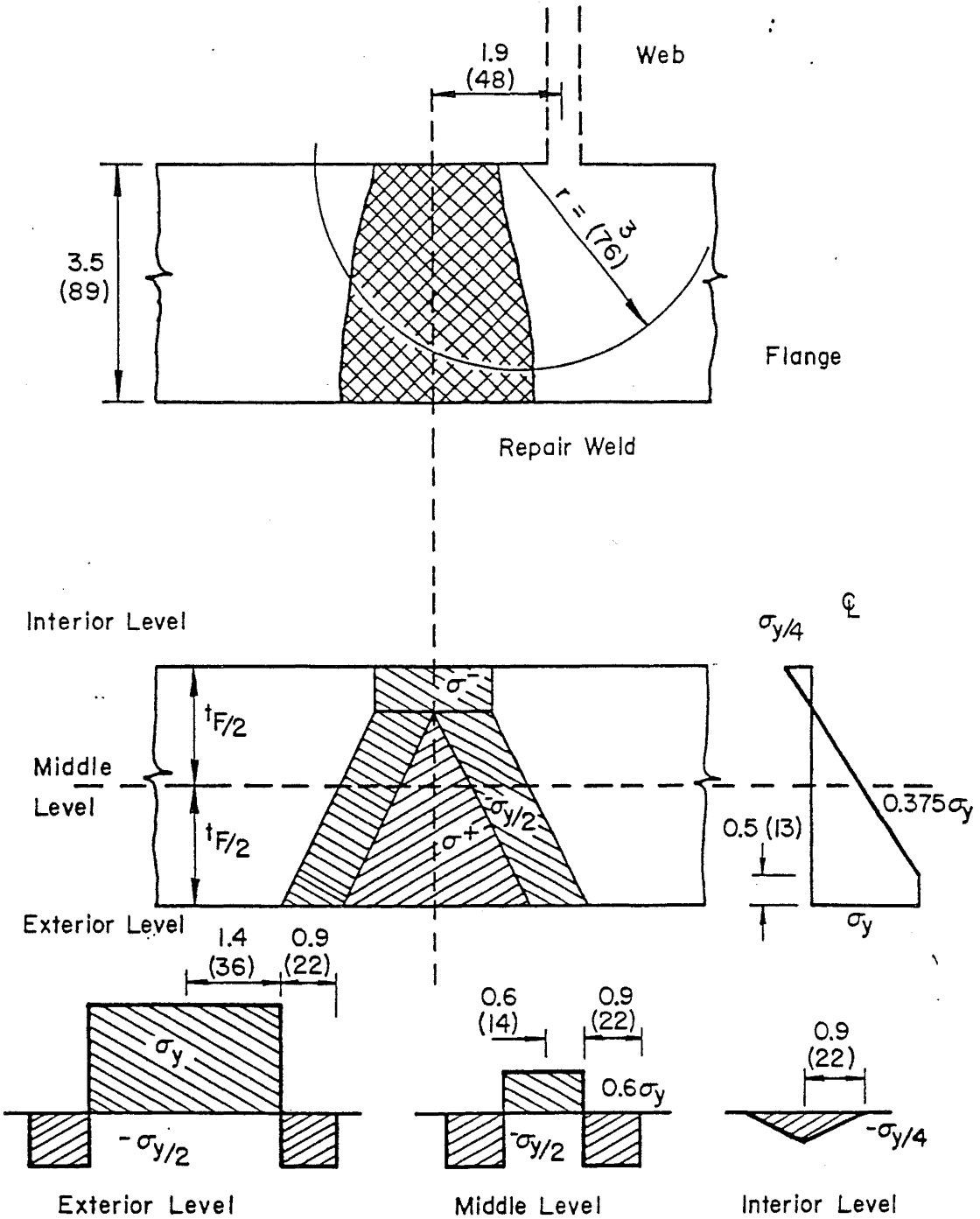

Fig. 78 Assumed Residual Stress Distribution as a Result of the Repair Weld

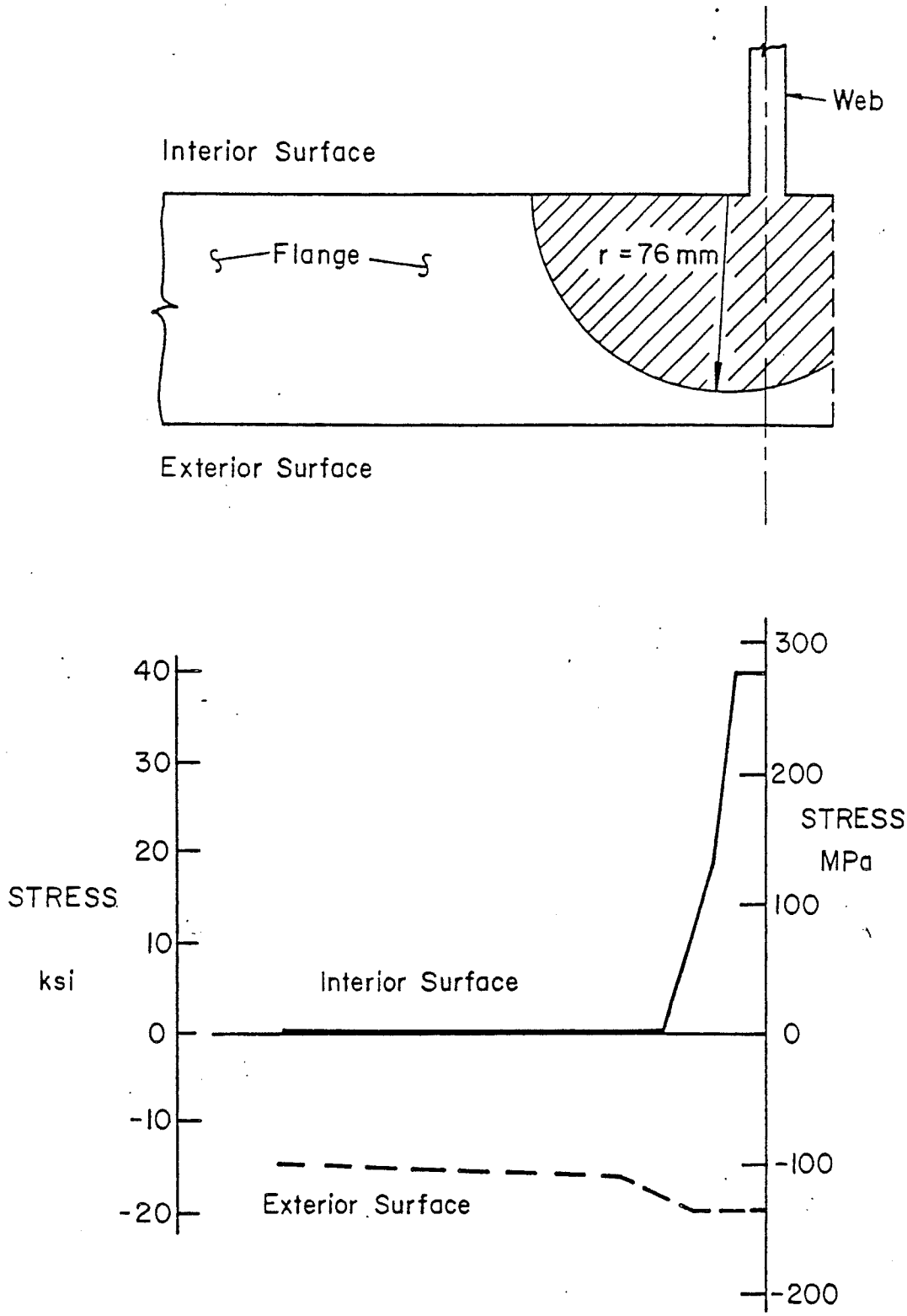

Fig. 79 Residual Stresses Resulting from the Web-to-Flange Weld

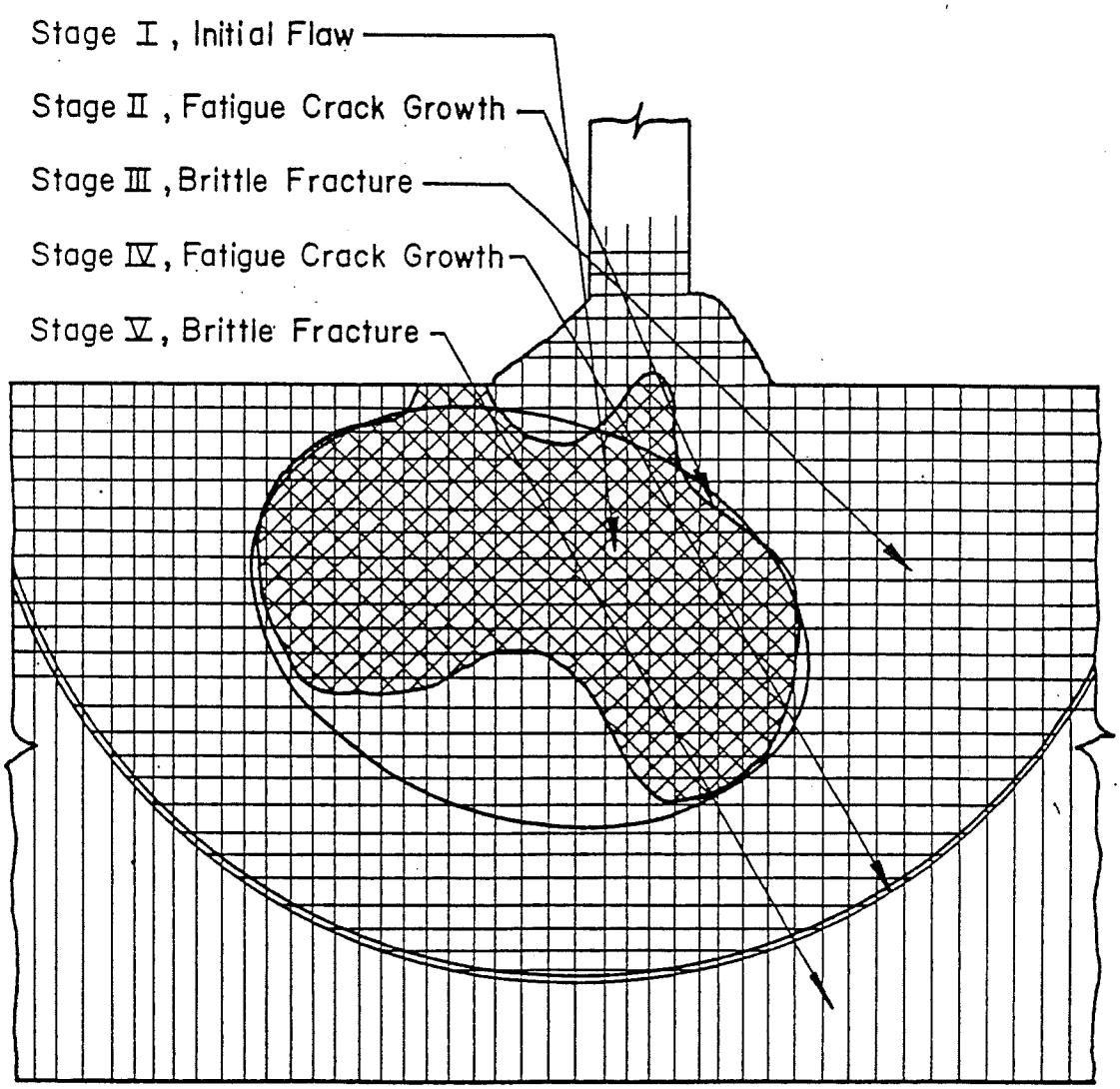

Fig. 80 Idealization of the Various Stages of Cracking at the Casualty Section

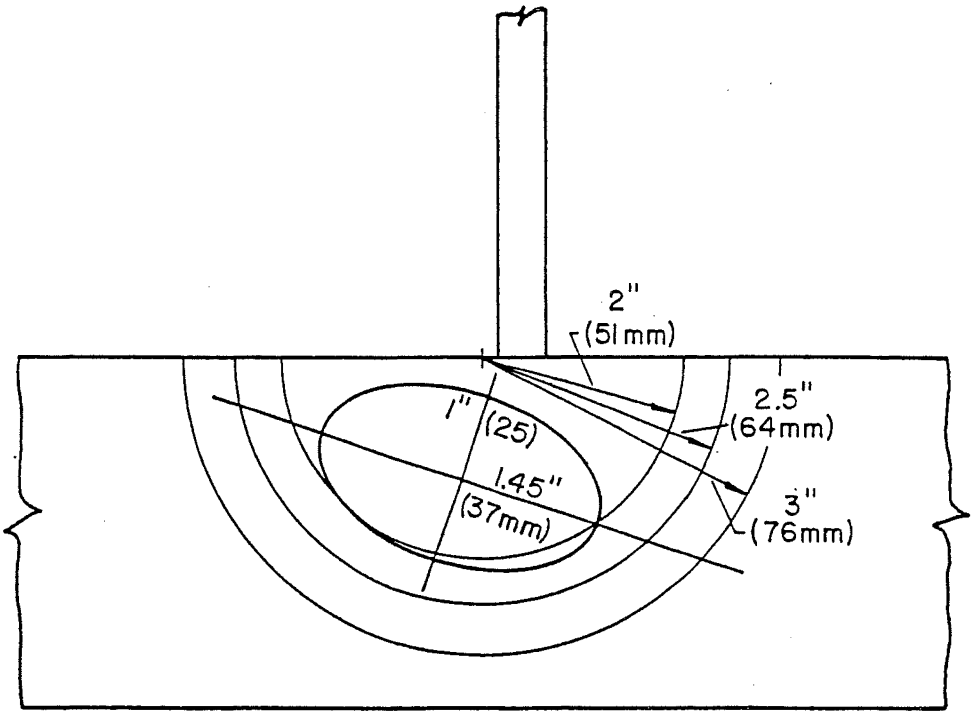

Fig. 81 Idealized Elliptical Shaped Initial Crack and Subsequent Penny-Shaped Crack Fronts

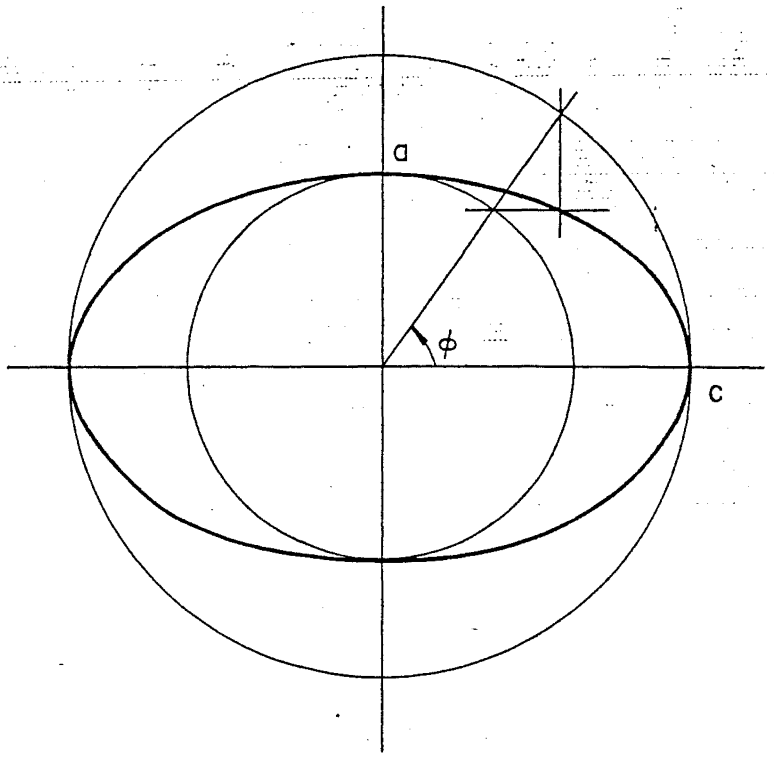

$$y = a \sin \phi$$

$$x = c \cos \phi$$

$$K = \sigma (\pi a)^{1/2} \cdot F_e$$

$$F_e = \frac{1}{E(k)} \left(\sin^2 \phi + \left(\frac{a}{c}\right)^2 \cos^2 \phi\right)^{1/4}$$

$$E(k) = \int_0^{\pi/2} (1 - k^2 \sin^2 \theta)^{1/2} \, d\theta$$

$$k^2 = 1 - \left(\frac{a}{c}\right)^2$$

Fig. 82 Stress Intensity Expression for an Elliptical Crack in an Infinite Plate

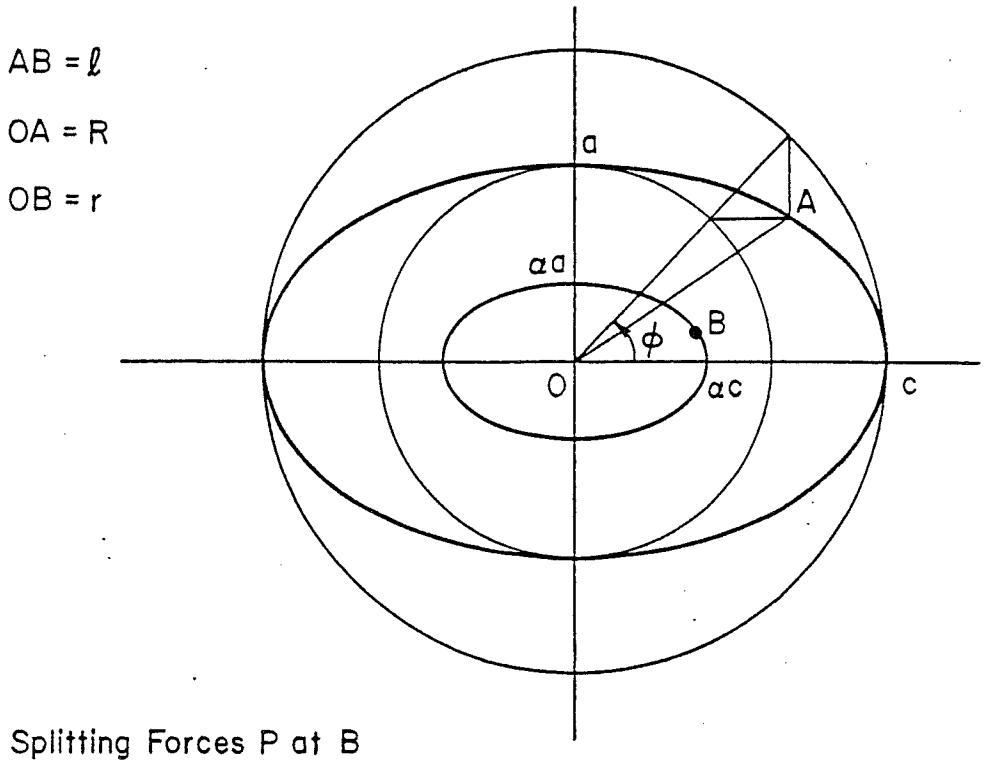

$$K = \frac{P\sqrt{a}}{\pi^{3/2}\ell^2}\sqrt{\frac{r}{R}}\;\frac{\sqrt{\frac{1}{\alpha^2}-1}}{\left\{1-k^2\cos^2\phi\right\}^{1/4}}$$

Fig. 83 Stress Intensity Factor at Point A for a Concentrated Force at Point B

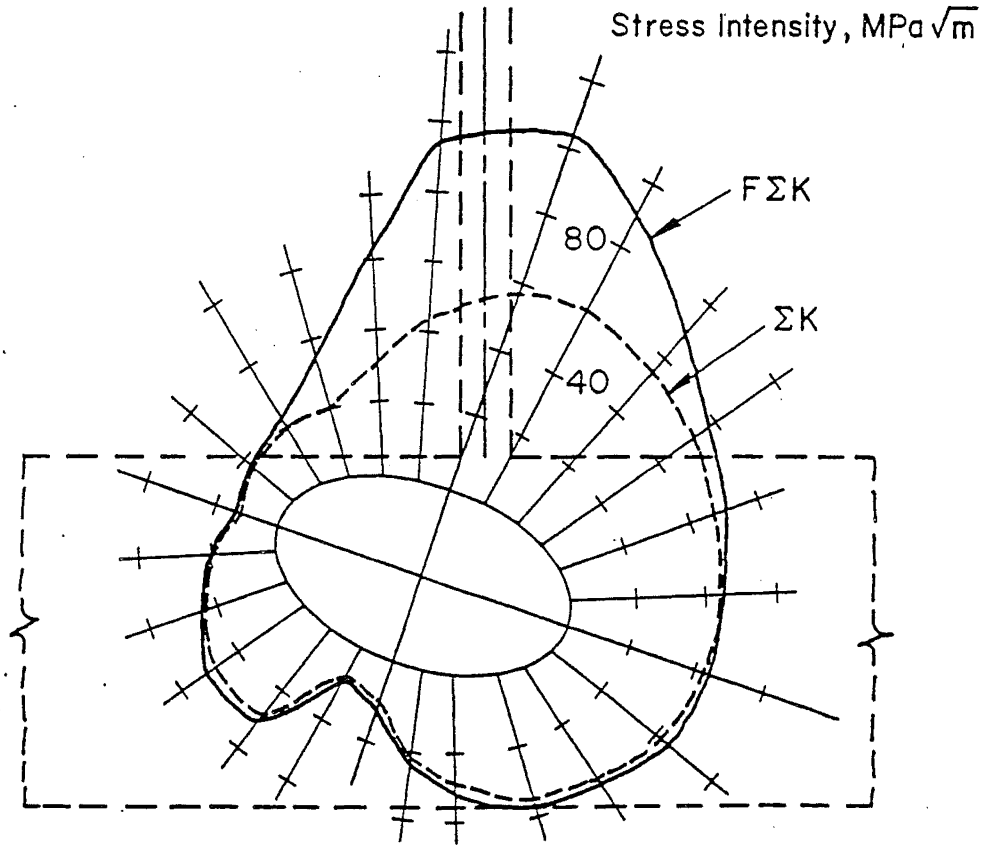

Fig. 84 Predicted Distribution of the Stress Intensity Factor Around the Boundaries of the Initial Flaw

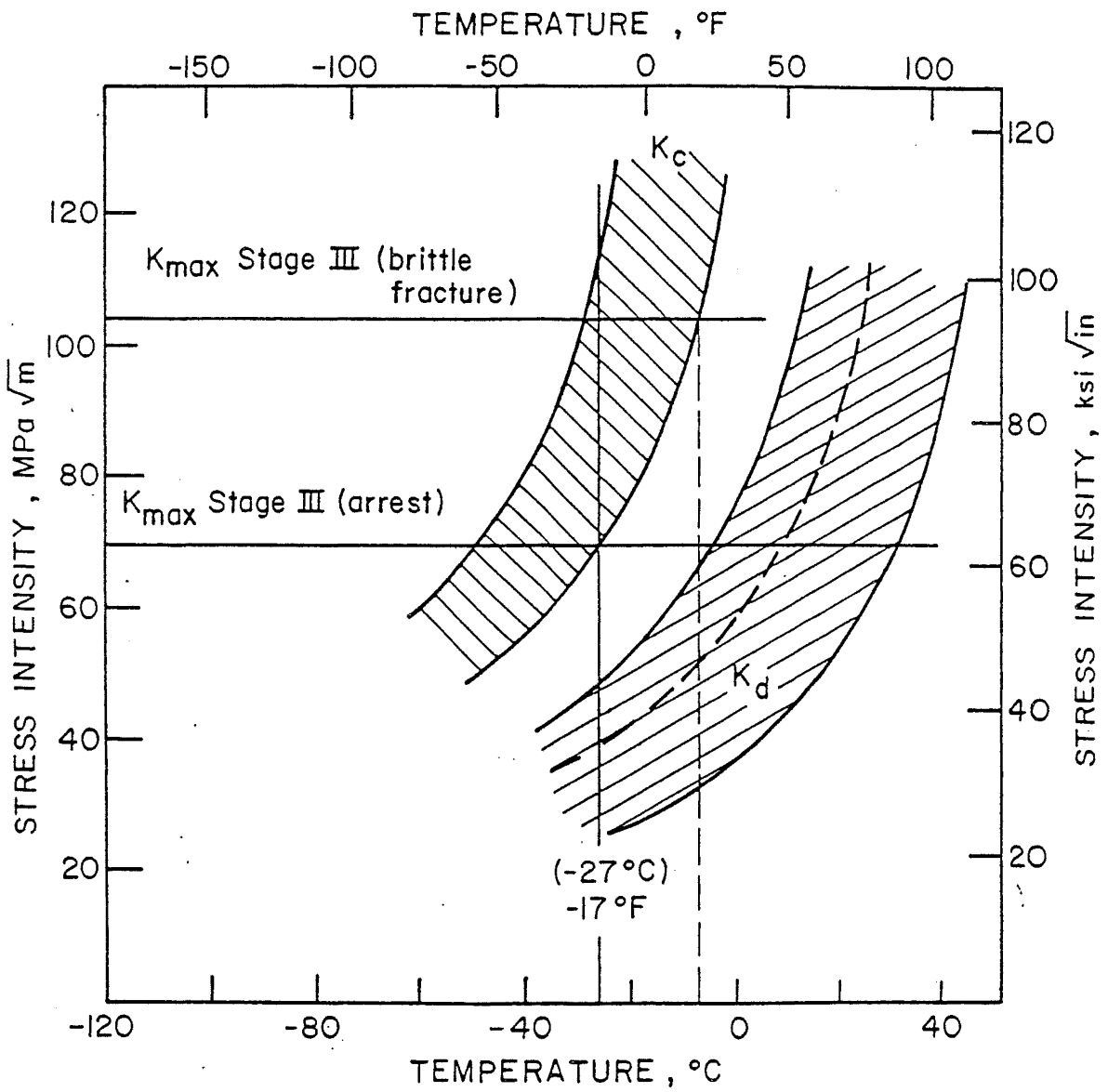

Fig. 85 Comparison of Estimated Stress Intensity Factor for Stage III Crack With Fracture Resistance of Electroslag Weldments

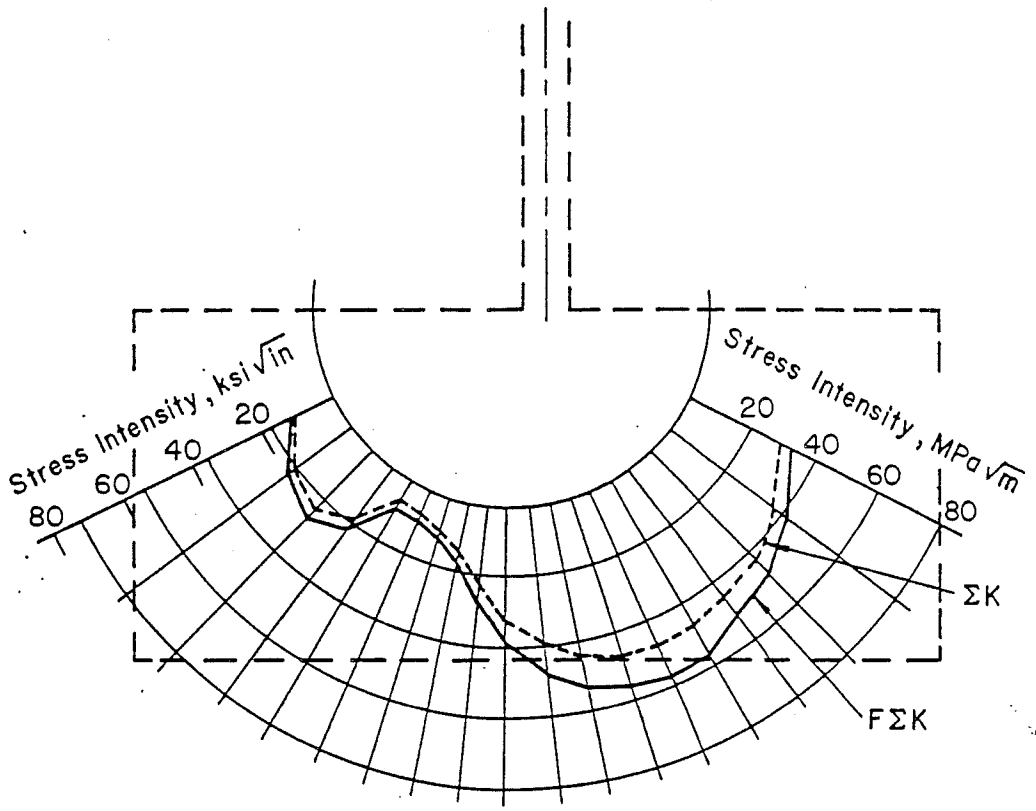

Fig. 86 Predicted Stress Intensity Factor Along 2 in. (51 mm) Radius Crack Front

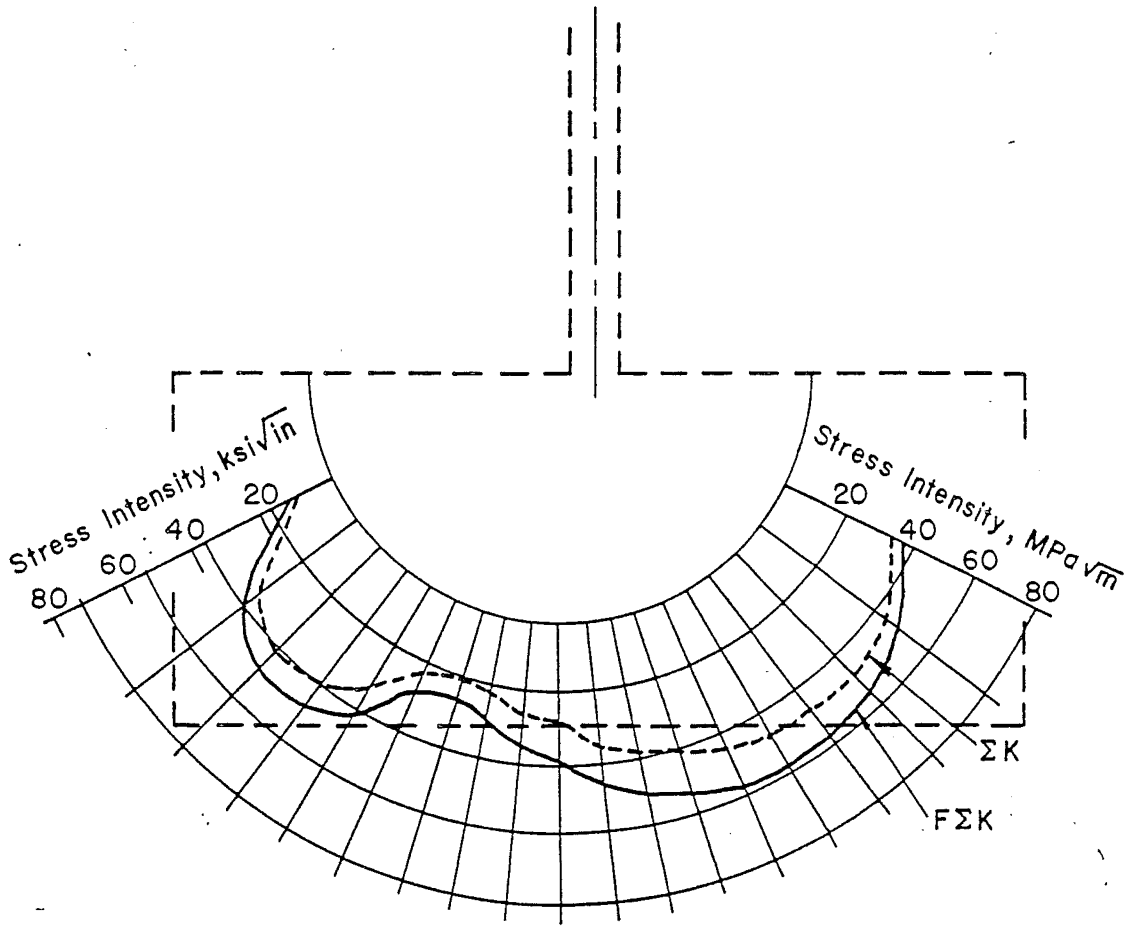

Fig. 87 Predicted Stress Intensity Factor Along 2.5 in. (64 mm) Crack Front

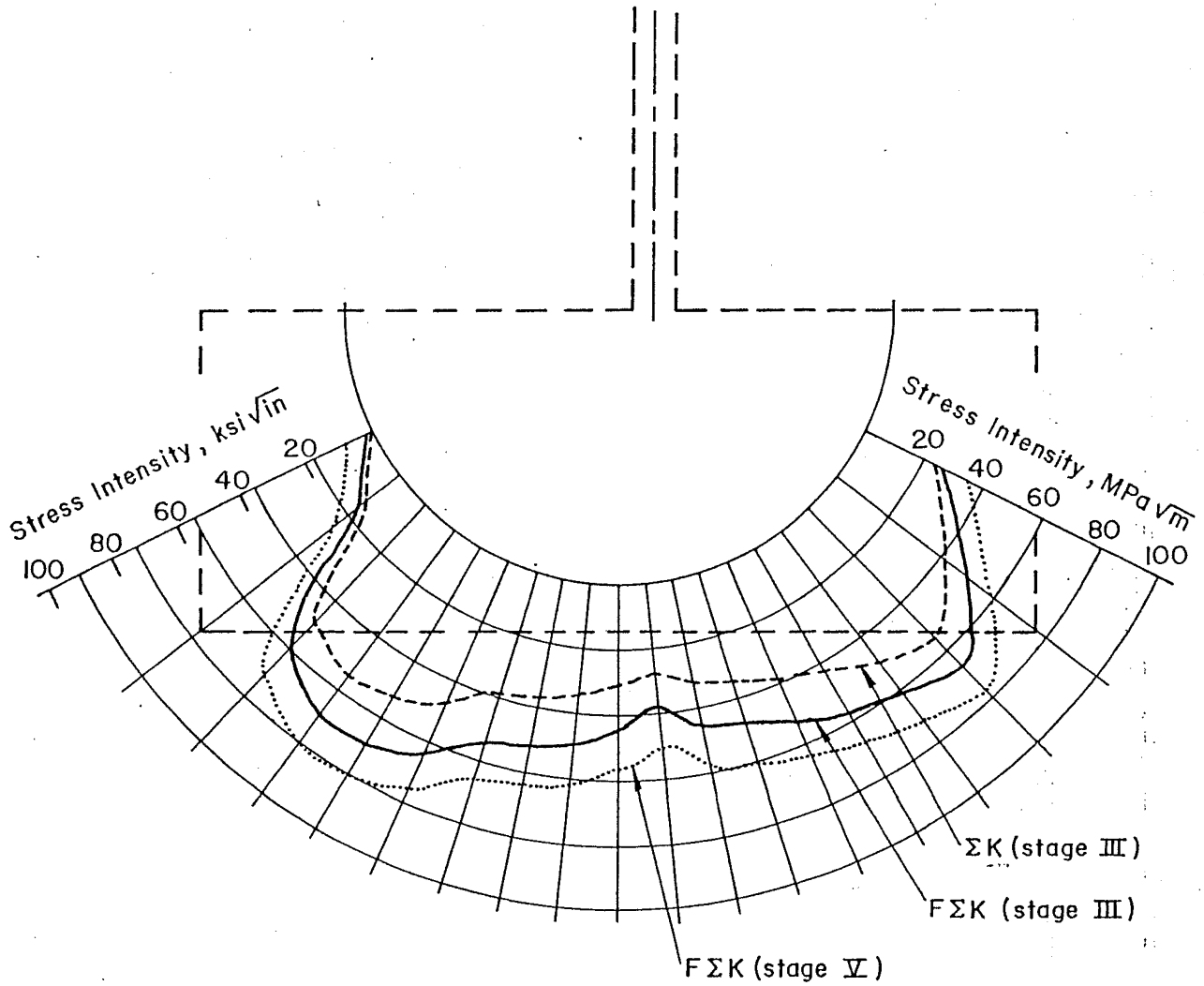

Fig. 88 Predicted Stress Intensity Factor Along 3 in. (76 mm) Crack Front

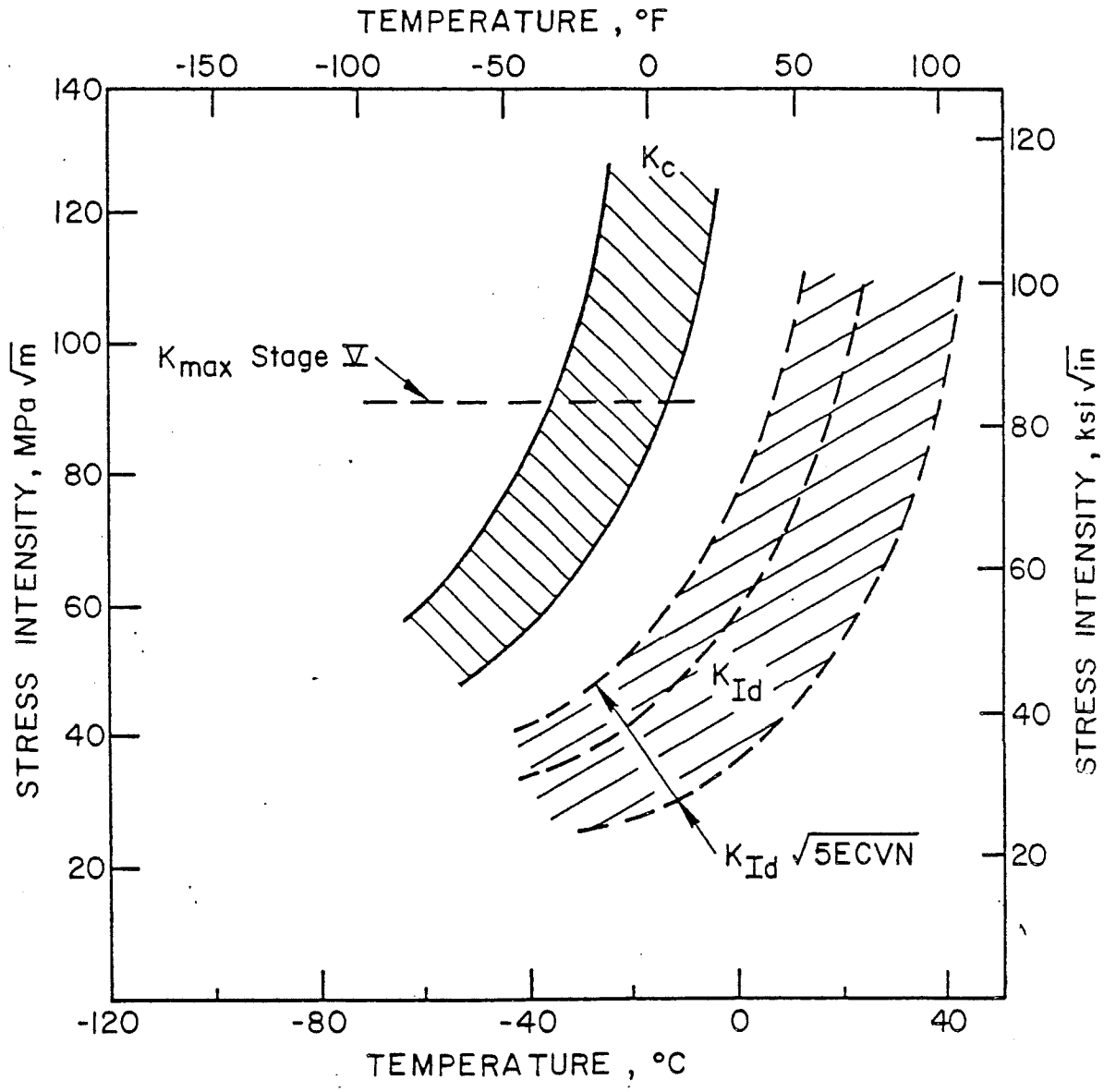

Fig. 89 Comparison of Predicted Stress Intensity Factor for Stage V Crack With Fracture Resistance of Electroslag Weldment

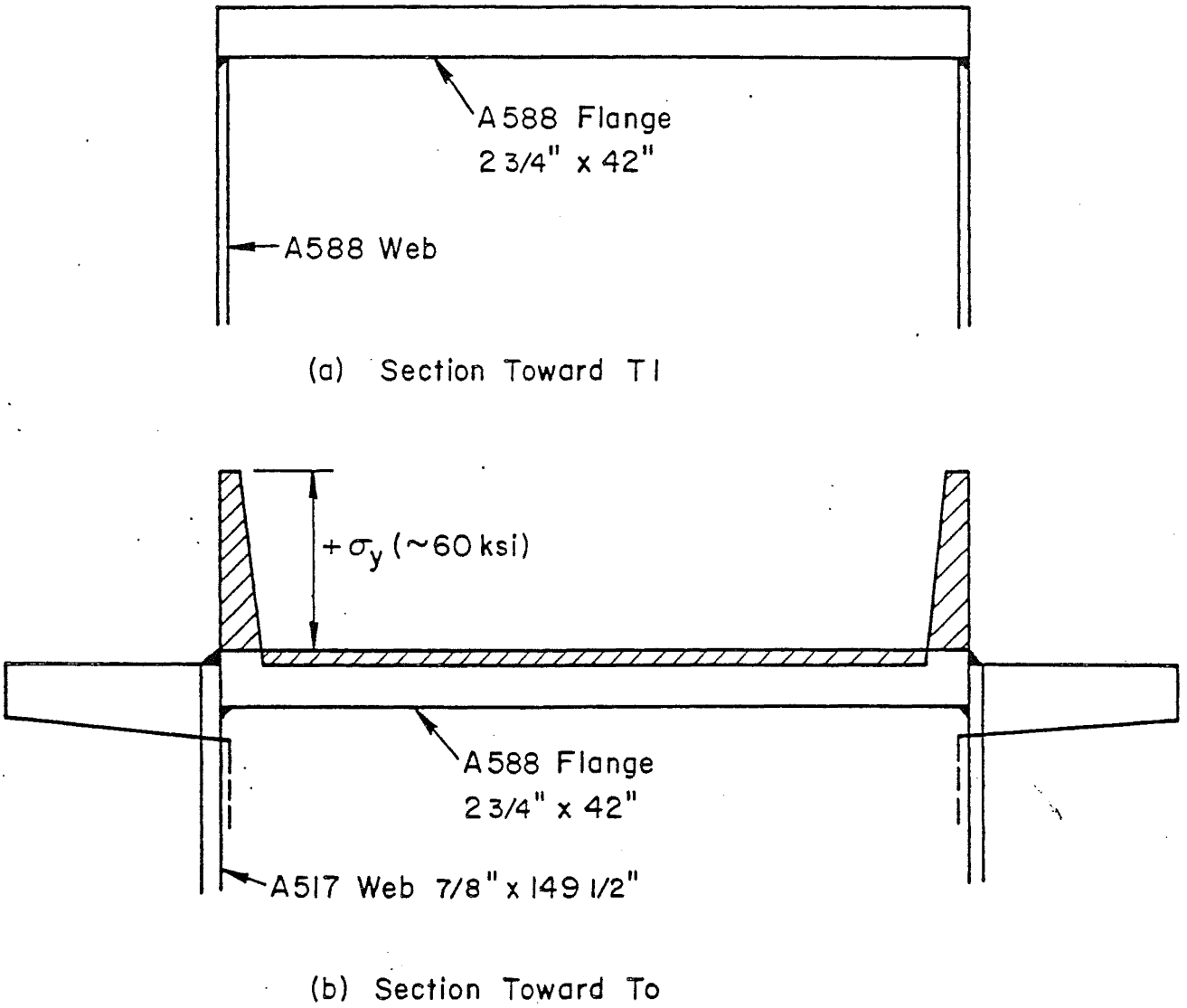

Fig. 90 Schematic of Assumed Longitudinal Residual Stress Distribution in Tee Girder

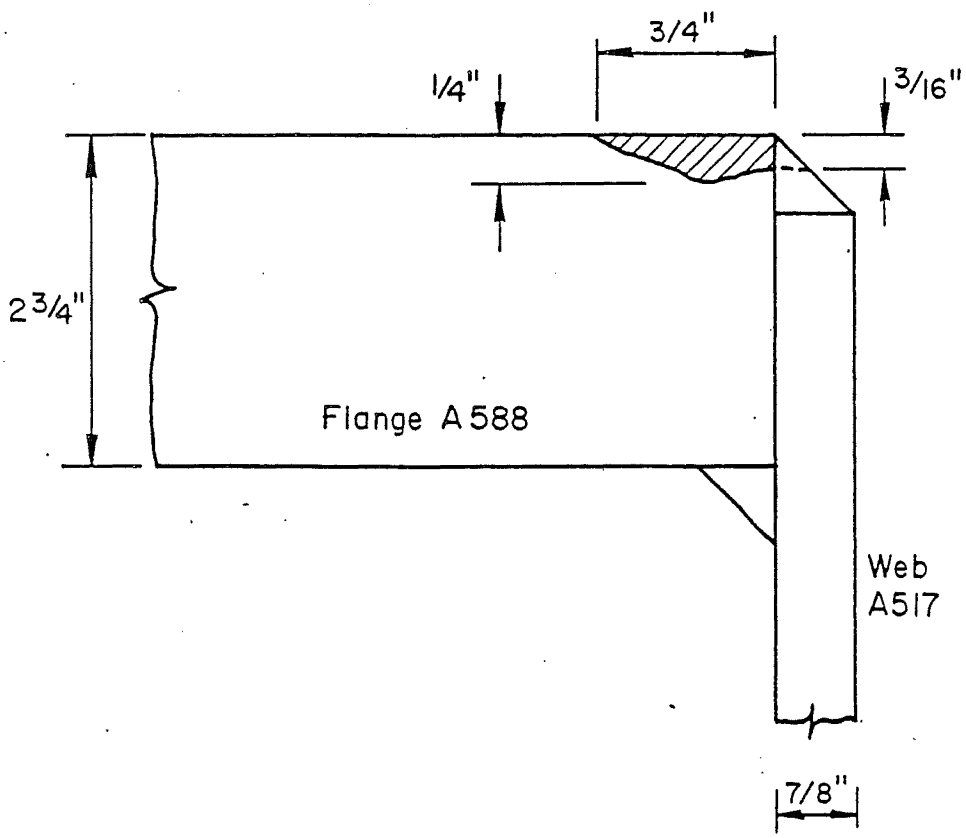

Fig. 91 Schematic of Crack in the Tie Girder

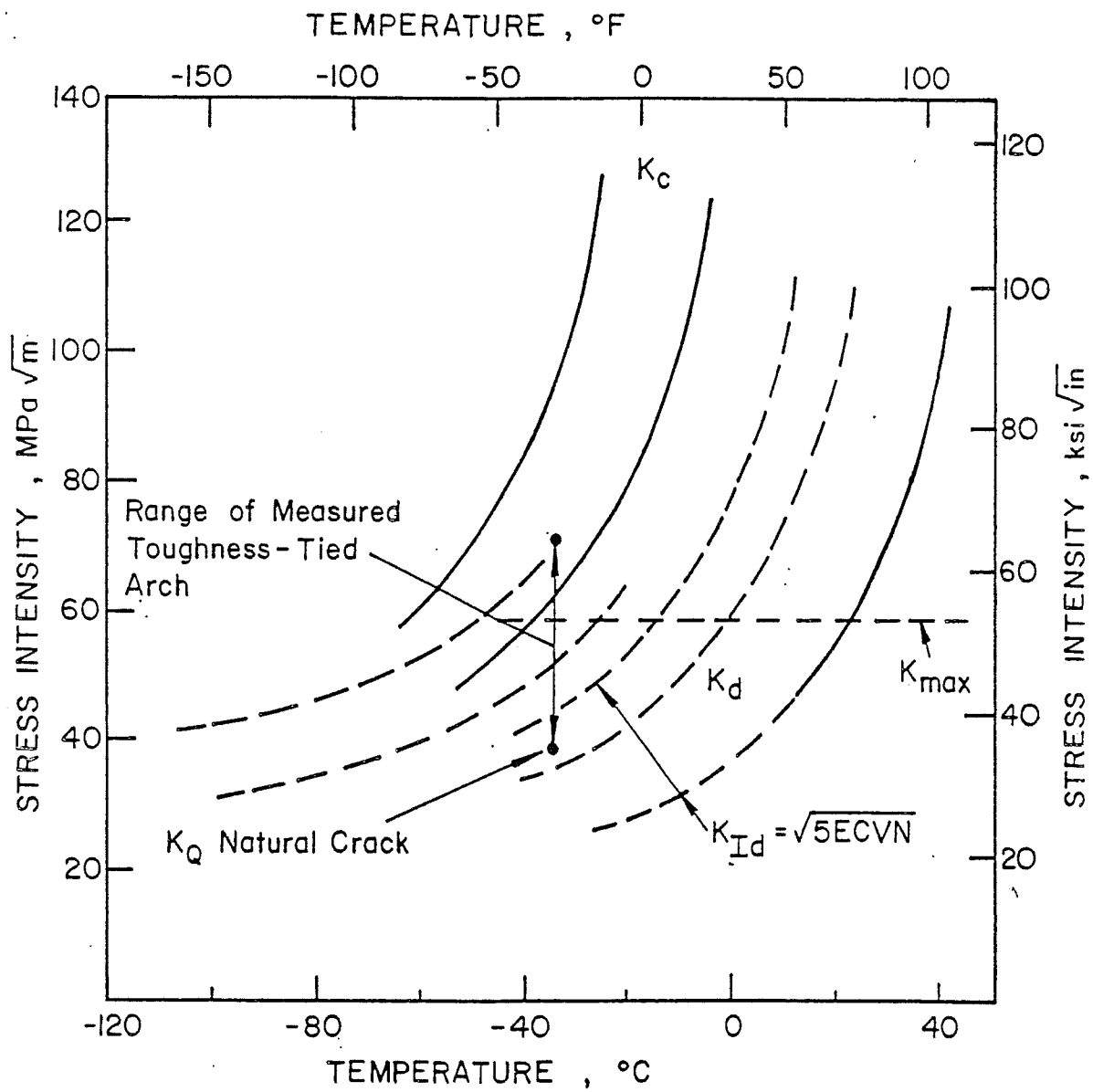

Fig. 92 Comparison of the Estimated Stress Intensity Factor at the Tie Girder Crack with the Estimated Electroslag Fracture Toughness and the two Bend K_Q Tests

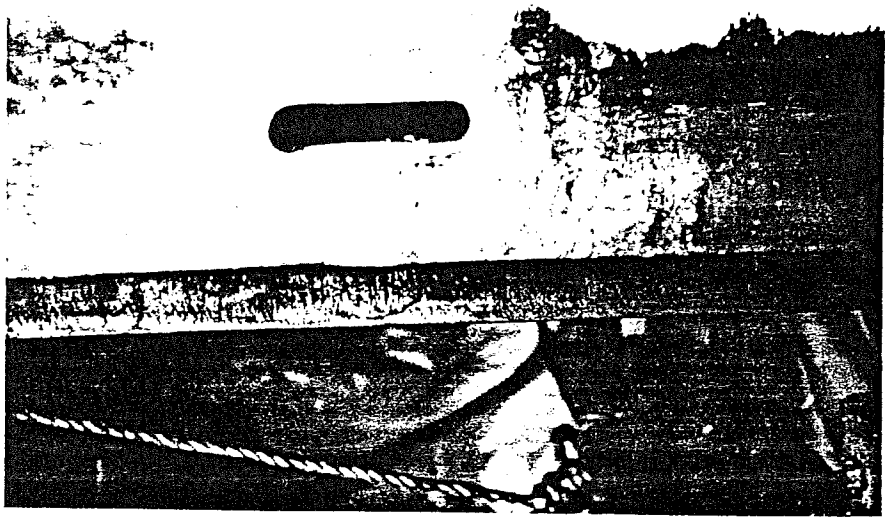

Fig. 93 Slot Placed in Tie Girder Web Above the Electroslag Flange Welds

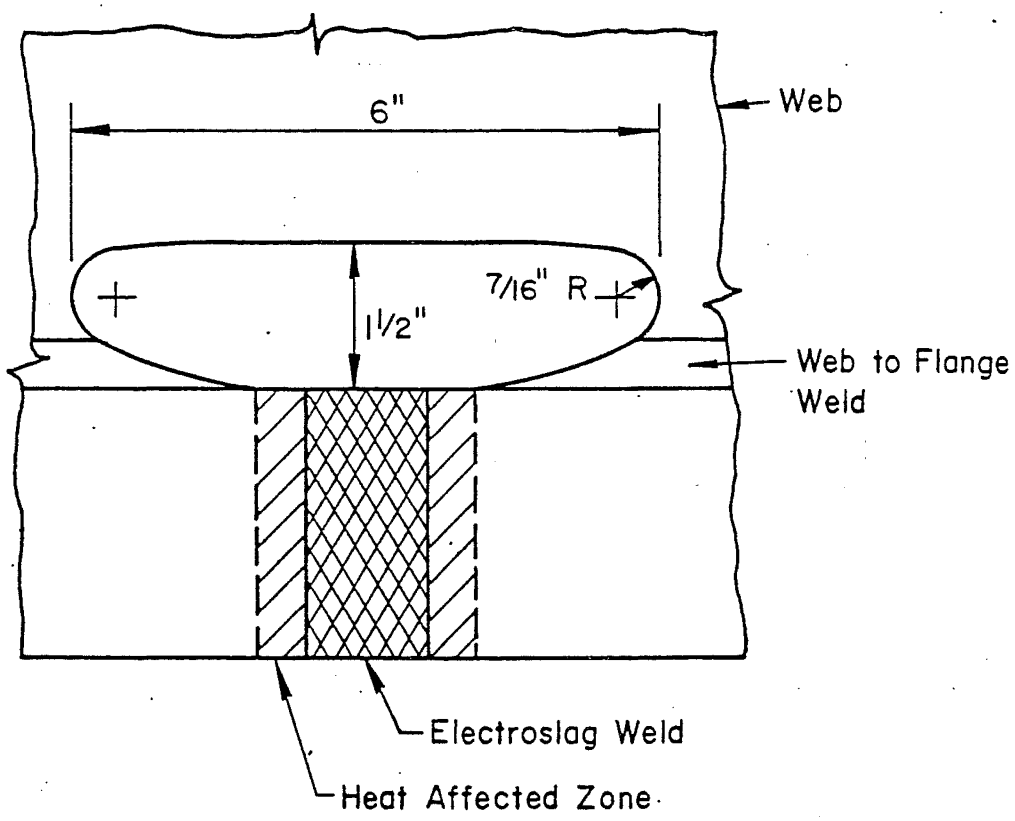

Fig. 94 Schematic of Slots Placed in the Back Channel Girder Web Above the Electroslag Weldments

REFERENCES

1. CRACKED GIRDER CLOSES I79 BRIDGE, Engineering News Record, February 10, 1977, p. 11.

2. Schwendeman, L. J. and Hedgren, A. W., Jr.
BOLTED REPAIR OF FRACTURED I79 GIRDER, Journal of the Structural Division, ASCE, Vol. 104, No. ST10, October 1978.

3. Pittsburgh Testing Laboratory
NONDESTRUCTIVE TESTING OF CERTAIN WELDS IN ARCH TIE OF NEVILLE ISLAND BRIDGE I79, February 21, 1977.

4. Minutes of meeting of February 28, 1979, District 11-0, Pennsylvania Department of Transportation.

5. Benter, W. P., Jr., Konkol, P. J., Kapadia, B. M., Shoemaker, A. K. and Sovak, J. F.
ACCEPTANCE CRITERIA FOR ELECTROSLAG WELDMENTS IN BRIDGES, Phase I, Final Report NCHRP Project 10-10, July 1976.

6. Ramos, J. B. deS., Pense, A. W., and Stout, R. D.
FRACTURE TOUGHNESS OF ELECTROSLAG WELDED A537G STEEL, Welding Research Supplement, January 1976.

7. Rolfe, S. T. and Barsom, J. M.
FRACTURE AND FATIGUE CONTROL IN STRUCTURES, Prentice-Hall, Inc., Englewood Cliffs, New Jersey, 1977.

8. American Welding Society (AWS),
STRUCTURAL WELDING CODE, 1st Edition, Section , 1972, New York City.

9. Report of the I79 Oversight Committee, S. J. Fenves, R. E. Untrauer and M. L. Williams, November 15, 1977.

10. Letter from F. Schmidt to Udani of August 30, 1977, Radiographic Inspection by Peabody.

11. Letter from J. W. Fisher to N. Udani of August 3, 1977.

12. Alpsten, G. A. and Tall, L.
RESIDUAL STRESSES IN HEAVY WELDED SHAPES, Welding Journal, Vol. 49, March 1970.

13. Roberts, R., Fisher, J. W., Irwin, G. R., Boyer, K. D., Hausamman, H., Krishna, G. V., Morf, U. and Slockbower, R. E.
DETERMINATION OF TOLERABLE FLAW SIZES IN FULL SIZE WELDED BRIDGE DETAILS, Report No. FHWA-RD-77-170, Federal Highway Administration, December 1977.

14. Tada, H., Paris, P., and Irwin, G. R.
THE STRESS ANALYSIS OF CRACKS HANDBOOK, Del Research Corporation, Hellertown, Pa., 1973.

15. Hertzberg, R. W. and Von Euw, E. F. J.
CRACK CLOSURE AND FATIGUE STRIATIONS IN 2024-T3 ALUMINUM ALLOY, Metallurgical Transactions, Vol. 4, March 1973, pp. 887-889.

16. Bates, R. C. and Clark, W. G., Jr.
FRACTOGRAPHY AND FRACTURE MECHANICS, Transactions Quarterly, American Society of Metals, Vol. 62, No. 2, June 1969, pp. 380-390.

17. Tada, H. and Irwin, G. R.
K-VALUE ANALYSIS IN BRIDGE STRUCTURES, Fritz Engineering Laboratory Report 399.1, Bethlehem, Pa., 1975.

18. Fisher, J. W., Yen, B. T., and Daniels, J. H.
FATIGUE DAMAGE IN THE LEHIGH CANAL BRIDGE FROM DISPLACEMENT-INDUCED SECONDARY STRESSES, Transportation Research Record 607, TRB, 1976.

19. Stress Sheet for Arch-Main Span, Sheet 10 of 167, Bridge S-9424.

20. Baldwin, J. W. and Guell, D. L.
PERMANENT DEFLECTIONS AND LOSS OF CAMBER IN STEEL BRIDGE BEAMS, Final Report NCHRP Projects 12-1 and 12-6.

21. Albrecht, P.
A STUDY OF FATIGUE STRIATIONS IN WELD TOE CRACKS, Fatigue Testing of Weldment Cracks, ASTM STP 684, ASTM 1978, pp. 197-217

22. Takahashi, E. and Iwai, K.
PREVENTION OF THE TRANSVERSE CRACKS IN HEAVY SECTION BUTT WELDMENTS OF 2-1/4 Cr - 1 Mo STEEL THROUGH LOW TEMPERATURE POSTWELD HEAT TREATMENT, Transactions of the Japan Welding Society, Vol. 10, No. 1, April 1979.

ACKNOWLEDGMENTS

This investigation was conducted at the Fritz Engineering Laboratory and Whitaker Laboratory, Lehigh University, Bethlehem, Pennsylvania. The project was sponsored by the Pennsylvania Department of Transportation and the Federal Highway Administration, U. S. Department of Transportation.

The authors wish to acknowledge the assistance provided by the Pennsylvania Department of Transportation during the various phases of this study. Records were made available, as needed, access was provided to the bridge structures for inspection and instrumentation, and assistance was provided as needed.

Appreciation is also due Dr. George R. Irwin for valuable discussions and assistance with the fracture analysis. Thanks are also due Mrs. Ruth Grimes who typed the manuscript, Mr. John Gera for preparation of the figures, Mr. Richard Sopko for photography and Mrs. Dorothy Fielding for assistance with reproduction of the report.